Iranian Hydraulic Association

Shahid Chamran University of Ahvaz

Journal of
Hydraulic Structures

Scientific Professional Journal



April 2026
Volume 12, Issue 2

ISSN (Online): 2345-4156
https://jhs.scu.ac.ir/

Aims and Scope

Journal of Hydraulic Structures is an interdisciplinary journal which publishes high-quality peer-reviewed articles addressing the latest developments and applied methods in analysis and design, construction, maintenance, management, and operation policy of Hydraulic Structures.

The Journal aims at providing an efficient route to fast-track publication, within 10-12 weeks after manuscript submission.

The general areas covered by the Journal include:

- Advances in numerical and analytical methods applicable to hydraulic structures
- Hydro informatics and soft computing
- Hydraulic aspects of hydraulic structures
- Applied surface and subsurface hydrology and hydrometeorology
- Forecasting approaches in water resources engineering
- Economic and social aspects of hydraulic structures
- Uncertainty analysis and risk management in hydraulics and water resources engineering
- Application of Nanotechnology in hydraulic structures
- Geotechnics of hydraulic structures
- Damage detection techniques
- Technical and methodological advances in application, design/selection, production, construction materials of hydraulic structures.
- Application of Artificial Intelligence techniques in all aspects of hydraulic structures.

General Information:

Title: Journal of Hydraulic Structures

Publisher: Shahid Chamran University of Ahvaz

ISSN (Print): 2345-413X

ISSN (Online): 2345-4156

Website: jhs.scu.ac.ir

Address: Faculty of Civil Engineering and Architecture, Shahid Chamran University of Ahvaz, Ahvaz, Iran

Email: jhs@scu.ac.ir

Journal of Hydraulic Structures

Department of Civil Engineering

Shahid Chamran University of Ahvaz

Journal of

Hydraulic Structures

Shahid Chamran University of Ahvaz

Director-in-Charge: Prof. Ali Haghighi

Editor-in-Chief: Prof. Hamid R. Ghafouri

Managing Editor: Dr. Amir H. Shafiee

Contents:

01

Geostatistical Analysis of Groundwater Levels at Tangab Dam Using IDW, Kriging, and Sequential Gaussian Simulation

Reza Dehshibi; Hadi Farhadian

22

Analytical solutions for steady downward flow of a wetting fluid in unsaturated soil using the Adomian decomposition method

Hamed Reza Zarif Sanayei

34

Assessing the Impact of Multi-Reservoir Rationing on Downstream Drought Occurrence: A Case Study of Dez and Gotvand Reservoirs

Sama Banitamim; Seyed Mohammad Ashrafi; Arash Adib

51

Numerical Study of Impulsive Wave Overtopping at Rigid Hydraulic Structures Using Incompressible Smoothed Particle Hydrodynamics Model

Rasoul Memarzadeh

74

The Optimal Selection of Submerged Vanes Geometric Dimensions in Curved Channels with Sediment Flow

Parisa Rezaei; Elham Fazel Najafabadi; Mohammad Shayannejad

103

Assessment of Site Suitability and Capacity for Sustainable Aquaculture Development Along the Northern Persian Gulf Coast

Morteza Jedari Attari; Aref Farhangmehr

Geostatistical Analysis of Groundwater Levels at Tangab Dam Using IDW, Kriging, and Sequential Gaussian Simulation

Reza Dehshibi[1], Hadi Farhadian[*,2]

1. Department of Engineering, University of Sistan & Baluchestan, Zahedan, Iran.
2. Department of Mining Engineering, Faculty of Engineering, University of Birjand, Birjand, Iran.

***Corresponding Author:**
Hadi Farhadian,

Email: farhadian@birjand.ac.ir
Received: 2025.05.13
Accepted: 2025.07.01
J. Hydraul. Struct., 2025; 12(2):1-21
DOI: 10.22055/jhs.2025.49615.1350

ABSTRACT

Monitoring groundwater levels at every point in dam abutments is often impractical; hence, geostatistical interpolation methods offer a viable alternative. This study applied inverse distance weighting (IDW), kriging, and sequential Gaussian simulation (SGS) to estimate groundwater levels at the Tangab Dam, based on data from 49 piezometers. After data normalization, variogram modeling identified the spherical model as the best fit, with a nugget-to-sill ratio of 19%, indicating strong spatial continuity. While IDW served for initial visualization, kriging and SGS revealed higher groundwater levels along the dam's right abutment, corresponding to fault zones and karst features. The SGS approach, performed through 100 realizations, accurately reproduced the spatial variability and statistical properties of the observed data. Validation showed a correlation coefficient of 0.93 and unbiased residuals, confirming the model's reliability in well-instrumented regions. However, estimations in the northeastern and eastern zones were less reliable due to sparse data. This study underscores the value of integrating geostatistics and geological context for characterizing groundwater behavior in complex karst environments. Future work should involve expanding the monitoring network and coupling geostatistical outputs with numerical flow models to improve prediction and support dam safety assessments.

KEYWORDS
geostatistics, kriging, sequential Gaussian simulation, groundwater level, Tangab Dam.

1. Introduction

One of the fundamental requirements in the exploratory stages of dam construction studies is assessing the permeability and joint conditions, as well as understanding hydrogeochemical behavior [1–3]. Hydrogeological measurements, such as hydraulic conductivity and transmissibility, can exhibit significant uncertainty due to the complexity of geological conditions [4–6]. As a result, various estimation and simulation techniques are employed to address this uncertainty in hydrogeological measurements. In recent years, the uncertainty associated with hydrogeological and geotechnical parameters has been extensively studied, with the hydraulic parameters of the aquifer being estimated using geostatistical methods. The application of geostatistical simulation techniques provides a useful approach to modeling the geometry of permeable layers [7–10].

Previous studies have investigated various aspects of the Tangab Dam site in southern Iran—ranging from karst development and hydraulic connectivity to fault zones and spring origins—each contributing valuable insights yet leaving several research gaps. Akhondi and Mohammadi [11] used 953 water pressure tests to assess the effective porosity and karst development in the Tangab Dam region. Using geostatistical techniques, they examined the behavior of the karst aquifer, the function of the epikarst region, the impact of nutrient input in karst aquifers on spring hydrographs, and the relationship between karstification and permeability (from water pressure tests). According to their study, the length of the major karst channel is one of the most influential factors affecting hydrograph and water fluctuation variations.

In a study by Madani Esfahani and Asghari [12], sequential Gaussian simulation (SGS) was employed to identify areas with varying rock-quality designation (RQD). They found that locations with an RQD of less than 20% were classified as fault areas, while regions with an RQD greater than 50% were less fragmented.

Karimi et al. [13] utilized hydrochemical time series data from springs in the Tangab Dam area to identify the sources of the springs and their interrelationships. The dam site is located between two impassable marl formations and consists of karst limestone and dolomite. The aquifer in the region is drained by 23 springs located to the south. The study measured the main ions, electrical conductivity, temperature, and pH of the springs over a period of 17 months, and they found that four springs were most likely sourced from the southern portion of the region, while the remaining springs were located in both the southern and northern areas.

In another study, Mozafari et al. [14] examined leakage on the right side of the Tangab Dam using a numerical model with SEEP/W software. Their research indicated that the majority of seepage occurred in karst areas, as well as in cracks and crevices.

Asadi [15] employed color detectors to propose two broad models: one for the branching of the main flow transfer channel and the other for identifying the origin of springs in the potential water escape range of the Tangab Dam. The study involved sampling, measuring, and analysis over seven months at 45 locations, with approximately 2000 water samples and 180 bags of activated charcoal evaluated. Their findings underscored the hydrogeological connection between the Tangab region springs and the dam, suggesting that this relationship is facilitated by a single-channel karst system.

Despite these contributions, a critical gap persists in quantitatively characterizing the spatial uncertainty of groundwater level variations—particularly in highly fractured and karstified environments like Tangab—using integrated geostatistical approaches that incorporate both hydrogeological and structural geological data. Huysmans and Dassargues [16] were among the first to apply multiple-point geostatistics in groundwater studies, using an aquifer in Belgium. Their study demonstrated how multiple-point geostatistics could be employed to assess the effects of geological heterogeneity on groundwater flow within the aquifer. They found that pollution clouds resulting from variogram-based simulations expanded more in both the horizontal and vertical directions compared to those simulated with multiple-point geostatistics.

Marache et al. [17] drew a directional variogram along boreholes in a French city. In their study, they used sequential indicator simulation to create a 3D model of geotechnical borehole data (bulk modulus) based on a set of threshold limitations. The results showed that integrating petrological data with geotechnical borehole data improved the simulation outcomes.

Geostatistical methods have been widely used to estimate hydraulic parameters of aquifers and investigate the uncertainty of

hydrogeological and geotechnical parameters. One method for modeling the geometry of permeable layers is geostatistical simulation. This method has been applied in fracture system modeling to study fluid flows inside rocks [18]. The geostatistical simulation method allows for the simulation of variables using statistical parameters derived from spatial data analysis. Sequential indicator simulation, in particular, is one of the most effective approaches for studying the uncertainty of random variables [19].

Furthermore, although studies by Hosseini et al. [20] and Bai et al. [21] highlight the effectiveness of such models in oil fields and groundwater pollution assessment, they do not address spatial uncertainty in groundwater levels in the context of dam safety. The leakage analysis at Tangab Dam, which accounts for both diffuse and conduit flow systems, further underscores the need for spatially explicit models. Under a diffuse flow assumption, leakage remains within acceptable thresholds, but under conduit flow conditions, small-diameter conduits can cause disproportionately high leakage—introducing major uncertainty into design and risk assessments. This necessitates a more rigorous spatial understanding of flow paths and the role of structural geology in controlling permeability, especially in regions outside the proposed grout curtain [22].

In response to these gaps, the primary aim of this study is to investigate groundwater level variations at the Tangab Dam site using an integrated geostatistical approach that combines kriging and Sequential Gaussian Simulation (SGS) with geological fault analysis. Unlike traditional deterministic methods such as IDW, which was applied here solely for preliminary visualization, this study emphasizes the use of SGS through 100 realizations to capture spatial variability and uncertainty in a complex karst aquifer system. By incorporating both hydrogeological data and structural geological features (e.g., fault density), the research provides a more comprehensive model of groundwater behavior. This approach enhances both the reliability of predictions and the interpretability of results, particularly in data-sparse regions. Ultimately, the findings aim to support more informed groundwater management and dam safety strategies in heterogeneous and fractured formations like those at Tangab.

2. Methodology

2.1. Geostatistical Analysis

In classical statistical studies, samples obtained from a population are typically considered random. The measured values of a particular quantity in one sample do not provide any information about the value of the same quantity in another sample. However, in geostatistics, it is possible to establish a relationship between the values of a quantity in the sample population and the distance and orientation of the samples relative to each other. In classical statistics, variability is assumed to be a random variable, whereas in geostatistics, part of this variability is random, and the other part is structured, depending on distance and direction [23].

Therefore, in geostatistics, the presence or absence of spatial structure in the data is first examined. If a spatial structure exists, the data is then analyzed [19]. In geostatistics, adjacent samples may exhibit spatial correlation up to a certain distance. In this case, the probability of similarity between values in closer samples is higher, as spatial structure implies that changes in a given area are more likely to affect nearby areas than those farther away [24,25].

Geostatistics is a branch of statistics based on the theory of regional variables. A regional variable is any variable that is distributed in three-dimensional space and exhibits spatial dependence. Such variables can be investigated in geostatistical studies. For example, the values of the permeability coefficient in a 9×9 km network are considered regional variables. The value of a regional variable Z(x) at any point (Eq. 1) can be decomposed into two components:

deterministic and random. This decomposition is expressed as follows [19]:

$$Z(x) = m(x) + L(x) \quad (1)$$

where Z(x) is the regional variable at coordinates x, L(x) is its random component, and m(x) is its deterministic component.

If a regional variable has an appropriate spatial structure, several analyses can be performed on it, including estimation of the target variable at unsampled locations, sample design, and error variance distribution. Geostatistical estimation begins by identifying and modeling the spatial structure of the variable, which is then, assessed using variogram analysis. The second stage is Kriging estimation. Geostatistical techniques can only be applied if the variable is stationary, which can be verified using a variogram. In linear geostatistics, the data distribution should also approximate a normal distribution [26,27].

2.2. Sequential Gaussian Simulation

Sequential Gaussian Simulation (SGS) is based on the multi-Gaussian model of random functions. Initially, this method was used to simulate a single variable using primary data only; it was later extended to incorporate secondary data and joint modeling approaches. To reproduce the spatial continuity of a variable z at N nodes within a network, the dataset $\{(u_a), a = 1, \dots, n\}$ is utilized. The steps involved in SGS are as follows [28]:

1. Model validation: The validity of the multi-Gaussian random function (RF) model is first assessed. For this, the primary data must be histogrammed, normalized, and transformed from the original z-values to Gaussian y-values using a common cumulative distribution function (CDF).

2. Simulation sequence (if the RF model for y is valid):

- Create a variogram using the normalized data.
- Define a random simulation path such that each node is visited only once.
- At each node, estimate the local mean and variance of the Gaussian CDF using kriging with the variogram model of the normalized data.
- Draw a value from the local CDF and add it to the conditioning dataset.
- Repeat the estimation and simulation steps for each subsequent node along the random path.
- Continue this process until all N nodes in the domain have been simulated.

SGS is computationally efficient because it requires solving only one kriging system per node. However, it has limitations: it may not accurately reproduce extreme (tail) values and can struggle with capturing spatial coherence across distinct value classes. To address these limitations, alternative non-Gaussian simulation algorithms—capable of preserving the continuity of extreme values over short ranges—can be used for improved performance [29].

3. Tangab Dam

3.1. Location and Geology

The Tangab Dam is situated on the Firouzabad River in Fars Province, approximately 90 kilometers south of Shiraz. The dam is located on the Podenow Anticline within the folded zone of the Zagros Mountains (Sadeh Zagros). As reported by Akhondi and Mohammadi [11], the dominant geological unit at the site is the Asmari Limestone Formation (AF), which overlies the Pabdeh-Gurpi Formation (PGF) and is itself overlain by the Razak Formation. To monitor the reservoir and assess subsurface conditions, 49 observation

wells were installed across the left and right abutments of the dam (Figure 1).

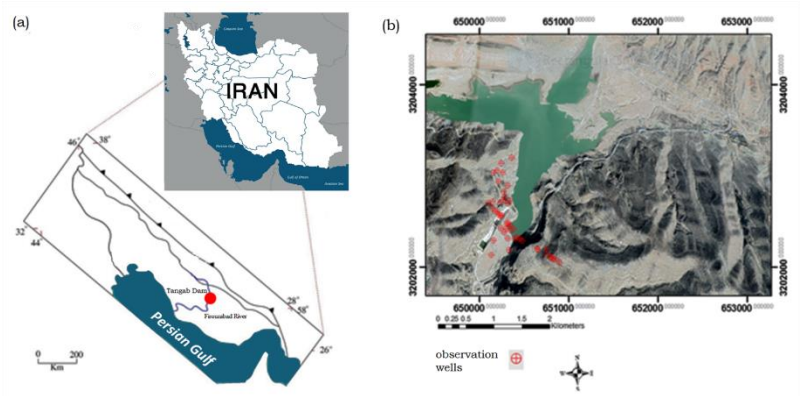


Figure 1. (a) Location of the research area; (b) Location of observation wells in the dam abutment.

The fold structure is predominantly composed of the PGF, AF, and Razak formations. The Firouzabad River has incised a 100-meter-deep channel through the saddle-shaped center of the Podenow Anticline in the Tangab Valley [30]. Prior to dam construction, several springs, with a combined average discharge of approximately 1 m^3/s, were actively discharging from the southern limb of the anticline (Figure 2a). Dye tracing experiments using Rhodamine and Uranine—conducted at the eastern and western abutments of the reservoir—revealed strong hydraulic connectivity within the karst system. The dyes were detected at Tangab and Atashkadeh Springs only a few days after injection [15,30], and the measured tracer velocities confirmed the existence of conduit flow between the northern and southern limbs of the anticline. These findings indicate a significant subsurface water transfer system that bypasses surface constraints. The leakage issue at the site has been extensively investigated by Mozafari et al. [14]. Initially, the site's water-tightness system included a concrete cut-off wall at the dam foundation, accompanied by a single-row grout curtain extending 256 meters into the western abutment and 206 meters into the eastern abutment (Figure 2b). These curtains, penetrating to depths of 80–180 meters, terminated within the AF and lacked connection to adjacent impermeable formations [31].

During the reservoir's first impoundment in 2009, the water level rose to 1413.65 meters above sea level (ASL), which was approximately 34.35 meters below the Normal Water Level Reservoir (NWLR), before dropping to 1405 m ASL over a 74-day period. During this time, whirlpool vortices were observed near the west abutment, and the discharge from the Atashkadeh Springs increased to 2 m^3/s—clear indications of significant leakage. To mitigate the leakage, a 300-meter extension of the grout curtain was added beyond the eastern abutment. Additionally, a new 570-meter grout curtain was constructed along the west side of the valley (Figure 2b). Despite these interventions, leakage rates remained largely unchanged. The reservoir rests against the northern limb of the anticline, in direct contact with the karstified Asmari Limestone Formation and the Razak aquitard. At both abutments, a preferential leakage pathway (PLP) appears to extend from the reservoir to the southern limb of the anticline. The lengths of the inlet windows at NWLR are at least 850 meters on the west and 600 meters on the east. Water is thought to be transmitted through the AF towards potential discharge zones on both riverbanks downstream of the dam. Notably, the PGF lies too deep beneath the central part of the anticline to act as an effective barrier. Ultimately, the initial grout curtains failed to seal the PLP

effectively. Iso-potential mapping revealed that leakage bypassed the ends of the grout curtains and traveled through the preferential pathways, affirming the necessity of further mitigation strategies [14].

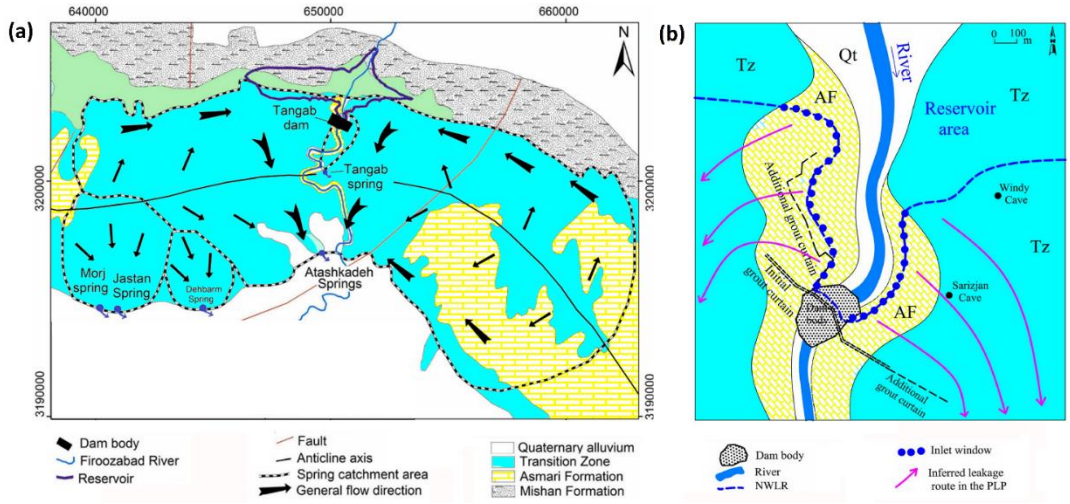


Figure 2. Geological map of (a) the central section of the Podenow Anticline [13] and (b) the Tangab Dam site [14].

3.2. Potential leakage routes

The Tangab Dam is located approximately 1000 meters within the Tangab Valley, where the reservoir water is in direct contact with the Asmari Formation, the Transition Zone, and the Razak Formation, all overlain by alluvial deposits. The Razak Formation and the Transition Zone contain frequent marlstone layers that inhibit vertical water movement, confining leakage pathways primarily to the karstified Asmari Aquifer. Reservoir seepage can occur in two main ways: directly through the Asmari Formation along the valley flanks, or indirectly via the alluvium at the valley floor. However, seepage through the alluvium appears negligible due to:

(a) the absence of vortex features on the reservoir surface, (b) lack of subsidence at the dam body and reservoir bed, and (c) stable readings from piezometers SP1–SP9 and FO-PIZ1 downstream of the cut-off wall and grout curtain (Figure 3).

At the left abutment, neither the original nor extended grout curtains intersect the key leakage window, as they are oriented nearly perpendicular rather than parallel to the valley slope (Figure 3). Although these curtains were designed to seal into the dense dolomitic limestone, water movement persists within this layer, especially in high-permeability zones (up to 100 Lu) with substantial grout take (>400 kg/m). Piezometers LG1P4U to LG1P14U (upstream) and LG1P1D to LG1P13D (downstream) installed in Gallery LG1 monitor hydraulic behavior around the grout curtains. On the right abutment, the initial grout curtain was similarly oriented perpendicular to the valley side, while subsequent curtains were aligned more parallel to the valley. However, these measures failed to fully seal the reservoir due to incomplete contact with the underlying Pabdeh Formation and lateral boundaries with the Razak Formation. As a result, water continues to bypass the grout curtains downstream. Piezometers RG2P1–RG2P7C in Gallery RG2 (downstream) and RBP1–RBP16 monitor leakage around both the initial and additional grout curtains. Geomorphologically, the Firouzabad River appears to be superimposed on the central part of the Podenow Anticline, where it incised the valley and likely established pathways for karst development. Portions of the riverbed on the northern limb are at higher elevations, allowing water

infiltration into the karst aquifer on the southern limb, particularly along faulted zones. Over geological time, these pathways evolved into mature conduits. The general alignment of the Windy and Sarizjan caves toward the southern limb supports this interpretation, suggesting paleo-flow from north to south. As the river downcut, older conduits became inactive, leaving abandoned cave levels now exposed at higher elevations. This proposed leakage route is further supported by two dye-tracing experiments conducted prior to dam construction. Although this pathway would require cross-bedding flow, the F1 and F2 faults—both striking roughly perpendicular to the fold axis—intersect bedding planes and likely facilitate such movement. At the left abutment, the F1 Fault aligns with the Tangab Spring. However, no significant increase in spring discharge was observed post-impoundment, likely due to extensive grouting in this area (Zone A, Figure 6). On the right abutment, water likely enters the karst system through the F4, F6, and F7 faults, further contributing to downstream leakage (Figure 3) [14,31].

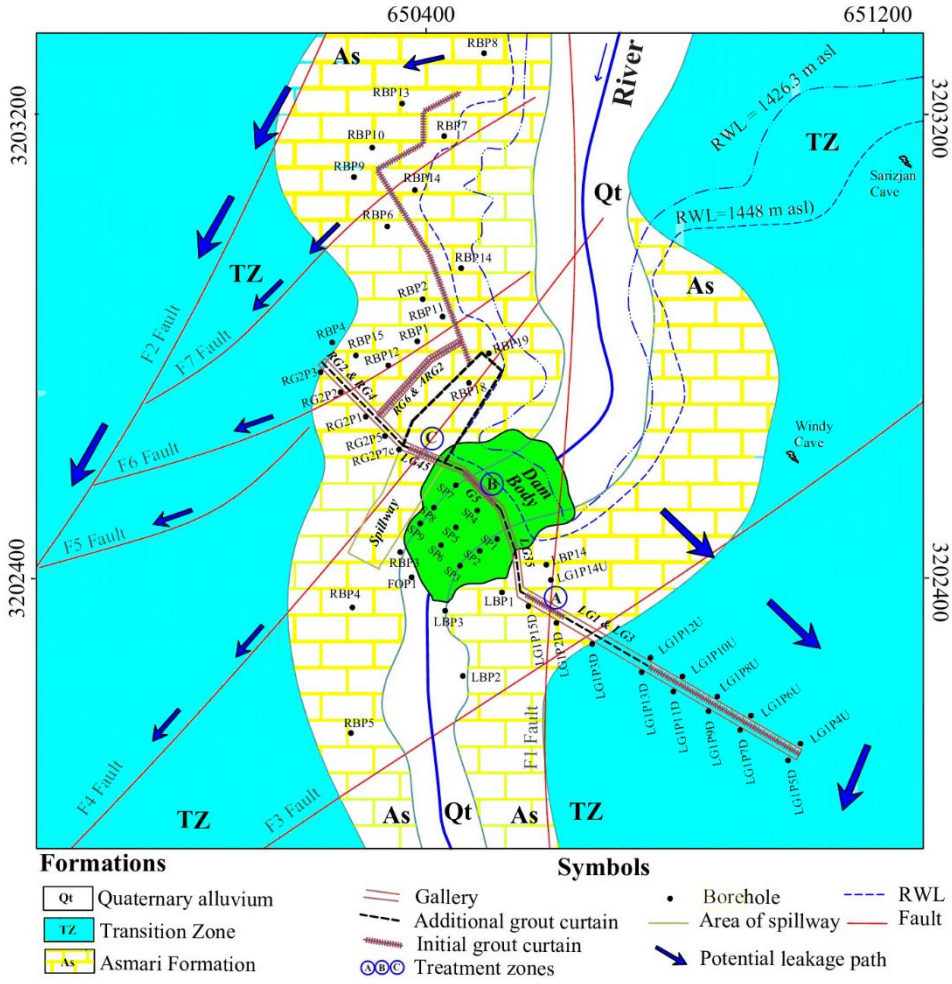


Figure 3. Engineering overlay on the geological map of the Tangab Dam site [14]

4. Discussion and results

4.1. Investigation of Groundwater Level Using the Sequential Gaussian Simulation Method

Initially, the distance-weighted interpolation method was applied using ArcMap to gain a preliminary understanding of spatial variations across the study area. This method, often referred to as the "photo distance" approach, provides estimated values that closely

resemble the observed data but does not support the generation of uncertainty maps. It is primarily used for initial visualization and pattern recognition.

Following this, the dataset was normalized, and spatial continuity was assessed by constructing a variogram. Geostatistical interpolation was then conducted using the kriging method, which also facilitated the creation of an uncertainty map. Finally, based on the kriging estimates, 100 sequential Gaussian simulations were performed in the study area using ISATIS software. The outputs of these simulations provide a spatially continuous depiction of groundwater levels throughout the dam abutments.

4.2. Exploratory Data Analysis

Table 1 presents the descriptive statistics for groundwater level measurements obtained from 49 piezometers. For effective interpolation and simulation, it is necessary for the data to follow a normal distribution. As shown in Figure 4a, the histogram of the raw water level data indicates non-normality, with a standard deviation of 12.54, skewness of 0.63, and kurtosis (elongation) of 4.02. Therefore, Gaussian normalization was applied. The resulting histogram of the normalized data is presented in Figure 4b, demonstrating improved statistical distribution suitable for geostatistical modeling.

Table 1. Descriptive statistics

Value	Frequency	Min (m)	Max (m)	Average (m)	Standard Deviation	Variance
Water lable	49	1362.99	1424.81	1382.25	12.54	157.25

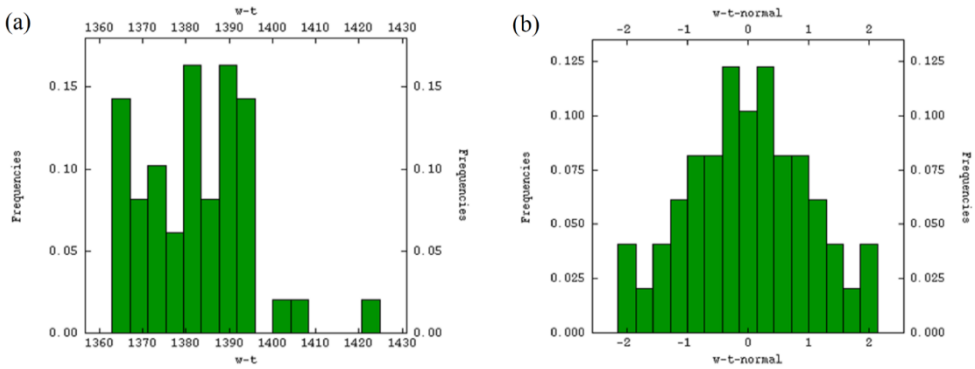


Figure 4. (a) Histogram of original water level data; (b) Histogram after Gaussian normalization.

4.3. Variable Spatial Continuity

Figure 5 presents the experimental variogram of groundwater levels along with the fitted spherical model. The spatial continuity of the water level was assessed through this variogram analysis. The degree of spatial structure is quantified using the nugget-to-sill ratio (referred to here as the "piece effect to roof ratio"). According to Isaaks and Srivastava [19], a ratio of less than 25% indicates strong spatial dependence, a ratio between 25% and 75% reflects moderate spatial dependence, and a ratio greater than 75% suggests weak spatial dependence. In this study, the spherical model showed a ratio within the range that implies a reasonable level of spatial correlation, thereby justifying the use of geostatistical interpolation methods such as kriging.

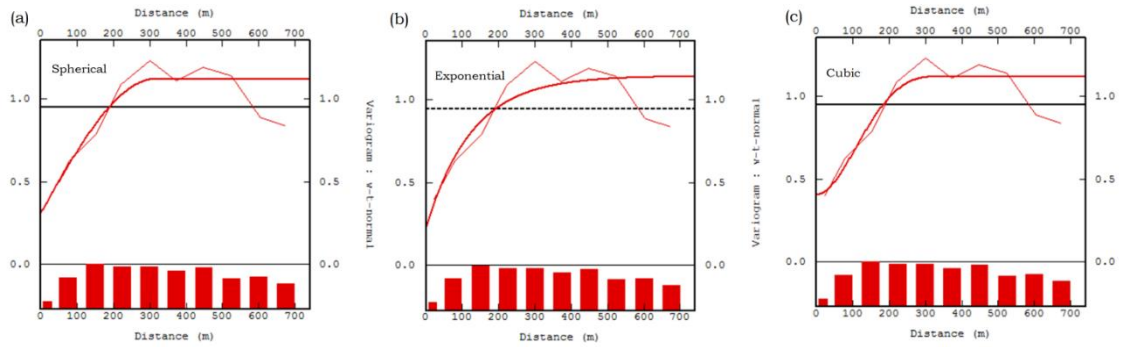


Figure 5. Experimental variograms of water level with fitted models: (a) spherical; (b) exponential; (c) cubic.

In this study, the exponential, spherical, and cubic variogram models exhibited nugget-to-sill ratios of 19%, 27%, and 35%, respectively. These values indicate that the exponential model demonstrates strong spatial continuity, while the spherical and cubic models exhibit moderate spatial dependence. Additionally, a larger range (or radius of influence) reflects a broader spatial structure, meaning fewer sampling points are needed to predict unsampled values with confidence. The range values for the exponential, spherical, and cubic models were 416.38 meters, 322.86 meters, and 376.6 meters, respectively. Among the three, the spherical model yielded the lowest sum of squared residuals, as shown in Table 2, indicating the best fit for subsequent kriging and simulation procedures.

Table 2. Variogram Features with a suitable spherical model

Model	Exponential	Spherical	Cubic
Nugget effect	0.23	0.31	0.41
Domain	416.38m	322.86	376.6
Threshold	0.95	0.82	0.73
Sum of squared residuals	0.000877	0.000527	0.000585
c_0+c	1.18	1.13	1.14
c_0/c	0.194915254	0.274336283	0.359649123

4.4. Variogram Validation

Several variogram models with different structural characteristics were considered to simulate the experimental variogram. Choosing an appropriate model and accurately estimating its parameters is critical, as these directly affect the reliability of geostatistical estimations. In this study, a cross-validation procedure was used to assess the accuracy and appropriateness of the selected variogram model. During cross-validation, one data point is removed at a time, and its value is estimated using the remaining dataset via the kriging method. This process is repeated sequentially for all data points. The differences between observed and estimated values were used to generate a correlation map, evaluating how well the model reproduces the actual data. Using the validation function in ISATIS software, a correlation coefficient of 0.73 was obtained between the observed and estimated groundwater levels, indicating a good level of agreement. Furthermore, the residual distribution (actual minus estimated values)

was plotted to assess the bias of the model. As shown in Figure 6, the residuals are symmetrically distributed around zero, confirming that the model is unbiased. Additionally, the normal probability plot in Figure 7 demonstrates that the residuals approximate a normal distribution, further validating the suitability of the selected variogram.

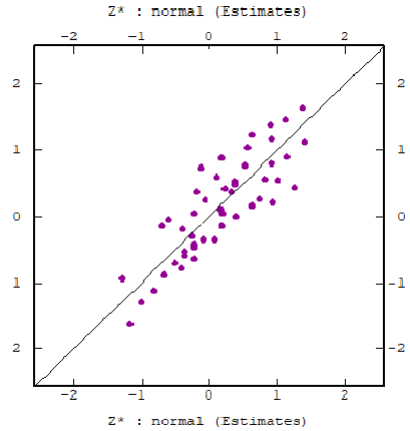


Figure 6. Cross-validation error distribution (residuals) between observed and kriging-estimated water levels.

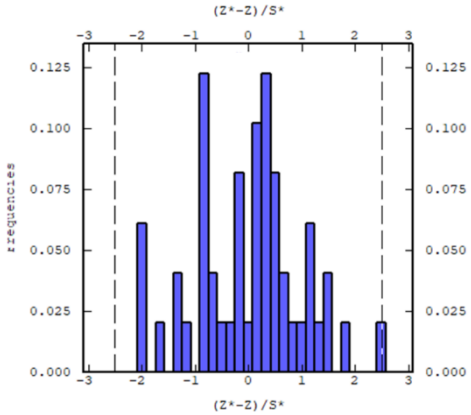


Figure 7. Normal probability plot of residuals from variogram cross-validation

4.5. Water Level Interpolation Using the IDW Method

The Inverse Distance Weighting (IDW) interpolation method has been employed as one of the precise and effective techniques for understanding and gaining a broad perspective of the spatial variations in water levels within the examined area. In this method, the estimated values closely resemble the observed sampling values. However, the estimated values may diverge from the sampled values in cases of imprecise data. Unlike some other methods, the distribution of data surrounding the estimated point is not directly taken into account. Instead, the position of each point is considered individually, with the weights assigned to points that are equidistant from the target point. The deterministic nature of the IDW method does not produce an uncertainty map and does not make assumptions about the data, such as the normality requirement that is typically necessary for geostatistical methods. The appropriate values for the power parameter, the number of neighboring points, and the search radius have been determined in this approach (Table 3). The interpolated map resulting from the IDW method is shown in Figure 8.

Table 3. Parameters to calculate IDW interpolation

Method	Inverse Distance Weighted Interpolation
Power	2
Max-Neighbors	10
Min-Neighbors	5
Major semiaxis	100
Minor semiaxis	100

The observed and estimated water levels of the observation wells are derived from the interpolation of the water levels, and the difference between these two values is indicated as the error in Figure 9. The distribution of the estimated and observed values, along with the best-fit line between them, determines the shape of the state diagram. The accuracy of the model's estimation increases as the values approach the 1:1 line. The regression equation was used to estimate the points, and the interpolation error is approximately 0.2. The independence of errors is a key assumption in regression analysis. If the errors are correlated, regression cannot be applied.

The Durbin-Watson test is used to assess the independence of errors. Based on the results shown in Figure 9, the error value is 1.85, indicating that the results are reliable, as the Durbin-Watson statistic (DW) lies between 1.5 and 2.5. If DW falls outside of this range, it confirms the presence of autocorrelation in the errors.

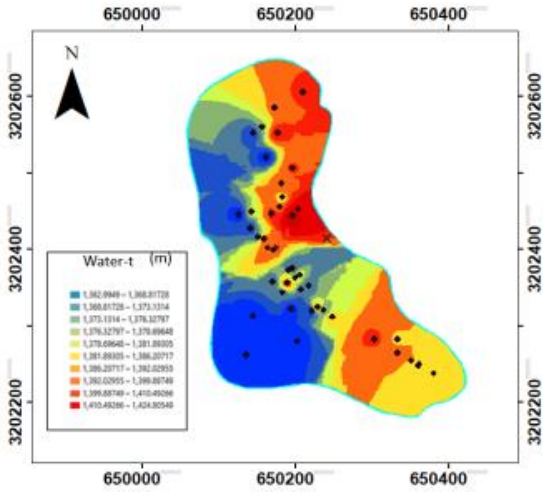


Figure 8. Water level interpolation using the IDW method.

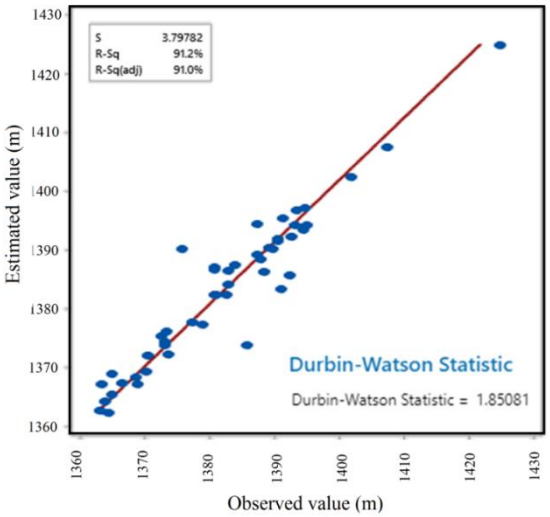


Figure 9. Correlation between the estimated and observed values of the water level in the IDW method, as assessed by the Durbin-Watson test.

4.6. Interpolation Using the Kriging Method

The water levels at unknown sites around the dam have been estimated using the normal data of the reservoir level and the exponential variogram model. The reservoir level was then interpolated (Figure 10a). As shown in the uncertainty map and the interpolation error value in Figure 10b, the estimation error is higher in areas with fewer data points or no water level measurements. Specifically, the estimations in the northern and eastern regions of the study area are considered unreliable.

Kriging-based techniques, such as sequential conditional simulation methods, analyze sampling points sequentially and randomly until all sampled points have been assessed. One of the key outcomes of using geostatistical methods is identifying the uncertainty surrounding the estimations. The error variance in the standard geostatistical approach is used to quantify this uncertainty. If the assumption of a Gaussian distribution holds, the estimate and error variance together fully represent the uncertainty at each unsampled location. While error variance can accurately predict the arrangement and location of nearby samples, it cannot precisely capture local uncertainty. Specifically, it overlooks regional uncertainty caused by spatial variations within the target area.

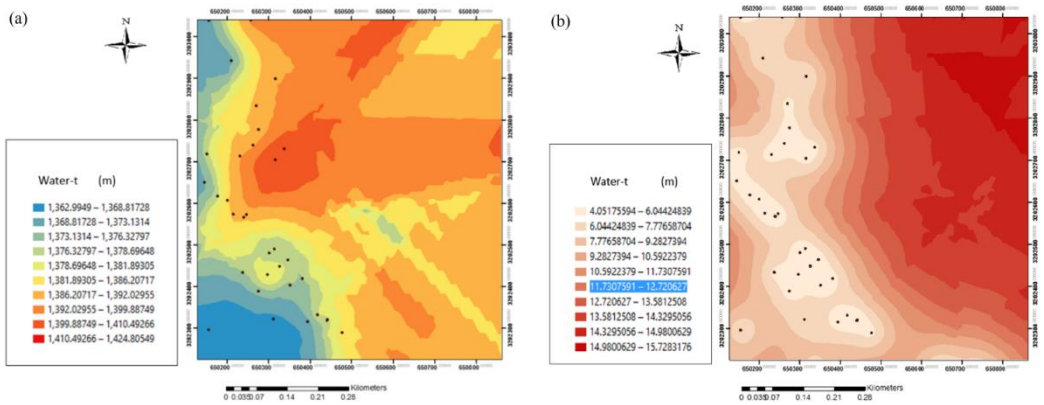


Figure 10. (a) Water level interpolation using Kriging method; (b) Error and uncertainty map resulting from kriging interpolation method.

Alternate probability images are generated through conditional simulation to account for local variability. Estimates and their associated uncertainties are defined and determined using a range of probabilities, incorporating local variability. In the next step, we perform a Gaussian simulation with 100 realizations and assess the results. The analyzed area has undergone 100 successive Gaussian simulations for the water level variable. Figure 11 illustrates the three-dimensional block of the simulation, with multiple layers of the simulation's output visible. Given the breadth of results, it is advisable to compute the average result of the simulation, which is discussed in the next phase, to determine the water level at a specific location.

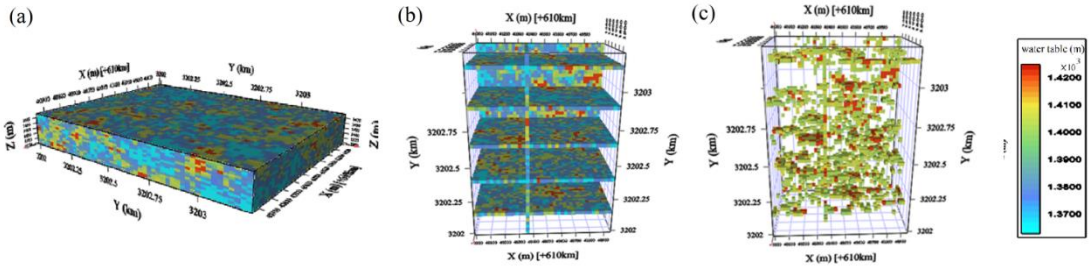


Figure 11. (a) 3D block model of SGS results; (b) Representative layers from simulations; (c) Zones with higher groundwater levels.

4.7. Mathematical Expectation of the Simulation

The average of the 100 realizations from the Gaussian simulation performed in the previous stage should be calculated, considering the comprehensiveness of the data and identifying the regions where water table changes are most pronounced (Figure 12). The estimated average value, visible at various levels in the figure, is consistent with the estimate generated using the kriging method.

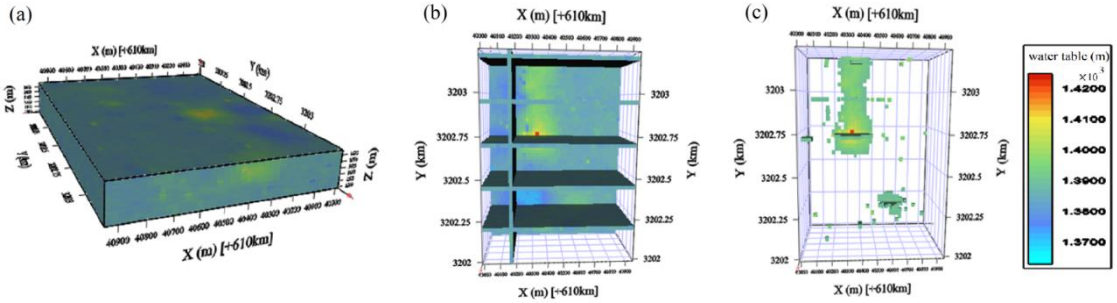


Figure 12. (a) average results of Gaussian simulation block in three dimensions; (b) average results of Gaussian simulation in different levels; (c) display of higher water level values in levels

At this stage, the exploratory analysis for each level is presented in Table 4, based on simulations run along the z-axis at 150 meters (15 cells, each 10 meters) in the direction of the boreholes. In the diagram, height is plotted against the range of changes for each level, with the range of extreme changes for some levels indicating larger values relative to smaller ones, which have a higher level of stability. The graph shows that as the height level increases, the variations in water level also increase.

In a karst system, two piezometers may be close to one another but not connected. On the other hand, the non-uniform depth of observation wells is the most significant issue in our analysis. While there is no guarantee in a karst system, this issue is

presented as a possibility: as the depth of an observation well increases, it is possible that a new layer of permeable material is encountered, which could cause the water level to either rise or fall.

To conduct a more detailed investigation and precisely identify locations where the water level is higher or lower than the average, it is preferable to display a map for each level separately, with a distance of 10 meters between each point. The maps obtained at various levels are shown in Figure 13.

Table 4. Descriptive statistics of different levels

number	from	to	Minimum	Maximum	Mean	Std.	Variance
1	1350	1360	1368.2	1394.82	1383.26	2.46	6.03
2	1360	1370	1368.3	1396.21	1383.14	2.58	6.66
3	1370	1380	1362.99	1404.34	1383.08	2.86	0.82
4	1380	1390	1367.98	1393.57	1382.9	3.18	10.09
5	1390	1400	1367.39	1400.33	1382.78	3.55	12.59
6	1400	1410	1364.37	1402.95	1382.75	3.77	14.22
7	1410	1420	1362.99	1397.63	1382.89	4.08	16.61
8	1420	1430	1362.99	1398.57	1383.13	4.35	18.89
9	1430	1440	1366.95	1406.13	1383.24	4.53	20.52
10	1440	1450	1368.26	1411.93	1383.5	4.79	22.91
11	1450	1460	1362.99	1410.06	1383.77	4.91	24.11
12	1460	1470	1363.28	1412.65	1383.95	4.73	22.35
13	1470	1480	1370.2	1424.59	1384.1	0.46	2.12
14	1480	1490	1369.09	1424.81	1384.1	4.36	18.99
15	1490	1500	1372.14	1413.21	1384.2	4.16	17.35

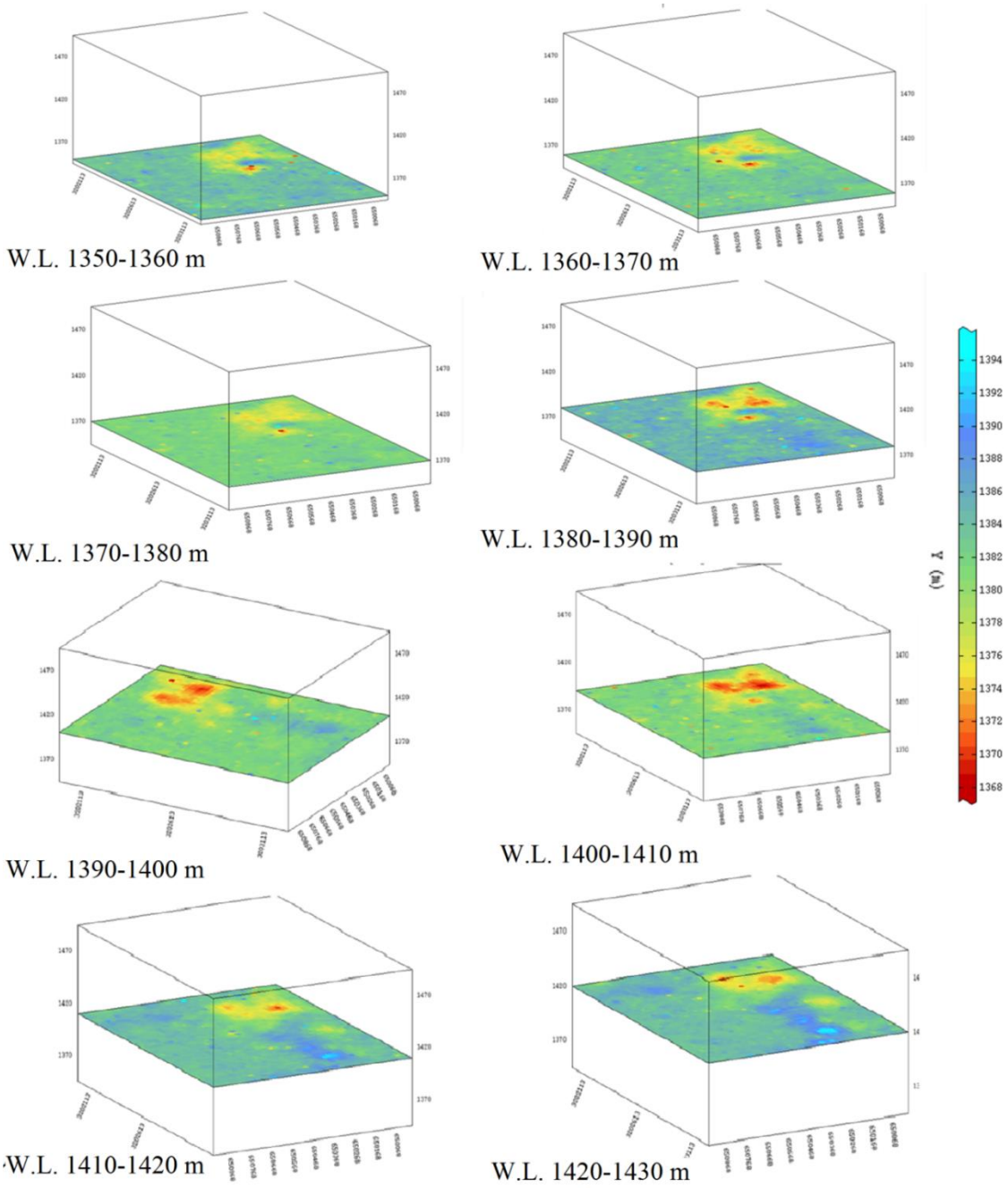


Figure 13. Simulated groundwater levels at 15 depth intervals (10 m each) from 1350 to 1430 m elevation.

The next step is to create a plan map, which represents the average of the various levels of the simulated block, for a more in-depth analysis. The output of the simulated average can be viewed in the two-dimensional map after the three-dimensional network, where 100 realizations of the simulation were conducted, has been transformed into a two-dimensional network. As shown in Figure 14a, reveals a clear groundwater mound in the north-central area, which may be attributed to topographic influences, recharge zones, or structural features (e.g., faults/fractures) facilitating upward flow. Also, Figure 14b overlays the same data on

the topographic landscape. Elevated groundwater zones appear to align with surface highs, suggesting a good correlation between topography and water table elevation. This might also reflect subsurface geological controls (e.g., permeable formations or fractures). The proximity of high groundwater levels to the reservoir indicates a potential hydraulic connection that may pose seepage or uplift risks for dam stability.

Additionally, the fault map in Figure 15 suggests that the density of faults in this region may contribute to the high water level variations on the right side of the dam. The F3 fault is of particular concern due to its orientation crossing beneath or adjacent to the reservoir. This suggests it may serve as a preferential path for groundwater movement or even seepage under pressure. The intersection of multiple faults in this region increases the potential for fracture permeability, which could amplify hydraulic connectivity and challenge dam safety or groundwater modeling accuracy. These structural features should be further evaluated for their hydrogeological behavior, especially in scenarios involving reservoir level fluctuations or seismic activity.

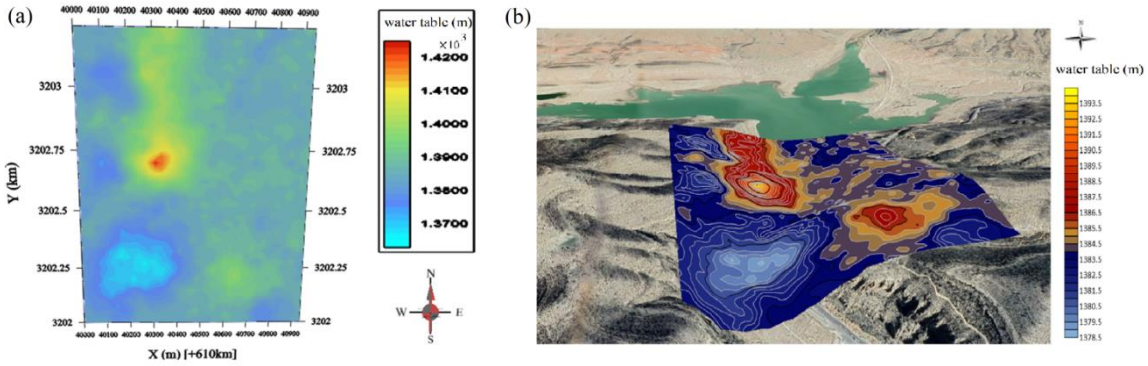


Figure 14. (a) Groundwater table distribution from Gaussian simulation showing high and low zones; (b) 3D view of the water table over terrain, highlighting elevated groundwater areas near the dam reservoir.

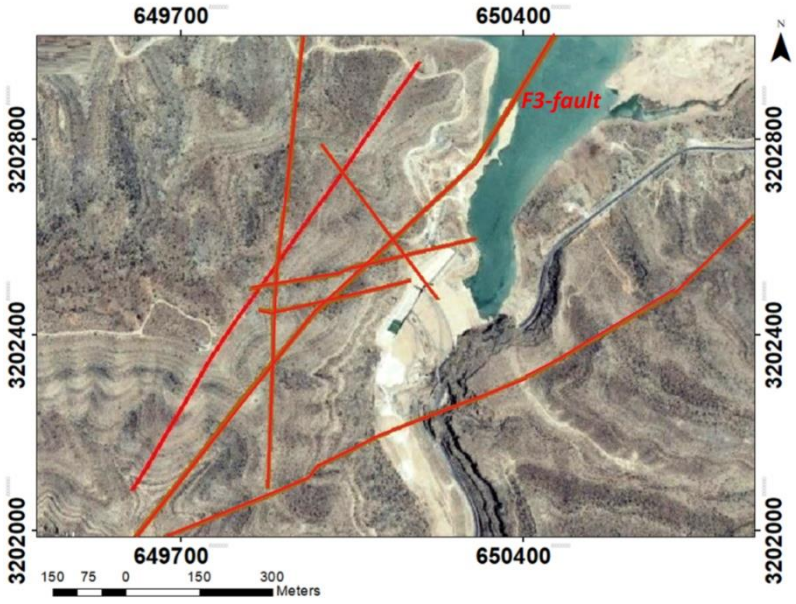


Figure 15. Fault density map on the dam's right abutment

4.8. Validation of Simulation Results

The simulation results (realizations) are considered acceptable when they can reproduce the statistical and geostatistical parameters of the exploration data. Figure 16 shows the histogram of the actual data (exploratory borehole data) alongside the frequency diagram obtained from the simulation results for this purpose. As observed, the average result of the simulation is nearly identical to the average result from the statistical analysis of the exploratory well data. Therefore, the simulation results accurately reproduce the statistical parameters of the data and are deemed valid.

Based on the average water level data, the variogram's segment-to-ceiling ratio is 19%, indicating that the water table level variable exhibits a fair degree of continuity. The results of the water table estimation revealed that the northeastern and eastern regions of the study area had unreliable water table estimations, which may have been caused by a lack of water table data in those regions.

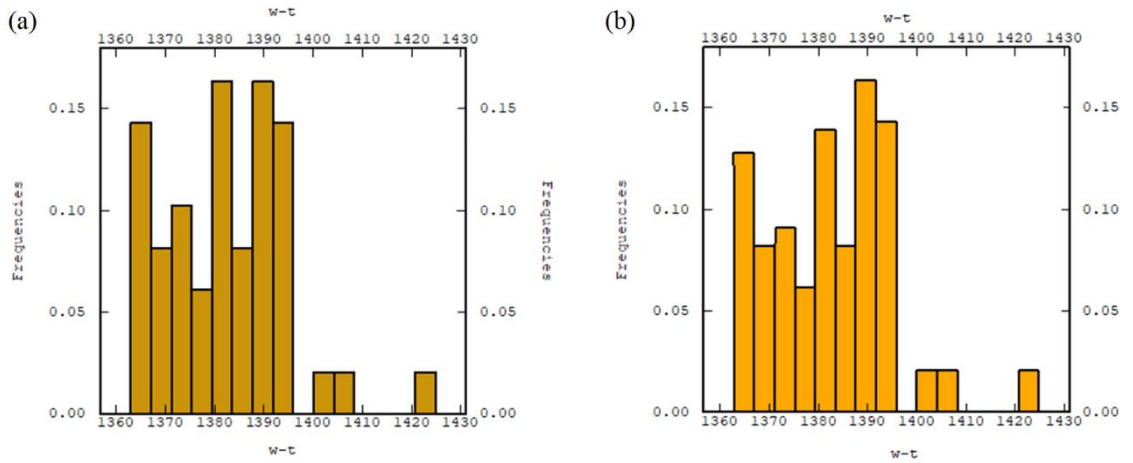


Figure 16. (a) Histogram of the actual data (exploratory borehole data); (b) Frequency diagram obtained from the simulation results.

In summary, the methodological framework of this study follows a structured and sequential approach designed to ensure robust groundwater level modeling in a complex karstic environment. The process begins with exploratory data analysis and normalization to meet the statistical requirements of geostatistical modeling. This is followed by variogram construction and model selection, where the spherical model was identified as the best fit based on the nugget-to-sill ratio and minimal residual error. Kriging is then applied to estimate spatial distributions, while Sequential Gaussian Simulation (SGS) with 100 realizations is used to capture local variability and uncertainty. Finally, the results are interpreted in conjunction with geological structures, particularly fault distributions, to better understand groundwater flow dynamics. This integrated methodology not only enhances the spatial accuracy of predictions but also provides a more realistic representation of uncertainty, making it a valuable tool for hydrogeological analysis and dam safety assessment in heterogeneous terrains.

4.9. Comparison of Interpolation Methods

To evaluate the relative performance of the three applied spatial estimation techniques—Inverse Distance Weighting (IDW), kriging, and Sequential Gaussian Simulation (SGS)—a comparative analysis was conducted based on interpolation accuracy, uncertainty representation, and spatial realism.

IDW was primarily used as a deterministic method for preliminary

visualization. It closely replicates observed data in areas with dense sampling but lacks the ability to model uncertainty or account for spatial correlation. The method assumes a uniform influence radius and is sensitive to outliers.

Kriging, a geostatistical estimator, improved upon IDW by incorporating spatial structure via a fitted variogram model. It provided smoother interpolations and generated an uncertainty map (kriging variance), which is valuable for evaluating prediction confidence. However, as a linear estimator, kriging tends to underestimate variability, especially in heterogeneous regions.

SGS offered a probabilistic modeling approach through 100 realizations, capturing both spatial variability and uncertainty more realistically. It was particularly effective in representing local fluctuations in water level, especially in faulted or karstic zones. SGS outputs also allowed the generation of 3D groundwater distribution models and probability maps, which are critical for risk analysis and decision-making in dam engineering. A summary of the performance characteristics of each method is provided in Table 5.

Table 5. Summary of the performance characteristics of IDW, Kriging, and SGS methods

Method	Type	Strengths	Limitations	Error/Validation Metrics
IDW	Deterministic	Simple, fast, intuitive for initial trends	No uncertainty modeling, sensitive to outliers	DW = 1.85, Error ≈ 0.2
Kriging	Geostatistical	Accounts for spatial continuity, provides variance map	May smooth data, underrepresents extremes	Correlation = 0.93, unbiased residuals
SGS	Stochastic	Captures spatial variability, uncertainty, and extreme values	Computationally intensive, requires variogram model	Closely matched observed mean, strong visual agreement

This comparative evaluation demonstrates that while IDW is suitable for initial analysis, kriging and SGS offer significant improvements for modeling in complex hydrogeological settings. SGS, in particular, emerges as the most robust method for groundwater level estimation in the Tangab Dam's karst terrain due to its ability to quantify uncertainty and replicate natural spatial variability.

5. Conclusion

This study applied a combination of geostatistical techniques—including inverse distance weighting (IDW), kriging, and sequential Gaussian simulation (SGS)—to estimate and analyze groundwater levels at the Tangab Dam using piezometric data from 49 observation wells. Preliminary statistical analysis revealed non-normality in the raw data, necessitating normalization before variogram modeling. Among the tested models, the spherical variogram exhibited the best fit with a nugget-to-sill ratio of 19%, indicating strong spatial continuity and justifying the application of geostatistical methods.

While IDW served as a preliminary visualization tool, kriging and SGS provided more accurate and interpretable insights into spatial trends. Both methods revealed elevated groundwater levels along the dam's right abutment—an area of high fault density—suggesting that geological structures significantly influence groundwater movement. SGS, through 100 realizations, successfully reproduced both the statistical distribution and spatial variability of the aquifer, with a strong match to empirical data. Validation metrics confirmed the robustness of the simulation, especially in well-instrumented regions, while acknowledging limitations in data-sparse zones such as the northeast and east.

Importantly, this study highlights the value of integrating geostatistical modeling

with geological fault data to improve the understanding of groundwater flow in complex karst environments. These findings carry practical implications for dam safety, as zones of elevated groundwater near fault intersections may pose seepage or uplift risks. Based on this, targeted recommendations include reinforcing monitoring systems in critical zones, expanding the piezometer network—especially in under-sampled areas—and using geostatistical uncertainty maps to prioritize grouting and sealing operations.

Future work should focus on enhancing spatial resolution through additional borehole data and incorporating numerical groundwater flow models to better simulate dynamic hydrological conditions. This integrated approach would support more effective groundwater management and risk mitigation strategies in structurally complex dam sites like Tangab.

Fundings
This research received no external funding.

Conflict of Interest
The authors declare that they have no conflict of interest.

Author Contributions
All authors contributed to the study conception and design.

References

1. Farhadian H, Bahmani Shahraki F. Enhancing analytical methods for estimating water inflow to tunnels in the presence of discontinuity areas. Environ Earth Sci. 2024;83:339.
2. Anvari AA, Katibeh H, Sharifzadeh M, Farhadian H. Estimation of fault zone permeability with fuzzy-delphi AHP (FDAHP) method. Rock Mech Civ Environ Eng - Proc Eur Rock Mech Symp EUROCK 2010. 2010. https://doi.org/10.1201/b10550-56
3. Qi S, Wen Z, Lu C, Shu L, Shao J, Huang Y, et al. A new empirical model for estimating the hydraulic conductivity of low permeability media. Proc Int Assoc Hydrol Sci. 2015;368:478–83. https://doi.org/10.5194/piahs-368-478-2015
4. Farhadian H, Nikvar-Hassani A. Water flow into tunnels in discontinuous rock: a short critical review of the analytical solution of the art. Bull Eng Geol Environ. 2019;78:3833–49. https://doi.org/10.1007/s10064-018-1348-9
5. Farhadian H, Maleki Z, Eslaminezhad SA. Assessment of the Optimum Depth of Sealing Cutoff Walls in the Clay Core of Peygham-Chay Dam. J Hydraul Struct. 2021;7:59–76. https://doi.org/10.22055/jhs.2021.37119.1168
6. Nikvar Hassani A, Farhadian H, Katibeh H. A comparative study on evaluation of steady-state groundwater inflow into a circular shallow tunnel. Tunn Undergr Sp Technol. 2018;73. https://doi.org/10.1016/j.tust.2017.11.019
7. Dehshibi R, Karami S, Maleki Z, Farhadian H. A comparative study on evaluation of steady-state groundwater quality in Sirjan's Golgohar mineral zone. Arab J Geosci. 2022;15:1–20. https://doi.org/10.1007/s12517-022-10074-w
8. Goovaerts P. Geostatistical approaches for incorporating elevation into the spatial interpolation of rainfall. J Hydrol. 2000;228:113–29. https://doi.org/10.1016/S0022-1694(00)00144-X
9. Barca E, Passarella G. Spatial evaluation of the risk of groundwater quality degradation. A comparison between disjunctive kriging and geostatistical simulation. Environ Monit Assess. 2008;137:261–73. https://doi.org/10.1007/s10661-007-9758-3
10. Rajaee T, Nourani V, Pouraslan F. Groundwater level forecasting using wavelet and kriging. J Hydraul Struct. 2016;2:1–21. https://jhs.scu.ac.ir/article_12848.html
11. Akhondi M, Mohammadi Z. Preliminary analysis of spatial development of karst using a geostatistical simulation approach. Bull Eng Geol Environ. 2014;73:1037–47. https://doi.org/10.1007/s10064-014-0599-3
12. Madani Esfahani N, Asghari O. Fault detection in 3D by sequential Gaussian

simulation of Rock Quality Designation (RQD) Case study: Gazestan phosphate ore deposit, Central Iran. Arab J Geosci. 2013;6:3737–47. https://doi.org/10.1007/s12517-012-0633-3
13. Karimi H, Raeisi E, Zare M. Physicochemical time series of karst springs as a tool to differentiate the source of spring water. Carbonates and Evaporites. 2005;20:138–47. https://doi.org/10.1007/BF03175457
14. Mozafari M, Milanović P, Jamei J. Water leakage problems at the Tangab Dam Reservoir (SW Iran), case study of the complexities of dams on karst. Bull Eng Geol Environ. 2021;80:7989–8007. https://doi.org/10.1007/s10064-021-02387-z
15. Asadi N. The study of water tightness problem in Tangab Dam by use of dye tracers [M. Sc. Thesis (in Farsi)]: Dept. of Earth Sciences. Shiraz Univ Shiraz, Iran. 1998;
16. Huysmans M, Dassargues A. Application of multiple-point geostatistics on modelling groundwater flow and transport in a cross-bedded aquifer. Hydrogeol J. 2009;17. https://doi.org/10.1007/s10040-009-0495-2
17. Marache A, Breysse D, Piette C, Thierry P. Geotechnical modeling at the city scale using statistical and geostatistical tools: The Pessac case (France). Eng Geol. 2009;107:67–76. https://doi.org/10.1016/j.enggeo.2009.04.003
18. Jaquet O, Siegel P, Klubertanz G, Benabderrhamane H. Stochastic discrete model of karstic networks. Adv Water Resour. 2004;27:751–60. https://doi.org/10.1016/j.advwatres.2004.03.007
19. Isaaks EH, Srivastava RM. Applied geostatistics. 1989;
20. Hosseini E, Gholami R, Hajivand F. Geostatistical modeling and spatial distribution analysis of porosity and permeability in the Shurijeh-B reservoir of Khangiran gas field in Iran. J Pet Explor Prod Technol. 2019;9:1051–73. https://doi.org/10.1007/s13202-018-0587-4
21. Bai L, Cai J, Liu Y, Chen H, Zhang B, Huang L. Responses of field evapotranspiration to the changes of cropping pattern and groundwater depth in large irrigation district of Yellow River basin. Agric Water Manag. 2017;188:1–11. https://doi.org/10.1016/j.agwat.2017.03.028
22. Farhadian H. A new empirical chart for rockburst analysis in tunnelling: Tunnel rockburst classification (TRC). Int J Min Sci Technol. 2021; https://doi.org/10.1016/j.ijmst.2021.03.010
23. Shademan M, Farhadian H. Contribution of geostatistical modeling on simulating a geomechanical parameter (case study: GSI in Gol-Gohar open pit iron mine, Kerman, southeastern Iran). J Geomine. 2023;1:81–91. 10.22077/jgm.2023.6696.1013
24. Farhadian H, Nikvar-Hassani A. Development of a New Empirical Method to Tunnel Squeezing Classification (TSC). Q J Eng Geol Hydrogeol. 2020; https://doi.org/10.1144/qjegh2019-108
25. Journel AG. Modelling uncertainty and spatial dependence: stochastic imaging. Int J Geogr Inf Syst. 1996;10:517–22. https://doi.org/10.1080/02693799608902094
26. Farhadian H, Maleki Z. Groutability classification of granular soils with cement grouts. J Rock Mech Geotech Eng. 2023;15:1580–90. https://doi.org/10.1016/j.jrmge.2022.09.007
27. Deutsch C V. Geostatistical modelling of geometallurgical variables—Problems and solutions. Proc Int Geometallurgy Conf Brisbane, Aust. 2013.
28. Rossi ME, Deutsch C V, Rossi ME, Deutsch C V. Recoverable Resources: Simulation. Miner Resour Estim. 2014;167–92. https://doi.org/10.1007/978-1-4020-5717-5_10
29. Mohammadi Z, Raeisi E, Bakalowicz M. Method of leakage study at the karst dam site. A case study: Khersan 3 Dam, Iran. Environmental Geology. 2007;52:1053–65.
30. Farhadian H. A new empirical chart for rockburst analysis in tunnelling: Tunnel rockburst classification (TRC). Int J Min Sci Technol. 2021; https://doi.org/10.1016/j.ijmst.2021.03.010
31. Shademan M, Farhadian H. Contribution of geostatistical modeling on simulating a geomechanical parameter (case study: GSI in Gol-Gohar open pit iron mine, Kerman, southeastern Iran). Journal of Geomine. 2023;1:81–91. 10.22077/jgm.2023.6696.1013

32. Farhadian H, Nikvar-Hassani A. Development of a New Empirical Method to Tunnel Squeezing Classification (TSC). Quarterly Journal of Engineering Geology and Hydrogeology. 2020; https://doi.org/10.1144/qjegh2019-108
33. Journel AG. Modelling uncertainty and spatial dependence: stochastic imaging. International Journal of Geographical Information Systems. 1996;10:517–22. https://doi.org/10.1080/02693799608902094
34. Farhadian H, Maleki Z. Groutability classification of granular soils with cement grouts. Journal of Rock Mechanics and Geotechnical Engineering. 2023;15:1580–90. https://doi.org/10.1016/j.jrmge.2022.09.007
35. Deutsch C V. Geostatistical modelling of geometallurgical variables—Problems and solutions. Proceedings of the International Geometallurgy Conference, Brisbane, Australia. 2013.
36. Rossi ME, Deutsch C V, Rossi ME, Deutsch C V. Recoverable Resources: Simulation. Mineral Resource Estimation. 2014;167–92. https://doi.org/10.1007/978-1-4020-5717-5_10
37. Talaei H. Investigation on the flow path through the karstic formation of the left abutment of Tangab Dam by the means of Rhodamine-B dye tracer [M. Sc. Thesis (in Farsi)]: Dept. of Earth Sciences. Shiraz University, Shiraz, Iran. 1999;
38. Mozafari M, Raeisi E. Potential leakage paths at the dams constructed on karst terrains in Iran. Quarterly Journal of Engineering Geology and Hydrogeology. 2022;55:qjegh2021-102.

© 2025 by the authors. Licensee SCU, Ahvaz, Iran. This article is an open access article distributed under the terms and conditions of the Creative Commons Attribution 4.0 International (CC BY 4.0 license) (http://creativecommons.org/licenses/by/4.0/).

Analytical solutions for steady downward flow of a wetting fluid in unsaturated soil using the Adomian decomposition method

Hamed Reza Zarif Sanayei [*,1]

1. Faculty of Engineering, Shahrekord University, Shahrekord, Iran

***Corresponding Author:**
Hamed Reza Zarif Sanayei

Email: hzarif63@gmail.com; zarif@sku.ac.ir
Received: 2025.06.12
Accepted: 2025.07.15
J. Hydraul. Struct., 2025; 12(2): 22-33
DOI: 10.22055/jhs.2025.49954.1355

ABSTRACT

Investigating and simulating the steady water flow in an unsaturated soil column containing oil is one of the most important studies in the field of optimizing oil extraction processes. In order to simulate this flow, governing equation for this field should be solved. The governing equation is strongly nonlinear with limited analytical solutions in the literature. In this paper, analytical solutions have been developed for the nonlinear equation in different soil properties using Adomian Decomposition Method (ADM). A total of three soils with different pore size distribution index are considered in this research. These pore size distribution indexes are 2, 3 and 4 for cases 1, 2 and 3, respectively. Results for the presented analytical solutions are capillary pressure head verses elevation in the unsaturated soil column containing oil. To investigate the accuracy of the derived analytical solutions, capillary pressure head values are obtained from a numerical solution and compared with the presented analytical solution values for all cases. An excellent agreement is observed between analytical and numerical results for three cases. These analytical solutions can be used as a benchmark for verification and efficiency assessment of numerical methods.

KEYWORDS

Analytical solution, ADM, Oil extraction, Unsaturated soil, Capillary pressure head

1. Introduction

Water injection is one of the important methods for increasing oil extraction from underground reservoirs. In this method, the water is injected into an underground reservoir to increase the internal pressure of the reservoir and collect the oil towards the well and the ground surface. Generally, there are two fluid phases in underground oil reservoirs for unsaturated soil zone. These two fluids are oil as the non-wetting fluid and the water as the wetting fluid. Considering this issue, modeling and simulating water movement for underground oil reservoirs is very important for optimal exploitation of oil reservoirs.

In the literature, many researches have been performed to investigate two-phase flow in unsaturated soils. These researches include numerical methods, analytical solutions and experimental studies. Van Duijn et al. [1] analyzed stability of steady, vertically upward and downward flow of water in a homogeneous layer of soil.

In that research, an extension of the Richards equation for investigating dynamic memory effects were considered. Szymkiewicz et al. [2] presented a mathematical model for two phase flow in a heterogeneous porous medium. They investigated this approach with two numerical examples concerning oil–water and CO2–brine flow, respectively. Du and Nydal [3] developed Flow models and numerical schemes for single/two-phase transient flow in one dimension. They presented two numerical schemes in forms of non-iterative and iterative for prediction of transient problems. Cogswell and Szulczewski [4] solved two-phase incompressible flow without capillary potential for large time steps by introducing a macroscopic surface tension and employing a convex energy splitting scheme. They used new homotopy method to increase time step by more than six orders. Zhang et al. [5] presented a numerical simulation of water distribution associated with internal corrosion induced by water wetting in upward inclined oil pipes. In their research, results of numerical simulation were coincided well with available experimental results. Ma et al. [6] developed Fully coupled hydro-mechanical modeling of two-phase flow in deformable fractured porous media based on combining discontinuous Galerkin (DG) and continuous Galerkin (CG) finite element methods (FEM). In their research, several benchmark cases were used for investigating accuracy of proposed method. Ghedira et al. [7] developed numerical simulation of incompressible two-phase flows with phase change process in porous media based on OpenFOAM solver. Their results validated with various test cases. Also, they compared numerical results with analytical solutions and other results in literature.

It should be noted that other numerical techniques have been proposed for investigating two-phase flow in unsaturated soils and/or porous media. These techniques include volume of fluid method (VOF), meshless method, finite volume method (FVM), Lattice Boltzmann method (LBM), Support vector machine (SVM), discontinuous Galerkin method, Green element method (GEM) and/or other numerical methods [8-20]. A number of researchers developed analytical solutions for two-phase flow in unsaturated soils and/or porous media [21-32].

In this study, Adomian Decomposition Method (ADM) is used to develop analytical solutions for steady water flow in an unsaturated soil column containing oil. Governing equation for this flow is strongly nonlinear and therefore, presenting analytical solutions for this equation is very valuable. A total of three soils with different pore size distribution index are considered in this research and analytical solutions by ADM are presented for these cases. These pore size distribution indexes are 2, 3 and 4 for cases 1, 2 and 3, respectively. Also, a comparison of presented analytical solutions with a numerical solution is performed for all cases.

2. Governing equation

The governing equation for steady flow of two fluid phases in unsaturated soil is expressed as [33]:

$$\frac{\partial p_c}{\partial x_i} = \left(\frac{q_{wi}\mu_w}{k_w} - \frac{q_{nwi}\mu_{nw}}{k_{nw}}\right) - (\Delta\rho)g_i \qquad (1)$$

Where p_c, is the capillary pressure and is defined the difference between non-wetting pressure and wetting pressure or $p_{nw} - p_w$, q, is the volume flux, μ, is the dynamic viscosity of fluid, k, is the permeability. In Eq. 1 index w is for wetting phase and index nw is for non-wetting phase. Also, $\Delta\rho$ is the difference between densities for wetting and non-wetting phases, g_i is the gravity acceleration for 3d and x_i, is the directions in x, y and z. Equation (1) is derived with combining flux and continuity equations. Also, Darcy's law is used for each fluid in soil. Therefore, advection-dispersion effects have been seen within the

governing equation. Eq. 1 for flowing single wetting phase is written as:

$$\frac{\partial p_c}{\partial x_i} = (\frac{q_{wi}\mu_w}{k_w}) + (\Delta\rho)g\frac{\partial h}{\partial x_i} \quad (2)$$

Where h is equivalent with z direction and g is the gravity acceleration for z direction. Therefore, $\frac{\partial h}{\partial x_i}$, is equal to $\frac{\partial z}{\partial x_i}$, which is $sin\,\beta$ and x_i is $\frac{h}{sin\,\beta}$ and consequently, Eq. 2 is expressed as:

$$\frac{dh_c}{dh} = 1 - \frac{|q_w|\mu_w}{(\Delta\rho)gk_w\,sin(\beta)} \quad (3)$$

Where h_c is the capillary pressure head and is equal to $\frac{p_c}{(\Delta\rho)g}$. k_w in Eq. 3 is depended on p_c and can be substituted with different equations in the literature. A schematic view of the steady downward flow of a wetting fluid (SDFWF) in unsaturated soil (Eq. 3) is presented in Fig. 1.

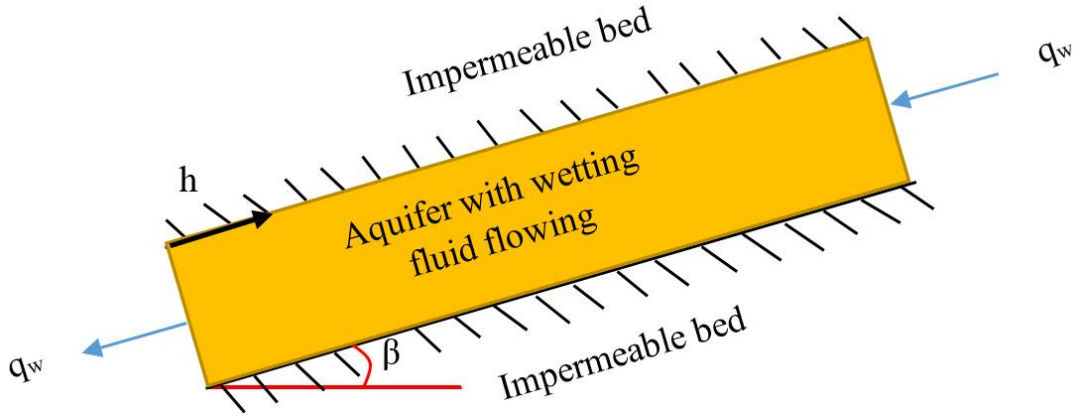


Figure 1. A schematic view of the steady downward flow of a wetting fluid (SDFWF) in unsaturated soil

In the current study, Brooks-Corey equation [33] is used for $k_w$which is:

$$k_w = k_m(\frac{P_d}{P_c})^{\eta} \quad (4)$$

Where η is $3\lambda + 2$, and λ is pore size distribution index. The typical values of λ are 2 to 5 for different soils. It should be noted that, $\lambda \to \infty$ for a soil with uniform pore size. In Eq. 4, k_m (L^2) is the saturated permeability and P_d is displacement pressure or critical P_c value. The displacement pressure is P_c value in saturation degree equal to 1. By substituting Eq. 4 to Eq. 3 and simplification, Eq. 5 is obtained:

$$\frac{dh_c}{dh} = 1 - a(\frac{h_c}{h_d})^{\eta} \quad (5)$$

Where h_d is $\frac{P_d}{(\Delta\rho)g}$ and a is:

$$a = \frac{|q_w|\mu_w}{(\Delta\rho)gk_m\,sin(\beta)} \quad (6)$$

Where a is dimensionless. To obtain the dimensionless form for Eq. 5, h_c and h should be divided by h_d. Therefore, the dimensionless form for Eq. 5 is obtained as follows:

$$\frac{dh_c^*}{dh^*} = 1 - ah_c^{*\eta} \quad (7)$$

Where h_c^* is $\frac{h_c}{h_d}$ and h^* is $\frac{h}{h_d}$. Eq. 7 is governing equation for the SDFWF in the dimensionless form. The current study presents analytical solutions for Eq. 7 in different values of η and a. The Adomian

decomposition method (ADM) is used for obtaining these analytical solutions.

3. Using the ADM for the SDFWF equation

The Adomian decomposition method presents an analytical solution to nonlinear ordinary differential equation without any simplification, linearization and change in governing equation at beginning of solution process. However, other analytical and semi-analytical methods use a simplification and linearization procedure and then present the final solution. Therefore, ADM provides very realistic and very close to reality solutions, which is one of the great advantages of this method over other analytical and semi-analytical methods. A nonlinear ordinary differential equation can be expressed in the following initial form:

$$F(y) = f \tag{8}$$

In this equation F, a nonlinear differential operator is applied to y and y itself is a function of x. Also, f itself can generally be a function of x and y. Eq. 8 can be written in more details in the form below:

$$Ly + Ry + Ny = f \tag{9}$$

In Eq. 9, L is a linear operator applied to y, for example, it can be $\frac{d}{dx}$ or $\frac{d^2}{dx^2}$. In fact, L is a linear operator as a fraction of F in Eq. 8, so that L is also invertible, i.e. if L is $\frac{d}{dx}$, it can derive the opposite action, which is integral once to x, Or, if L is $\frac{d^2}{dx^2}$, or if L is an example, it could have twice the derivative inverse of the integral of x. In Eq. 9, R is a linear operator applied to y for the remainder of the linear part F. Finally, N in Eq. 9 is a nonlinear operator; in other words, N contains nonlinear forms F. Now, by comparison of Eq. 9 with governing equation in this research (Eq. 7) and inverting the operator L, which is integral, on the sides of Eq. 9 yields:

$$L^{-1}Lh_c^* = L^{-1}f - L^{-1}Rh_c^* - L^{-1}Nh_c^* \tag{10}$$

Where L is the $\frac{d}{dh^*}$ and $L^{-1}$is the integral respect to h^*. Since the integral is associated with the integral constant and this integral constant is the initial condition of the problem, by applying the initial condition in the problem in Eq. 10, yields:

$$h_c^* = h_c^*(0) + L^{-1}f - L^{-1}Rh_c^* - L^{-1}Nh_c^* \tag{11}$$

Consequently, the final answer for h_c^* is:

$$h_c^* = \sum_{n=0}^{\infty} h_{c_n}^* = h_{c_0}^* + h_{c_1}^* + h_{c_2}^* + h_{c_3}^* + \cdots \tag{12}$$

The first two terms on the right side of Eq. 11 are introduced as $h_{c_0}^*$ in Eq. 12. This method is used for the nonlinear term Nh_c^* in Eq. 11, as follows:

$$Nh_c^* = \sum_{n=0}^{\infty} A_n\left(h_{c_0}^*, h_{c_1}^*, \ldots, h_{c_n}^*\right) = A_0 + A_1 + A_2 + \cdots \tag{13}$$

In Eq. 13, the coefficients A_0, A_1, A_2, ... are defined as:

$$A_0 = Nh_c^*(h_{c_0}^*) \tag{14a}$$

$$A_1 = h_{c_1}^* \left(\frac{d}{dh_{c_0}^*}\right) Nh_c^*(h_{c_0}^*) \tag{14b}$$

$$A_2 = h_{c_2}^* \left(\frac{d}{dh_{c_0}^*}\right) Nh_c^*(h_{c_0}^*) + \left(\frac{h_{c_1}^{*2}}{2!}\right)\left(\frac{d^2}{dh_{c_0}^{*2}}\right) Nh_c^*(h_{c_0}^*) \tag{14c}$$

$$A_3 = h_{c_3}^* \left(\frac{d}{dh_{c_0}^*}\right) Nh_c^*(h_{c_0}^*) + h_{c_1}^* h_{c_2}^* \left(\frac{d^2}{dh_{c_0}^{*2}}\right) Nh_c^*(h_{c_0}^*) + \left(\frac{h_{c_1}^{*3}}{3!}\right)\left(\frac{d^3}{dh_{c_0}^{*3}}\right) Nh_c^*(h_{c_0}^*) \tag{14d}$$

And etc. (see Adomian [34]). Now the Eq. 11 can be written as given by the Eqs. 12 and 13:

$$h_c^* = \sum_{n=0}^{\infty} h_{c_n}^* = h_{c_0}^* - L^{-1}R \sum_{n=0}^{\infty} h_{c_n}^* - L^{-1} \sum_{n=0}^{\infty} A_n \tag{15}$$

So, $h_{c_1}^*$,$h_{c_2}^*$, ... can be written as:

$$h_{c_1}^* = -L^{-1}Rh_{c_0}^* - L^{-1}A_0 \tag{16a}$$

$$h_{c_2}^* = -L^{-1}Rh_{c_1}^* - L^{-1}A_1 \tag{16b}$$

And etc. Now, by comparing Eq. 7 with the format written in Eq. 9, the parameters of Eq. 9 in this research are:

$$L = \frac{d}{dh^*}\ , R = 0\ , f = 0\ , \quad Nh_c^* = -\left(1 - ah_c^{*\eta}\right) \tag{17}$$

And the new form of Eq. 11 based on Eq. 7 is:

$$h_c^* = h_c^*(0) + L^{-1}Nh_c^* \tag{18}$$

In Eq. 18, $h_c^*(0)$ is the capillary pressure value at $h^* = 0$. Therefore, the solutions for $h_{c_1}^*$, $h_{c_2}^*$, ... are obtained in Eqs. 16a and 16b with R=0, and finally the value of h_c^* in Eq. 15 is expressed as:

$$h_c^* = h_{c_0}^* + \int A_0 dx + \int A_1 dx + \int A_2 dx + \int A_3 dx + \cdots \tag{19}$$

In Eq. 19, the second, third, fourth and etc. terms are h_{c1}^*,h_{c2}^*,h_{c3}^* and etc., respectively. Also, $h_{c_0}^*$ in Eq. 19 is the boundary condition value for Eq. 7.

4. ADM solution of SDFWF equation for λ=2 and η=8

In this section, λ is considered equal 2 and in accordance with the described process in the previous sections, η value is 8. By substituting η into Eq. 7, $f(h_{c_0}^*)$ is defined as:

$$f(h_{c_0}^*) = (1 - ah_{c_0}^{*\,8}) \tag{20}$$

According to Eq. 20 and the mentioned explanations in Eqs. 15 to 19, the answers for h_{c1}^* , h_{c2}^* , h_{c3}^* and etc. are obtained. Considering that the answers are long, only the first five terms of h_c^* in Eq. 19 are presented here:

$$h_{c_1}^* = (1 - a{h_{c_0}^*}^8)h^* \quad (21)$$

$$h_{c_2}^* = -4(1 - a{h_{c_0}^*}^8)a{h^*}^2{h_{c_0}^*}^7 \quad (22)$$

$$h_{c_3}^* = \frac{32}{3}(1 - a{h_{c_0}^*}^8){h^*}^3a^2{h_{c_0}^*}^{14} - \frac{28}{3}(1 - a{h_{c_0}^*}^8)^2{h^*}^3a{h_{c_0}^*}^6 \quad (23)$$

$$h_{c_4}^* = -8a{h_{c_0}^*}^7\left(\frac{8}{3}(1 - a{h_{c_0}^*}^8){h^*}^4a^2{h_{c_0}^*}^{14} - \frac{7}{3}(1 - a{h_{c_0}^*}^8)^2{h^*}^4a{h_{c_0}^*}^6\right) + 56(1 - a{h_{c_0}^*}^8)^2{h^*}^4a^2{h_{c_0}^*}^{13} - 14(1 - a{h_{c_0}^*}^8)^3{h^*}^4a{h_{c_0}^*}^5 \quad (24)$$

$$h_{c_5}^* = -8a{h_{c_0}^*}^7(-8a{h_{c_0}^*}^7((\frac{8}{15}(-a{h_{c_0}^*}^8 + 1))h^{*5}a^2{h_{c_0}^*}^{14} - (\frac{7}{15})(-a{h_{c_0}^*}^8 + 1)^2h^{*5}a{h_{c_0}^*}^6) + (56/5)(-a{h_{c_0}^*}^8 + 1)^2h^{*5}a^2{h_{c_0}^*}^{13} - (14/5)(-a{h_{c_0}^*}^8 + 1)^3h^{*5}a{h_{c_0}^*}^5) - 56a{h_{c_0}^*}^6((8/5)(-a{h_{c_0}^*}^8 + 1)^2h^{*5}a^2{h_{c_0}^*}^{14} + (1/5(-a{h_{c_0}^*}^8 + 1))h^{*5}((32/3(-a{h_{c_0}^*}^8 + 1))a^2{h_{c_0}^*}^{14} - (28/3)(-a{h_{c_0}^*}^8 + 1)^2a{h_{c_0}^*}^6)) + (672/5)(-a{h_{c_0}^*}^8 + 1)^3h^{*5}a^2{h_{c_0}^*}^{12} - 14(-a{h_{c_0}^*}^8 + 1)^4h^{*5}a{h_{c_0}^*}^4 \quad (25)$$

By summating these answers according to Eq. 19, the h_c^* function is obtained for λ=2 and η=8. In order to plot h_c^* verses h^*, example values for a and h_{c0}^* should be selected. These values are selected based on discharge value and soil properties. By considering a=0.1, 0.5 and 0.7 and h_{c0}^* (boundary condition) equal to 1 in these answers, h_c^*functions for the approximately eighth sentences are presented in Table 1.

Table 1. h_c^* functions for different values of *a* in *λ=2* and *η=8*

Values for *a*	Values for h_{c0}^*	h_c^* functions
0.1	1	$h_c^* = 1 + 0{,}9h^* - 0{,}36{h^*}^2 - 0{,}66{h^*}^3 - 0{,}435{h^*}^4 + 0{,}72354{h^*}^5 + 1{,}891052{h^*}^6 + 0{,}8468553721{h^*}^7$
0.5	1	$h_c^* = 1 + 0{,}5h^* - 1{,}00{h^*}^2 + 0{,}166666666{h^*}^3 + 2{,}458333334{h^*}^4 - 1{,}470833331{h^*}^5 - 8{,}790277781{h^*}^6 + 9{,}669543642{h^*}^7$
0.7	1	$h_c^* = 1 + 0{,}3h^* - 0{,}84{h^*}^2 + 0{,}98{h^*}^3 + 0{,}833{h^*}^4 - 4{,}30514{h^*}^5 + 2{,}611046666{h^*}^6 + 13{,}51103507{h^*}^7$

Replacing h^* values in the analytical solutions (Table 1), the dimensionless capillary pressure head (h_c^*) can be plotted. Figure 2 shows a comparison of h_c^*values using ADM (Table 1) and numerical solution values (to Eq. 7) for a dimensionless length (h^*) of 0.5 in a vertical soil column with $\beta = 90°$. Finite difference method (FDM) with $\Delta h^* = 0.01$is used for the numerical solution. As shown in Figure 2, there is an excellent agreement between ADM and FDM results. The comparison confirms high accuracy of h_c^* functions in Table 1 as analytical solutions for SDFWF equation with soil properties of λ=2 and η=8.

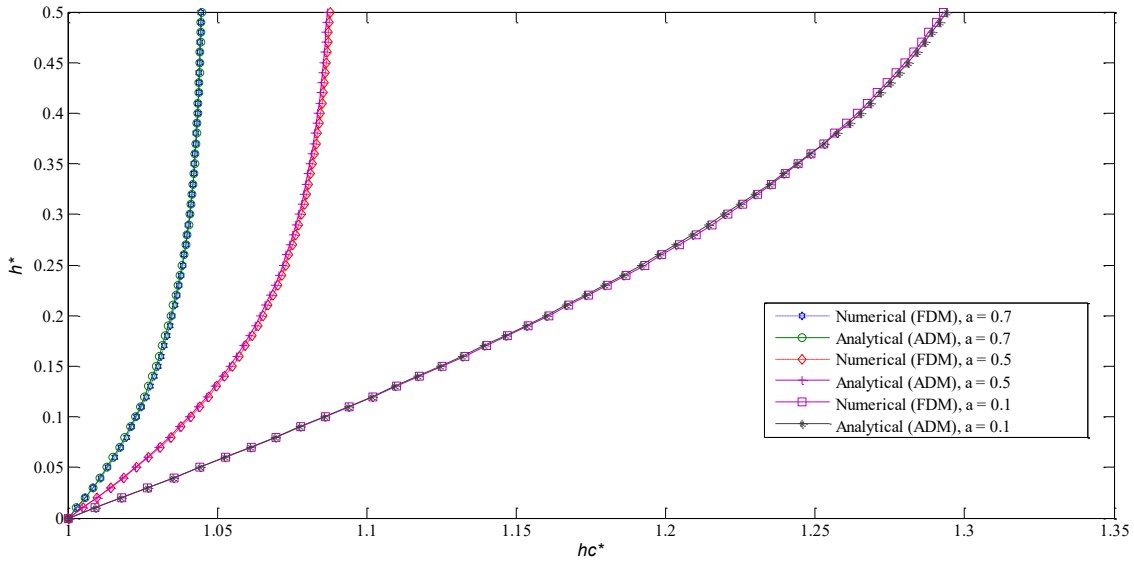


Figure 2. Comparison of normalized capillary pressures head verses normalized elevation values in numerical and analytical methods for λ=2 and η=8

5. ADM solution of SDFWF equation for λ=3 and η=11

In this section, λ is considered equal 3 and in accordance with the described process in the previous sections, η value is 11. By substituting η into Eq. 7, $f(h_{c_0}^*)$ is defined as:

$$f(h_{c_0}^*) = (1 - a{h_{c_0}^*}^{11}) \quad (26)$$

According to Eq. 26 and the mentioned explanations in Eqs. 15 to 19, the answers for h_{c1}^*, h_{c2}^*, h_{c3}^* and etc. are obtained. Considering that the answers are long, only the first four terms of h_c^* in Eq. 19 are presented here:

$$h_{c_1}^* = (1 - a{h_{c_0}^*}^{11})h^* \quad (27)$$

$$h_{c_2}^* = -\frac{11}{2}\left(1 - a{h_{c_0}^*}^{11}\right){h^*}^2 a{h_{c_0}^*}^{10} \quad (28)$$

$$h_{c_3}^* = \frac{121}{6}\left(1 - a{h_{c_0}^*}^{11}\right){h^*}^3 a^2{h_{c_0}^*}^{20} - \frac{55}{3}\left(1 - a{h_{c_0}^*}^{11}\right)^2 {h^*}^3 a{h_{c_0}^*}^{9} \quad (29)$$

$$h_{c_4}^* = -11a{h_{c_0}^*}^{10}\left(\frac{121}{24}\left(1 - a{h_{c_0}^*}^{11}\right){h^*}^4 a^2{h_{c_0}^*}^{20} - \frac{55}{12}\left(1 - a{h_{c_0}^*}^{11}\right)^2 {h^*}^4 a{h_{c_0}^*}^{9}\right) + \frac{605}{4}\left(1 - a{h_{c_0}^*}^{11}\right)^2 {h^*}^4 a^2{h_{c_0}^*}^{19} - \frac{165}{4}\left(1 - a{h_{c_0}^*}^{11}\right)^3 {h^*}^4 a{h_{c_0}^*}^{8} \quad (30)$$

By summating these answers according to Eq. 19, the h_c^* function is obtained for λ=3 and η=11. In order to plot h_c^* verses h^*, example values for a and $h_{c_0}^*$ should be selected. These values are selected based on discharge value and soil properties. By considering a=0.1, 0.5 and 0.7 and $h_{c_0}^*$ (boundary condition) equal to 1 in these answers, h_c^* functions for the approximately eighth sentences are presented in Table 2.

Table 2- h_c^* functions for different values of a in $\lambda=3$ and $\eta=11$

Values for a	Values for $h_{c_0}^*$	h_c^* functions
0.1	1	$h_c^* = 1 + 0.9h^* - 0.495{h^*}^2 - 1.3035{h^*}^3 - 1.4235375{h^*}^4 + 2.26372575{h^*}^5 + 11.03425936{h^*}^6 + 12.36402593{h^*}^7$
0.5	1	$h_c^* = 1 + 0.5h^* - 1.375000000{h^*}^2 + 0.229166666{h^*}^3 + 6.559895834{h^*}^4 - 3.921614573{h^*}^5 - 47.23721789{h^*}^6 + 51.09599910{h^*}^7$
0.7	1	$h_c^* = 1 + 0.3h^* - 1.155{h^*}^2 + 1.8095{h^*}^3 + 2.4072125{h^*}^4 - 15.50947475{h^*}^5 + 9.61202517{h^*}^6 + 101.8603676{h^*}^7$

Substituting h^* values in the analytical solutions (Table 2), the dimensionless capillary pressure head (h_c^*) may be plotted. Figure 3 shows a comparison of h_c^* values using ADM (Table 2) and numerical solution values (to Eq. 7) for a dimensionless length (h^*) of 0.5 in a vertical soil column with $\beta = 90°$. Finite difference method (FDM) with $\Delta h^* = 0.01$is used for the numerical solution. As shown in Figure 3, there is an excellent agreement between ADM and FDM results. The comparison confirms accuracy of h_c^* functions in Table 2 as analytical solutions for SFWF equation with soil properties of λ=3 and η=11.

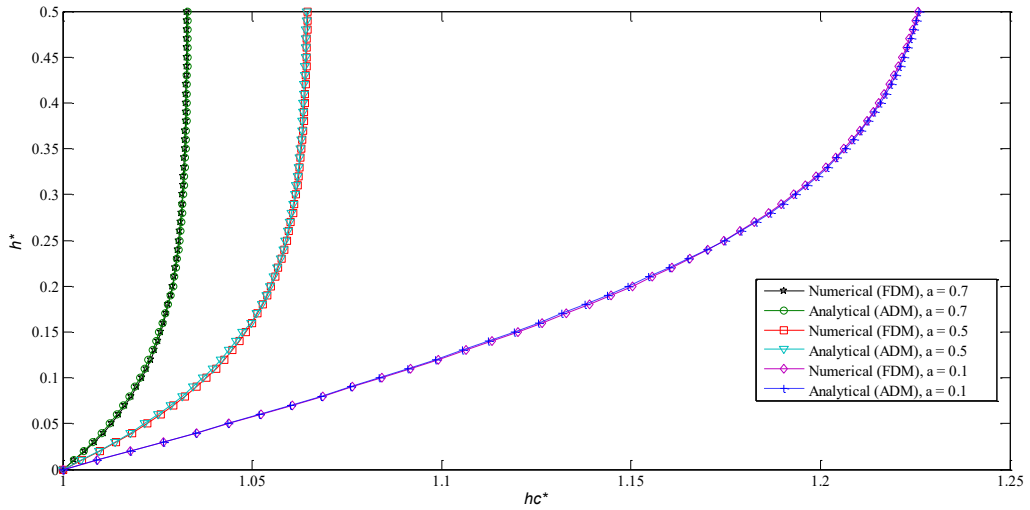


Figure 3. Comparison of normalized capillary pressures head verses normalized elevation values in numerical and analytical methods for λ=3 and η=11

6. ADM solution of SDFWF equation for λ=4 and η=14

In this section, λ is considered equal 4 and in accordance with the described process in the previous sections, η value is 14. By substituting η into Eq. 7, $f(h_{c_0}^*)$ is defined as:

$$f(h_{c_0}^*) = (1 - a{h_{c_0}^*}^{14}) \quad (31)$$

According to Eq. 31 and the mentioned explanations in Eqs. 15 to 19, the answers for h_{c1}^* , h_{c2}^* , h_{c3}^* and etc. are obtained. Considering that the answers are long, only the first four terms of h_c^* in Eq. 19 are presented here:

$$h_{c_1}^* = (1 - a{h_{c_0}^*}^{14})h^* \quad (32)$$

$$h_{c_2}^* = -7\left(1 - a{h_{c_0}^*}^{14}\right){h^*}^2 a{h_{c_0}^*}^{13} \quad (33)$$

$$h_{c_3}^* = \frac{98}{3}\left(1 - a{h_{c_0}^*}^{14}\right){h^*}^3 a^2{h_{c_0}^*}^{26} - \frac{91}{3}\left(1 - a{h_{c_0}^*}^{14}\right)^2 {h^*}^3 a{h_{c_0}^*}^{12} \quad (34)$$

$$h_{c_4}^* = -14a{h_{c_0}^*}^{13}\left(\frac{49}{6}\left(1 - a{h_{c_0}^*}^{14}\right){h^*}^4 a^2{h_{c_0}^*}^{26} - \frac{91}{12}\left(1 - a{h_{c_0}^*}^{14}\right)^2 {h^*}^4 a{h_{c_0}^*}^{12}\right) + \frac{637}{2}\left(1 - a{h_{c_0}^*}^{14}\right)^2 {h^*}^4 a^2{h_{c_0}^*}^{25} - 91\left(1 - a{h_{c_0}^*}^{14}\right)^3 {h^*}^4 a{h_{c_0}^*}^{11} \quad (35)$$

By summating these answers according to Eq. 19, the h_c^* function is obtained for λ=4 and η=14. In order to plot h_c^* verses h^*, example values for a and $h_{c_0}^*$ should be selected. These values are selected based on discharge value and soil properties. By considering a=0.01, 0.001 and 0.0001 and $h_{c_0}^*$ (boundary condition) equal to 1 in these answers, h_c^* functions for the approximately eighth sentences are presented in Table 3.

Table 3. h_c^* functions for different values of *a* in *λ=4* and *η=14*

Values for a	Values for $h_{c_0}^*$	h_c^* functions
0.01	1	$h_c^* = 1 + 0.99h^* - 0.0693{h^*}^2 - 0.294063{h^*}^3 - 0.8414637{h^*}^4 - 1.646118428{h^*}^5 - 1.923599743{h^*}^6 + 0.1642565113{h^*}^7$
0.001	1	$h_c^* = 1 + 0.999h^* - 0.006993{h^*}^2 - 0.030240063{h^*}^3 - 0.09030356937{h^*}^4 - 0.1965245847{h^*}^5 - 0.3186765805{h^*}^6 - 0.3795618968{h^*}^7$
0.0001	1	$h_c^* = 1 + 0.9999h^* - 0.00069993{h^*}^2 - 0.003032400063{h^*}^3 - 0.00909302457{h^*}^4 - 0.0199831278{h^*}^5 - 0.03321588658{h^*}^6 - 0.04240053504{h^*}^7$

Substituting h^* values in the analytical solutions (Table 3), the dimensionless capillary pressure head (h_c^*) may be plotted. Figure 4 shows a comparison of h_c^* values using ADM (Table 3) and numerical solution values (to Eq. 7) for a dimensionless length (h^*) of 1.5 in a vertical soil column with $\beta = 90°$. Finite difference method (FDM) with $\Delta h^* = 0.01$is used for the numerical solution. As shown in Figure 4, there is an excellent agreement between ADM and FDM results. The comparison confirms high accuracy of h_c^* functions in Table 3 as analytical solutions for SFWF equation with soil properties of λ=4 and η=14. By comparing Figures 2, 3, and 4, it is found that as the values of λ and η increase, the graph slope of h^* versus h_c^* increase. Also, by increasing λ, the graphs at high values for h^* are formed as almost straight vertical lines. In other words, as the pore size distribution index (λ) increases, the pore size of the soil increases and the flow rate passes through the soil column at a faster rate.

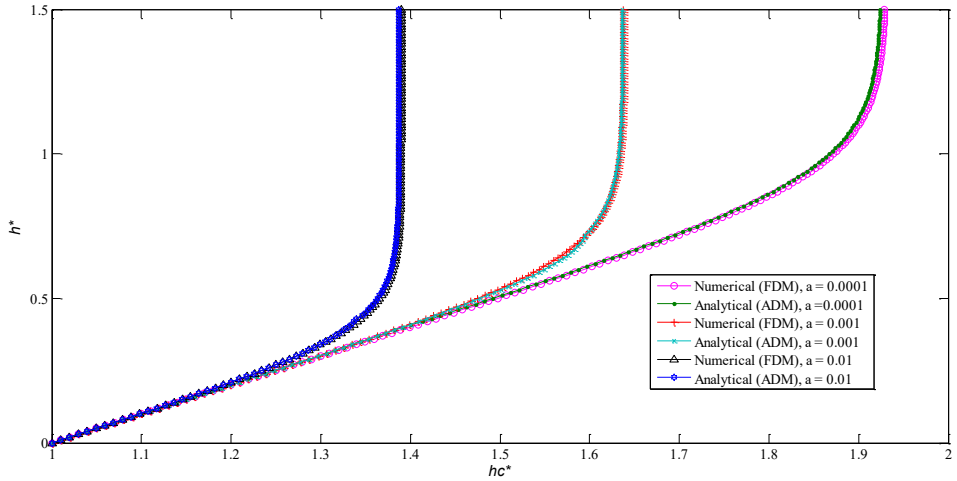


Figure 4. Comparison of normalized capillary pressures head verses normalized elevation values in numerical and analytical methods for λ=4 and η=14

Conclusion

This paper presented analytical solutions for the steady downward flow of a wetting fluid (SDFWF) in unsaturated soil. Governing equation for SFWF is an ordinary differential equation with strongly nonlinear form and therefore, presenting analytical solutions for this equation is very important. The Adomian decomposition method (ADM) were applied to SDFWF equation for obtaining analytical solutions. A total of 3 cases were considered in this study for different soil properties. The pore size distribution index in these cases were 2, 3 and 4. A comparison between ADM and finite difference method (FDM) results were performed in three cases. An excellent agreement between ADM and FDM results were seen in all cases. Therefore, it was concluded that ADM may be used to obtain analytical solutions for SFWF equation in vertical soil column with a high level of accuracy. Presented analytical solutions in this research can be used as reference solutions for efficiency assessment of various numerical techniques and similar laboratory works that calculate capillary pressure distribution in soil column with SFWF.

Funding statement:

This research received no external funding.

Conflict of Interest:

The authors declare that they have no conflict of interest.

AI Statement:

During the preparation of this work the author used check spelling tools in order to grammar correct. After using this tool, the author reviewed and edited the content as needed and takes full responsibility for the content of the publication.

Author Contributions:

All authors contributed to the study conception and design. Material preparation, data collection, and analysis … were performed by Hamed Reza Zarif Sanayei. The first draft of the manuscript was written by Hamed Reza Zarif Sanayei. The author reads and approved the final manuscript.

References

1. Van Duijn CJ, Pieters GJM, Raats PAC. Steady flows in unsaturated soils are stable. Transport in Porous Media. 2004; 57:215–244. https://doi.org/10.1023/B:TIPM.0000038250.72364.20
2. Szymkiewicz A, Helmig R, Kuhnke H. Two-phase flow in heterogeneous porous media with non-wetting phase trapping. Transport in Porous Media. 2011;86: 27–47. https://doi.org/10.1007/s11242-010-9604-x
3. Du X, Nydal OJ. Flow models and numerical schemes for single/two-phase transient flow

in one dimension. Applied Mathematical Modelling. 2017; 42:145–160. https://doi.org/10.1016/j.apm.2016.10.017
4. Cogswell DA, Szulczewski ML. Simulation of incompressible two-phase flow in porous media with large time steps. Journal of Computational Physics. 2017; 345:856–865. https://doi.org/10.1016/j.jcp.2017.06.007
5. Zhang H, Lan H, Lin N. A numerical simulation of water distribution associated with internal corrosion induced by water wetting in upward inclined oil pipes. Journal of Petroleum Science and Engineering. 2019; 173:351–361. https://doi.org/10.17632/6h5nzf9zb4.1
6. Ma T, Jiang L, Shen W, Cao WZ, Guo C, Nick HM. Fully coupled hydro-mechanical modeling of two-phase flow in deformable fractured porous media with discontinuous and continuous Galerkin method. Computers and Geotechnics. 2023; 164:105823. https://doi.org/10.1016/j.compgeo.2023.105823
7. Ghedira A, Lataoui Z, Benselama AM, Bertin Y, Jemni A. Numerical simulation of incompressible two-phase flows with phase change process in porous media. Results in Engineering. 2025; 25: 103706. https://doi.org/10.1016/j.rineng.2024.103706
8. Rao X, Cheng L, Cao R, Song W, Du X, He Y, Dai D. Numerical simulation of two-phase flow in porous media based on mimetic Green element method. Engineering Analysis with Boundary Elements. 2019; 101: 113-120. https://doi.org/10.1016/j.enganabound.2019.01.010
9. Tran LK, Kim JC, Matthäi SK. Simulation of two-phase flow in porous media with sharp material discontinuities. Advances in Water Resources. 2020; 142: 103636. https://doi.org/10.1016/j.advwatres.2020.103636
10. Lee EJ, Wang W, Chen P, Jiao Z, Gong Y, Mu D, Liao WY. Mesh-free simulation of two-phase fluid flow in porous media based on the shock-fitting method. Journal of Petroleum Science and Engineering. 2022; 215(B): 110637. https://doi.org/10.1016/j.petrol.2022.110637
11. Li X, Li L, Ma W, Wang W. Two-phase flow patterns identification in porous media using feature extraction and SVM. International Journal of Multiphase Flow. 2022; 156: 104222. https://doi.org/10.1016/j.ijmultiphaseflow.2022.104222
12. Shen B., Riviere B. A sequential discontinuous Galerkin method for two-phase flow in deformable porous media. Computer Methods in Applied Mechanics and Engineering. 2022; 399: 115266. https://doi.org/10.1016/j.cma.2022.115266
13. Ballini E, Formaggia L, Fumagalli A, Keilegavlen E, Scotti A. A hybrid upwind scheme for two-phase flow in fractured porous media. Computer Methods in Applied Mechanics and Engineering. 2024; 432: 117437. https://doi.org/10.1016/j.cma.2024.117437
14. Feng J., Liu Y., Min J. A pore-scale investigation of viscous coupling effect on immiscible two-phase flow in porous media. Chemical Engineering Research and Design. 2024; 211: 379-390. https://doi.org/10.1016/j.cherd.2024.10.019
15. Zhan W, Zhao H, Liu Y, Wei Z, Rao X. A novel meshless numerical simulation of oil-water two-phase flow with gravity and capillary forces in three-dimensional porous media. Engineering Analysis with Boundary Elements. 2024; 169(A): 105975. https://doi.org/10.1016/j.enganabound.2024.105975
16. Li X, Yan Y, Chen H. A class of high-order physics-preserving schemes for thermodynamically consistent model of incompressible and immiscible two-phase flow in porous media. Journal of Computational Physics. 2025; 529: 113864. https://doi.org/10.1016/j.jcp.2025.113864
17. Peng J, Xia B, Lu Y, Song R, Wang L. Pore-scale analysis and modeling of heterogeneous wettability in immiscible two-phase flow inside natural porous media. Geoenergy Science and Engineering. 2025; 247: 213676. https://doi.org/10.1016/j.geoen.2025.213676
18. Vakili A. H., Falamaki A. An investigation on the parameters affecting the behavior of broadly graded, dispersive base soil-filter systems in earth dams. Journal of Hydraulic structures. 2025; 11(32): 44-60. https://doi.org/10.22055/JHS.2024.46910.1299
19. Mohtashami A., Hashemi Monfared S. A., Azizyan G., Akbarpour A. Estimation of Parameters in Groundwater Modeling by Particle Filter linked to the meshless local

Petrov-Galerkin Numerical Method. Journal of Hydraulic structures. 2021; 7(15): 16-37. https://doi.org/10.22055/JHS.2021.37091.1167

20. Talebi M. Investigating the vulnerability of underground water to pollution (case study: East and Northeast of Chaharmahal and Bakhtiari province). Journal of Hydraulic structures. 2025; 11(32): 87-105. https://doi.org/10.22055/JHS.2024.47643.1316
21. Pan L, Webb SW, Oldenburg CM. Analytical solution for two-phase flow in a wellbore using the drift-flux model. Advances in Water Resources. 2011; 34(12): 1656-1665. https://doi.org/10.1016/j.advwatres.2011.08.009
22. Borazjani S, Bedrikovetsky P, Farajzadeh R. Analytical solutions of oil displacement by a polymer slug with varying salinity. Journal of Petroleum Science and Engineering. 2016; 140: 28–40. https://doi.org/10.1016/j.petrol.2016.01.001
23. Fučík R, llangasekare TH, Beneš M. Multidimensional self-similar analytical solutions of two-phase flow in porous media. Advances in Water Resources. 2016; 90: 51-56. https://doi.org/10.1016/j.advwatres.2016.02.007
24. Mohammadein SA, Shalaby GA, Abu-Bakr AF, Abu-Nab AK. Analytical solution of gas bubble dynamics between two-phase flow. Results in Physics. 2017; 7: 2396-2403. https://doi.org/10.1016/j.rinp.2017.07.007
25. Hajra SG, Kandel S, Pudasaini SP. On analytical solutions of a two-phase mass flow model. Nonlinear Analysis: Real World Application. 2018; 41: 412-427. https://doi.org/10.1016/j.nonrwa.2017.09.009
26. Rybdylova O, Sazhin SS, Osiptsov AN, Kaplanski FB, Begg S, Heikal M. Modelling of a two-phase vortex-ring flow using an analytical solution for the carrier phase. Applied Mathematics and Computation. 2018; 326: 159-169. https://doi.org/10.1016/j.amc.2017.12.044
27. Rabinovich A. An analytical solution for cyclic flow of two immiscible phases. Journal of Hydrology. 2019; 570: 682-691. https://doi.org/10.1016/j.jhydrol.2018.12.056
28. Zarif Sanayei HR, Talebbeydokhti N, Rakhshandehroo GR. Analytical solutions for water infiltration into unsaturated–semi-saturated soils under different water content distributions on the top boundary. Iranian Journal of Science and Technology, Transactions of Civil Engineering. 2019; 43: 747-760. https://doi.org/10.1007/s40996-019-00245-3
29. Apolinário FD, Paula AS, Pires AP. Injection of water slug containing two polymers in porous media: Analytical solution for two-phase flow accounting for adsorption effects. Journal of Petroleum Science and Engineering. 2020; 188: 106927. https://doi.org/10.1016/j.petrol.2020.106927
30. Barros WQ, Pires AP, Peres AMM. Analytical solution for one-dimensional three-phase incompressible flow in porous media for concave relative permeability curves. International Journal of Non-Linear Mechanics. 2021; 137: 103792. https://doi.org/10.1016/j.ijnonlinmec.2021.103792
31. Yang Y, Xu Y, Yuan C, Wang J, Wu H, Zhang T. Water cut measurement of oil–water two-phase flow in the resonant cavity sensor based on analytical field solution method. Measurement. 2021; 174: 109078. https://doi.org/10.1016/j.measurement.2021.109078
32. Zarif Sanayei HR, Javdanian H, Rakhshandehroo GR. Assessment of confined aquifer response to recharge variations and water inflow distributions using analytical approach. Environmental Science and Pollution Research. 2021; 28:50878–50889. https://doi.org/10.1007/s11356-021-14314-6
33. Corey AT. Mechanics of immiscible fluids in porous media. Water Resources Publications, LLC, Colorado, USA; 1994.
34. Adomian G. Nonlinear Stochastic Operator Equations. Academic Press, USA; 2014

© 2025 by the authors. Licensee SCU, Ahvaz, Iran. This article is an open access article distributed under the terms and conditions of the Creative Commons Attribution 4.0 International (CC BY 4.0 license) (http://creativecommons.org/licenses/by/4.0/).

Assessing the Impact of Multi-Reservoir Rationing on Downstream Drought Occurrence: A Case Study of Dez and Gotvand Reservoirs

Sama Banitamim [1], Seyed Mohammad Ashrafi [*,1] , Arash Adib [2]

1. Department of Civil Engineering, Faculty of Civil Engineering and Architecture, Shahid Chamran University of Ahvaz, Ahvaz, Iran.
2. Department of Environmental Engineering, Faculty of Civil Engineering and Architecture, Shahid Chamran University of Ahvaz, Ahvaz, Iran.

***Corresponding Author:**
Seyed Mohammad Ashrafi,

Email: ashrafi@scu.ac.ir
Received: 2025.07.04
Accepted: 2025.07.21
J. Hydraul. Struct., 2025; 12(2):34-50
DOI: 10.22055/jhs.2025.50084.1357

ABSTRACT

Water resource management in multi-reservoir systems is critical for meeting diverse demands while ensuring sustainability. In this study, we delve into optimizing the operating rule curve for such systems by integrating the Particle Swarm Optimization algorithm. Our overarching goal is to minimize relative deficiencies in water supply, considering both standard operating policies (SOP) and discrete two-level hedging policies. Our case study focuses on the Great Karun basin, a real-world scenario where water scarcity poses significant challenges. By coupling the PSO algorithm with a system simulation model, we search for optimal hedging levels across all reservoirs and months. Additionally, we rigorously compare the output results of our combined simulation-optimization model with those obtained from a SOP-based simulator. Furthermore, we analyze the flow drought index at key points throughout the basin under both rationing and SOP policies. Notably, while rationing generally reduces average drought severity, it may inadvertently exacerbate conditions in severely water-stressed areas like the Dez basin. The novelty of this study lies in coupling PSO-based optimization with detailed system simulation to develop dynamic hedging policies for multi-reservoir drought management. Our research contributes valuable insights into multi-reservoir system operation, shedding light on effective strategies for meeting water demands while mitigating the impact of droughts.

KEYWORDS

Reservoir operation, Hydrological drought, Simulation-optimization, Great Karun System, Water resource.

1. Introduction

The water resources crisis necessitates efficient utilization of water for various purposes, including municipal, drinking, agriculture, and industry. Structural facilities, such as large dam reservoirs, can play a crucial role in mitigating the effects of drought through their operational strategies [1, 2]. Reservoir operating policies directly impact the severity and duration of drought periods in watersheds that include storage reservoirs. While the Standard Operating Policy (SOP) ensures demand fulfillment, it requires adaptation during droughts [3, 4]. In this regard, hedging policy based on the optimum rationing strategy is recommended to minimize shortages and enhance reservoir system efficiency [5]. Although various optimization techniques have been proposed to achieve optimal operating rule curves [6], developing suitable operational strategies becomes more challenging when multiple purposes must be met across the entire basin. Real-world problems involving conflicting objectives—such as supplying agricultural demands, hydropower energy production,

and flood protection pose significant challenges [7, 8]. Meanwhile, effective drought mitigation measures have been proposed and investigated [9], extending beyond structural facilities. Given that drought, unlike other natural disasters, evolves over an extended period, effective cost reduction can be achieved by developing appropriate mitigation strategies, which should be planned meticulously, based on the suitable drought monitoring [10, 11, 12].

López-Moreno et al. [13] conducted research focusing on the impact of reservoirs on hydrological droughts downstream. Their study evaluated how a large reservoir affects hydrological droughts in a border river shared by two countries. Li et al. [14] quantitatively assessed the effects of reservoir outlets on hydrological droughts at downstream stations. Guo et al. [15] proposed an operation rule that combines parametric and rationing approaches to mitigate severe shortages during drought periods in multi-reservoir water management. Chang et al. [16] introduced a specialized reservoir policy based on rationing to minimize losses caused by water scarcity during droughts. To assess flow dynamics, calculating Indicators of Hydrologic Alteration (IHA) is common practice. Al-Faraj et al. [17] used these indicators to analyze temporal changes and the mutual influence of upstream human development on consecutive basin droughts. In a related study, Al-Faraj et al. [18] investigated the effects of successive droughts and human activities in the upstream region on a semi-arid border basin. Wu et al. [19] proposed a valuable method for assessing the impact of reservoir operating rules during droughts on multiscale correlations between hydrological and meteorological droughts at the basin level.

Men et al. [20] have made significant advancements in reservoir management by introducing the joint hedging rule as an improvement over the traditional rationing approach. They applied this novel rule to the Yuqiao Reservoir in Tianjin, China, and compared it with conventional hedging and standard operating policies. Meanwhile, Wu et al. [21] investigated the impact of anthropogenic regulations on hydrological drought development and recovery processes. Their findings highlight the reservoir operation's influence on short-term drought severity reduction and duration. Additionally, Ahmadianfar and Zamani [22] explored the effects of future climate change on agricultural reservoir utilization. Floods and droughts, as natural hazards linked to water resources, have caused significant harm to human societies. Proper management is crucial to prevent further disasters related to climate change risks [23, 24]. Meanwhile, evaluating the effects of climate change requires specialized methods to address related uncertainties [25, 26]. Obtaining a reliable projection of future runoff and streamflow across a watershed enables system managers to mitigate uncertainties and make informed decisions based on more accurate forecasts [27]. In a separate study, Ren et al. [28] emphasized that water and soil resource protection projects significantly alter river flow variability. These changes result from intricate interactions between natural processes and human activities, which remain incompletely understood. They investigated these interactions in a large river basin with multiple reservoirs to identify exploitation scenarios aimed at mitigating drought and flood effects [28].

In recent years, several studies have investigated the impact of regulating uncontrolled surface flows on hydrological drought occurrence [29, 30]. The primary objective of this research is to assess the influence of operating policies on hydrological drought characteristics within a regulated watershed. To achieve this, we employ hedging policies and standard operating policy models. Additionally, we extract optimal policies using the Particle Swarm Optimization (PSO) algorithm as an optimizer. The calculation of the surface flow drought index relies on reservoir

outputs from a multi-reservoir system, and we evaluate how operating policies affect this index. Given the significance of the Great Karun watershed's water resources system in the country [3], we conduct a case study within this system.

2. Case study:

In pursuit of our research objectives, we have selected the Great Karun multi-reservoir system, consists of the Karun and Dez rivers in Khuzestan province, as our study area. The Great Karun watershed covers an extensive area of 67,257 square kilometers in the southwest of Iran and ranks among the most significant watersheds of the Persian Gulf. Approximately 67% of this basin comprises mountainous terrain, while the remaining 33% consists of high plains. Our investigation centers around a water resources system that includes six reservoir dams and their associated power plants, strategically positioned along the Dez and

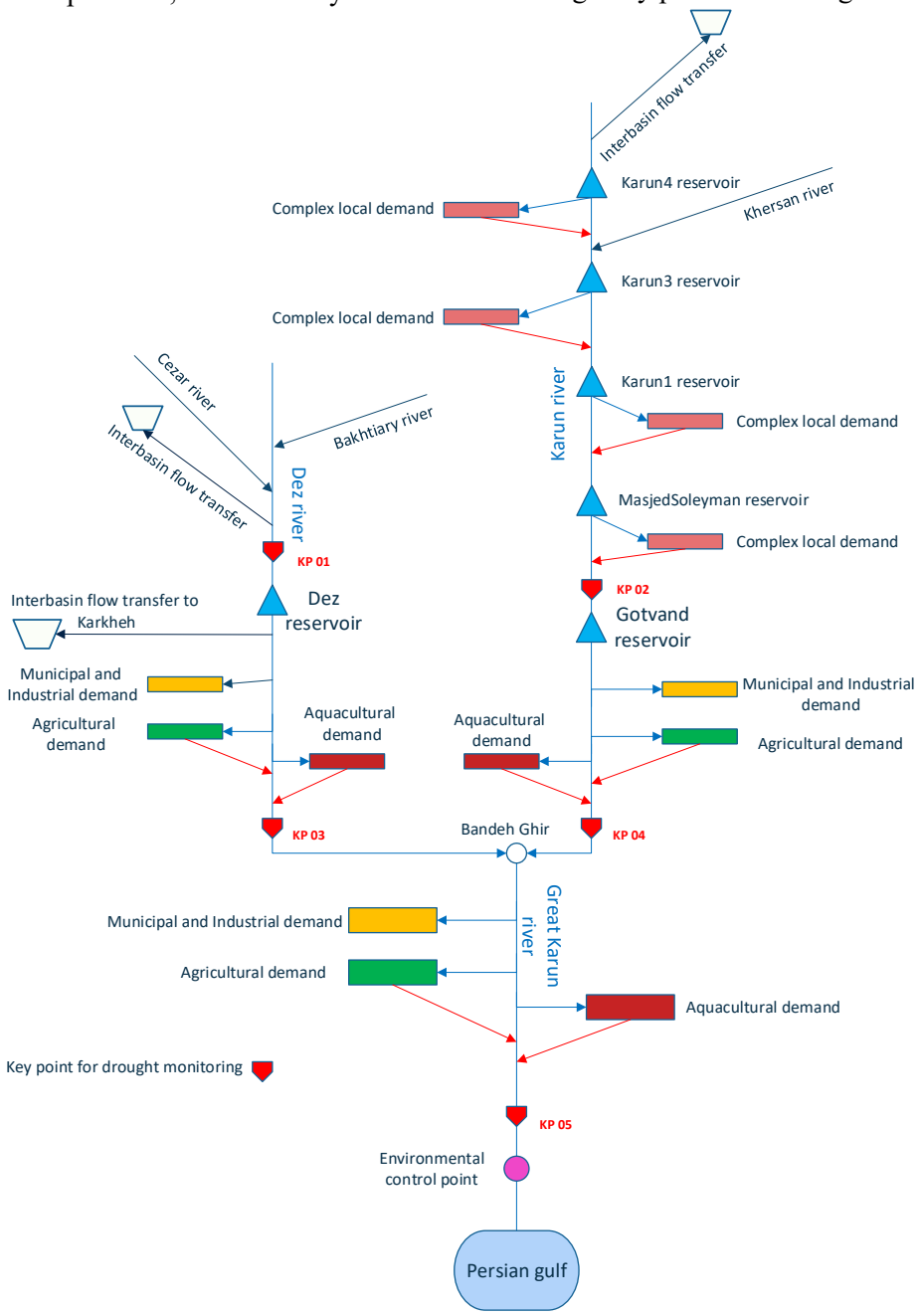


Figure 1. Schematic diagram of the investigated system

Karun rivers. Additionally, tributary rivers such as Khersan, Cesar, and Bakhtiari contribute to the flow into these two main rivers. The system serves various purposes, including drinking-urban supply, agriculture-industry, aquaculture, environmental conservation, and water transfer [3]. The average annual water discharge in the Great Karun basin amounts to 20.4 billion cubic meters, representing approximately 20% of Iran's total surface water resources. However, the current annual water demand in the region exceeds this, reaching 24.9 billion cubic meters. The vast irrigated agricultural area—spanning more than 755,500 hectares—makes the Great Karun basin a crucial food producer for Iran. Presently, the multi-reservoir system has a total storage capacity of 18.5 billion cubic meters. Figure 1, shows the investigated Schematic diagram of the Great Karun water resources system in our study.

3. The proposed methodology

In this research, we utilize the Particle Swarm Optimization (PSO) algorithm to optimize the operating rule curves in a multi-reservoir system. PSO algorithm and the simulation models were implemented in the Visual Basic for Applications (VBA) programming environment. Leveraging various operating strategies can lead to mitigating drought effects based on basin characteristics [31]. Our objective is to minimize the square of relative deficiencies. In this context, various indices have been recently proposed and evaluated [32]. While more complex indices offer greater capabilities, they require additional information for accurate calculation and introduce increased uncertainty, especially when data is scarce. In our research, we have chosen a well-known water shortage index, WSI [33, 34], as the objective function to determine the optimal rule curves. To achieve the optimum performance of the system, we connect the PSO algorithm to a system simulator based on standard operating policies (SOP) and discrete two-level hedging policies. Under the discrete hedging policy, the reservoir volume is divided into three regions using two different rule curves [35]. When the reservoir volume is in the first area (above the two hedging levels), all demands are met. In the second area (between the two levels), mild hedging begins for lower-priority demands. For instance, upstream reservoirs (such as Karun 4, Karun 3, Karun 1, and Masjed Soleyman) experience slight shortages in meeting hydropower generation demand. Downstream of Gotvand Dam, agriculture, industry, aquaculture, and transfer to Karkheh are also hedged. Finally, when the reservoir volume plus inflow falls below the two rationing levels (the lowest area), severe rationing is applied. All demands except Drinking demand, are significantly limited, and four fixed rationing coefficients (two for hydropower generation and two for downstream demands) are defined.

The combined simulation-optimization model searches for optimal hedging levels across all reservoirs and months. We separately code a simulation model based on standard operating policies (SOP). By comparing the output results of this simulator with those of the combined simulation-optimization model, we assess the impact of the hedging policy. Within the hedging model, three constraints elucidate the operational rules of the model:

$$R_t = S_t + In_t \quad \text{if} \quad S_t + In_t \le D_t \tag{1}$$

$$R_t = D_t \quad \text{if} \quad D_t \le S_t + In_t \le D_t + S_{max} \tag{2}$$

$$R_t = S_t + In_t - S_{max} \quad \text{if} \quad S_t + In_t \ge D_t + S_{max} \tag{3}$$

Here, R_t represents the reservoir outflow in time step t, In_t denotes the reservoir inflow in period t, (S_t) represents the storage volume at the beginning of period t, D_t corresponds to the demand amount in period t, and S_{max} represents the maximum

capacity of the reservoir storage volume. Under the standard operation policy, the frequency of water shortages in the water resources system is typically lower during this period. However, this approach does not provide control over the severity of the shortages. This method is approximately optimal whenever there is sufficient water to meet the planned demands [36].

The objective function in this research is accounted for by the following equation. In fact, the optimization model seeks the minimum of the sum-of-squares values of relative deficiencies of all system demands:

$$Objective\ Function = \sum_{i=1}^{N}\sum_{j=1}^{J}\sum_{t=1}^{T}\left(\frac{R_{j,i,t} - D_{j,i,t}}{D_{j,i,t}}\right)^2 \quad (4)$$

Where, $D_{j,i,t}$ represents the amount of the *j*th demand downstream of the *i*th reservoir during the period *t*, $R_{j,i,t}$ denotes the released flow for supplying the *j*th demand from the *i*th reservoir during the period *t*, The indices *T*, *J*, and *N* correspond, respectively, to the total number of demand sites downstream of each reservoir, the total length of the time steps, and the number of reservoirs throughout the multi-reservoir system. The decision variables in this research are the threshold volumes in all reservoirs and the different phases of rationing for each month.

The constraints in the reservoir operation problem are divided into primary and secondary constraints [7]. The primary constraints must be applied in all models, while the secondary constraints are defined according to the type of problem and the handling of the system. The first and most important constraint in reservoir operation is the mass balance equation. Other primary constraints include the upper and lower limits for the variables of reservoir storage volume and release. The secondary constraints, which depend on the type of problem, can include factors such as the average long-term shortage and the maximum and minimum values of production in hydropower plants. The main equations for reservoir simulation models are as follows:

$$S_{i,t+1} = S_{i,t} + Q_{i,t} - R_{i,t} - Spill_{i,t} - loss_{i,t} \quad (5)$$

$$S_{i,min} \leq S_{i,t+1} \leq S_{i,max} \quad (6)$$

$$S_1 = S_{T+1} \quad (7)$$

$$R_{i,min} \leq R_{i,t} \leq R_{i,max} \quad (8)$$

$$S_{i,t}, Q_{i,t}, R_{i,t}, Spill_{i,t} \geq 0 \quad (9)$$

In the above equations, $S_{i,t}$ represents the storage volume of the *i*th reservoir in month *t*, $Q_{i,t}$ is the volume of water entering the *i*th reservoir in month *t*, $R_{i,t}$ is the release flow from the *i*th reservoir in month t, $Spill_{i,t}$ is the amount of spilled water from the *i*th reservoir in month t, and $loss_{i,t}$ includes evaporation, drainage, and leakage from the *i*th reservoir in month *t*. In this study, to reduce the volume of calculations and accept a certain error margin, evaporation and other reservoir losses are omitted. Additionally, $S_{i,min}$ is the minimum storage volume of the *i*th reservoir, $S_{i,max}$ is the maximum storage volume of the *i*th reservoir, S_1 is the storage volume of the reservoir at the beginning of the simulation period, and S_{T+1} is the storage volume of the reservoir at the end of the simulation period (where *T* being the length of the simulation period). For the reservoir release, limits must be set to ensure the minimum amount of water entering the downstream area to control water quality, maintain the survival of living organisms and fish, and protect the downstream area from flooding risks [7]. Here, $R_{i,max}$ is the maximum release flow from the *i*th reservoir, and $S_{i,min}$ is the minimum release flow from the *i*th reservoir. The upper and lower limits of the reservoir storage volume must ensure the maximum volume for flood control and the minimum level for dead storage and power plant operation. Additionally, the

reservoir's storage volume at the beginning and end of the operation period should be the same. To ensure feasible solutions, the values of the reservoir storage volume, release flow, inlet, and overflow should always be greater than or equal to zero.

In this research, a simulation model has been coded separately based on the Standard Operating Policy (SOP) in the VBA (Visual Basic for Applications) environment. The studied system is simulated using this policy as a baseline to investigate the performance of other policies. The results of the combined simulation-hedging optimization model are compared with the output of this SOP policy simulator as a baseline. According to the SOP, the release from the reservoir is based solely on the demand of the same period. If there is enough water to meet the demand, the reservoir output is adjusted to satisfy the total demand. If there is insufficient water to meet the demand, the entire available water is released. Additionally, if the available water exceeds the demand, the reservoir starts to fill, and if necessary, the excess water is overflowed [37]. The mathematical representation of this operating policy is as follows:

$$R_t = S_t + In_t \quad \text{if} \quad S_t + In_t \le D_t \tag{10}$$

$$R_t = D_t \quad \text{if} \quad D_t \le S_t + In_t \le D_t + S_{max} \tag{11}$$

$$R_t = S_t + In_t - S_{max} \quad \text{if} \quad S_t + In_t \ge D_t + S_{max} \tag{12}$$

Finally, the flow series passing through key points throughout the basin, based on both hedging and Standard Operating Policies (SOP), is introduced into the drought model. The model calculates the flow drought index for each of these points. Subsequently, we investigate the impact of the operation policy under each of these two policies on the index results at different key points.

The research methodology of this study is outlined in a general flowchart, as depicted in Figure 2.

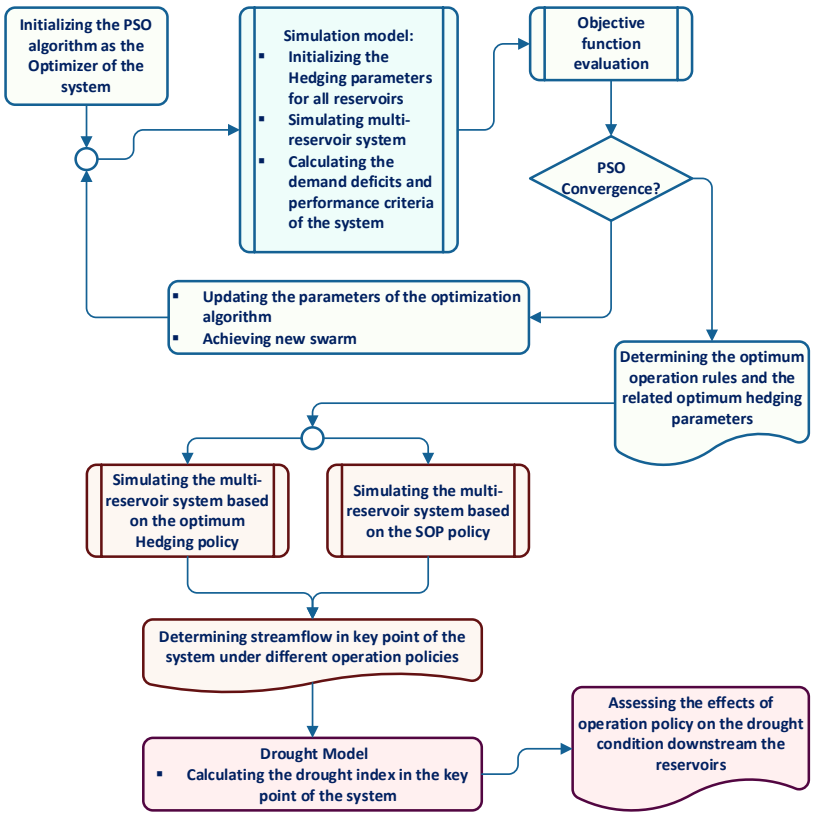


Figure 2. Flowchart of the proposed methodology

Many drought indices have been developed to describe and evaluate drought characteristics such as severity, duration, and temporal extent for each type of drought [19]. Based on the desired drought criteria, the intensity and duration of drought are expressed with an index. An index consolidates various meteorological and hydrological parameters, such as rainfall, temperature, evapotranspiration, runoff, and other indicators of water supply, into a single format or formula, providing a comprehensive tool for decision-making. These indicators are usually expressed as a single number to maximize the use of raw data, enhance comprehensibility, and empower designers and planners in their decision-making processes [38].

Hydrological drought indices such as the Palmer PHDSI index [39], SWSI surface water storage index [40], SDI surface flow drought index [41, 42], SRI standard runoff index [43], and SSI standard surface flow index [44] are among the most common tools for determining the characteristics of hydrological drought. The Palmer index and surface water storage index have received less attention due to their complexity and the extensive calculations they require. Therefore, an index similar to the SPI standardized precipitation index, called the SDI surface flow drought index, can be used. This index, based on the average monthly flow, was first proposed by Benzoy [41]. The calculation principles of the SDI index are the same as those of the SPI index. In this research, the SDI index has been used to investigate hydrological drought. The drought control points are specified in Figure 1 as the *control points for drought monitoring*. The predetermined Control points, such as KP05, were chosen based on their strategic locations downstream of key reservoirs and major river confluences, allowing for effective monitoring of cumulative hydrological impacts and drought propagation throughout the basin. These points represent critical nodes for water allocation, operational decision-making, and assessing downstream drought severity, ensuring the results directly inform practical management and policy interventions.

To calculate the drought index of the streamflow, the drought index calculation software such as DrinC can be applied, but due to the impossibility of connecting this software to the programming code and also the slowing down of the simulation and optimization process, the calculations related to the SDI index was coded in the VBA programming environment as a drought model. After simulating and optimizing the system, the output results are given to the drought model to calculate the drought index according to these flow outputs. After extracting the outflow data on a monthly scale during a statistical period (preferably 30 years or more), it is necessary to form a time series on a desired scale. Then a suitable statistical distribution is fitted to the time series of flow values. Log normal distribution is considered to fit the time series.

If the monthly time series of flow volumes $Q_{i,j}$ are available, the cumulative flow volume $V_{i,\mathrm{k}}$ can be obtained. Here, i and j stands for the water year and month respectively.

$$V_{i,\mathrm{k}} = \sum_{j=1}^{3k} Q_{i,j} \quad i = 1,2,\dots \quad j = 1,2,\dots,12 \quad k = 1,2,3,4 \tag{13}$$

The SDI data for analysis should ideally follow a normal or log-normal distribution. In small watersheds, flows may exhibit a probability distribution with skewness, similar to the gamma distribution. To address this, the distribution is transformed to a normal distribution [42]. Consequently, the surface flow drought index is calculated for the reference period k of the ith year, based on the log-normal distribution.

In the following formulas, the two-parameter lognormal distribution is utilized

for transformation. The natural logarithms of the cumulative flow data, with mean $\overline{y_K}$ and standard deviation $S_{y,k}$, are taken into account.

$$SDI_{i,k} = \frac{y_{i,k} - \overline{y_K}}{S_{y,k}} \qquad i = 1,2,\dots \qquad k = 1,2,3,4 \tag{14}$$

$$y_{i,k} = \ln(V_{i,k}) \qquad i = 1,2,\dots \qquad k = 1,2,3,4 \tag{15}$$

The drought status of a region is determined by comparing the calculated value of this index with the classification presented in Table 1.

Table 1. Drought classification according to the SDI values [45]

SDI value	Drought status
$SDI > 0$	Non-drought
$-1 < SDI < 0$	Mild drought
$-1.5 < SDI < -1$	Moderate drought
$-2 < SDI \leq -1.5$	Severe drought
$SDI \leq -2$	Extreme drought

4. Results

In the optimization process, the monthly hedging levels in the reservoirs serve as decision variables for the problem. Modeling occurs on a monthly basis, considering two levels of rationing in each reservoir. All simulation and optimization codes were developed and executed in VBA within the Microsoft Excel environment. In this study, rationing coefficients, based on the common operational standards, are fixed for meeting demands at each level. Consequently, the total number of decision variables equals 144—representing the thresholds for monthly rationing across all system reservoirs. Repeated model executions revealed that achieving better results requires a particle count in the algorithm at least twice the number of decision variables. In this study, the model employed 576 particles. Initially, a larger population significantly improved convergence speed. Given the problem's complexity and variable count, the algorithm was iterated 5000 times to reach convergence. Optimal levels are determined as upper (target level) and lower limits (firm level) based on the maximum and minimum volumes of Dez, Gotvand, Karun 4, Karun 3, Karun 1, and Masjed Soleyman reservoirs.

4.1. System simulation results based on SOP and optimal hedging policies

In order to evaluate the system's performance under the two policies of optimal hedging and SOP policies, we use the objective function of the relative shortage index and performance criteria such as reliability, quantitative reliability, maximum vulnerability, and average vulnerability. These results demonstrate the long-term system performance from 1955-56 to 2014-15, as well as its behavior during the last 10-year drought period from 2005-06 to 2014-15.

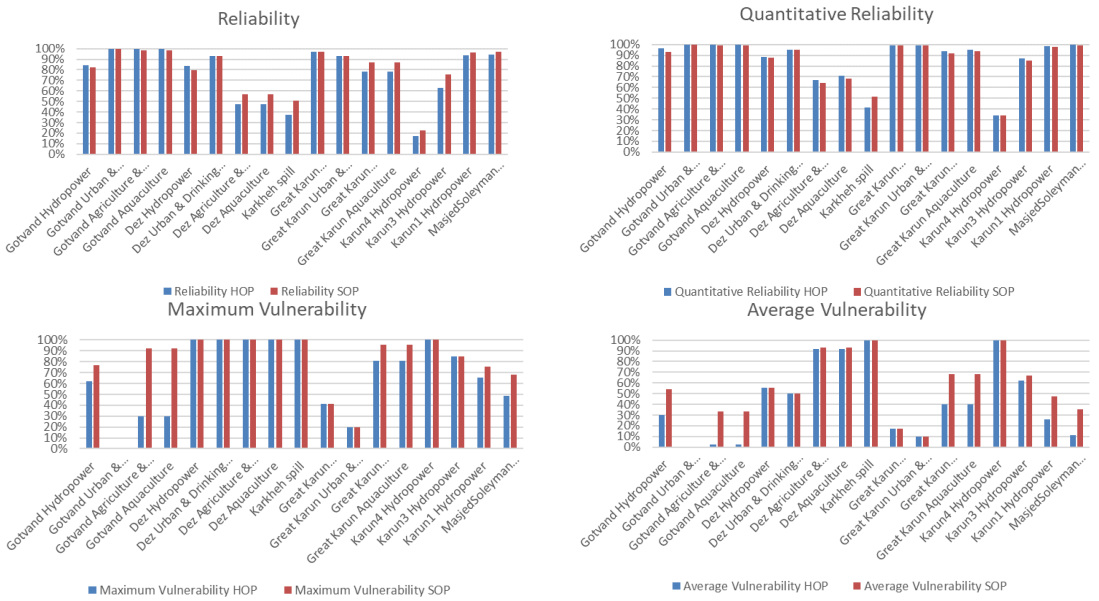


Figure 3. Comparison of reservoir performance under different exploitation policies: Left Side: Dez Reservoir, Right Side: Gotvand Reservoir, First Row:

Figure 3, represents the comparative chart bars for performance criteria of SOP, and optimum HOP. The analysis of the Dez and Gotvand reservoirs reveals critical insights into the impact of multi-reservoir rationing on downstream water management. Gotvand exhibited high reliability across all sectors, consistently achieving near or full satisfaction of water demands under both HOP and SOP scenarios. Conversely, Dez experienced lower reliability, particularly in agriculture and aquaculture, where demand satisfaction rates fell below 70%. Quantitative reliability reinforced these trends, with Gotvand maintaining strong performance across sectors, while Dez struggled, especially in agriculture and aquaculture. Vulnerability analysis highlighted significant challenges for Dez, with maximum and average vulnerabilities in agricultural and aquaculture sectors exceeding 91% in both scenarios, underscoring the high risk of unmet demands. In contrast, Gotvand showed relatively low vulnerabilities, particularly in urban and drinking water supplies, which remained stable and minimally impacted. Overall, the findings emphasize the differential performance of these reservoirs under rationing scenarios, highlighting the need for targeted strategies to address vulnerabilities, especially for the more affected sectors like agriculture and aquaculture in the Dez system. As illustrated in Figure 3, the Gotvand Reservoir consistently achieves high reliability in meeting water demands across all sectors under both SOP and hedging policies, whereas the Dez Reservoir struggles particularly in agricultural and aquaculture sectors, with demand satisfaction rates falling below 70%. This underscores the greater vulnerability of Dez to shortages even under optimized operation.

Comparative results for all reservoirs within the system are presented, with a focus on the Dez and Gotvand reservoirs (see Figure 4). Notably, both hedging and SOP models exhibit similar effects on the storage volume of the Dez reservoir. However, in specific months, the hedging policy leads to higher storage volumes than SOP. This difference is particularly evident in 1988 and 1990. Interestingly, the hydropower production remains nearly the same between the two models. The output flow from the Dez reservoir also reflects similar behavior under optimum hedging and SOP policies. In the Gotvand Reservoir, except for the early years of the last 10-year period, where both policies yield similar storage volumes, the years 2007 to 2014 reveal a clear difference.

The hedging policy conserves more water during these years, resulting in increased hydropower generation compared to SOP. Furthermore, when comparing the output flow from the Gotvand reservoir, the hedging policy consistently outperforms SOP in meeting water demands. This performance disparity extends to other reservoirs within the Karun cascade.

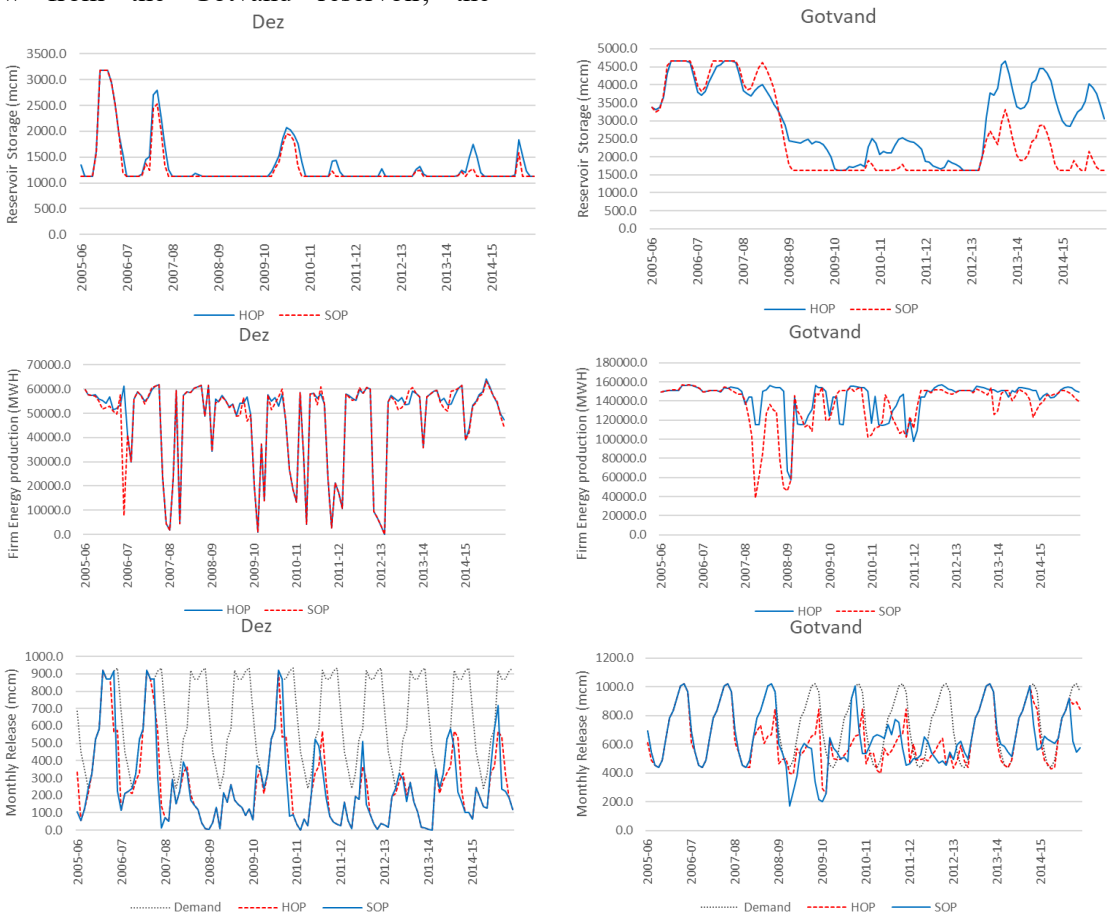


Figure 4. Comparison of reservoir performance under different exploitation policies: Left Side: Dez Reservoir, Right Side: Gotvand Reservoir, First Row: Storage volume of reservoirs, Second Row: Produced hydropower energy, Third Row: Output flow to meet demands

Figure 4 reveals that while storage volumes and outflows for the Dez Reservoir remain similar under both policies, the hedging policy occasionally maintains higher storage in critical months. For Gotvand, the hedging approach provides notably improved storage and outflows during drought years, resulting in increased hydropower production relative to SOP.

4.2. Results of drought assessment model

A comprehensive comparative study was conducted for all control points within the system. To succinctly summarize the results, we focus on the last control point in the system (*KP05*, in figure 1). We calculated the SDI (Streamflow Drought Index) series for the monthly flow passing through the *KP05* control point. Subsequently, we investigated the impact of reservoir management under both SOP policies and optimal hedging policy on the drought index series. The statistical characteristics of hydrological droughts at *KP05* over a 60-year period (1955-2015) were extracted and are presented in details in Table 2.

Table 2. Drought status for KP05, based on SOP and hedging policies

	SOP (months)	Hedging Policy (months)
Mild drought	196	123
Moderate drought	34	31
Severe drought	39	90
Extreme drought	34	22

Table 2 demonstrates that the number of extreme and severe drought months at KP05 is reduced under the hedging policy, even though the duration of severe droughts may be longer, indicating a trade-off between drought intensity and frequency. Based on the results from Table 2, we observe that under the SOP policy, a very severe drought persisted for 34 months. However, this duration decreased to 22 months when implementing the optimal hedging policy. Specifically, the SOP policy resulted in more months falling within the severe drought category compared to the optimal hedging policy. Additionally, when considering mild droughts, there were 196 months classified as mild droughts under the SOP policy, whereas the optimal rationing policy had 123 months falling into this category. Table 3, summarizes the drought characteristics for *KP05* control point, under both SOP and hedging (HOP) policies.

Table 3. Calculated drought characteristics for *KP05*, based on SOP and hedging policies

Policy	ND	NE	Max DD	Mean DD	P	S_{ave}	S_{Max}
SOP	303	39	34	7	5.13	0.9	46.92
Hedging	266	27	39	9	3.64	1.08	56.52

As summarized in Table 3, the total number of drought months and the number of drought events decrease when the hedging policy is applied, but the average duration and severity of individual drought events increase slightly. This suggests that the hedging policy consolidates drought occurrences, resulting in fewer yet longer events. In this table ND is the number of total months of drought, DE is the number of observed drought events, Max DD is the maximum duration of the observed drought events (months), Mean DD is the average of the observed drought events (months). The peak of drought (P) is another studied characteristic that is considered to be the maximum absolute value of the SDI below the threshold level for the occurrence of drought. Another characteristic estimated in this study for drought is the drought severity (S), which is by definition the cumulative absolute value of the dimensionless SDI during a continuous drought event. The average value (S_{ave}) and the maximum value (S_{Max}) of this parameter have been reported under two compared operating strategies. Based on the characteristics' values, the average intensity of drought periods at this point is nearly 20% higher under the optimal hedging policy compared to the SOP policy. When comparing drought intensities across the entire period and both policies, we find that the peak intensity occurs in the SOP policy. Rationing has extended the maximum duration of droughts to 39 months, whereas the SOP policy had a criterion of 34 months. The application of the hedging policy has led to greater intensity between drought periods than the SOP policy due to the increased duration of droughts. During the statistical period, there were 303 months of drought based on the SOP policy and 266 months based on the optimal rationing. These findings align with similar research conducted by Guo et al. [15]. Their findings indicated that implementing an optimal rule of operation for a multi-reservoir system in North China can effectively prevent severe shortages during drought periods. In contrast, another study conducted by Li et al. [14] concluded that the way reservoirs are utilized has minimal impact on exacerbating droughts downstream. Instead, the general trend of

hydrological droughts in downstream stations is primarily influenced by water conditions and natural weather changes, which are determined by variations in precipitation. The discrepancies in results may arise from differences in climatical and hydrological conditions across the studied areas. Additionally, Li et al. [14] investigated the impact of the presence or absence of a large single-reservoir system in the region but did not derive an optimal operating policy.

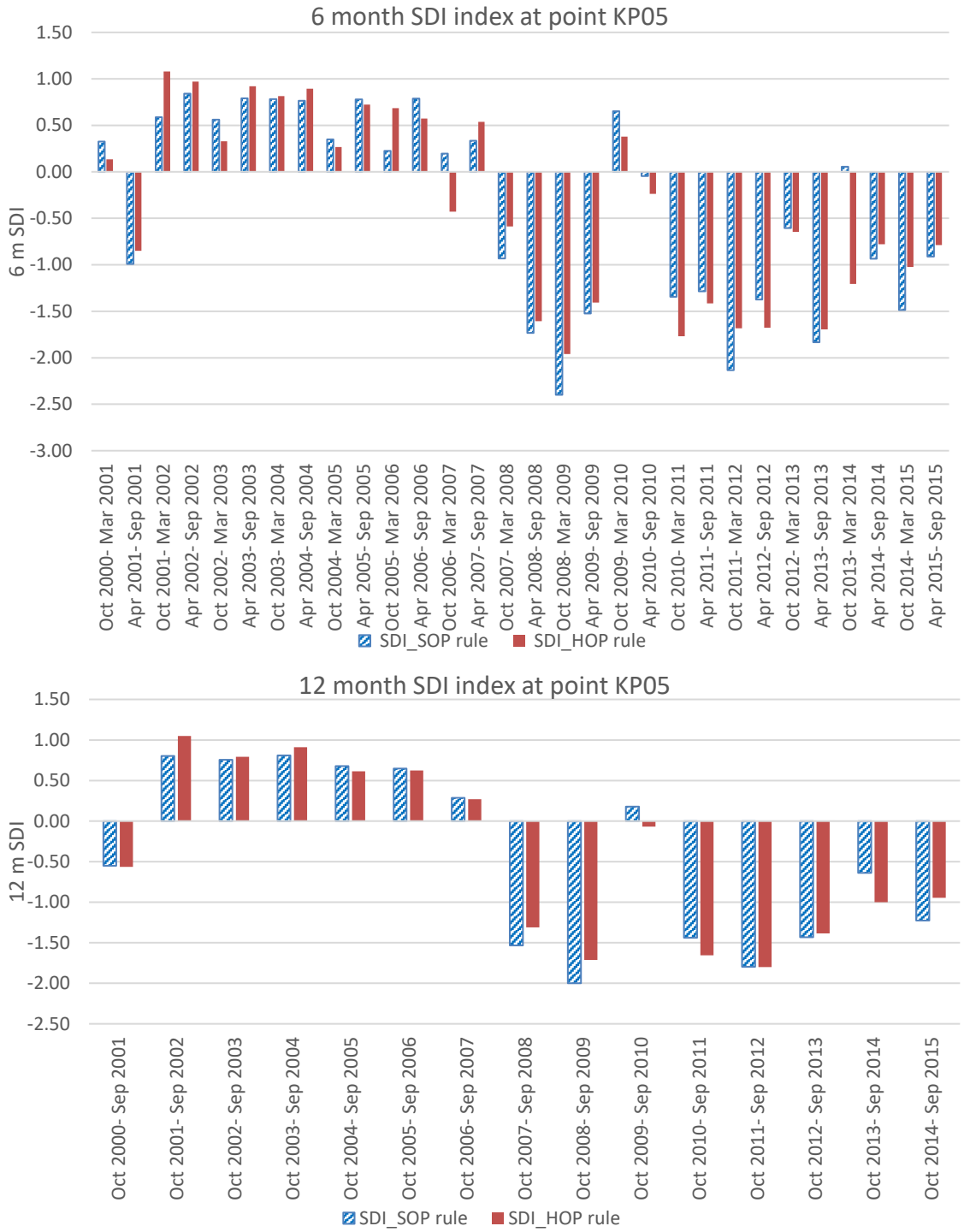


Figure 5. The impacts of operating policies on the SDI drought index downstream of the reservoirs across 6-, and 12-month scales

The graphs in Figure 5 illustrate the differences in the impacts of two policies—SOP and optimal rationing—on the SDI drought index at point KP05 (downstream of the reservoirs) across 6-, and 12-month scales. This distinction is particularly pronounced during the 2001-2015 period. The KP05, located downstream of Karun-e-Bozorg and after major tributary confluences, was chosen as it reflects the integrated effect of all upstream reservoir operations and basin inflows, making it an ideal reference for evaluating overall system performance under different management policies. The varying scales of the SDI time series at control point *KP05* reveal that, in wet years, the SOP policy lacked foresight for impending droughts. Consequently, the index under this policy often reflected normal conditions even in the years leading up to a drought. In contrast, during drought years, the index values under the SOP policy would abruptly turn negative, plunging the basin into a severe drought. On the other hand, the optimal rationing policy mitigated this effect by transitioning into the drought phase more gradually, thereby preventing acute shortages in the basin and averting severe drought conditions. Figure 5 clearly shows that SOP policy results in abrupt transitions to severe drought phases, as indicated by sharp drops in the SDI index, while the hedging policy cushions these impacts by enabling a more gradual entry into drought conditions, thus reducing the frequency of extreme events.

By comparing the results across all control points, it becomes clear that during severe water shortages in the basin, the application of the rationing policy not only fails to improve the system's condition but may even exacerbate the basin's challenges. This is particularly evident at *KP05*, located downstream of Karun-e-Bozorg. At this location, a comparison of the impacts of the two policies on drought conditions and an analysis of the calculated drought criteria indicate that, for most metrics, rationing has not alleviated drought conditions in the basin. In fact, it has worsened the situation during certain months. Conversely, at *KP04*, downstream of Gotvand, the differences in the effects of applying the two policies—rationing and SOP—on the system are striking. The impact of rationing on alleviating drought conditions downstream of Gotvand is particularly noteworthy.

Based on the series of SDI indices at different scales, the large fluctuations in this index values at shorter-term scales (1, 3, and 6 months) suggest that the impact of reservoir operations is limited. These fluctuations appear to be more strongly influenced by intra-annual rainfall. Although in certain months the differences between the two policies' effects on the basin are marginal, it can be inferred that, likely due to rainfall variability and its impact on streamflow, the basin exited the drought phase in some months, while experiencing very severe droughts in others. Consequently, the indices at these scales exhibit significant month-to-month variability. However, when considering the 12-month SDI scale, the influence of reservoir operations on hydrological drought becomes more evident.

The results of this study are generally consistent with recent research on multi-reservoir drought management. For example, Guo et al. [15] and Chang et al. [16] demonstrated the effectiveness of optimized hedging policies in reducing the risk of severe shortages during droughts in complex reservoir systems. Similarly, Khorshidi et al. [8] and Ahmadianfar & Zamani [22] found that employing advanced optimization and risk-based approaches can enhance the performance and resilience of water systems under drought conditions. However, some studies, such as Li et al. [14] and Wu et al. [21], emphasize that while reservoir operation policies can mitigate certain impacts, the underlying hydrological regime and precipitation variability remain dominant factors influencing downstream drought (see also [28, 33]). Notably, our finding that hedging policies can sometimes increase drought severity or duration at specific downstream locations—such as the

Dez basin—aligns with these broader insights, highlighting the need for context-specific strategies. Overall, this study adds nuance to the literature by demonstrating both the potential benefits and trade-offs associated with optimized reservoir operations in semi-arid basins.

It is worth noting that the presented modeling approach is subject to several limitations. First, the simulation and optimization framework assume perfect knowledge of reservoir inflows and does not explicitly incorporate hydrological or demand forecast uncertainties, which may affect real-world applicability. In addition, secondary processes such as evaporation losses and operational constraints related to water quality and ecosystem needs were simplified or omitted. The use of a two-level hedging policy, while practical, might not capture all the flexibility required for complex, multi-purpose water systems. Calibration of the PSO algorithm and choice of control points may also influence the generalizability of results across different basin configurations.

Future research could address these issues by integrating stochastic inflow forecasting, expanding the model to account for evaporation and ecological constraints, exploring multi-objective optimization with additional system performance metrics, and applying advanced or adaptive hedging strategies. Furthermore, extending the analysis to include socio-economic impacts or stakeholder-driven scenarios would enhance the practical value of reservoir operation policies in real-world water management contexts.

5. Summary and conclusion

In our research, the operating rule curves for a multi-reservoir system is optimized using the PSO algorithm. The primary objective is to minimize relative deficiencies in water supply. Two strategies are compared: SOP and discrete two-level hedging policy. The proposed approach is applied to a real-world case study, focusing on the Great Karun basin. By integrating the PSO algorithm with a system simulator, optimal hedging levels are searched across all reservoirs and months. Additionally, the impact of the hedging policy is assessed by comparing the output results of our combined simulation-optimization model with those of a SOP-based simulation. Furthermore, the flow drought index at key points throughout the basin is analyzed under both rationing and SOP policies. The results indicate that applying the hedging policy improves the system's ability to meet demands compared to the SOP policy. By accepting more shortage periods and storing water in reservoirs, the rationing policy reduces vulnerabilities and prevents severe shortages and system failures during water scarcity. Investigating the impact of SOP policies and rationing at downstream points of Dez and Gotvand reservoirs on the flow drought index reveals that hedging prevents high-intensity drought periods by increasing less severe drought occurrences. Moreover, while rationing reduces the average severity of droughts compared to the SOP policy, the SDI index results for the downstream of Dez reveal no improvement under the rationing policy. Considering the severe water shortage in the Dez basin, applying the rationing policy actually exacerbates drought conditions rather than improving them. This insight is crucial for system managers. These findings offer practical guidance for water resource managers and policymakers in semi-arid regions, highlighting the value of optimization-based reservoir operation strategies to enhance drought resilience and support more informed, adaptive decision-making for sustainable water allocation.

Funding Statement

This research was funded by Shahid Chamran University of Ahvaz, under the grant number **SCU.C1402.31254**. The authors are grateful for the financial support provided.

Conflict of Interest declaration

The authors declare that they have no conflict of interest.

AI using declaration

During the preparation of this manuscript the authors used Chat GPT for paraphrasing some sentences and enhancing the readability of the text. After using this tool/service, the authors reviewed and edited the content as needed and take full responsibility for the content of the publication.

Author contributions declaration:

The first idea of the research was proposed and polished by Seyed Mohammad Ashrafi, and Arash Adib. Data collection was done by Sama Banitamim, and Seyed Mohammad Ashrafi. Material preparation, model development, and result analysis were performed by Sama Banitamim under the supervision of Seyed Mohammad Ashrafi. The first draft of the manuscript was written by Sama Banitamim and has been edited by Seyed Mohammad Ashrafi, and Arash Adib, and all authors commented on previous versions of the manuscript. All authors read and approved the final manuscript.

References

1. Takeshima H. Distributional effects of agricultural infrastructure in developing countries: Large irrigation dams and drought mitigation in Nigeria. The Journal of Developing Areas. 2018; 52(3): 1-3. https://doi.org/10.1353/jda.2018.0032
2. Adib A, Mirsalari SB, Ashrafi SM. Prediction of meteorological and hydrological phenomena in different climatic scenarios in the Karkheh watershed (southwest of Iran). Scientia Iranica. 2020 Aug 1;27(4):1814-25. https://doi.org/10.24200/sci.2018.50953.1934
3. Mohammad Ashrafi S. Two-stage metaheuristic mixed integer nonlinear programming approach to extract optimum hedging rules for multireservoir systems. Journal of Water Resources Planning and Management. 2021 Oct 1;147(10):04021070. https://doi.org/10.1061/(ASCE)WR.1943-5452.0001460
4. Beshavard M, Adib A, Ashrafi SM, Kisi O. Establishing effective warning storage to derive optimal reservoir operation policy based on the drought condition. Agricultural Water Management. 2022 Dec 1;274:107948. https://doi.org/10.1016/j.agwat.2022.107948
5. Shih JS, ReVelle C. Water-supply operations during drought: Continuous hedging rule. Journal of Water Resources Planning and Management. 1994 Sep;120(5):613-29. https://doi.org/10.1061/(ASCE)0733-9496(1994)120:5(613)
6. Kangrang A, Prasanchum H, Sriworamas K, Ashrafi SM, Hormwichian R, Techarungruengsakul R, Ngamsert R. Application of optimization techniques for searching optimal reservoir rule curves: A Review. Water. 2023 Apr 25;15(9):1669. https://doi.org/10.3390/w15091669
7. Ashrafi SM. Investigating pareto front extreme policies using semi-distributed simulation model for Great Karun River Basin. Journal of Hydraulic Structures. 2019 Jun 1;5(1):75-88. https://doi.org/10.22055/jhs.2019.14701
8. Khorshidi MS, Nikoo MR, Sadegh M, Nematollahi B. A multi-objective risk-based game theoretic approach to reservoir operation policy in potential future drought condition. Water Resources Management. 2019 Apr 15;33:1999-2014. https://doi.org/10.1007/s11269-019-02223-w
9. Rossi G. Drought mitigation measures: a comprehensive framework. InDrought and drought mitigation in Europe 2000 (pp. 233-246). Dordrecht: Springer Netherlands. https://doi.org/10.1007/978-94-015-9472-1_18
10. Rossi G, Castiglione L, Bonaccorso B. Guidelines for planning and implementing drought mitigation measures. Methods and tools for drought analysis and management. 2007:325-47. https://doi.org/10.1007/978-1-4020-5924-7_16
11. Adib A, Kashani A, Ashrafi SM. Merge L-moment method, regional frequency analysis and SDI for monitoring and zoning map of short-term and long-term hydrologic droughts in the Khuzestan Province of Iran. Iranian Journal of Science and Technology, Transactions of Civil Engineering. 2021 Dec;45(4):2681-94. https://doi.org/10.1007/s40996-020-00447-0
12. Saki Malehi E, Ashrafi SM, Ghafouri HR. Performance evaluation of using Shannon's entropy crossing time to monitor drought: A case study of the Karkheh. Hydrological Sciences Journal. 2022 Oct 3;67(13):1971-87. https://doi.org/10.1080/02626667.2022.2116981
13. López-Moreno JI, Vicente-Serrano SM,

Beguería S, García-Ruiz JM, Portela MM, Almeida AB. Dam effects on droughts magnitude and duration in a transboundary basin: The Lower River Tagus, Spain and Portugal. Water Resources Research. 2009 Feb;45(2). https://doi.org/10.1029/2008WR007198
14. Li S, Xiong L, Dong L, Zhang J. Effects of the Three Gorges Reservoir on the hydrological droughts at the downstream Yichang station during 2003–2011. Hydrological Processes. 2013 Dec 30;27(26):3981-93. https://doi.org/10.1002/hyp.9541
15. Guo X, Hu T, Wu C, Zhang T, Lv Y. Multi-objective optimization of the proposed multi-reservoir operating policy using improved NSPSO. Water resources management. 2013 May;27:2137-53. https://doi.org/10.1007/s11269-013-0280-9
16. Chang J, Guo A, Wang Y, Ha Y, Zhang R, Xue L, Tu Z. Reservoir operations to mitigate drought effects with a hedging policy triggered by the drought prevention limiting water level. Water Resources Research. 2019 Feb;55(2):904-22. https://doi.org/10.1029/2017WR022090
17. Al-Faraj FA, Al-Dabbagh BN. Assessment of collective impact of upstream watershed development and basin-wide successive droughts on downstream flow regime: The Lesser Zab transboundary basin. Journal of Hydrology. 2015 Nov 1;530:419-30. https://doi.org/10.1016/j.jhydrol.2015.08.019
18. Al-Faraj FA, Tigkas D. Impacts of multi-year droughts and upstream human-induced activities on the development of a semi-arid transboundary basin. Water Resources Management. 2016 Nov;30:5131-43. https://doi.org/10.1007/s11269-016-1473-9
19. Wu J, Liu Z, Yao H, Chen X, Chen X, Zheng Y, He Y. Impacts of reservoir operations on multi-scale correlations between hydrological drought and meteorological drought. Journal of Hydrology. 2018 Aug 1;563:726-36. https://doi.org/10.1016/j.jhydrol.2018.07.025
20. Men B, Wu Z, Li Y, Liu H. Reservoir operation policy based on joint hedging rules. Water. 2019 Feb 26;11(3):419. https://doi.org/10.3390/w11030419
21. Wu J, Chen X, Yu Z, Yao H, Li W, Zhang D. Assessing the impact of human regulations on hydrological drought development and recovery based on a 'simulated-observed' comparison of the SWAT model. Journal of Hydrology. 2019 Oct 1;577:123990. https://doi.org/10.1016/j.jhydrol.2019.124242
22. Ahmadianfar I, Zamani R. Assessment of the hedging policy on reservoir operation for future drought conditions under climate change. Climatic Change. 2020 Mar;159(2):253-68. https://doi.org/10.1007/s10584-020-02672-y
23. Fasihi S, Lim WZ, Wu W, Proverbs D. Systematic review of flood and drought literature based on science mapping and content analysis. Water. 2021 Oct 8;13(19):2788. https://doi.org/10.3390/w13192788
24. Moazami S, Abdollahipour A, Zakeri Niri M, Ashrafi SM. Hydrological assessment of daily satellite precipitation products over a basin in Iran. Journal of Hydraulic Structures. 2016 Dec 1;2(2):35-45. https://doi.org/10.22055/jhs.2016.12850
25. Cai X, Zeng R, Kang WH, Song J, Valocchi AJ. Strategic planning for drought mitigation under climate change. Journal of Water Resources Planning and Management. 2015 Sep 1;141(9):04015004. https://doi.org/10.1061/(ASCE)WR.1943-5452.0000510
26. Seidenfaden IK, Jensen KH, Sonnenborg TO. Climate change impacts and uncertainty on spatiotemporal variations of drought indices for an irrigated catchment. Journal of Hydrology. 2021 Oct 1;601:126814. https://doi.org/10.1016/j.jhydrol.2021.126814
27. Sheikhi Y, Ashrafi SM, Nikoo MR, Haghighi A. Enhancing daily rainfall prediction in urban areas: a comparative study of hybrid artificial intelligence models with optimization algorithms. Applied Water Science. 2023 Dec;13(12):232. https://doi.org/10.1007/s13201-023-02036-8
28. Ren K, Huang Q, Huang S, Ming B, Leng G. Identifying complex networks and operating scenarios for cascade water reservoirs for mitigating drought and flood impacts. Journal of Hydrology. 2021 Mar 1;594:125946. https://doi.org/10.1016/j.jhydrol.2020.125946
29. Xing Z, Ma M, Zhang X, Leng G, Su Z, Lv J, Yu Z, Yi P. Altered drought propagation under the influence of reservoir regulation. Journal of Hydrology. 2021 Dec 1;603:127049. https://doi.org/10.1016/j.jhydrol.2021.127049
30. Zolfagharpour F, Saghafian B, Delavar M.

Adapting reservoir operation rules to hydrological drought state and environmental flow requirements. Journal of Hydrology. 2021 Sep 1;600:126581. https://doi.org/10.1016/j.jhydrol.2021.126581
31. Bandyopadhyay N, Bhuiyan C, Saha AK. Drought mitigation: Critical analysis and proposal for a new drought policy with special reference to Gujarat (India). Progress in Disaster Science. 2020 Jan 1;5:100049. https://doi.org/10.1016/j.pdisas.2019.100049
32. Liao R. Water scarcity assessment index from the realistic perspective of human basic water requirements. Environmental and Sustainability Indicators. 2024 Jun 1;22:100404. https://doi.org/10.1016/j.indic.2024.100404
33. Zeng X, Lund JR, Cai X. Linear versus nonlinear (convex and concave) hedging rules for reservoir optimization operation. Water Resources Research. 2021 Dec;57(12):e2020WR029160. https://doi.org/ 10.1029/2020WR029160
34. Shiau JT. Analytical optimal hedging with explicit incorporation of reservoir release and carryover storage targets. Water resources research. 2011 Jan;47(1). https://doi.org/10.1029/2010WR009166
35. Taghian M, Rosbjerg D, Haghighi A, Madsen H. Optimization of conventional rule curves coupled with hedging rules for reservoir operation. Journal of Water Resources Planning and Management. 2014 May 1;140(5):693-8. https://doi.org/10.1061/(ASCE)WR.1943-5452.0000355
36. Alimohammadi H, Massah Bavani AR, Roozbahani A. Mitigating the impacts of climate change on the performance of multi-purpose reservoirs by changing the operation policy from SOP to MLDR. Water Resources Management. 2020 Mar;34:1495-516. https://doi.org/ 10.1007/s11269-020-02516-5
37. Oliveira R, Loucks DP. Operating rules for multireservoir systems. Water resources research. 1997 Apr;33(4):839-52. https://doi.org/ 10.1029/96WR03745
38. Smakhtin VU, Hughes DA. Review, automated estimation and analyses of drought indices in South Asia.
39. Alley WM. The Palmer drought severity index: limitations and assumptions. Journal of Applied Meteorology and Climatology. 1984 Jul;23(7):1100-9. https://doi.org/10.1175/1520-0450
40. Shafer BA. Developemnet of a surface water supply index (SWSI) to assess the severity of drought conditions in snowpack runoff areas. InProceedings of the 50th Annual Western Snow Conference, Colorado State University, Fort Collins, 1982. https://doi.org/10.1175/1520-0442
41. Ben-Zvi A. Indices of hydrological drought in Israel. Journal of hydrology. 1987 Jun 30;92(1-2):179-91. https://doi.org/10.1016/0022-1694(87)90095-3
42. Nalbantis I, Tsakiris G. Assessment of hydrological drought revisited. Water resources management. 2009 Mar;23:881-97. https://doi.org/10.1007/s11269-008-9305-1
43. Shukla S, Wood AW. Use of a standardized runoff index for characterizing hydrologic drought. Geophysical research letters. 2008 Jan;35(2). https://doi.org/10.1029/2007GL032487
44. Vicente-Serrano SM, López-Moreno JI, Beguería S, Lorenzo-Lacruz J, Azorin-Molina C, Morán-Tejeda E. Accurate computation of a streamflow drought index. Journal of Hydrologic Engineering. 2012 Feb 1;17(2):318-32. https://doi.org/10.1061/(ASCE)HE.1943-5584.0000433
45. Tigkas D, Vangelis H, Tsakiris G. DrinC: a software for drought analysis based on drought indices. Earth Science Informatics. 2015 Sep;8:697-709. https://doi.org/10.1007/s12145-014-0178-y

© 2025 by the authors. Licensee SCU, Ahvaz, Iran. This article is an open access article distributed under the terms and conditions of the Creative Commons Attribution 4.0 International (CC BY 4.0 license) (http://creativecommons.org/licenses/by/4.0/).

Numerical Study of Impulsive Wave Overtopping at Rigid Hydraulic Structures Using Incompressible Smoothed Particle Hydrodynamics Model

Rasoul Memarzadeh[1]

1. Department of Civil Engineering, Faculty of Engineering, Vali-e-Asr University of Rafsanjan, Iran, P.O. Box 518.

***Corresponding Author:**
Rasoul Memarzadeh,

Email: r.memarzadeh@vru.ac.ir
Received: 2025.03.22
Accepted: 2025.07.21
J. Hydraul. Struct., 2025; 12(2):51-73
DOI: 10.22055/jhs.2025.48919.1345

ABSTRACT

Understanding the behavior of wave overtopping at hydraulic structures is critical for ensuring the stability and longevity of dams and coastal defenses. This study presents a validated Incompressible Smoothed Particle Hydrodynamics – Large Eddy Simulation (ISPH–LES) model for accurately simulating solitary wave overtopping events. The ISPH–LES model integrates advanced improvements, including a newly developed solid boundary treatment that enhances numerical stability and fidelity near rigid walls. Given the highly turbulent nature of overtopping flows, the integration of LES into the SPH framework enables detailed resolution of vortex structures and energy dissipation mechanisms. The model was validated against experimental data from nine overtopping scenarios, with predictions of key hydrodynamic parameters—maximum overtopping depth, overtopping volume, and wave overtopping duration—yielding average errors of 9.5%, 15%, and 5.9%, respectively. Temporal pressure distributions over 27 time frames were analyzed to illustrate the model's ability to capture impact, peak, and dissipation phases of overtopping. The results indicate that the ISPH–LES model performs exceptionally well in high-energy overtopping events, while suggesting potential refinements in scenarios with smaller overtopping volumes. These findings underscore the model's practical utility for designing hydraulic structures in regions prone to extreme wave conditions, offering critical insights into optimizing structural resilience under a wide range of overtopping scenarios

KEYWORDS

Numerical study, ISPH – LES model, Modified wall boundary condition, Solitary impulse wave, Rigid hydraulic structures, Wave overtopping.

1. Introduction

Dams and coastal defense structures, whether human-made or natural, are designed to suppress floods and protect urban, industrial, or agricultural areas. The weakness in the performance of these structures can lead to downstream flooding. One of the main concerns in designing dams and breakwaters is their stability. One of the important issues that can cause the hydraulic structures to be unstable is the overtopping caused by different waves created on the coats or dam's reservoir. The waves in dam reservoirs are caused by a variety of factors, including wind and landslides. On the coastal areas, waves are also caused by factors such as submarine earthquakes, tides and marine storms.

The purpose of the present study is to investigate the overtopping of shock waves at hydraulic structures such as waves from materials collapsing in dams or tsunami waves from marine breakwater.

Turbulence modeling plays a pivotal role in the accurate simulation of complex hydraulic flows associated with hydraulic structures such as gates, spillways, and overtopping scenarios. These flows are characterized by high-energy transitions, rapid depth changes, and multi-scale vortical structures that demand robust and high-fidelity numerical modeling approaches. The flow examined in this study—consisting of a high-speed, high-energy solitary wave impacting a rigid structure—undergoes significant changes in depth, velocity, and turbulence, making it inherently complex and highly unsteady. Similar to the turbulent flow fields passing through gates or spillways, this type of flow involves intricate vortex formations and energy dissipation patterns. Capturing these turbulent structures with precision is essential to improving the predictive capability and reliability of hydrodynamic simulations. Previous studies have demonstrated the necessity of using advanced turbulence-resolving models in such applications. For example, Kheybar et al. [1] studied the hydraulic performance of pivot side weirs with sills; Tahmasbipour et al. [2] examined T-jump stabilization mechanisms using water jets and corrugated beds; and Taheri Talavari et al. [3] conducted a numerical analysis of flow behavior through multiple elliptic Lopac gates. Similarly, advanced CFD approaches were employed by Ahadiyan et al. [4] to optimize flexible gate operations in intake systems, and Shahabi et al. [5] revealed turbulence patterns in V-shaped fishways. Furthermore, turbulent interactions of counter-flow jets [6], elliptical Lopac gate flows [7], sudden canal contractions [8], energy losses in stepped spillways [9], and the effects of vortex breakers in morning glory spillways [10] have all underscored the importance of using high-fidelity turbulence models in hydraulic simulations.

In this context, solitary waves offer a valuable and widely accepted benchmark for evaluating the performance of turbulence-resolving hydrodynamic models of overtopping problems. Although solitary waves are idealized and not fully representative of real-world storm waves or tsunamis, they effectively replicate the key characteristics of impulsive wave events - namely, rapid onset, high velocity, and concentrated energy. These attributes make solitary waves particularly suitable for investigating wave-structure interactions under extreme conditions such as landslide-induced waves or tsunami impacts. Their use in numerical simulations allows for controlled, repeatable testing of model performance in capturing complex free surface dynamics, turbulent vortex development, and energy dissipation processes critical to structural safety assessments.

Due to the importance of wave overtopping from coastal structures and dams, many researchers have investigated it from different perspectives. EurOtop [11] have studied the different characteristics of the oscillatory wave overtopping from coastal defense structures, and they presented details of this phenomenon in a manual design. In Chapter 5 of this manual, the relationships of oscillatory wave overtopping with different return periods for different configurations of breakwater were presented. In this chapter, they present the relationships for calculating discharge and flow volume due to oscillatory wave overtopping with specified return periods by considering effect of various parameters such as roughness, oblique waves, wave walls for simple and composite coastal dikes [11]. Despite extensive study of oscillatory wave overtopping at sea defense structures, the overtopping of impulsive waves has been studied less [11]. Examples of the studies in this area are Özhan and Yalçıner [12], Müller [13], Jervis and Peregrine [14], Stansby [15], Xiao et al.

[16], Heller et al. [17], Kobel et al. [18] and chi et al. [14]. In these studies, different equations have been proposed to predict the volume of flow overtopping.

The study method for presenting the equations of wave overtopping in the mentioned studies was physical modeling. Analytical, experimental and numerical methods can be used to calculate wave overtopping characteristics from structures including flow volume. An important advantage of validated numerical models for the study of wave overtopping from hydraulic structures is their non-limitation for structures with different designs [11]. The available numerical models for studying the overtopping are nonlinear shallow water equations models and Navier-Stokes equations models [11]. Navier-Stokes equations models are generally based on one of two categories techniques including Volume of Fluid (VOF) method [20] and Smoothed Particle Hydrodynamics (SPH) method [21]. SKYLLA model based on VOF method is one of the business models available for studying the overtopping at coastal structures [22]. This model can be easily applied to model the overtopping caused by regular waves at breakwaters.

In the present paper, a two-dimensional vertical (2DV) model based on Incompressible Smoothed Particle Hydrodynamics (ISPH) method with sub-particle scale – large eddy simulation (SPS - LES) closure model is developed to study the impulsive wave overtopping at hydraulic structures. The SPH method is an integral interpolation-based method in which the computational domain is expressed by particles containing physical properties including mass and density [23]. Details about the SPH method can be found in the previous research e.g. Monaghan [21]. The SPH method has two different approaches for calculating pressure of particles; weakly compressible perspective (WCSPH) and incompressible perspective (ISPH) [24]. Since its introduction by Monaghan [21], this method has rapidly evolved, and it has been used successfully to study various hydraulic problems (e.g. [25-32]).

In the case of impulsive wave overtopping at hydraulic structures, despite the proven power of the SPH method in simulating high varied free surface flows, this method has not been used to study the details of this phenomenon with different conditions. However, the solitary wave overtopping problem is one of the main benchmarks for evaluation of the accuracy of developed models by SPH method (e.g. Akbari [33]). In one study related to mesh-less Lagrangian methods, Luo et al. [34] developed a 2DV CPM-based hydrodynamic model for studies of some properties of solitary wave impinging on and overtopping a seawall. In their study, they demonstrated the effectiveness of the CPM hydrodynamic model for simulating solitary wave impact on a seawall. Then, using the numerical model, a parametric study was carried out to investigate the effect of transverse cross-section geometry on wave overtopping properties. Therefore, in the present study the ISPH - LES hydrodynamics model has been utilized to investigate the solitary wave overtopping at rigid hydraulic structures.

Large Eddy Simulation (LES) is a high-fidelity turbulence modeling approach widely employed in fluid dynamics to resolve the behavior of large-scale turbulent structures while modeling the effects of smaller, subgrid-scale (SGS) motions. Unlike Reynolds-Averaged Navier–Stokes (RANS) models, which average all turbulent fluctuations, LES resolves the larger, energy-containing eddies directly, capturing transient and spatially-evolving phenomena more accurately. This makes LES especially suitable for simulating highly unsteady and vortical flows, such as those found in wave breaking, overtopping, or jet impingement in hydraulic engineering. In the context of mesh-free numerical methods like Smoothed Particle Hydrodynamics (SPH), LES offers a promising pathway for enhancing turbulence representation without the excessive computational cost of Direct

Numerical Simulation (DNS) [24]. The ability of LES to simulate vortex shedding, turbulence dissipation, and transitional flow regimes makes it a critical tool for high-resolution hydrodynamic studies involving free-surface and multiphase interactions.

This study introduces a two-dimensional Incompressible Smoothed Particle Hydrodynamics – Large Eddy Simulation (ISPH–LES) model developed for detailed simulation of solitary wave overtopping at rigid hydraulic structures. Recognizing the complex and highly dynamic nature of such flows—particularly near solid boundaries—the model incorporates advanced modifications, including an improved wall-boundary pressure treatment. This enhancement effectively prevents the penetration of flow particles into rigid boundaries and ensures higher numerical stability and fidelity in simulating wave-structure interactions. To comprehensively validate the model's performance, the simulation results were compared with experimental data from Kobel et al. [18], focusing on critical hydrodynamic parameters such as wave profile evolution, overtopping depth, overtopping volume, and overtopping duration. Given the critical importance of accurate overtopping prediction for the safety of hydraulic infrastructures, the integration of LES turbulence modeling with SPH offers a powerful approach to capturing the intricate turbulent structures and transient behaviors inherent to high-energy wave impacts. By addressing existing limitations in resolving pressure and flow characteristics during impulsive wave events, this research presents a robust numerical framework that can significantly enhance the design and safety assessments of dams, seawalls, and other coastal defense systems exposed to extreme wave conditions.

2. Methodology

2.1. Governing equations

The present ISPH–LES model solves the Navier-Stokes equations as presented below:

$$\frac{D\rho}{Dt} + \rho(\nabla \cdot \bar{u}) = 0 \quad (1)$$

$$\frac{D\bar{u}}{Dt} = -\frac{1}{\rho}\nabla P + \nu(\nabla^2 \bar{u}) + g + \frac{1}{\rho}\nabla.\vec{\tau} \quad (2)$$

Where ρ and ν are density and kinematic viscosity of flow, $\bar{u}$ is velocity of flow, P is pressure of flow, $\boldsymbol{g}$ is gravity force, t is time, and $\vec{\tau}$ is the SPS stress tensor. The SPS stress tensor is modeled using the Boussinesq eddy viscosity assumption [23]:

$$\frac{\tau_{ij}}{\rho} = 2\nu_t \bar{E}_{ij} - \frac{2}{3}k\delta_{ij} \quad (3)$$

Where ν_t is the kinematic eddy viscosity, $\bar{E}_{ij}$ is the strain tensor, k is the turbulence kinetic energy. The eddy viscosity is calculated using the standard Smagorinsky model as follows:

$$\nu_t = (C_s dr)^2 II_{\bar{E}} \quad (4)$$

In which C_s is the Smagorinsky constant equal to 0.15, dr is particle spacing indicating the characteristic length scale of the small eddies and $II_{\bar{E}}$ is second invariant of the filtered-field deformation tensor. The k incorporated in the pressure term by defining the following equation [23]:

$$P_E = P + (\frac{2}{3})\rho k \quad (5)$$

Since in physics, $k$is much smaller than P, so P can be used instead of P_E [35]. Finally, by putting the terms of equation 3 in equation 2, the final momentum equation will be expressed as:

$$\frac{D\bar{u}}{Dt} = -\frac{1}{\rho}\nabla P + \nu_e(\nabla^2 \bar{u}) + g \quad (6)$$

Where ν_e is equal to $\nu + \nu_t$.

2.2. Two-step solution scheme

Solving the governing equations using the SPH method is performed with two approaches including weakly compressible

and incompressible methods. In the weakly compressible approach, which is used in standard SPH method, the pressure is calculated using the state equation based on particle density. However, in the incompressible approach, the pressure is calculated implicitly by applying the incompressible conditions. The model developed in this study is based on the incompressible approach. The present ISPH – LES model follows the following steps to calculate the results:

Firstly, the second principal invariant of the tensor of shear strain rate is calculated, and the eddy viscosity of particles is calculated using equation (4).

Secondly, which is known as the predictor step, the temporary position and velocity of particles (u^* and r^*) are computed by neglecting the pressure gradient term:

$$u^* = u^t + \Delta t(\nu_e \nabla^2 . u + g)^t \quad (7)$$

$$r^* = r^t + \Delta t . u^* \quad (8)$$

The discrete form of the Laplacian of the viscosity term in equation (7) using the SPH method formulation is the following equation [35]:

$$(\nu_e \nabla^2 . u)_i \approx \sum_j \frac{2m_j((\nu_e)_i + (\nu_e)_j) r_{ij} . \nabla_i \hat{W}_{ij}}{(\rho_i + \rho_j)(|r_{ij}|^2 + \lambda^2)} (u_i . u_j) \quad (9)$$

Where $\hat{W}$ is the interpolation kernel function, $\boldsymbol{r}$ is position vector, $r_{ij} = r_i - r_j$ and λ is a constant small number.

Thirdly, which is known as the corrector step, the pressure Poisson equation is solved to calculate the pressure of particles:

$$\nabla . (\frac{1}{\rho_*} \nabla P_{t+1}) = \frac{\rho_0 - \rho_*}{\rho_0 \Delta t^2} \quad (10)$$

Where ρ_0 is the density of particles at the current time step, and ρ_* is the intermediate density of particles. Employing the relevant SPH formulation to the left-hand side of equation (10), a linear equation system can be obtained [23]:

$$\nabla . (\frac{1}{\rho} \nabla P)_i \approx \sum_j m_j \frac{8}{(\rho_i + \rho_j)^2} \frac{P_{ij} \mathbf{r}_{ij} . \nabla_i W_{ij}}{|\mathbf{r}_{ij}|^2 + \lambda^2} \quad (11)$$

Fourthly, the new velocities of particles are computed by the equations (12) and (13):

$$u^{t+1}{}_{=u^*} + \Delta t(-\frac{1}{\rho^*} \nabla P^{t+1}) \quad (12)$$

$$r^{t+1} = r^t + \frac{u^{t+1} + u^t}{2} \Delta t \quad (13)$$

2.3. Improved solid boundary conditions

In the present model, the solid boundary condition is implemented by using fixed particles as wall particles and placing multiple rows of dummy particles outside the wall particles. The Newman boundary condition is established by equating the pressure of wall particles with dummy particles perpendicular to them. In this method, the governing equations for these particles are solved like the flow particles. As the flow particles approach the wall particles, the pressure in them will be calculated so that the flow particles will not penetrate the wall. This solid boundary condition has been widely used in previous researches, and it has presented satisfactory results e.g. Shao and Lo [36], Shao [37], Memarzadeh and Hejazi [26], and Akbari [33]. However, when the velocities of particles are high near the wall particles, some of them will penetrate the wall. For this purpose, the additional pressure term, called molecular force, is applied to the calculated pressure for the wall particles. This term was first introduced by Monaghan [21] to simulate the wall particles in the standard SPH method. The essence of this term is that if the distance between the wall particle and its adjacent fluid particles is reduced to a certain distance that allows water particles to penetrate the wall, the following equation is added to the wall particle pressure:

$$f(r) = \frac{d_0}{r}((\frac{r_0}{r})^4 - (\frac{r_0}{r})^2) \quad (14)$$

Where r is the distance between the wall particle and the water particles in its neighborhood, d_0 is a fixed number equal to 5 and r_0 is $0.9 \times dr$. By applying this additional term, the flow particle motion modeling adjacent to wall particles has been more accurately performed.

2.4. Free surface boundary conditions

In this study, the free surface boundary condition was determined using the particle density criterion. Specifically, particles with a density between 0.9 and 0.99 times the reference water density were identified as free surface particles. A zero-pressure condition was then applied to these particles to simulate atmospheric exposure. Additionally, to ensure the stability and accuracy of pressure calculations near the free surface, a pressure gradient symmetry condition was imposed. This approach assumes that the pressure distribution across the free surface behaves symmetrically, thereby avoiding artificial pressure spikes and ensuring a smooth transition in the pressure field.

2.5. Description of the problem used to evaluate the ISPH–LES hydrodynamic model

Validating the ISPH–LES hydrodynamic model against the experimental results of Kobel et al. [18] represents a crucial step toward ensuring its accuracy in simulating complex hydrodynamic phenomena like solitary wave overtopping at rigid hydraulic structures. The experimental data gathered at ETH Zurich provides a robust framework for comparison, with precise measurements of key overtopping parameters under carefully controlled conditions.

Kobel et al. [18] experimentally studied solitary wave overtopping at a rigid dam in various scenarios at ETH University, Zurich. Their experiments were conducted in a laboratory flume measuring 11 m in length and 0.5 m in width. The solitary wave in this flume was generated by a piston type wave maker located 4.85 meters from the dam. The dam structure and flume are made of PVC and glass, respectively. The height of the dam (HD) is considered constant at 30 cm. In their study, three parameters including the wave overtopping volume (V), maximum wave overtopping depth (d_{max}) and wave overtopping duration (t_0) have been studied. In mentioned study, the effect of water depth behind dam (h), wave height (a), dam angle in reservoir (β) and dam crest width (b_k) were investigated as influential parameters on hydrodynamics of solitary wave overtopping. The schematic illustration of the geometry of the problem is shown in Figure 1. In the study of Kobel et al. [18] 75 tests have been performed. From these tests, nine tests have been selected for the validation of the present ISPH – LES model as described in Table 1. The intended tests are selected so that all the important parameters in the solitary wave overtopping can be seen. In cases of 1, 2 and 3, the effect of solitary wave height, in cases of 4 and 5, the effect of water depth, in cases of 6 and 7, the effect of dam angle in reservoir, and finally in cases of 8 and 9, the effect of dam crest width in the overtopping of solitary wave from the rigid structures are numerically studied.

The free surface profiles and the initial velocity of the solitary wave based on the analytical solution of the Boussinesq equation are applied as follows [38]:

$$\eta(x,t) = a\ sec\, h^2\ [\sqrt{\frac{3a}{4h^3}}\ (x - ct)\ ] \quad (15)$$

$$u = \eta\sqrt{\frac{g}{d}} \quad (16)$$

Where η is water surface elevation, $c = \sqrt{g(d+a)}$ is wave celerity and t is time of propagation. In the numerical modeling, the initial diameter of the particles was considered to be 0.0125 m after performing convergence analysis and ensuring the best results. It is worth noting that the functional

form of Equation (15), which describes the free surface elevation of a solitary wave, bears a close resemblance to the Gaussian distribution. This similarity is not coincidental—it reflects the localized, symmetric nature of solitary waves. Physically, the shape results from a balance between nonlinear steepening and dispersive spreading, yielding a waveform with a smooth crest and exponentially decaying tails. While not derived from statistical considerations like the Gaussian distribution, the mathematical structure of solitary wave solutions often appears similar due to these shared characteristics of symmetry and concentration. This similarity enhances their suitability for use in numerical and analytical modeling, as they exhibit predictable, well-defined profiles that lend themselves to validation and calibration tasks.

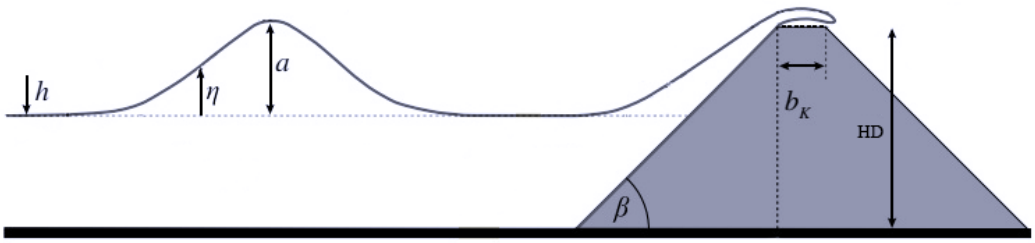


Figure 1. Schematic diagram of the model used to evaluate the ISPH–LES model.

Table 1. Parameters of solitary wave overtopping at rigid dams.

Case number	$h\ (m)$	$a\ (m)$	$\varepsilon = a/h$	β (deg)	$b_k\ (cm)$
1	0.25	0.175	0.7	90	2
2	0.25	0.125	0.5	90	2
3	0.25	0.075	0.3	90	2
4	0.2	0.14	0.7	90	2
5	0.3	0.21	0.7	90	2
6	0.2	0.14	0.7	18.4	2
7	0.2	0.14	0.7	45	2
8	0.25	0.125	0.5	90	6
9	0.25	0.125	0.5	90	16

3. Results and discussion

3.1. Qualitative Comparison of Free Surface Profiles

Figure 2 provides a visual comparison of the free surface profiles of the solitary wave as it overtops the rigid dam, as predicted by the ISPH–LES model, compared with the experimental data from Kobel et al. [18]. This qualitative analysis is essential for assessing the model's ability to replicate the key physical phenomena observed during wave overtopping, including the evolution of the wave crest, the overtopping flow, and the dissipation of energy after overtopping.

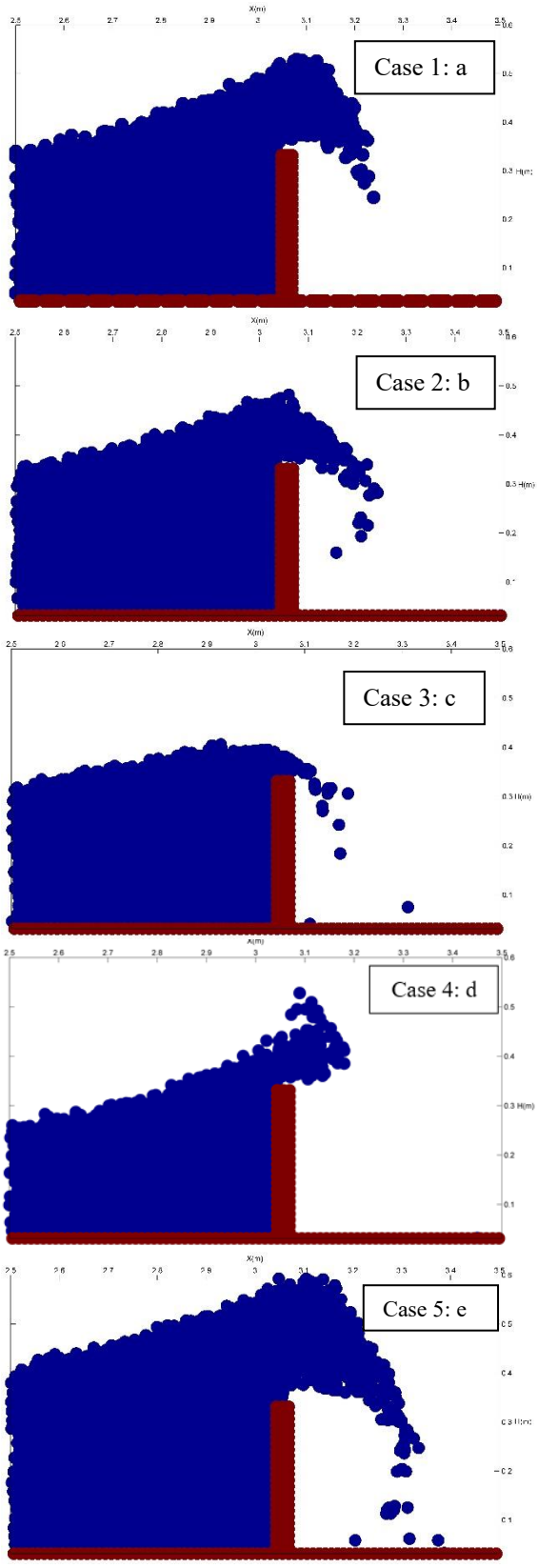
The ISPH–LES model demonstrates a high degree of agreement with the experimental data across all nine cases, capturing the nuances of wave-structure interaction. The free surface profiles at various stages of the overtopping event—particularly during the critical phases of maximum wave cresting and overtopping—are closely matched with experimental observations. Accurately simulating these stages is crucial, as they represent the moments of peak force exerted on the structure, which directly impacts its structural integrity.

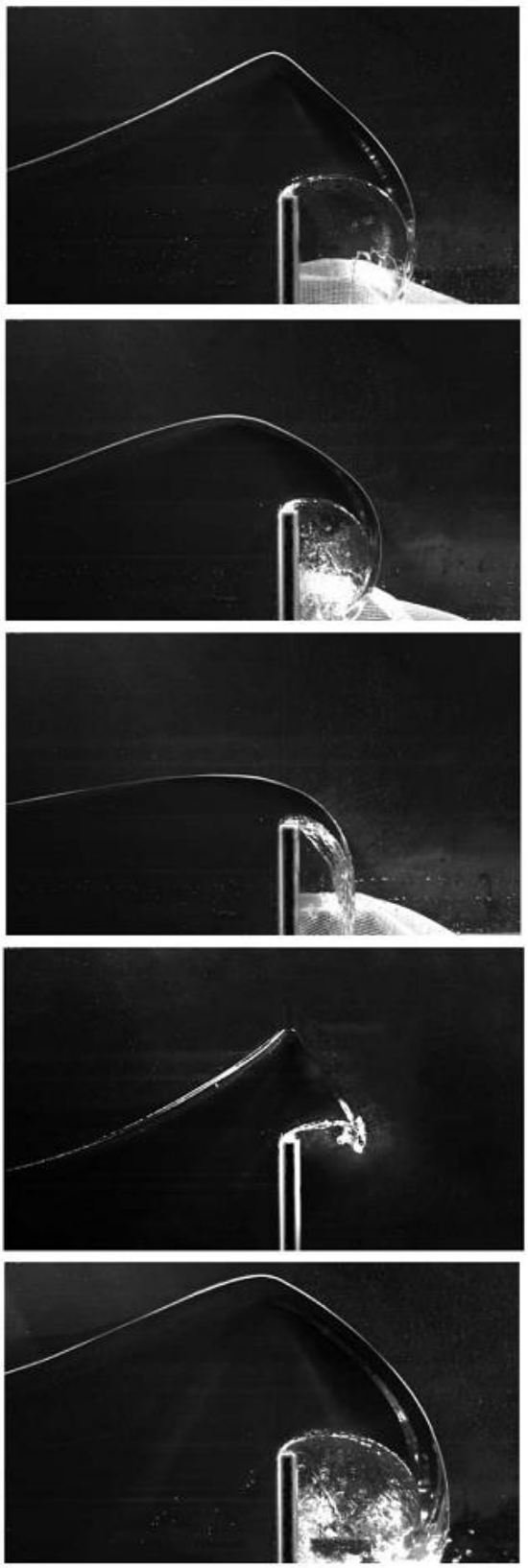
Figures 2a–2c show that as the height of the solitary wave decreases, the volume of the overtopping flow correspondingly decreases. This trend is not only consistent with the experimental data but also aligns with fundamental hydrodynamic principles, where smaller waves carry less energy and momentum, resulting in lower overtopping volumes. The ISPH model successfully captures this behavior, demonstrating its sensitivity to wave height variations—a critical factor for simulating wave forces on structures subjected to different wave conditions.

In Figures 2d and 2e, the effect of varying water depth behind the dam is clearly depicted. As expected, deeper water results in higher overtopping volumes and greater overtopping depths. This behavior is accurately modeled by the ISPH–LES model, showing that it is capable of simulating the influence of reservoir depth on overtopping dynamics. This is particularly important for hydraulic structures in environments where water levels fluctuate due to tides, seasonal changes, or other environmental factors.

Figures 1f and 1g show the influence of sloping the dam. The introduction of a slope reduces the height of the overtopping wave as it dissipates more energy upon impact with the angled surface. The ISPH–LES model closely mirrors this experimental result, further proving its ability to simulate how structural design modifications—such as changing the angle of the dam—affect overtopping behavior. This finding is valuable for designing dams and coastal defenses, as slope modifications can be used to mitigate the intensity of overtopping forces.

Finally, Figures 2h and 2i, which explore the effects of varying dam crest width, reveal that the ISPH–LES model performs well in simulating wave overtopping over different structural geometries. Interestingly, the results show that crest width has a relatively minor impact on the overall overtopping flow, a conclusion that is supported by both the model and the experimental data. This indicates that other factors, such as wave height and water depth, play more significant roles in determining overtopping behavior.


Case 1: a
Case 2: b
Case 3: c
Case 4: d
Case 5: e



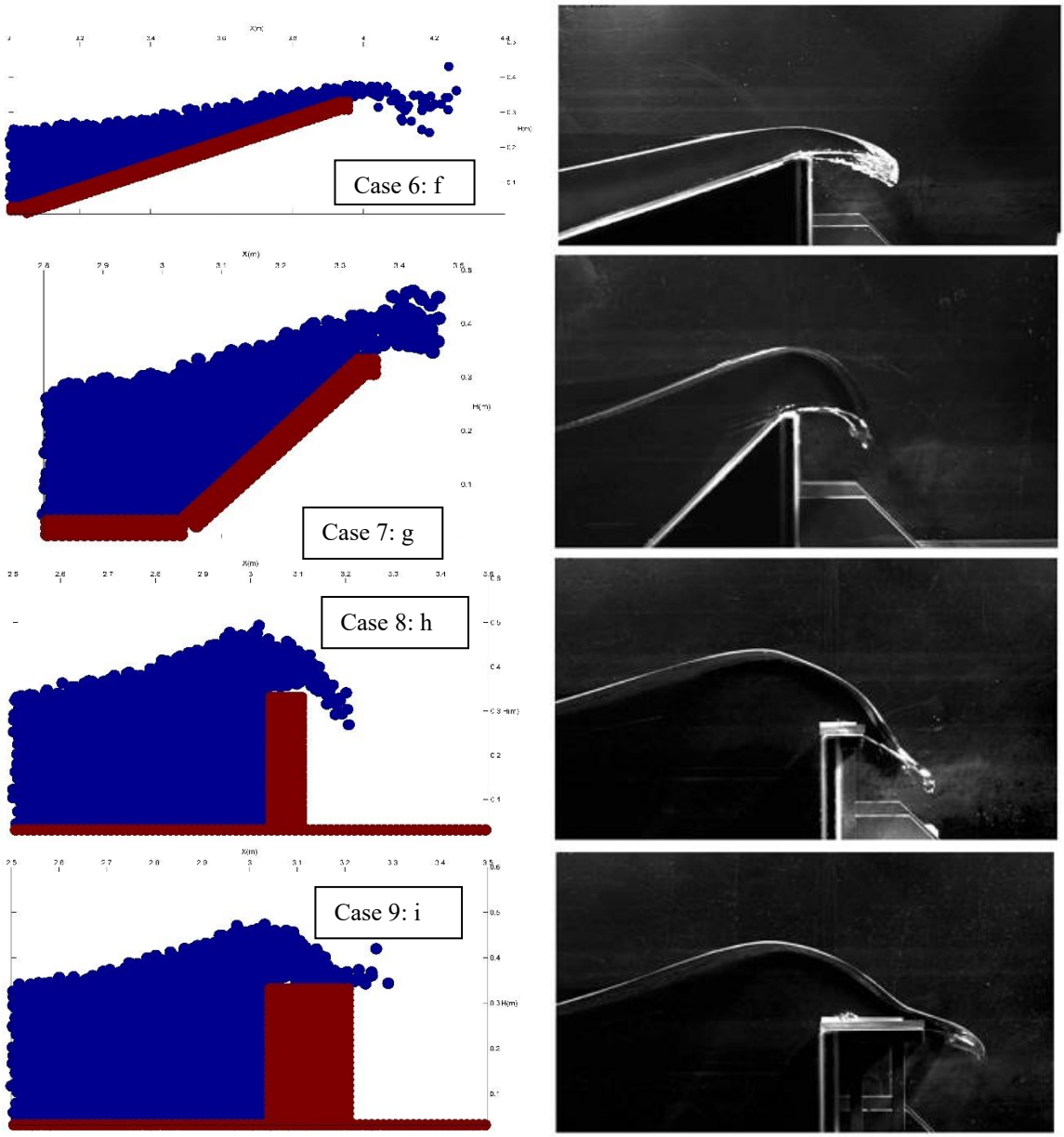


Figure 2. Qualitative comparison of free surface profiles in the present ISPH-LES numerical model and experimental data of Kobel et al. [18] during solitary wave overtopping of the rigid structure. The horizontal and vertical axes are both meters (m).

3.2. Quantitative Comparison: Maximum Overtopping Depth, Overtopping Volume, and Duration

In addition to the qualitative comparison, Table 2 presents a detailed quantitative analysis of the ISPH model's performance by comparing it with experimental data for maximum overtopping depth, overtopping volume, and wave overtopping duration. This quantitative validation is crucial for assessing the model's precision and identifying areas where further refinement may be necessary.

Maximum Overtopping Depth

The ISPH model shows strong performance in estimating the maximum overtopping depth, with an average error of 9.5% across all scenarios. This parameter directly reflects the peak hydraulic load exerted by incoming waves, which is critical for the design of coastal defenses

and flood protection structures. In this context, the overtopping depth serves not only as an indicator of wave intensity but also as a proxy for estimating the vertical pressure gradient and the required freeboard height in design calculations.

Case 5, which involved the most intense overtopping event, exhibited the lowest error (3.6%), corresponding to a high wave energy condition. This accuracy under extreme loading highlights the robustness of the ISPH–LES approach in capturing nonlinear wave deformation, energy transfer, and momentum flux during solitary wave impact. Such precise prediction is particularly useful for evaluating structural vulnerability under rare but destructive wave events, including those induced by landslides or tsunamis.

In contrast, Cases 6 and 7, which featured reduced wave heights and overtopping volumes, presented slightly higher errors (14.3% and 16.7%). These discrepancies may result from amplified sensitivity in small-scale flows where viscous effects, turbulence dissipation, and local flow separations play a relatively larger role. From a hydrodynamic perspective, the model still captures the trend of decreasing overtopping depth with lower wave energy but highlights the need for resolution improvement or turbulence modeling refinement in low-energy regimes.

Importantly, the ISPH model allows for dynamic tracking of free surface evolution and pressure gradients over the structure.

Overtopping Volume

Overtopping volume is a more complex parameter due to the dynamic and transient nature of the flow during wave overtopping. The ISPH model achieved an average error of 15% in predicting overtopping volume, indicating that it performs reasonably well in capturing the flow behavior during overtopping events.

Cases 1, 8, and 9, which represent moderate to large overtopping volumes, exhibited relatively low errors (9.1% to 10.5%), demonstrating the model's strong ability to simulate overtopping in cases where wave height and flow are substantial. The alignment between the numerical and experimental results in these cases validates the model’s accuracy for predicting flow volumes under higher-energy conditions.

Cases 6 and 7, with the smallest overtopping volumes, showed the highest errors (20.00% and 22.2%, respectively). This suggests that the model's sensitivity to smaller wave volumes introduces some limitations, particularly in cases where the overtopping flow is minimal. These discrepancies highlight the need for further refinement of the ISPH model in low-volume overtopping scenarios. Potential improvements could include enhanced resolution in the particle dynamics or better handling of flow separation effects, which tend to be more pronounced in smaller overtopping events.

Wave Overtopping Duration

The ISPH model excels in predicting wave overtopping duration, with an average error of only 5.86%. Accurate prediction of overtopping duration is crucial for understanding the long-term exposure of structures to wave forces, which has significant implications for material fatigue and structural longevity.

Cases 8 and 9, which featured longer overtopping durations, had the lowest errors (1.2%), highlighting the model’s precision in simulating sustained overtopping events. The ability to accurately capture the duration of overtopping is essential for assessing the cumulative impact of wave forces over time, particularly in environments where repeated overtopping events are expected.

Even in Case 6, where the error was highest at 10.1%, the ISPH model’s prediction remained within acceptable limits. This consistency across a range of overtopping durations reinforces the model’s reliability for simulating both short, high-intensity overtopping events and longer, more gradual flows.

Table 2. Comparison of ISPH-LES Model Results and Experimental Data of Kobel et al. [8] for Maximum Overtopping Depth, Overtopping Volume, and Wave Overtopping Duration with Approximate Errors.

	Maximum Overtopping Depth (m)			Overtopping Volume (m^3/s)			Wave Overtopping Duration (s)		
	ISPH Result	Experimental data	Approximate error	ISPH Result	Experimental data	Approximate error	ISPH Result	Experimental data	Approximate error
Case 1	0.20	0.22	9.1	0.017	0.019	10.5	0.81	0.86	5.8
Case 2	0.13	0.14	7.1	0.010	0.012	16. 7	0.75	0.81	7.4
Case 3	0.06	0.07	14.3	0.005	0.006	16.7	0.60	0.65	7.7
Case 4	0.16	0.17	5.9	0.006	0.007	14.3	0.47	0.50	6.00
Case 5	0.27	0.28	3.6	0.033	0.039	15.4	1.29	1.34	3.7
Case 6	0.06	0.07	14.3	0.008	0.010	20.00	0.71	0.79	10.1
Case 7	0.10	0.12	16.7	0.007	0.009	22.2	0.57	0.63	9.5
Case 8	0.13	0.14	7.1	0.010	0.011	9.1	0.80	0.81	1.2
Case 9	0.13	0.14	7.1	0.009	0.010	10.00	0.80	0.81	1.2
Approximate average error			9.5 %	Approximate average error		15 %	Approximate average error		5.9 %

3.3. Pressure Distribution Analysis: A Detailed Investigation of Structural Impacts

The temporal and spatial pressure distributions predicted by the ISPH–LES model across 27-time frames for the nine test cases (Figures 3–11) provide valuable insights into wave-structure interaction dynamics. These results go beyond simple visualization, offering a deeper understanding of pressure wave propagation, reflection, dissipation, and the influence of structural geometries on pressure magnitudes. The ability to capture such high-resolution temporal behavior is critical for identifying vulnerable structural zones and designing cost-effective, durable hydraulic defenses.

Initial Wave Impact Phase

In the early stages (first 5–10-time frames), the solitary wave approaches and collides with the upstream face of the rigid structure. In Cases 1 to 3 - representing variations in wave height - the pressure concentration is initially localized at the toe or base of the structure. The magnitude of this impact pressure increases significantly with wave height, as seen through the intensified red bands at the impact zone in Figures 3–5.

These localized impulses are consistent with theoretical predictions based on conservation of momentum and the Froude number, and they present key design concerns. Structures experiencing such steep gradient pressures must be reinforced at the base to prevent cracking, anchorage failure, or shear-induced movement. The ISPH–LES model accurately simulates the formation of these concentrated pressure zones, validating its applicability for assessing short-duration, high-magnitude loading.

In Cases 4 and 5, where the water depth behind the structure is increased, pressure is not only higher but also covers a wider region along the vertical face. This suggests the influence of higher hydrostatic backpressure and elevated energy levels in the impinging wave. The simulation reveals that overtopping behavior becomes more diffused, initiating earlier in the overtopping timeline, and the pressure is transmitted higher on the wall.

Wave Crest Impact and Maximum Pressure Phase

The middle stages of the simulations correspond to the wave crest reaching the crest of the dam or wall. Here, in almost all cases, a sharp rise in pressure is observed both on the crest and downstream face - particularly in Cases 1, 5, and 8, which feature high wave energy and deeper

reservoirs. This phase simulates the maximum pressure exerted on the structure and is crucial for the assessment of surface damage, local scouring, and structural fatigue.

One key insight across all cases is the directional shift of pressure vectors - from vertical (during impact) to horizontal and downward (during overtopping). In this phase, the ISPH–LES model demonstrates strong agreement with physical expectations and experimental data in Kobel et al. [18], effectively capturing the complex, multiphase flow behavior of the wave as it wraps over the structure.

For Cases 6 and 7 - featuring sloped wall geometries - the model reveals a significantly lower peak pressure compared to vertical cases. The sloped face acts as a passive energy dissipation element, elongating the impact period and reducing peak values. This demonstrates the energy-reducing effect of inclined geometries and validates their role in modern coastal engineering practice. Similarly, in Cases 8 and 9, the broader crest widths result in a redistribution of pressure toward the rear crest edge, reducing localized loads on any single point.

These outcomes highlight the ISPH model's ability to capture small but critical shifts in pressure location and magnitude due to geometric modification, an important tool for engineers seeking optimized wave energy management in design.

Dissipation and Post-Overtopping Phase

The final time frames illustrate the wave's energy dissipation phase. In most cases, pressure gradually subsides and reverts toward the base, accompanied by partial recirculation or backflow. Cases 1 to 3, involving lower reservoir depths, show relatively quick pressure drop-offs, indicating short-duration impulses and lower long-term structural stress. In contrast, Cases 4 and 5 demonstrate longer pressure tails - especially downstream - reflecting the prolonged presence of overtopping flow.

A critical observation is that in geometries with greater slope and width (Cases 6–9), pressure decay is both smoother and more gradual. This indicates a more favorable energy dissipation profile, less risk of structural resonance, and lower potential for erosive damage on downstream slopes. The simulation successfully visualizes pressure shedding and redistribution patterns, capturing not only the peak loads but the transient response of the structure to the wave's passage.

These findings are instrumental in identifying zones of prolonged exposure and informing choices related to downstream slope material (e.g., use of rock armor vs. concrete apron).

Engineering Interpretation and Model Utility

The pressure results validate the ISPH–LES model's robustness in accurately reproducing complex wave-structure interactions. Key takeaways from this analysis include:

- Vertical walls experience sharper but more intense pressures—necessitating stronger reinforcement at the impact zone.
- Sloped geometries reduce peak pressures but increase the area of influence—useful for energy spread but requiring larger protected surfaces.
- Broader crest widths redistribute pressure over a larger footprint—beneficial for structural wear reduction.
- Pressure decay rates correlate well with wave volume and reservoir depth, confirming the physical accuracy of the model.

This level of analysis shows that the ISPH–LES framework can be confidently used for parametric studies, design optimization, and resilience assessment of coastal and hydraulic infrastructure subjected to impulsive wave conditions.

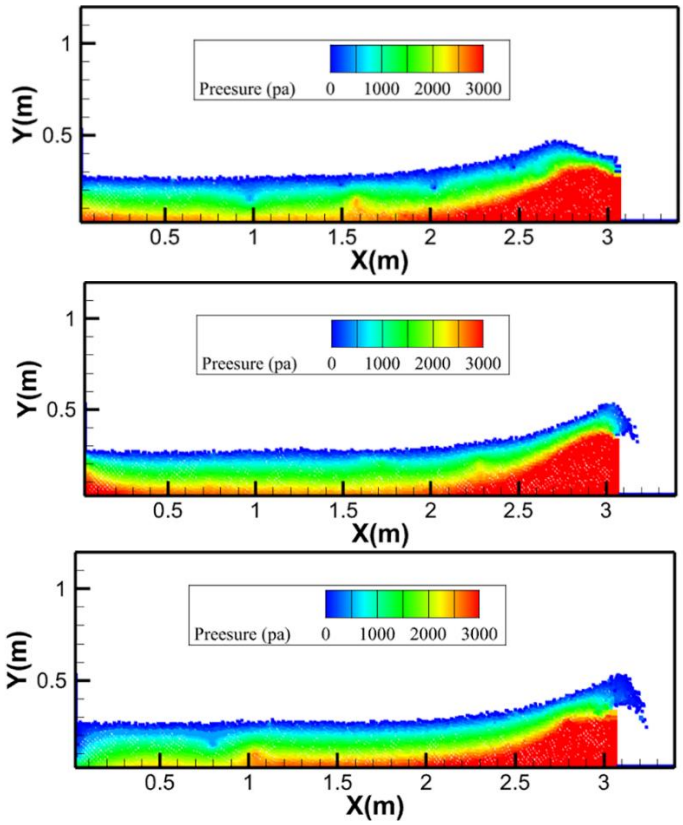


Figure 3. Time Frame Pressure Distributions for Solitary Wave Overtopping: Case [1]

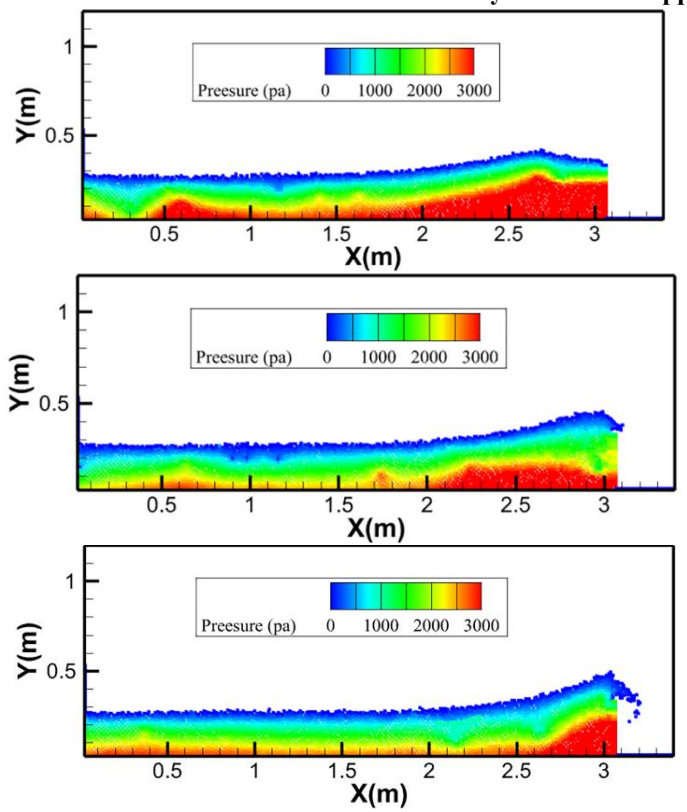


Figure 4. Time Frame Pressure Distributions for Solitary Wave Overtopping: Case [2].

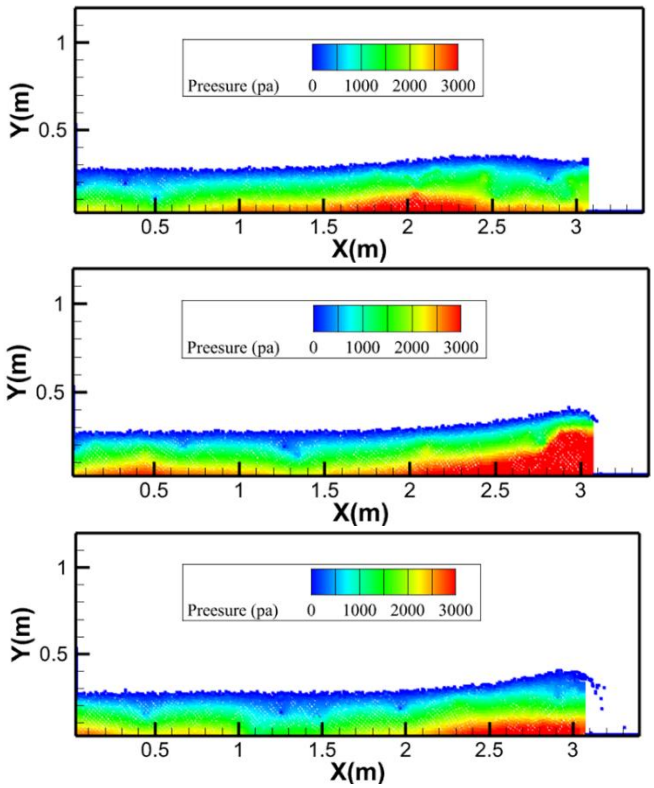


Figure 5. Time Frame Pressure Distributions for Solitary Wave Overtopping: Case [3].

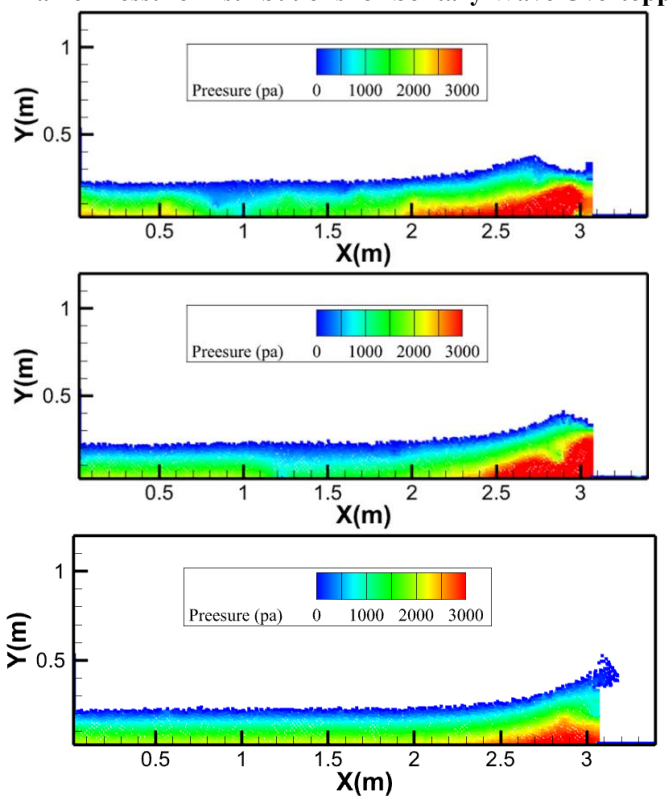


Figure 6. Time Frame Pressure Distributions for Solitary Wave Overtopping: Case [4].

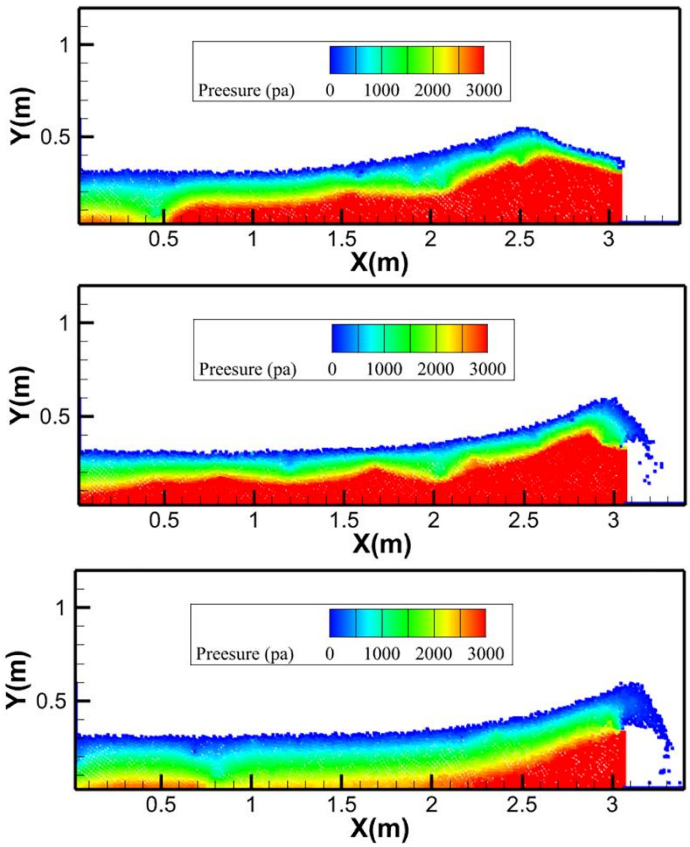


Figure 7. Time Frame Pressure Distributions for Solitary Wave Overtopping: Case [5].

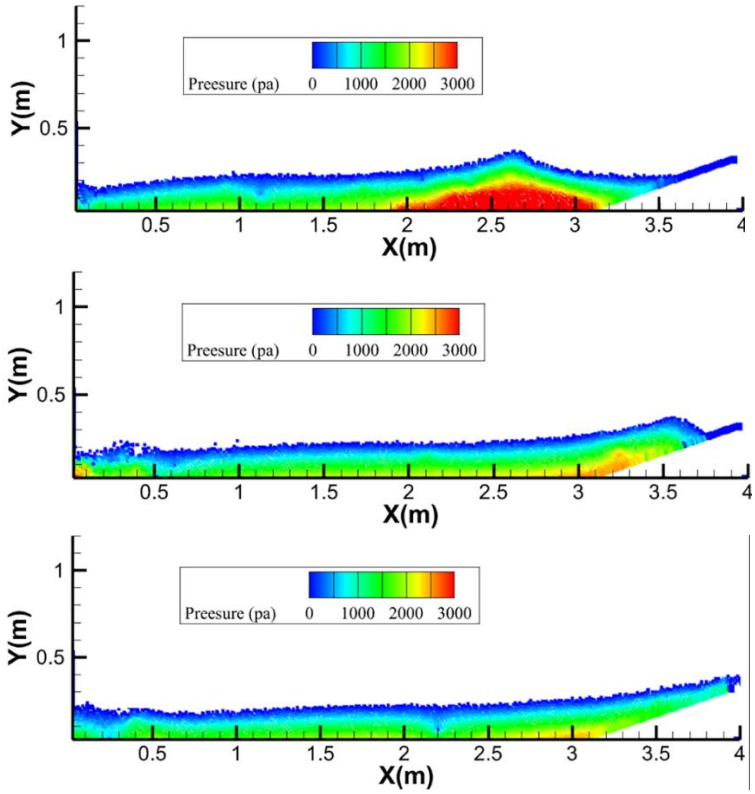


Figure 8. Time Frame Pressure Distributions for Solitary Wave Overtopping: Case [6].

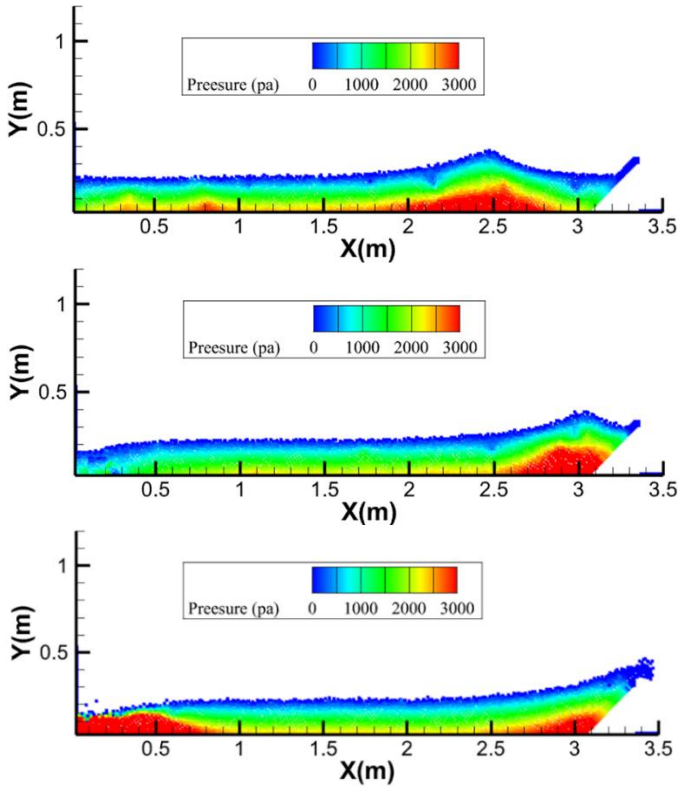


Figure 9. Time Frame Pressure Distributions for Solitary Wave Overtopping: Case [7].

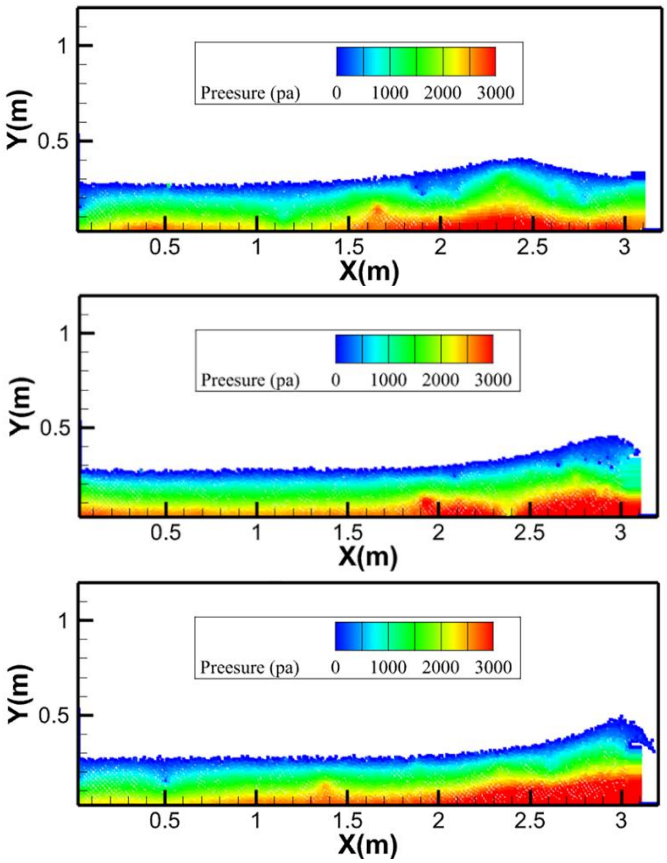


Figure 10. Time Frame Pressure Distributions for Solitary Wave Overtopping: Case [8].

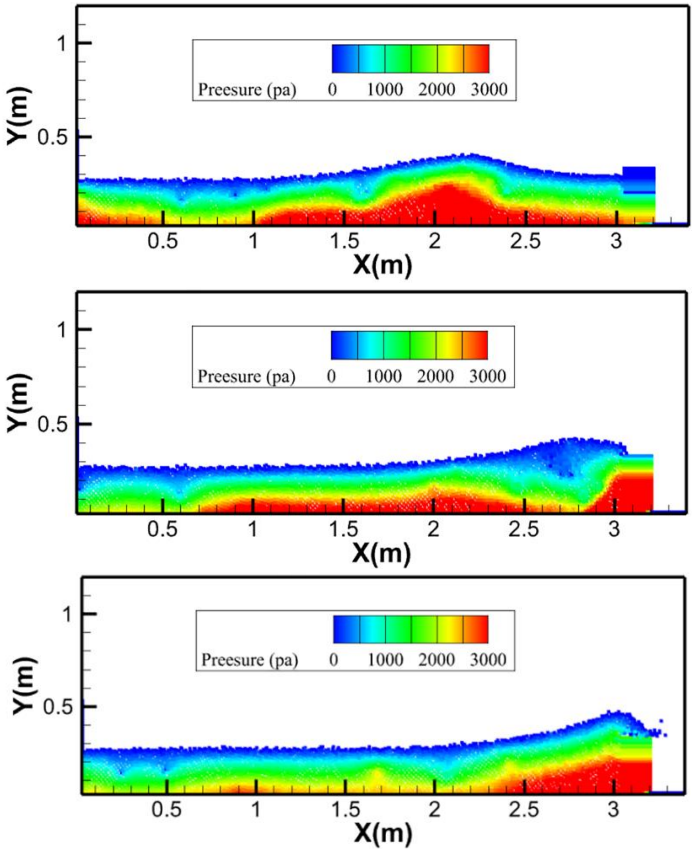


Figure 11. Time Frame Pressure Distributions for Solitary Wave Overtopping: Case [9].

4. Conclusion

This study presented a comprehensive numerical investigation of solitary wave overtopping at rigid hydraulic structures using a modified ISPH–LES (Incompressible Smoothed Particle Hydrodynamics – Large Eddy Simulation) model. The model was validated against experimental data across nine scenarios and demonstrated strong predictive accuracy with average errors of 9.5% for maximum overtopping depth, 15% for overtopping volume, and 5.9% for overtopping duration.

A key contribution of the study was the detailed analysis of temporal and spatial pressure distributions over 27-time frames per case. The model successfully captured the pressure build-up at impact, maximum crest pressures during overtopping, and dissipation patterns, all of which are critical for assessing structural integrity. It also reflected the effects of dam geometry variations (slope and crest width) on pressure magnitude and distribution, showing that sloped and wider geometries reduce localized peak pressures and help distribute wave energy more evenly.

The findings indicate that the ISPH–LES framework is highly reliable for simulating high-energy, turbulent overtopping flows and provides actionable engineering insights, such as identifying critical impact zones, supporting structural optimization, and improving protective design strategies. While the model showed robust performance under extreme overtopping conditions, further refinement is recommended for scenarios involving low-energy or short-duration overtopping events, where particle resolution and pressure diffusion may impact accuracy.

Overall, the ISPH–LES model proves to be a practical and high-fidelity tool for engineers and researchers engaged in the design, risk assessment, and resilience evaluation of coastal and hydraulic

infrastructures. Future work may extend this model's application to 3D configurations, real-time simulation scenarios, and integration with sediment transport or debris flow modules.

Funding

This research received no external funding.

Conflict of interests

The author declares that he has no conflict of interest.

Artificial intelligence (AI) usage

During the preparation of this work the author did not use any AI tools.

Author Contributions

All sections of the manuscript were prepared by the author.

References

1. Kheybar H, Sajjadi SM, Ahadiyan J, Ghomeshi M. Hydraulic Analysis of Pivot Side Weirs with Sill. Iranian Journal of Soil and Water Research. 2025 Mar 21;56(1):229-46. https://doi.org/10.22059/ijswr.2024.382426.669790
2. Tahmasbipour M, Azizi Nadian H, Ahadiyan J, Oliveto G, Sajjadi SM, Kiyani AM. Experimental Investigation of T-Jump Stabilization Using Water Jets and Sinusoidal Corrugated Beds. Water. 2024 Dec 6;16(23):3513. https://doi.org/10.3390/w16233513
3. Taheri Talavari T, Sajjadi SM, Ahadiyan J, Azizi Nadian H. Numerical hydraulic and hydrodynamic investigation of flow passing through multiple elliptic lopac gates with Flow 3D software. Advanced Technologies in Water Efficiency. 2024 Sep 22;4(3):40-60. https://doi.org/10.22126/atwe.2024.10747.1127
4. Ahadiyan J, Chenari SA, Nadian HA, Katopodis C, Valipour M, Sajjadi SM, Omidvarinia M. Sustainable systems engineering by CFD modeling of lateral intake flow with flexible gate operations to improve efficient water supply. International Journal of Sediment Research. 2024 Aug 1;39(4):629-42. https://doi.org/10.1016/j.ijsrc.2024.05.003
5. Shahabi M, Ahadiyan J, Ghomeshi M, Narimousa M, Katopodis C, Azizi Nadian H. Numerical study of the effect of a V-shaped weir on turbulence characteristics and velocity in V-weir fishways. River Research and Applications. 2023 Jan;39(1):21-34. https://doi.org/10.1002/rra.4064
6. Sharoonizadeh S, Ahadiyan J, Scorzini AR, Di Bacco M, Sajjadi M, Moghadam MF. Turbulence characteristics of the flow resulting from the hydrodynamic interaction of multiple counter flow jets in expanding channels. Acta Mechanica. 2022 Sep;233(9):3867-80. https://doi.org/10.1007/s00707-022-03250-2
7. Mobarak F, Sajjadi SM, Ahadiyan J, Zeynivand M. Numerical modeling of the effect of elliptical elongation on the hydraulic performance of an elliptical Lopac gate. Water and Irrigation Management. 2022 Jun 22;12(2):263-75. https://doi.org/10.22059/jwim.2022.335817.952
8. Kheybar H, Sajjadi SM, Ahadiyan J. Effect of sudden canal contraction on the discharge coefficient and the energy dissipation coefficient of the elliptical LOPAC gate. Irrigation and Drainage. 2021 Dec;70(5):1145-54. https://doi.org/10.1002/ird.2622
9. Sarkamaryan S, Ahadiyan, J. Mathematical modeling of energy loss on Stepped Spillway Using ANSYS-CFX Numerical Model. Irrigation Sciences and Engineering. 2021 Mar;43(1):43-56. https://doi.org/10.22055/jise.2017.22269.1593
10. Noruzi S, Ahadiyan J. Effect of vortex breaker blades 45 degree on discharge coefficient of morning glory spillway using flow-3D. Journal of Irrigation

Sciences and Engineering. 2017 Jan 1;40(1):191-200. https://doi.org/10.22055/jise.2017.12677
11. EurOtop. Wave overtopping of sea defences and related structures: assessment manual. 2007. Available from: http://www.overtopping-manual.com/assets/downloads/EAK K073_EurOtop_2007.pdf
12. Özhan E, Yalcmer AC. Overtopping of solitary waves at model sea dikes. InCoastal Engineering 1990 1991 (pp. 1487-1498). https://doi.org/10.1061/9780872627765.113
13. Müller DR. Auflaufen und Überschwappen von Impulswellen an Talsperren (Doctoral dissertation, ETH Zurich).
14. Jervis M, Peregrine DH. Overtopping of waves at a wall: A theoretical approach. InCoastal Engineering 1996 1997 (pp. 2192-2205). https://doi.org/10.1061/9780784402429.170
15. Stansby PK. Solitary wave run up and overtopping by a semi-implicit finite-volume shallow-water Boussinesq model. Journal of Hydraulic Research. 2003 Nov 1;41(6):639-47. https://doi.org/10.1080/00221680309506896
16. Xiao H, Huang W, Tao J. Numerical modeling of wave overtopping a levee during Hurricane Katrina. Computers & Fluids. 2009 May 1;38(5):991-6. https://doi.org/10.1016/j.compfluid.2008.01.025
17. Heller V, Hager WH, Minor HE. Landslide generated impulse waves in reservoirs: Basics and computation. VAW-Mitteilungen. 2009;211. https://doi.org/10.1142/9789814277426_0109
18. Kobel J, Evers FM, Hager WH. Impulse wave overtopping at rigid dam structures. Journal of Hydraulic Engineering. 2017 Jun 1;143(6):04017002. https://doi.org/10.1061/(asce)hy.1943-7900.0001271
19. Chi SH, Zhang C, Sui TT, Cao ZB, Zheng JH, Fan JS. Field observation of wave overtopping at sea dike using shore-based video images. Journal of Hydrodynamics. 2021 Aug;33(4):657-72. https://doi.org/10.1007/s42241-021-0073-1
20. Hirt CW, Nichols BD. Volume of fluid (VOF) method for the dynamics of free boundaries. Journal of computational physics. 1981 Jan 1;39(1):201-25. https://doi.org/10.1016/0021-9991(81)90145-5
21. Monaghan JJ. Simulating free surface flows with SPH. Journal of computational physics. 1994 Feb 1;110(2):399-406. https://doi.org/10.1006/jcph.1994.1034
22. Van der Meer JW, Petit HA, Van den Bosch P, Klopman G, Broekens RD. Numerical simulation of wave motion on and in coastal structures. InCoastal Engineering 1992 1993 (pp. 1772-1784). https://doi.org/10.1061/9780872629332.134
23. Memarzadeh R, Barani G, Ghaeini-Hessaroeyeh M. Numerical modeling of sediment transport based on unsteady and steady flows by incompressible smoothed particle hydrodynamics method. Journal of Hydrodynamics. 2018 Oct; 30:928-42. https://doi.org/10.1007/s42241-018-0111-9
24. Memarzadeh R, Barani G, Ghaeini-Hessaroeyeh M. Application of a weakly compressible smoothed particle hydrodynamics multi-phase model to non-cohesive embankment breaching due to flow overtopping. Frontiers of Structural and Civil Engineering. 2018 Sep; 12:412-24. https://doi.org/10.1007/s11709-017-0432-8
25. Dalrymple RA, Rogers BD. Numerical modeling of water waves with the SPH method. Coastal engineering. 2006 Feb 1;53(2-3):141-7.

https://doi.org/10.1016/j.coastaleng.2005.10.004
26. Memarzadeh R, Hejazi K. ISPH numerical modeling of nonlinear wave run-up on steep slopes. J Persian Gulf (Marine Sci). 2012;10(3):17–26.
27. Lind SJ, Xu R, Stansby PK, Rogers BD. Incompressible smoothed particle hydrodynamics for free-surface flows: A generalised diffusion-based algorithm for stability and validations for impulsive flows and propagating waves. Journal of Computational Physics. 2012 Feb 20;231(4):1499-523. https://doi.org/10.1016/j.jcp.2011.10.027
28. Didier E, Neves DR, Martins R, Neves MG. Wave interaction with a vertical wall: SPH numerical and experimental modeling. Ocean engineering. 2014 Sep 15; 88:330-41. https://doi.org/10.1016/j.oceaneng.2014.06.029
29. He M, Gao XF, Xu WH. Numerical simulation of wave-current interaction using the SPH method. Journal of Hydrodynamics. 2018 Jun;30(3):535-8. https://doi.org/10.1007/s42241-018-0042-5
30. Tsurudome C, Liang D, Shimizu Y, Khayyer A, Gotoh H. Incompressible SPH simulation of solitary wave propagation on permeable beaches. Journal of Hydrodynamics. 2020 Aug; 32:664-71. https://doi.org/10.1007/s42241-020-0042-0
31. Wang Z, Zhang C, Haidn OJ, Hu X. An Eulerian SPH method with WENO reconstruction for compressible and incompressible flows. Journal of Hydrodynamics. 2023 Apr;35(2):210-21. https://doi.org/10.1007/s42241-023-0025-z
32. Feng R, Fourtakas G, Rogers BD, Lombardi D. Modelling internal erosion using 2D smoothed particle hydrodynamics (SPH). Journal of Hydrology. 2024 Aug 1; 639:131558. https://doi.org/10.1016/j.jhydrol.2024.131558
33. Akbari H. Simulation of wave overtopping using an improved SPH method. Coastal Engineering. 2017 Aug 1; 126:51-68. https://doi.org/10.1016/j.coastaleng.2017.04.010
34. Luo M, Reeve DE, Shao S, Karunarathna H, Lin P, Cai H. Consistent Particle Method simulation of solitary wave impinging on and overtopping a seawall. Engineering Analysis with Boundary Elements. 2019 Jun 1; 103:160-71. https://doi.org/10.1016/j.enganabound.2019.03.012
35. Aly AM, Asai M, Sonda Y. Modelling of surface tension force for free surface flows in ISPH method. International Journal of Numerical Methods for Heat & Fluid Flow. 2013 Apr 12;23(3):479-98.
36. Shao S, Lo EY. Incompressible SPH method for simulating Newtonian and non-Newtonian flows with a free surface. Advances in water resources. 2003 Jul 1;26(7):787-800. https://doi.org/10.1016/s0309-1708(03)00030-7
37. Shao S. Incompressible smoothed particle hydrodynamics simulation of multifluid flows. International Journal for Numerical Methods in Fluids. 2012 Aug 20;69(11):1715-35. https://doi.org/10.1002/fld.2660
38. Lee JJ, Skjelbreia JE, Raichlen F. Measurement of velocities in solitary waves. Journal of the Waterway, Port, Coastal and Ocean Division. 1982 May;108(2):200-18. https://doi.org/10.1061/jwpcdx.00002

© 2025 by the authors. Licensee SCU, Ahvaz, Iran. This article is an open access article distributed under the terms and conditions of the Creative Commons Attribution 4.0 International (CC BY 4.0 license) (http://creativecommons.org/licenses/by/4.0/).

The Optimal Selection of Submerged Vanes Geometric Dimensions in Curved Channels with Sediment Flow

Parisa Rezaei [1], Elham Fazel Najafabadi [*,1], Mohammad Shayannejad [1]

1. Department of Water Science and Engineering. College of Agriculture, Isfahan University of Technology, Isfahan, Iran.

***Corresponding Author:**
Elham Fazel Najafabadi,

Email: efazel@iut.ac.ir
Received: 2025.05.07
Accepted: 2025.06.23
J. Hydraul. Struct., 12(2):74-102
DOI: 10.22055/jhs.2025.49586.1349

ABSTRACT

One of the major challenges in diverting water from rivers is the intrusion of sediment into intakes, which can cause operational issues and damage infrastructure. Various methods have been explored to mitigate this problem, including the use of submerged vanes. This study employed simulations to evaluate the effectiveness of submerged vanes and the impact of their geometric parameters on reducing sediment inflow. Results showed the sediment transport estimation error for the optimal computational mesh size (2.7cm × 1cm) was 0.55%. The findings indicated that the optimal vane height and length were 0.5 times the flow depth and 2.5 times the vane height, respectively. Additionally, the optimal transverse and longitudinal spacing between vanes, as well as the distance from the nearest vane row to the intake wall, were determined to be 2.17, 5, and 2 times the vane height, respectively. Flow analysis showed that near the bed, the maximum velocity cores were directed toward the outer bend and the intake, whereas at the water surface, these cores became more widely distributed across the channel. Negative vertical velocities were concentrated at the intake entrance. In the absence of submerged vanes, the maximum secondary flow strength was found near the bed across the full channel width. However, when vanes were present, the strongest secondary currents shifted to the left side of the vanes.

KEYWORDS
Sediment discharge, Water intake, Curved channel, Geometric parameters, Simulation.

1. Introduction

The continuous growth of the global population and industrial development has significantly increased water demand. On the other hand, declining water resources and rising pollution levels have become major concerns for water resource engineers. Among the most accessible sources of water are surface waters, particularly rivers. Understanding river behavior and sediment transport—especially in meandering sections—is crucial for effective river engineering.

One common method of water diversion for industrial, agricultural, and municipal uses involves the use of lateral intake channels branching from the main river flow. However, along with the diverted water, mobile sediment also enters these lateral channels and is transported to pumping stations, treatment plants, and farmland. This sediment intrusion can lead to a range of physical, hydraulic, and environmental problems.

As a result, controlling and reducing sediment entry into lateral intakes has become a key focus in hydraulic engineering over recent decades. Various methods and structural solutions have been proposed to mitigate sediment intrusion. These include the use of skimming walls [e.g., 1-4], spur dikes [e.g., 5-8], permeable and impermeable groynes [e.g., 9-12], dikes [13, 14], and submerged vanes. Although the use of these structures has been mainly aimed at reducing transported sediment, their use can also be mentioned with a focus on flow structure [15, 16] and reducing scour around the bridge pier [17, 18, 19].

Submerged vanes are among the most commonly employed sediment control structures to the intakes, designed to mitigate sediment intrusion effectively. Beyond their role in sediment management, these structures have proven valuable in various critical riverine environments for both flow regulation and sediment control. For instance, in areas with complex flow patterns, submerged vanes can be utilized to reduce local scour around hydraulic structures such as bridge piers—submerged vanes often placed in straight river sections due to structural or stability constraints [20, 21, 22, 23]. Moreover, the accumulation of floating woody debris—resulting from factors such as flooding and deforestation—presents a significant challenge to hydraulic infrastructure, including the submerged vanes [24]. Despite these broader applications, the present study is specifically focused on evaluating the effectiveness of submerged screens in reducing sediment inflow into reservoirs.

Submerged vanes are one of the most widely used methods of preventing and reducing sediments entering the lateral channels in research. Odgaard was one of the first researchers in the field of the use of submerged vanes, and by conducting his laboratory research from 1983 to 2009, he provided one of the most comprehensive research projects in the field of submerged vanes.

Following other laboratory, field and numerical researches such as Odgaard and Lee [25] and Odgaard and Mosconi [26], Odgaard and Wang [27], Barkdoll et al. [28], Marelius and Sinha [29], Gupta et al. [30], Tan et al. [31], Ouyang [32], Sharma et al. [33], Karami et al. [34], Biswas and Barbhuiya [35]. In line with the specific application of submerged vanes to control and reduce the sediment input to the lateral channels, many researches have been done, including Nakato et al. [36], Raudkivi [37], Wang et al. [38], Ouyang [39], Ho et al. [40], Michel et al. [41], Sarhadi and Jabbarri [42].

Tseng et al. [43] conducted their study in a quasi-field-scale laboratory channel, where permeable vanes were installed next to one of the channel walls under live-bed conditions dominated by bed load transport, with negligible suspended sediment.

Estimates of bed load transport along the channel showed that the vanes were effective in redirecting sediment laterally. Under laboratory conditions, the maximum rate of lateral sediment transfer ranged from 9% to 18% of the total average stream-wise transport within the domain. Mhsen and Hilo [44] investigated the installation angle of submerged vanes under various discharge conditions. Their results indicated that a 20-degree angle was most effective in deflecting sediment. The optimal performance of submerged vanes was observed when the lateral channel discharge was less than 20% of the total flow.

Hilo [45] developed a physical model comprising a main channel, a lateral sub-channel, and a sediment feeding mechanism to reduce sediment entry into the sub-channel and redistribute sediment flow. The results indicated that vane performance was more effective at lower flow rates, with a 20-degree installation angle identified as optimal. Aminian et al. [46] examined the impact of submerged vanes positioned at angles of 30°, 45°, and 60° relative to the main flow direction on sediment diversion into a 90-degree lateral channel. Their findings revealed that increasing the Froude number by 0.3 led to a 22.2% reduction in

diverted water discharge and a 53.3% reduction in diverted sediment load. Additionally, the study concluded that under lower Froude numbers and shallower flow depths, a 30-degree vane angle offers the most effective sediment diversion performance.

Chauhan et al. [47] reviewed recent advances in sediment diversion using submerged vanes, highlighting current limitations and offering suggestions for future research. Their study provided a detailed analytical foundation on the physics governing vane performance and thoroughly examined design parameters through analytical relationships. Additionally, the paper reviewed various applications of submerged vanes and proposed a research agenda to enhance riverine navigation through improved vane implementation. In a separate study, Gumgum et al. [48] conducted 26 experimental tests to evaluate the impact of submerged vane parameters and discharge ratios on bed erosion and morphology at a 90-degree lateral channel. Their findings identified the vane deviation angle and water discharge ratio as the most influential factors affecting erosion, while other parameters showed minimal effects within the tested range. The optimal configuration, offering the highest efficiency, was achieved with a vane angle of 45 degrees.

Bor [49] conducted experiments to analyze three-dimensional flow patterns and sediment distribution over a mobile bed in the presence of submerged vanes during sediment inflow. The study concluded that a row of three submerged vanes could reduce sediment diversion by approximately 20%. Baltazar et al. [50] carried out experimental investigations on the role of submerged vanes in limiting sediment entry into a 90-degree lateral channel. Their findings indicated that in the presence of submerged vanes, the circulating current is not formed in the main channel, thereby reducing bed load transfer to the lateral intake by about 75%. Additionally, submerged vanes increased the flow separation zone within the lateral intake and generated higher levels of turbulence kinetic energy. Kalathil et al. [51] examined the effect of collars and submerged vanes on reducing sediment ingress into lateral channels. Their results showed the lowest performance at a vane angle of 15 degrees, with a 46.82% reduction in sediment, and the highest at 40 degrees, achieving an 85.36% reduction compared to conditions without vanes. The study also found that collars enhanced vane performance at 40 degrees and were effective in reducing sediment diversion at 15 degrees when the collar diameter was three times the vane height.

Serajian et al. [52] conducted experiments in a converging arc with a 90-degree angle to investigate the effects of channel convergence, submerged vane angle, and Froude number on sediment diversion. Their findings indicated that while an increase in the Froude number leads to greater sediment diversion, the installation of submerged vanes reduces it. Among the tested configurations, vanes installed at the smallest angle (25 degrees) were most effective in minimizing sediment entry into the lateral channel. Karami Moghadam et al. [53] carried out laboratory tests using submerged vanes and lateral channels with a 55-degree angle, examining both round-edged and sharp-edged intake openings. Vanes were arranged in a zigzag pattern at angles of 10 and 30 degrees relative to the flow. Results showed that round-edged openings increased scouring while decreasing sediment inflow to the lateral channel. In another study, Karmi et al. [34] calibrated a three-dimensional Computational Fluid Dynamics (CFD) model with experimental data to assess flow patterns, discharge deviation ratios, secondary flow intensities, and vortex structures. Their results demonstrated that increasing the narrowing ratio of the channel reduces diverted flow, while greater longitudinal spacing between vanes intensifies the velocity gradient, causing more severe bed erosion near the vanes.

A review of previous studies reveals that most existing research has been primarily experimental, with limited use of numerical

methods for parameter optimization. Moreover, prior optimization efforts have largely focused on the dimensions of submerged vanes, often within a narrow range of values. In light of these gaps, the present study aimed to optimize both the geometric characteristics of submerged vanes—specifically their length and height—as well as their longitudinal and transverse spacing, including the distance between the first row of vanes and the intake. The objective function for all optimization scenarios was to minimize the sediment inflow rate into the water intake.

Materials and Methods

In this study, the SSIIM software was employed as a numerical solver of the Navier–Stokes equations to simulate three-dimensional flow patterns and sediment deviation at the entrance of a diversion channel. SSIIM is well-suited for sediment-related studies, capable of simulating both suspended and bed load transport, including non-uniform sediment distributions. The software supports modeling of complex sediment processes such as sorting, armoring, and bed stratification—features that often require significant customization in more generic CFD platforms. Additionally, SSIIM2 facilitates the simulation of morphological changes in riverbeds, intakes, and reservoirs through its ability to use multiblock and nested block grids, reducing the need for extensive user intervention or advanced coding.

Governing equations

The fundamental governing equations used in the simulation are the continuity and momentum equations. The continuity equation, expressed in Cartesian coordinates (x, y, z) and assuming constant fluid density, is given as follows:

$$V_f \frac{\partial \rho}{\partial t} + \frac{\partial}{\partial x}(\rho u A_x) + \frac{\partial}{\partial y}(\rho v A_y) + \frac{\partial}{\partial z}(\rho u w) = 0 \quad (1)$$

Here, V_F denotes the flow volume fraction; ρ is the fluid density; t represents time; u, v, and w are the velocity components in the x, x, and x directions, respectively; and A_x, A_y, and A_z represent the surface flow fractions in the respective directions. Equation (2) presents the momentum equations in three dimensions:

$$\begin{aligned}
\frac{\partial u}{\partial t} + \frac{1}{V_F}\left\{uA_x\frac{\partial u}{\partial x} + vA_y\frac{\partial u}{\partial y} + wA_z\frac{\partial u}{\partial z}\right\} &= -\frac{1}{\rho}\frac{\partial P}{\partial x} + Gr_x + Vi_x \\
\frac{\partial u}{\partial t} + \frac{1}{V_F}\left\{uA_x\frac{\partial u}{\partial x} + vA_y\frac{\partial u}{\partial y} + wA_z\frac{\partial u}{\partial z}\right\} &= -\frac{1}{\rho}\frac{\partial P}{\partial x} + Gr_x + Vi_x \\
\frac{\partial w}{\partial t} + \frac{1}{V_F}\left\{uA_x\frac{\partial w}{\partial x} + vA_y\frac{\partial w}{\partial y} + wA_z\frac{\partial w}{\partial z}\right\} &= -\frac{1}{\rho}\frac{\partial P}{\partial z} + Gr_z + Vi_z
\end{aligned} \quad (2)$$

where Gr_x, Gr_y, and Gr_z are the accelerations caused by gravity; and Vi_x, Vi_y, and Vi_z are the accelerations caused by viscosity in the x, y, and z directions, respectively.

Sediment transport is composed of two components: bed load and suspended load. The suspended load is calculated using the convective-diffusion equation based on sediment concentration:

$$\frac{\partial c}{\partial t} + U_j\frac{\partial c}{\partial x_j} + \omega\frac{\partial c}{\partial z} = \frac{\partial c}{\partial x_j}\left(\Gamma_T\frac{\partial c}{\partial x_j}\right) \quad (3)$$

Where ω is the sediment fall velocity, x Cartesian distance, and Γ_T is the dispersion coefficient, which can be calculated as follows:

$$\Gamma_T = \frac{\vartheta_T}{S_C} \quad (4)$$

ν_T is the Eddy viscosity and S_c is the Schmidt number, which varies in the range of 0.7-1 [54].

Additionally, the numerical model applies

the van Rijn [55] equation to calculate the bed load transport within the layer between the bed surface and the foundation surface.

Turbulence modeling

The SSIIM software is designed to support a variety of turbulence models, including the standard k-ε model, the RNG-enhanced k-ε model, a localized k-ε model based on wind shear, the Spalart-Allmaras model, and two versions of the k-ω model—one incorporating Wilcox's wall laws and the other utilizing k-ε wall laws. Since the software is available in two versions (SSIIM 1 and SSIIM 2), the availability of specific turbulence models may vary between them. Comparative evaluation against laboratory experiments indicated that the RNG k-ε model yields the most accurate results. Therefore, this study primarily employed the standard k-ε model. The standard k-ε model is a widely adopted two-equation turbulence model, where one equation governs the turbulent kinetic energy (k) and the other governs its dissipation rate (ε) [56]. These governing equations are expressed as follows [57]:

$$\frac{\partial}{\partial t}(\rho k)+\frac{\partial}{\partial x_i}(\rho k u_i) = \frac{\partial}{\partial x_i}\left[(\mu+\frac{\mu_t}{\sigma_k})\frac{\partial k}{\partial x_i}\right] + G_k + G_b - \rho\varepsilon - Y_M + S_k \quad (5)$$

$$\frac{\partial}{\partial t}(\rho \varepsilon)+\frac{\partial}{\partial x_i}(\rho \varepsilon u_i) = \frac{\partial}{\partial x_j}\left[(\mu+\frac{\mu_t}{\sigma_\varepsilon})\frac{\partial \varepsilon}{\partial x_j}\right] + C_{1\varepsilon}\frac{\varepsilon}{k}(G_k + C_{3\varepsilon}G_b) - C_{2\varepsilon}\rho\frac{\varepsilon^2}{k} + S_\varepsilon \quad (6)$$

$$\mu_t = \rho C_\mu \frac{k^2}{\varepsilon} \quad (7)$$

In these equations, G_b and G_k represent the production of turbulent kinetic energy due to buoyancy and velocity gradients, respectively. The term Y_M accounts for the contribution of compressibility to the production of turbulence. The constants $C_{1\varepsilon}$, $C_{2\varepsilon}$, $C_{3\varepsilon}$, and C_μ are empirical coefficients with typical values of 1.44, 1.92, 0.09, and 0.09, respectively. S_k and S_ε are the turbulent Prandtl numbers for k and ε, typically taken as 1.0 and 1.3, respectively. μ_t denotes the eddy viscosity.

Boundary conditions and gridding

In this study, the flow field was simulated using SSIIM2, employing two computational blocks: one for the main channel and one for the lateral intake. The main channel consisted of two straight sections—upstream and downstream—connected by a 180-degree bend. For the hydraulic boundary conditions, the discharge and cross-sectional flow area were specified at the upstream and downstream ends, respectively. Sediment-related input parameters, including particle size, sediment type, and fall velocity, were also provided to the software for sediment transport calculations. Since SSIIM2 does not independently support the complex meshing required for this geometry, auxiliary tools such as AutoCAD, MATLAB, and Excel were used to generate the computational mesh. The mesh density was adapted to the significance of different regions, with finer mesh elements placed near the submerged vanes and coarser elements at the channel's inlet and outlet. Based on the main channel width, intake width, and vane positioning, a grid resolution of 2.7 × 1 cm was selected in the longitudinal and transverse directions, respectively. The computational domain included 235 longitudinal sections, 34 transverse sections, and 11 vertical layers, which were imported into SSIIM2 for simulation.

The boundary conditions for the main mesh block included specified inflow discharge, water depth, and the Manning–Strickler roughness coefficient at the channel entrance; an outflow condition at the downstream end; and wall boundaries applied to the channel bed and sidewalls. For the diversion channel, boundary conditions included symmetry at the

entrance and upper boundary, outflow at the exit, and wall conditions for all remaining surfaces.

Model verification

The numerical simulation was verified using experimental data from Shirali et al. [58]. In that study, a rectangular main channel with a relative curvature of R/B = 4.7 was used. The intake was positioned at a 120° angle along the outer arc of the bend, with an intake alignment angle of 70°. Eight submerged vanes were installed in the main channel, arranged in two longitudinal rows of four, positioned opposite the intake (Fig. 1). The main channel inflow rate was 20 L/s, with a water depth of 12 cm and a Froude number of 0.26. The intake flow rate was measured at 4.27 L/s.

To validate the simulation results and mesh quality, the output from the SSIIM software (after reaching convergence) was compared with the experimental results of Shirali et al. [58]. Upon identifying discrepancies attributed to the mesh resolution, the mesh was refin ed, and the simulations were rerun. The optimal mesh was selected when the results from two consecutive simulations showed minimal variation, indicating mesh independence. The percentage error was calculated using the following formula:

$$\frac{|Predicted\ Sediment - Measured\ Sediment|}{Measured\ Sediment} \times 100 = \%\ ERROR \quad (8)$$

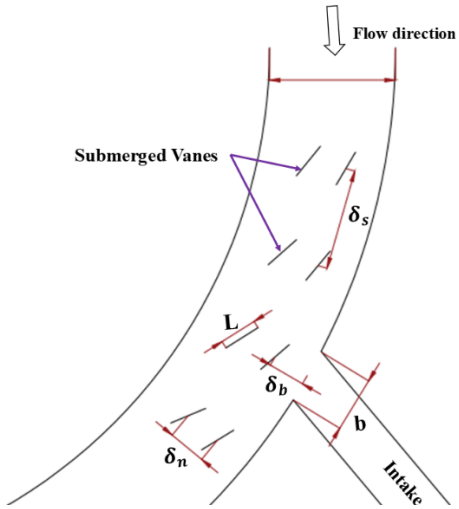


Figure 1. Position of submerged vanes in the channel

Parameter variations

In line with the stated objectives, this study investigated variations in five key parameters: vane height, vane length, longitudinal spacing between vanes, transverse spacing between vanes, and the distance of the first row of vanes from the water intake. The variation ranges for these parameters were selected based on the recommendations from Odgaard [59] and are summarized in Table 1.

In this table, H represents the height of

Table 1. Recommended and used range for parameters [59, 39]

Parameter	Recommended range	The range used
$H(cm)$	$0.2 \leq {}^{H}/_{y} \leq 0.4$	$0.5 \leq {}^{H}/_{y} \leq 0.2$
$L(cm)$	3H	$2H \leq L \leq 3H$
$\delta_s(cm)$	$10H \leq \delta_s \leq 30H$	$4H \leq \delta_s \leq 12H$
$\delta_n(cm)$	3H	$2H \leq \delta_n \leq 3H$
$\delta_b(cm)$	3H	3H

the submerged vanes, L is the length of the vanes, δ_s refers to the longitudinal spacing between vanes, $\delta_n$is the transverse spacing, and δ_b indicates the distance of the vanes from the intake. Throughout these parameter variations, the angle between the flow direction and the vanes, along with key hydraulic parameters such as flow depth and discharge, were kept constant.

The following steps were taken in this study:

a) *Vane Height Optimization:* In the first step, the height of the submerged vanes was varied between 3 and 6 cm to evaluate its effect on sediment inflow to the intake. The sediment discharge values obtained from SSIIM simulations were used as input to the PSO algorithm. The PSO algorithm, implemented in MATLAB, was then used to determine the optimal vane height.

b) *Vane Length Optimization:* After determining the optimal height, the vane length was varied between 12 and 18 cm (corresponding to 2 to 3 times the vane height). Sediment discharge results from SSIIM were again used as input to the MATLAB-based PSO algorithm to identify the optimal vane length.

c) *Spacing Optimization:* In the third step, spacing parameters were investigated. The transverse spacing between vanes was varied from 2 to 3 times the vane height (12–18 cm), longitudinal spacing from 4 to 12 times the vane height (24–72 cm), and the distance from the first vane row to the intake from 2 to 3 times the vane height (12–18 cm). Sixteen different scenarios were simulated to identify the optimal combination of spacing parameters.

3. Results and Discussion

3.1. Optimal mesh and sediment diversion efficiency to the side channel

To ensure simulations are accurate and reliable, the optimal mesh size was first determined. Meshes were categorized into five different classes regarding their grid dimensions (i×j): 5.4×2cm, 4.1×1.5cm, 3.5×1.25cm, 2.7×1cm, and 1.3×0.5cm. It is noteworthy that *i* values (5.4, 4.1, 3.5, 2.7, and 1.3 cm) correspond to the grid spacing along the flow direction, while the *j* values (2, 1.5, 1.25, 1, and 0.5 cm) show the spacing across the channel width. Among these configurations, Scenario 4—with a mesh dimension of 2.7×1cm, and sediment simulation error of less than 1%—was identified as optimal. Simulations were performed under flow conditions consisting of a 20 L/s discharge in the main channel, a 4.27 L/s intake flow rate, and a Froude number of 0.26.

The primary goal of the SSIIM simulations was to estimate both the sediment transport rate and the amount of sediment entering the intake. The optimal mesh was selected by comparing the SSIIM results for each mesh configuration against experimental data reported by Shirali et al. [58]. These comparative results are presented in Table 2. In this table, $\mathbf{Q_{SM}}$ denotes the sediment flow rate at the end of the main channel, while $\mathbf{Q_{SI}}$ refers to the sediment flow rate entering the water intake.

As can be seen, mesh refinement does not necessarily lead to optimal results. The reason for this can be stated as follows: One of the main limitations of the SSIIM software—and a significant challenge in mesh generation—is the restriction on the number of computational cells. Specifically, the grid dimensions in the *i* and *j* directions must not exceed 300 × 300 cells. Additionally, the number of cells in the *j* direction must remain constant along the entire channel length. During simulation, when the mesh is refined, especially near submerged vanes, the lack of compatibility

Table 2. Dimensions of meshing, review, and comparison of laboratory results with SSIIM software

No.	Cell Dimensions		Number of cells	$Q_{SM}+Q_{SI}$(gr/s)	Error %
	Longitude direction(cm)	Transverse direction(cm)			
1	5.4	2	60750	4189.52	5.81
2	4.1	1.5	66440	4265.95	4.09
3	3.5	1.25	72290	4344.13	2.33
4	2.7	1	78300	4423.43	0.55
5	1.3	0.5	117720	4896	10.09

between adjacent cells can lead to convergence problems, large numerical errors, or even cause the simulation to fail entirely. This limitation was evident in the simulation results: as the mesh resolution was increased from 1 cm to 0.5 cm, the network error (or result divergence) rose sharply.

3.2 Optimal values of parameters

According to the ranges provided in previous research, parameter values were considered for each parameter at each stage, and by keeping other parameters constant, a simulation was performed using SSIIM software. Thus, a total of 29 scenarios were defined and simulated (Table 3). Based on the proposed range parameters in previous studies, values were assigned to each parameter, and simulations were performed while keeping the others constant. In general, a total of 29 simulation scenarios were defined and executed (Table 3).

Table 3: Range of submerged vane heights investigated

Scenario	$H(cm)$	$L(cm)$	$\delta_n(cm)$	$\delta_s(cm)$	$\delta_b(cm)$	$Q_{SI}(\%)$
1	3	18	18	48	18	31.36
2	3.5	18	18	48	18	30.69
3	4	18	18	48	18	29.78
4	4.5	18	18	48	18	29.26
5	5	18	18	48	18	28.91
6	5.5	18	18	48	18	28.43
7	6	18	18	48	18	27.40
8	6	12	18	48	18	29.05
9	6	13.2	18	48	18	30.26
10	6	14.4	18	48	18	26.97
11	6	15.6	18	48	18	25.64
12	6	16.8	18	48	18	29.06
13	6	18	18	48	18	27.4
14	6	15	12	48	18	25.69
15	6	15	13.2	48	18	25.46
16	6	15	14.4	48	18	25.78
17	6	15	15.6	48	18	26.18
18	6	15	16.8	48	18	26.61
19	6	15	18	48	18	26.84
20	6	15	13	24	18	25.15
21	6	15	13	36	18	21.46
22	6	15	13	48	18	25.77

Scenario	$H(cm)$	$L(cm)$	$\delta_n(cm)$	$\delta_s(cm)$	$\delta_b(cm)$	$Q_{SI}(\%)$
23	6	15	13	60	18	23.13
24	6	15	13	72	18	23.93
25	6	15	13	30	12	14.8
26	6	15	13	30	13.2	16.31
27	6	15	13	30	14.4	17.53
28	6	15	13	30	15.6	19.57
29	6	15	13	30	16.8	20.38

The water depth in all simulations was fixed at 12 cm, and according to the inequality proposed by Odgaard [59], the height of the submerged vanes was set within the range of 3 to 6 cm (Scenarios 1–7). Considering the optimal depth value, Vane length values were evaluated between 12 and 18 cm (Scenarios 8–13). Similarly, with the optimal depth and length of vanes and according to Odgaard's suggestion, the vanes' transverse spacing was varied from 12 to 18 cm (Scenarios 14–19). Using the optimal values for vane height, length, and transverse spacing and regarding the recommendations of Odgaard [59] and Ouyang [39], longitudinal vane spacing was varied between 24 and 72 cm (Scenarios 20–24). Finally, considering the optimal four parameters mentioned, the distance from the intake to the first row of vanes was selected in the range of 12 to 18 cm (Scenarios 25–29), also in accordance with Odgaard's inequality.

The objective function of all simulations was to minimize the percentage of sediment entering the water intake. After each simulation, the percentage of sediment entering the intake was calculated as a proportion of the total transported sediment and recorded in Table 3. Results from the seven scenarios for vane height changes illustrated that increasing the height from 3 to 6 cm reduced sediment entering the intake from 31.36% to 27.40%—a 3.96% decrease. Both the SSIIM simulation and the PSO algorithm results identified a vane height of 6 cm as optimal, which was then used in subsequent simulations. Simulation results of decreasing vane lengths exhibited oscillatory behavior in performance. A minimum percentage of sediment entering the intake was observed at 15.6 cm in SSIIM simulations, while the PSO algorithm recommended a length of 15 cm as optimal length. This value was used for the next stages.

Increasing the transverse spacing from 12 to 13.2 cm caused a decreasing trend for the sediment entering the intake. However, beyond 13.2 cm, further increases of distance led to a decrease in vane effectiveness, with sediment entering the intake increasing to 26.84% at 18 cm. Thus, the lowest sediment entering the intake occurred at 13.2 cm, by 25.66%, while the PSO algorithm revealed an optimal spacing of 13 cm, which was selected for further analysis. Changes in the longitudinal space of vanes demonstrated an oscillatory pattern in sediment intake. Based on SSIIM results, the minimum sediment entering (21.46%) occurred at a longitudinal space of 36 cm, but the PSO algorithm recommended 30 cm as the optimal longitudinal distance. The different distances between the intake and the first vane row were also investigated. Results showed that as this distance increased from 12 to 18 cm, vane effectiveness decreased, and sediment intake increased from 14.8% to 21.98%. The PSO algorithm proposed 12 cm as the optimal distance.

3.3 Velocity Contours

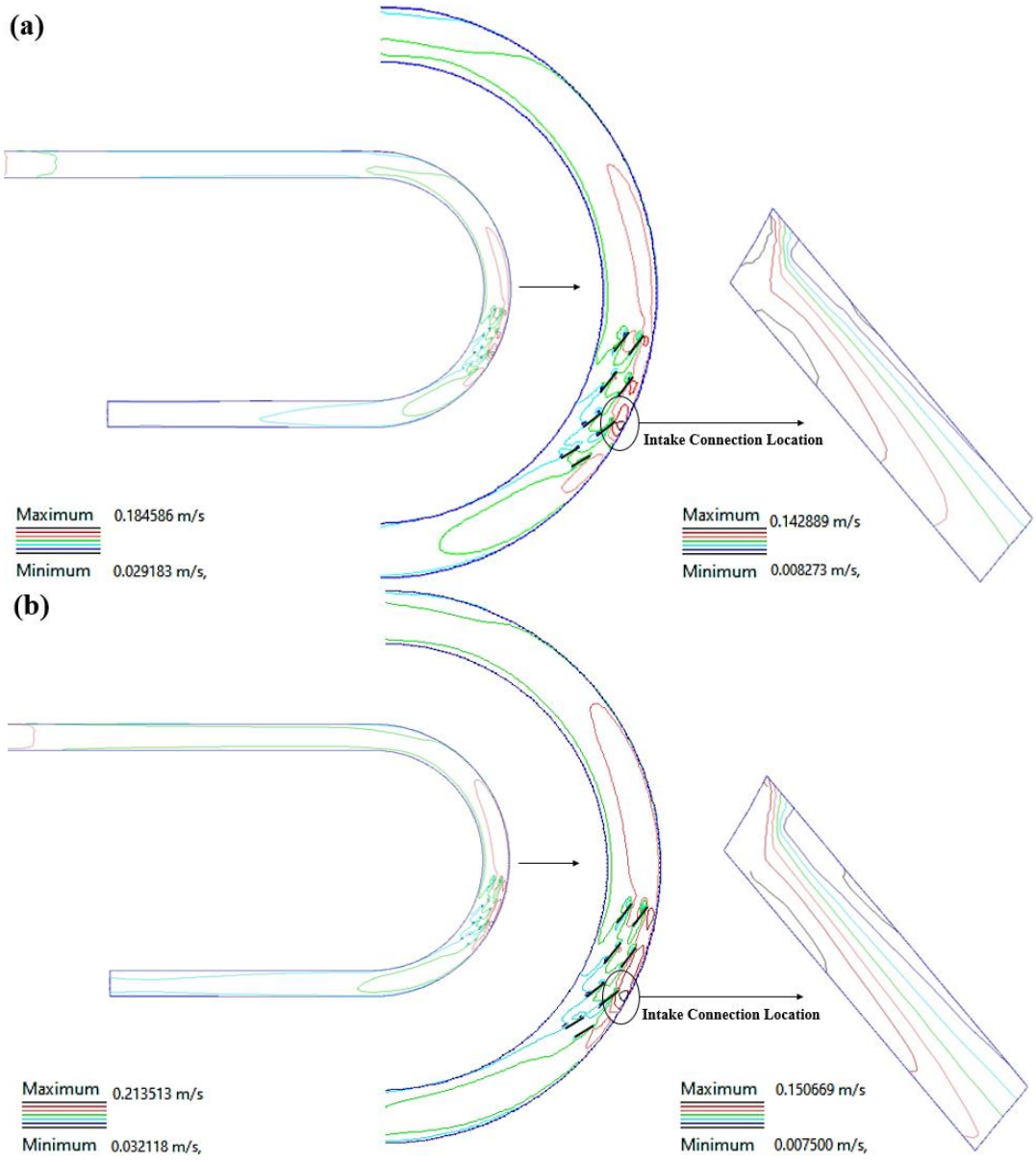
After determining the optimal values for the five parameters, in this stage, the horizontal and vertical velocity contour lines associated with each parameter were investigated. Due to the high similarity among the contour-line plots and the large

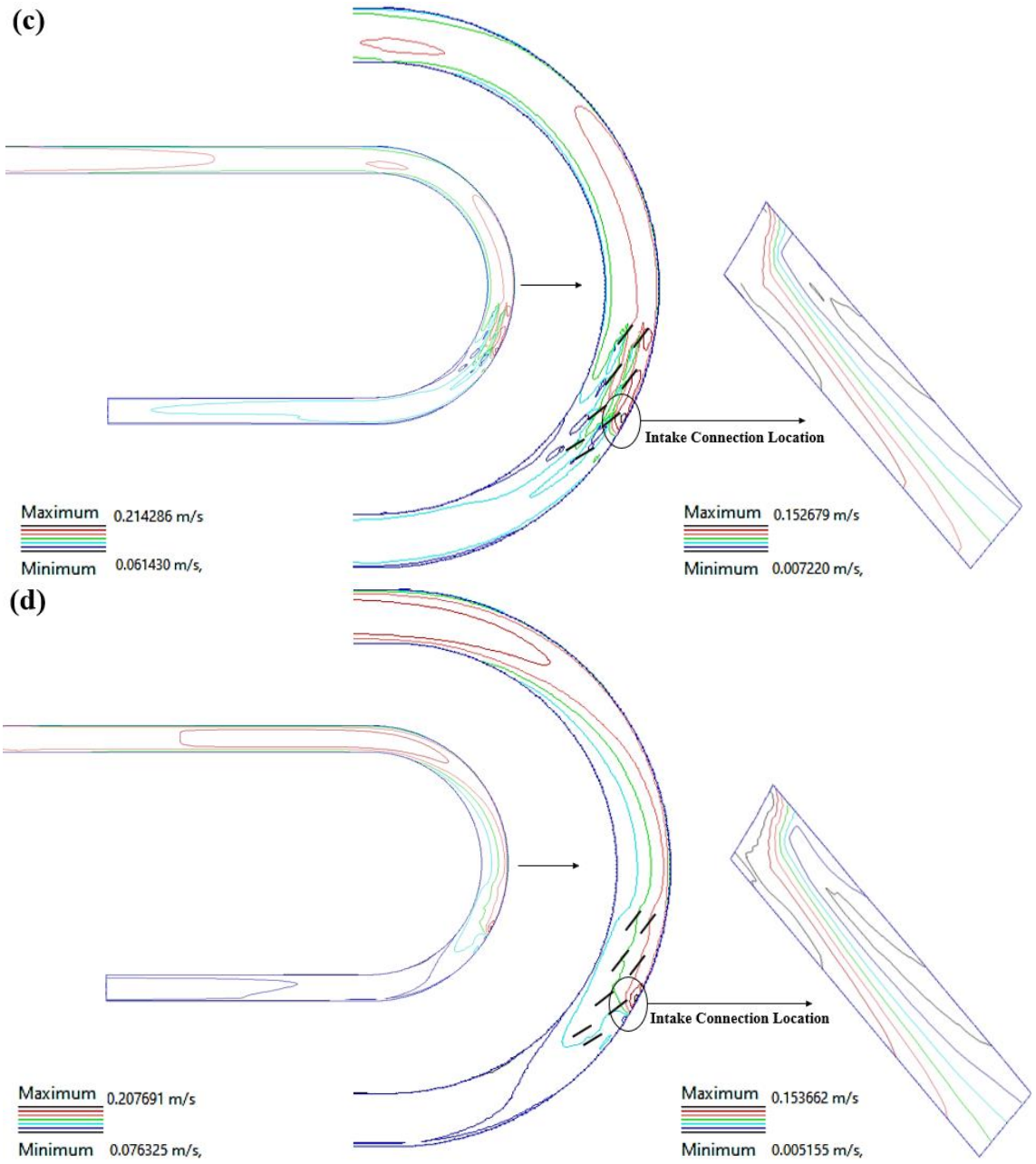
number of diagrams, only the contour lines related to the optimal vane height are presented in the main text. The other contour-line plots for the remaining scenarios are included in the appendix, while their explanations are provided in the main text. It should be noted that consistent depth levels were used across all stages of the analysis.

3.3.1 Vane Optimal Height

Figures 2 and 3 represent the streamwise and vertical velocity contour-line plots at five depth levels for a vane height of 6 cm. The mentioned levels include: (a) bed, (b) h/y = 0.3, (c) h/y = 0.6, (d) h/y = 0.8, and (e) h/y = 0.975, where *h* represents the vertical distance from the bed to the specified level.

The velocity variations displayed that by moving flow from the bed towards the water surface, the highest velocity gradients occur in the adjacent of submerged vanes and also the intake. As shown in Figure 2c, the flow above the submerged vanes remains influenced by the vane structures yet, and high stream wise velocity gradients are observed.




(c)
Intake Connection Location
Maximum 0.214286 m/s
Minimum 0.061430 m/s,
Maximum 0.152679 m/s
Minimum 0.007220 m/s,
(d)
Intake Connection Location
Maximum 0.207691 m/s
Minimum 0.076325 m/s,
Maximum 0.153662 m/s
Minimum 0.005155 m/s,

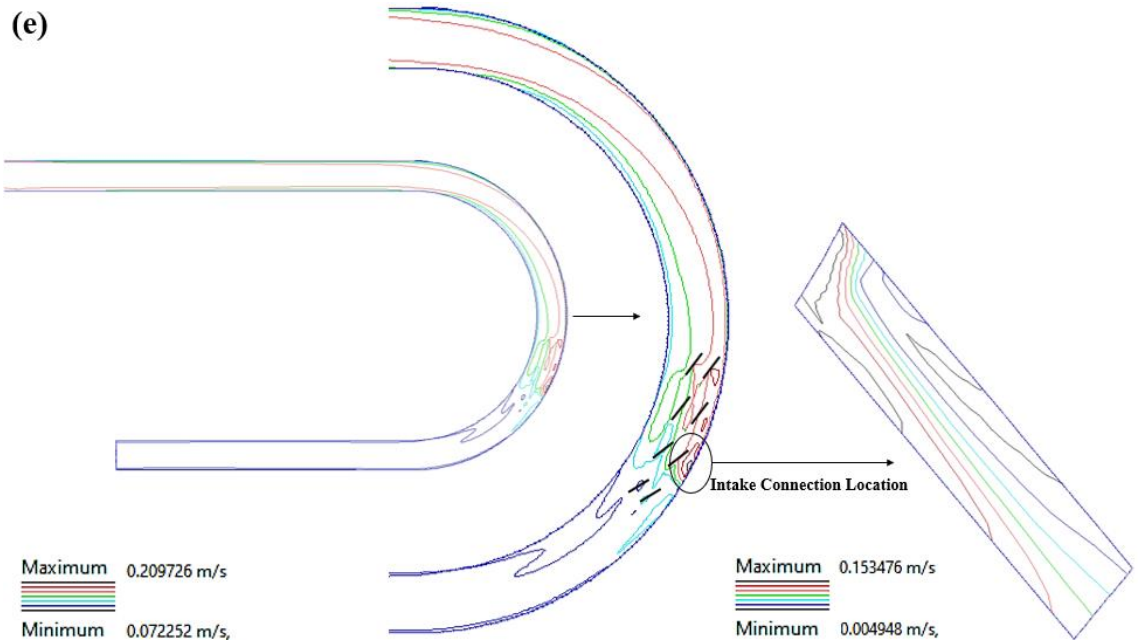


Figure 2. Stream-wise velocities in main channel and intake (Vane Height is 6cm) a) h/y=0, b) h/y=0.3, c) h/y=0.6, d) h/y=0.8, e) h/y=0.975

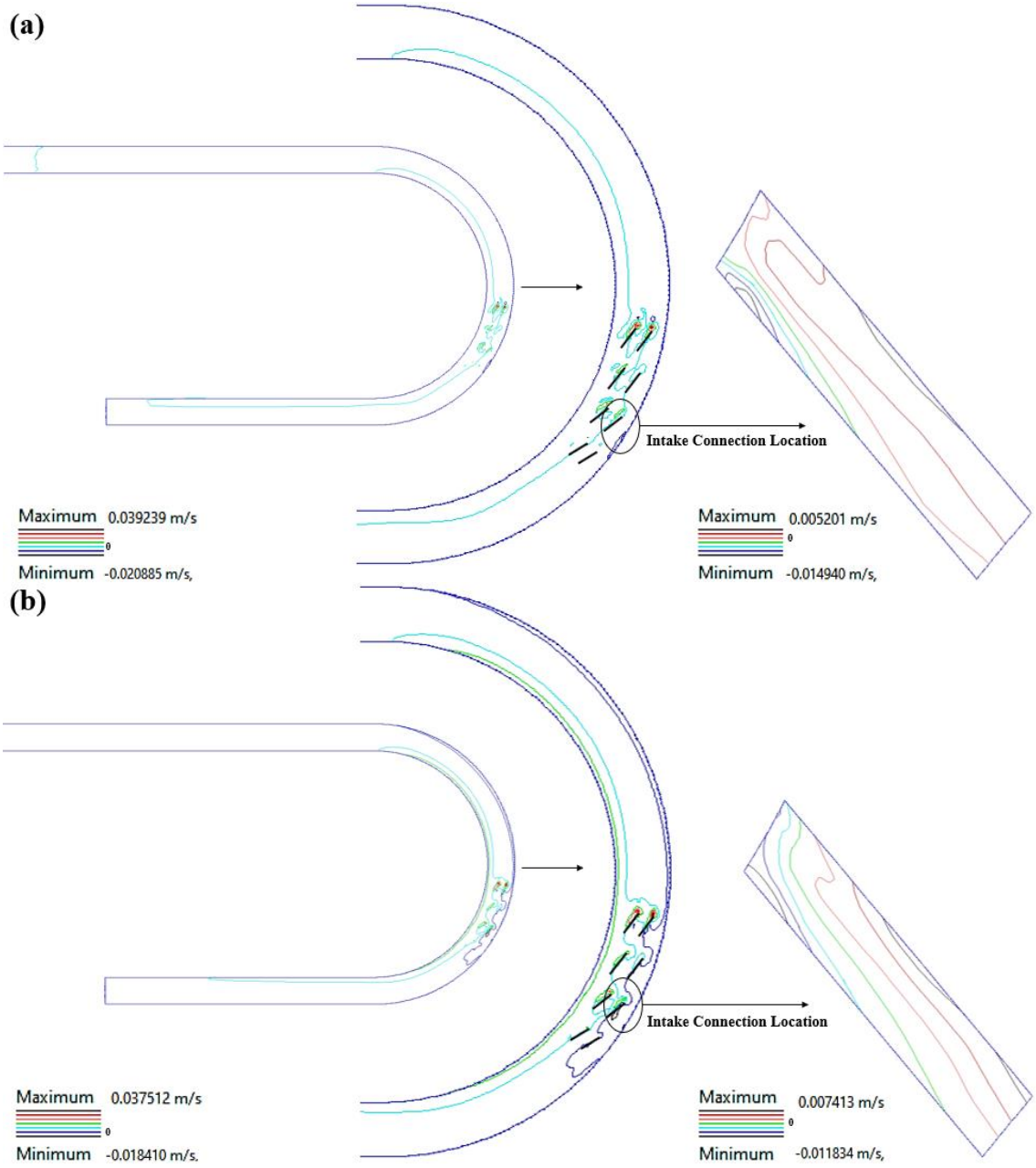
A comparison of streamwise velocities at five levels in the main channel, as shown in Figure 2, revealed that the minimum velocities occurred on the side opposite the vane-induced (inner wall bend). These velocities increased from the bed toward the water surface, likely due to the presence of the submerged vanes and the effect of bed friction.

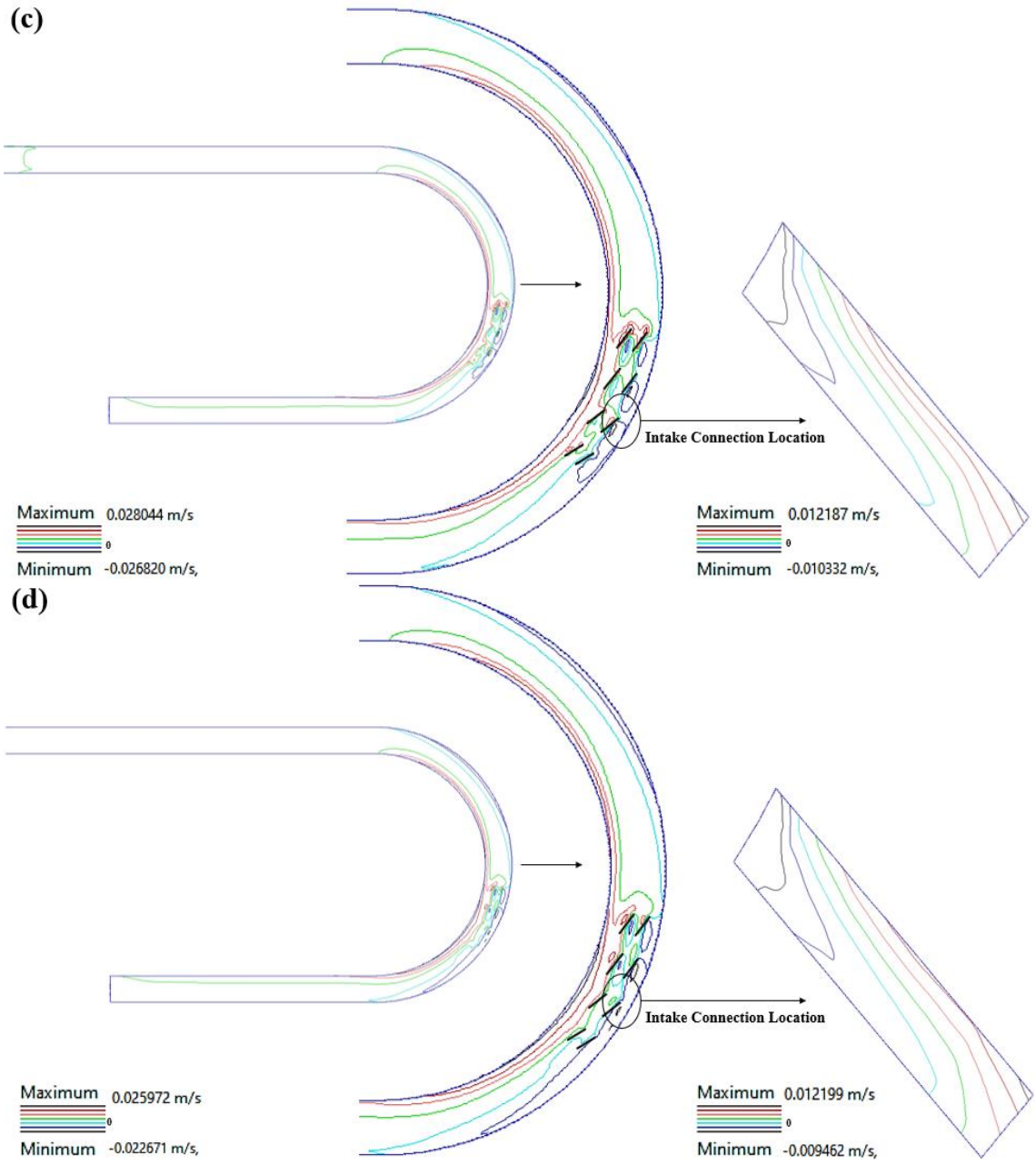
Analysis of maximum streamwise velocities at different levels showed an initial increase from the bed up to $h/y = 0.8$, then decreased toward the water surface. The highest streamwise velocities were observed near the outer bend of the main channel, just downstream of the first row of four paired submerged vanes and in front of the intake. However, the minimum velocities occurred near the inner bend of the main channel, after the end of the intake.

Notably, near-bed maximum velocity cores tended toward the outer bend and intake, while at upper levels, these cores became more dispersed. From the beginning of the channel bend, the trend of increasing velocity with depth was evident; the minimum streamwise velocity decreased, and the maximum streamwise velocity increased.

Within the intake as flow entering the water intake, streamwise velocity patterns showed that, as the flow moved from the bed to the surface, minimum velocities decreased while maximum velocities increased. The highest velocities were recorded at the intake entrance and along the right wall, whereas the lowest velocities occurred along the left wall of the intake.

As shown in Figure 3a, the maximum vertical velocity cores occurred near the first pair of vanes, with the higher values occurring near the vanes. Moving away from this region—both laterally and longitudinally—the vertical velocities decrease.


(a)
Intake Connection Location
Maximum 0.039239 m/s
0
Minimum -0.020885 m/s,
Maximum 0.005201 m/s
0
Minimum -0.014940 m/s,
(b)
Intake Connection Location
Maximum 0.037512 m/s
0
Minimum -0.018410 m/s.
Maximum 0.007413 m/s
0
Minimum -0.011834 m/s,


(c)
Intake Connection Location
Maximum 0.028044 m/s
0
Minimum -0.026820 m/s,
Maximum 0.012187 m/s
0
Minimum -0.010332 m/s,
(d)
Intake Connection Location
Maximum 0.025972 m/s
0
Minimum -0.022671 m/s,
Maximum 0.012199 m/s
0
Minimum -0.009462 m/s,

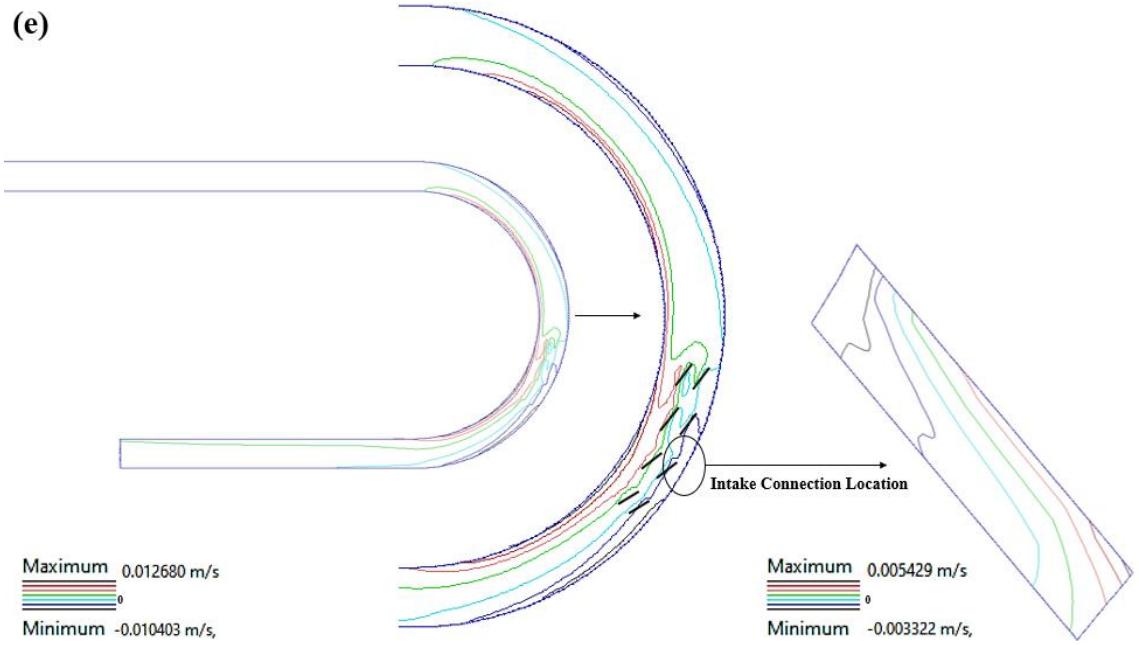


Figure 3. Vertical velocities in main channel and intake (Vane Height is 6cm) a) h/y=0, b) h/y=0.3, c) h/y=0.6, d) h/y=0.8, e) h/y=0.975

After the flow passed the first pair of vanes, the vertical velocity contour lines around the other vane pairs showed lower velocities compared to those near the initial vanes. At higher levels above the bed, the maximum vertical velocity cores shifted toward the inner bend, even though they initially occurred near the first vane pair. Notably, at the last measured depth (Figure 3e), the maximum velocity core moved toward the inner bend, and the influence of the vanes became negligible.

As seen in Figures 3a and 3b, negative vertical velocities occurred near the initial pair of vanes and extended widely across the channel width. In contrast, above the submerged vanes (Figures 3c and 3d), negative velocity cores appeared near the outer bend, particularly in the vicinity of the first row of vanes. This pattern indicates the presence of localized pressure gradients and vertical flow directed toward the bed, resembling scour-inducing conditions observed around bridge foundations [60]. Closer to the water surface, although negative vertical velocities were still observed near the outer bend, their cover extent diminished, and the velocity contours also became more parallel. This observation indicates a decreased influence of the submerged vanes. The variation in minimum vertical velocity from the bed of the main channel to the water surface showed an oscillatory trend. In such a way that initially, the absolute value of the vertical velocity decreased up to h/y = 0.3, then increased at h/y = 0.6, and finally decreased again as it approached the water surface. The highest concentration and gradient of velocity contour lines were observed at the same level of h/y = 0.6.

Maximum positive vertical velocities were detected near the first pair of vanes and at the inner bend of the channel, indicating an upward flow direction toward the water surface in these regions.

Negative vertical velocities were observed at the intake inlet, with their absolute values decreasing as the flow moved away from the bed. At all levels, velocity contours representing negative values extended across much of the intake area, shifting toward the right wall. The maximum positive vertical velocities increased with increasing levels from the bed up to h/y = 0.8, after which they decreased as the flow neared the water surface. The overall maximum absolute

vertical velocity in the main channel occurred near the bed, where negative velocity values indicated a downward flow.

3.3.2 Vane optimal length

For the optimal vane length, considerable stream-wise velocity gradients were observed near the submerged vanes and at the intake inlet (Figure App.1 in the appendix). Moving away from the bed, the concentration of average velocity cores formed around the submerged vanes, indicating their continued influence on the flow field. Even beyond the footprint of the vanes, their impact persisted, as evidenced by the presence of distinct velocity cores above them. However, this influence diminished at h/y = 0.975, where the velocity contours became nearly parallel and the lower velocity values were observed near the inner bend.

It is also noteworthy that the concentration of maximum velocity cores consistently tended toward the outer bend wall. As the flow approached the water surface, these cores extended toward the upstream section of the bend, indicating a wider dispersion of high-velocity regions in the upper flow layers.

Additionally, a comparison across different levels revealed that, as the distance from the bed increased, the minimum stream-wise velocity in the main channel also increased, while it decreased within the intake. The lowest stream-wise velocities were observed along the inner bend of the main channel and near the left wall of the intake. In contrast, the highest stream-wise velocities in the main channel occurred along the outer bend, just downstream of the first pair of submerged vanes. Within the intake, the maximum velocities originated near the left corner of the inlet and extended toward the central axis and right wall. Furthermore, the results indicated that reducing the vane length from 18 cm to 15 cm led to a general decrease in stream-wise velocity in both the main channel—particularly in the region influenced by the submerged vanes—and the intake.

Analysis of the vertical velocity contours illustrates that near the bed, maximum vertical velocity cores formed around the submerged vanes and extended toward the inner bend (Figure App.2 in the appendix). From the bed up to y/h = 0.6, strong velocity cores remained visible around the first pair of vanes, while velocities around the subsequent vane pairs gradually decreased. lose to the bed, the minimum vertical velocities—characterized by negative values—were concentrated near the outer bend and in a small area behind the first pair of vanes. Moving away from the bed to y/h = 0.3, the extent of negative velocity regions expanded, still concentrated near the outer bend and behind the first pair of vanes. At this level, the negative vertical velocities covered a larger section of the main channel width, including areas behind all the vane rows and near the outer bend, indicating a notable downward flow up to the vane height. Beyond the height of the submerged vanes, the influence of the vanes diminished, and the negative velocity cores became smaller, primarily near the outer bend and downstream of the vanes. As the flow passed the lateral intake and exited from the bend, the vertical velocity contours became more uniform and parallel, with maximum positive velocities observed near the inner bend and minimum (negative) velocities persisting near the outer bend.

A comparison of the vertical velocity contours within the intake at different levels revealed that, near the bed, maximum vertical velocities originated from the left corner of the intake inlet and aligned parallel to the intake wall as the flow progressed. The maximum positive vertical velocities were concentrated near the left wall, while the lowest (negative) velocities were observed along the right wall. Moving away from the bed, the contours representing minimum velocities originating from the left corner and extending diagonally toward the far-right corner of the intake. As the vane length decreased from 18 cm to 15.6 cm, negative vertical

velocities continued to appear in the regions influenced by the submerged vanes, near the outer bend of the main channel, and at the intake inlet. In the main channel, the variation in absolute negative vertical velocities from the bed to the water surface exhibited an oscillatory pattern, whereas in the intake, this trend showed a consistent decrease. Similarly, the maximum vertical velocity in the main channel followed an oscillatory trend with depth, mirroring the behavior of the absolute minimum values. In contrast, within the intake, the maximum vertical velocity increased up to y/h = 0.6 and then decreased as the flow approached the water surface.

3.3.3 Vane optimal transverse distance

Stream-wise velocities in different levels revealed that the maximum velocities occurred near the outer bend, with the highest concentrations found close to the bed, particularly around the submerged vanes and the intake (Fig. App.3 in the appendix). As the flow approached the water surface, these high-velocity regions expanded and extended upstream toward the beginning of the bend. In contrast, the minimum velocities were observed along the inner bend wall, gradually shifting toward the water surface and extending downstream after passing the intake, eventually covering the entire width of the main channel. The velocity contours indicated that the maximum velocity core was concentrated around the first pair of submerged vanes, on the side opposite the flow direction. As the flow continued past the subsequent vane pairs, the streamwise velocities decreased. Moving upward from the bed, the velocities around and downstream of the vanes declined, showing strong velocity gradients. Further along the channel, stream-wise velocities continued to decrease, and the velocity contours tended toward the inner bend. Near the water surface, the velocity gradients became weaker, and at the highest depth level, the velocity cores associated with the submerged vanes and intake disappeared—indicating the diminishing effect of the submerged vanes. The results also indicated that the highest stream-wise velocities within the intake, near the bed, originated from the left corner of the intake and developed parallel to the intake wall as the flow progressed. Maximum vertical velocities were observed along the right wall of the intake, while minimum velocities occurred near the left wall. This pattern persisted with increasing height from the bed, where the minimum velocities consistently appeared near the left wall and the maximum velocities near the right wall.

Overall, it can be concluded that decreasing the transverse spacing between the submerged vanes led to a reduction of the maximum streamwise velocity. Furthermore, the results revealed that the highest stream-wise velocities occurred not only at the outer bend of the main channel and the intake inlet but also in the region between the first two pairs of vanes facing the flow. In the main channel, both minimum and maximum velocities generally increased with height. However, while the maximum stream-wise velocity increased up to the level of y/h = 0.8, it declined beyond this point toward the water surface. In contrast, the minimum velocity continued to increase throughout the vertical profile. Analysis of the vertical velocity contour lines revealed that the maximum vertical velocity cores formed near the bed around the second pair of submerged vanes facing the flow. As the distance from the vanes increased, vertical velocities progressively decreased (Fig. App.4 in the appendix). However, as the distance from the bed increased, velocity gradients intensified. Minimum velocity cores developed on the left side of the vanes, while maximum velocity cores formed on the right, extending toward the outer and inner bend walls, respectively. Notably, even in regions without submerged vanes, their influence persisted, as evidenced by the continued presence of velocity cores. At y/h = 0.975, although prominent velocity gradients remained

around the submerged vanes and the intake, the velocity cores appeared more localized. In this layer, the maximum vertical velocities tended toward the inner bend wall, while the minimum velocities moved toward the outer bend wall. Within the intake, the vertical velocity gradients consistently decreased from the bed to the water surface, with maximum velocities observed near the left wall and minimum velocities concentrated near the right wall.

Overall, the results indicated that positive vertical velocities near the bed and around the submerged vanes were higher than at other depth levels within the main channel. The minimum vertical velocities, which were negative, were observed at various levels—near the bed at the downstream end of the submerged vane region, and near the water surface beyond the zone influenced by the vanes. In the intake, the maximum vertical velocity occurred near the left wall at a depth corresponding to y/h = 0.6, which is approximately above the height of the submerged vanes. In contrast, the minimum vertical velocities—also negative—were present across the entire width of the intake at all evaluated levels. As the flow progressed, these negative velocity regions expanded laterally toward the right wall of the intake. Near the bed, the area covered by negative velocities was relatively limited, but this area increased with elevation, occupying a larger portion of the flow field at higher levels.

3.3.4 Vane optimal longitude distance

Compared to the previous sections, the results for the optimal longitudinal spacing of the vanes show that reduced spacing led to greater concentration and density of stream-wise velocity contours. The maximum velocity cores were observed near the outer bend wall, within the region influenced by the submerged vanes and the intake (Fig. App.5 in the appendix). Around the submerged vanes, velocities decreased, and as the flow moved toward the inner bend wall, a continued reduction in velocity was observed. With increasing distance from the bed, the maximum velocity cores expanded upstream, toward the entrance of the bend and the approaching straight channel. Up to y/h = 0.8, the presence of significant velocity gradients indicated that the influence of the submerged vanes remained pronounced. However, by y/h = 0.975, this effect had nearly dissipated, and the velocity contours became nearly parallel, reflecting a diminished impact of the vanes. At the intake inlet, the maximum stream-wise velocities covered the entire width of the intake, with the highest velocity contours gradually tending toward the right wall. As the flow progressed along the intake, the minimum velocity contours appeared near the left wall and persisted to the end of the intake—this pattern was consistent across all levels. In the main channel, the minimum stream-wise velocity showed an increasing trend from the bed toward the water surface. In contrast, in the intake, an oscillatory pattern is exhibited in its minimum velocity distribution with depth. Similarly, the maximum stream-wise velocity in the main channel followed an oscillatory trend with increasing depth, whereas in the intake, it increased steadily as the flow approached the water surface.

The results indicated that for the vane's optimal longitudinal spacing, the maximum vertical velocity cores formed around the vanes from near the bed up to the top of the vane height, particularly near the vanes located adjacent to the inner bend wall (Fig. App.6 in the appendix). Moving laterally away from the vanes toward the outer bend wall, vertical velocities gradually decreased. Similarly, near the bed, velocities also declined when moving toward the inner bend wall. However, at the depth of y/h = *0.3*, the region of maximum vertical velocities expanded toward the inner bend. In this region, the area occupied by negative vertical velocities also widened, covering a larger portion of the main channel width. As the distance from the bed increased, the velocity cores continued to reflect the influence of the submerged vanes, although the vertical velocity gradients became

weaker closer to the water surface. At the upper three depth levels, the maximum velocity cores tended toward the inner bend wall, while the minimum (negative) velocity cores were concentrated near the outer bend wall. A comparison of vertical velocity contours at different depth levels revealed that, at the intake inlet, the minimum vertical velocities initially covered the entire width of the intake. As the flow progressed, these low-velocity regions expanded and occupied a larger portion of the flow field. Conversely, the maximum vertical velocities were concentrated near the left wall of the intake and gradually extended toward its downstream end. In the main channel, both the maximum vertical velocity and the absolute minimum vertical velocity (the latter being negative) displayed oscillatory trends with increasing depth. In contrast, the absolute minimum vertical velocity within the intake decreased consistently from the bed to the water surface. Meanwhile, the maximum vertical velocity in the intake also exhibited an oscillatory pattern, similar to that observed in the main channel.

3.3.5 Optimal distance of the first row from the intake

As previously noted, the maximum stream-wise velocity contours were concentrated near the outer bend wall (Fig. App.7 in the appendix). The results further indicated that these maximum velocities extended not only along the outer bend but also into the region between the submerged vanes. In contrast, lower velocities were observed around the vanes. As the flow progressed, low-velocity cores developed around the vanes and gradually tended toward the inner bend wall. With increasing distance from the bed, the general trend remained: maximum velocities were concentrated near the outer bend wall, while minimum velocities were directed toward the inner bend wall. However, the stream-wise velocity gradients decreased with height.

At the intake inlet, the highest stream-wise velocities initially occupied the entire width of the intake but progressively tended toward the right wall as the flow moved downstream. Meanwhile, the minimum stream-wise velocities were observed near the left wall, farther from the intake entrance. A comparison of the maximum velocities at various distances from the bed in the main channel revealed an increasing trend up to $y/h = 0.6$, followed by a gradual decrease toward the water surface. This decrease occurred with significantly smaller gradients compared to the lower levels. In contrast, the minimum velocity decreased up to $y/h = 0.3$ and then increased toward the water surface. In the intake, the maximum stream-wise velocity consistently increased with height. However, the minimum velocities showed an oscillatory pattern—initially decreasing, then increasing, and finally decreasing again as the flow approached the water surface.

The analysis of vertical velocity contour lines showed that the maximum vertical velocity cores were concentrated around the submerged vanes at the three levels closest to the bed. As the distance from the bed increased, the velocity gradients around the vanes decreased (Fig. App.8 in the appendix). Closer to the water surface, with decreasing velocity gradients in the region influenced by the submerged vanes, the area occupied by the maximum velocities expanded laterally and tended toward the inner bend wall, consistent with observations from previous sections. The minimum velocity contours were consistently located near the outer bend wall at all examined levels. At the intake inlet, the minimum velocities covered the entire width of the intake at all levels. As the distance from the bed increased, these minimum velocities occupied a larger portion of the intake cross-section and tended toward the right wall. Conversely, the maximum velocities consistently appeared farther downstream from the intake inlet, near the left wall, and extended toward the end of the intake. The negative values of the minimum vertical velocities in both the main channel and the intake indicate the presence of downward flow. In

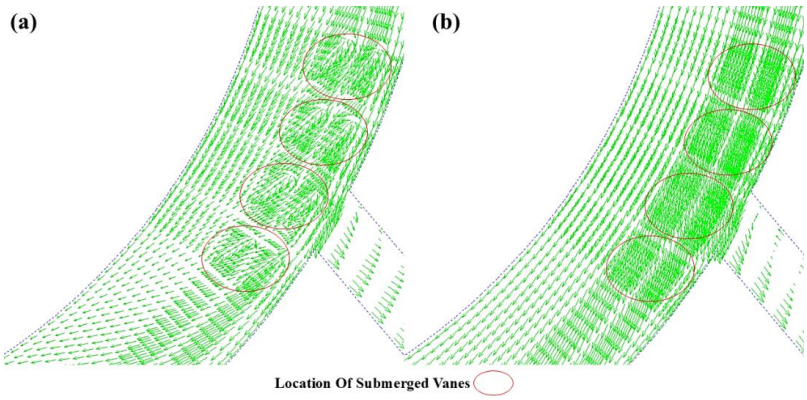


Figure 4. Streamlines at (a) the bed and (b) the water surface.

the main channel, these negative velocities were concentrated near the outer bend and, at levels y/h = 0.3 and 0.6, covered a significant portion of the channel width. However, closer to the water surface, the extent of the area affected by negative velocities decreased. At the intake inlet, all vertical velocities were negative. As the flow progressed, negative velocity contours tended toward the right wall, while positive velocities developed near the left wall. The analysis also revealed that with increasing distance from the bed, a larger portion of the intake became dominated by negative vertical velocities. In the main channel, the absolute minimum vertical velocity increased with height up to y/h = 0.8, beyond which it began to decrease toward the water surface. Similarly, in the intake, the absolute minimum vertical velocity increased up to y/h = 0.6, followed by a gradual decrease near the surface. Notably, the trends in maximum vertical velocity differed between the intake and the main channel. In the intake, the maximum vertical velocity increased with height up to y/h = 0.8 and then decreased toward the water surface. In contrast, the maximum vertical velocity in the main channel exhibited an oscillatory pattern throughout the flow depth.

3.4 Vorticity and Secondary Flow

When the water flows in a channel with the aspect ratio of less than 5, or when the flow path is curved—causing centrifugal forces to become dominant—secondary flows are typically intensified. Additionally, the presence of submerged vanes on the bed of the main channel further enhances these secondary and vortex flows, significantly influencing the overall flow structure [61, 62, and 63]. On the other hand, installation of submerged vanes caused modification in formed secondary flows from the outer wall to the inner wall, near the bed. This modification caused a reduction in the strength of secondary currents and reduced bank erosion [64]

Figure 4 illustrates the streamlines interacting with the submerged vanes and their deflection toward the intake at two levels: the channel bed and the water surface. As evident from the figure, the combined influence of the submerged vanes, channel bend, and intake generates strong eddy currents.

Given the significance of the vortices formed within the flow, vorticity contour lines are presented in Figure 5 to quantitatively illustrate this flow parameter. In the figure, the direction of flow is oriented downward.

In Figure 5, the stream-wise vorticity is defined as:

$$Vor = \frac{\partial w}{\partial r} - \frac{\partial u}{\partial z} \tag{8}$$

The channel with a 180° bend is shown for the simulation run.

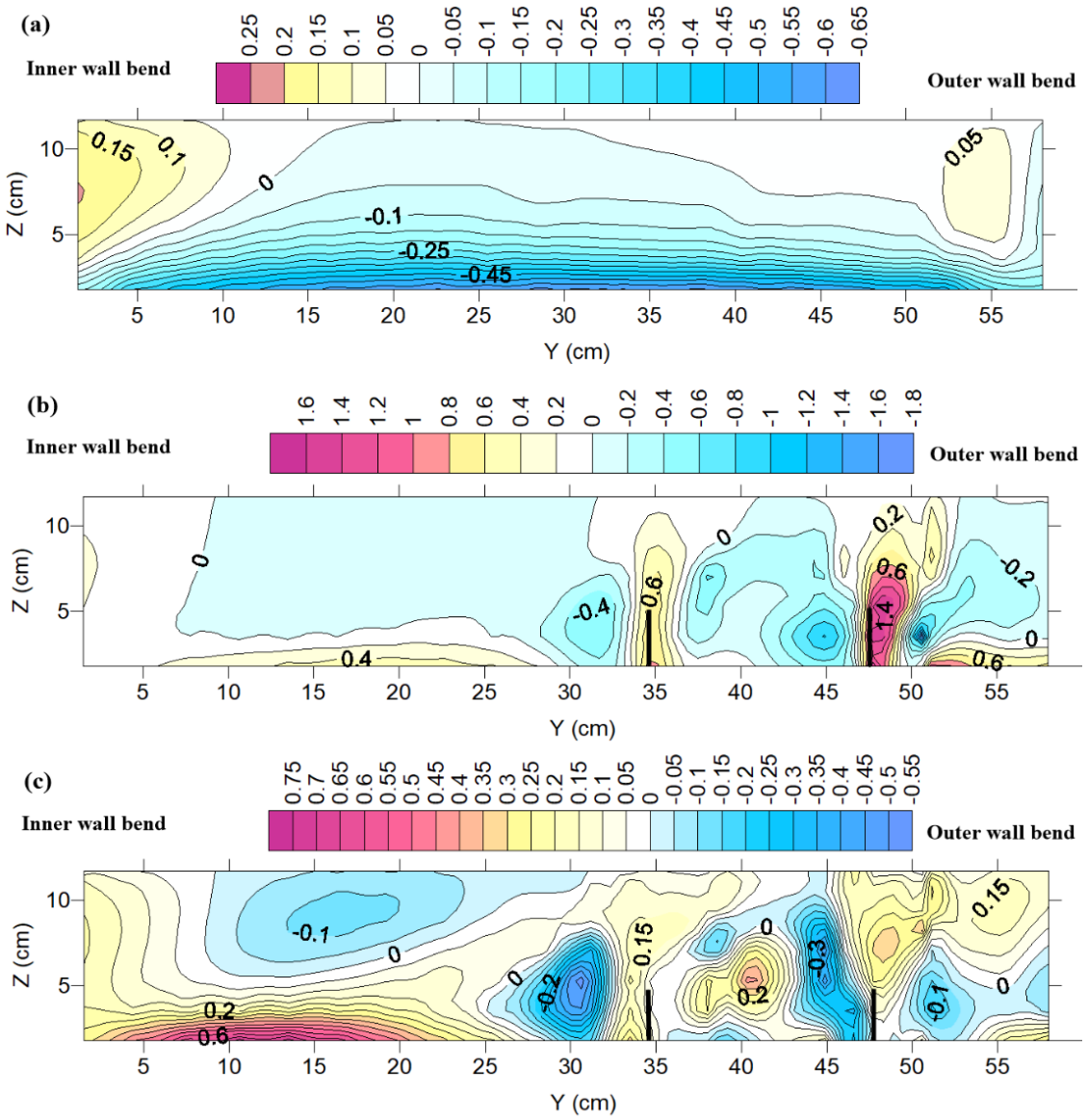


Figure 5. Vorticity in three cross-sections a) in the middle of the curvature of the bend, b) in front of the water intake, and c) after the water intake in line with the last pair of submerged vanes

Vorticity contour lines were analyzed at three cross-sections: in the middle of the bend, in front of the water intake, and downstream of the intake near the last pair of submerged vanes. As shown in Figure 5a, in the middle of the 180-degree bend, two positive vorticity cores appear near the inner and outer walls. Vorticity values decrease toward the center of the main channel width. The presence of negative vorticity in the middle of the channel and near the bed suggests stronger longitudinal velocity gradients compared to vertical velocity gradients. The contour lines are mostly parallel, with steeper gradients observed near the channel bed.

In contrast, the vorticity distribution at the cross-section aligned with the midpoint of the intake reveals a different pattern due to the influence of the submerged vanes (Fig. 5 b). In this figure, the submerged vanes are represented by two bold black vertical lines. Positive vorticity cores are clearly concentrated around the vanes, with the highest vorticity occurring near the vane closest to the intake. Since turbulence

intensity is derived from velocity fluctuations, and vorticity also arises from changes and fluctuations in velocity; it discussed that there is a relationship between turbulence intensity and vorticity and turbulence intensity increased near the intake inlet. This indicates strong vertical velocity gradients and intensified secondary flow in the vicinity of the vanes as showed in Figure 3a previously. Elsewhere in the flow field, negative vorticity dominates, suggesting that longitudinal velocity gradients exceed vertical gradients. Additionally, positive vorticity values are observed near the bed and are inclined toward the inner bend.

As previously noted, the final cross-section was selected downstream of the intake, aligned with the midpoint of the last pair of submerged vanes (Fig. 5c). The contour lines in this section indicate that the maximum vorticity occurred near the bed and tended toward the inner wall of the bend. In addition, positive vorticity values were present in the region between the two vanes and in the upper flow layers above the vane closest to the intake, reaching toward the outer bend wall. Negative vorticity cores appeared on the right side of both vanes (moving in the direction of the flow), reflecting the dominance of longitudinal velocity gradients over vertical ones in those regions. Observation of Figures 5b and 5c clearly highlights the role of the presence of the water intake. The presence of the intake induced strong secondary flows and concentrated positive vorticity near the bed in the cross-section aligned with the center of the intake. However, downstream of the intake, these intensified flow patterns shifted upward, with strong currents observed closer to the water surface.

From another perspective, spiral flows induced by centrifugal forces in a curved channel are another clear manifestation of secondary flow development [65]. The strength of these secondary flows can be quantified using the following equation:

$$V_s = V_i - V_{i-1} \quad (9)$$

Where V_i is the transverse velocity component at the upper layer of the water column, and V_{i-1} is the transverse velocity component at the adjacent lower layer. The index i corresponds to the vertical discretization levels used in the depth-wise mesh. Figure 6 illustrates the variations in the dimensionless secondary flow strength (Vs/V), where V is the average transverse velocity component in the main channel, across three different cross-sections.

As shown in Figure 6, at the first cross-section—located in the middle of the bend—the secondary flow strength was greatest near the bed and gradually decreased with depth, reaching a minimum value of -0.05 at the water surface.

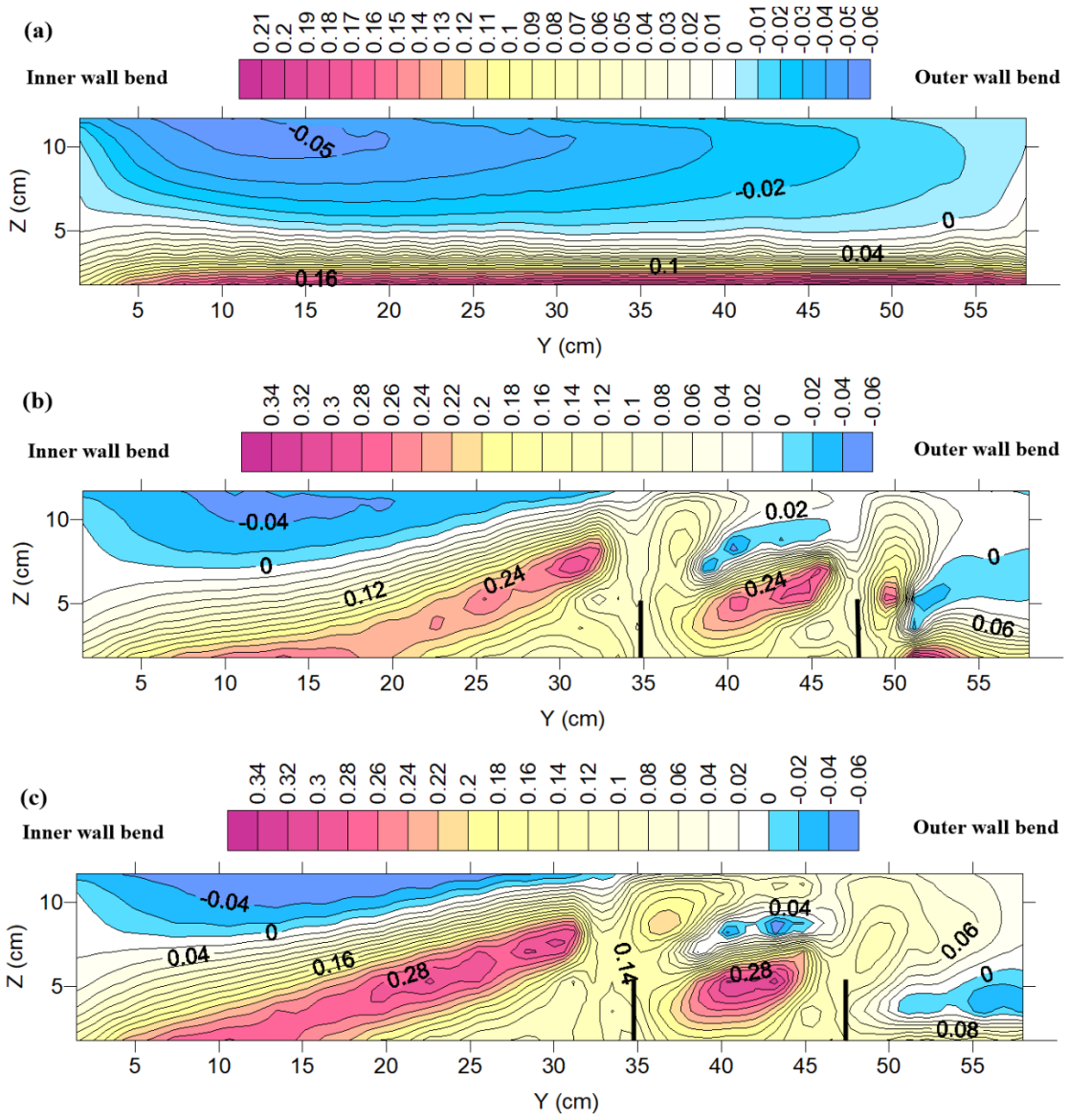


Figure 6. dimensionless strength of the secondary flow for three cross-sections a) in the middle of the curvature of the bend, b) in front of the water intake, and c) after the water intake in line with the last pair of submerged vanes

Additionally, a comparison of secondary flow strength between the inner and outer walls of the bend reveals that, although the difference was small, the strength was slightly higher along the outer wall. In the second cross-section, located opposite the midpoint of the intake, the presence of submerged vanes and the intake itself significantly influenced the formation of secondary flow strength contours. In this section, the cores of maximum secondary flow strength were observed on the right side of the submerged vanes (assuming flow direction is used as the reference). The results also indicated that the positive secondary flow strength values above both vanes extended all the way to the water surface. Unlike the previous section, no negative values of secondary flow strength were present at the surface. Furthermore, the maximum strength of secondary flow in this cross-section was greater than that in the previous one. At the intake inlet, the highest secondary flow strength occurred

near the bed, with positive values observed both near the bed and at the water surface, while negative values appeared in the mid-depth region. This distribution clearly reflects the presence of vortex and spiral flow structures. In the third cross-section—located downstream of the intake within the main channel—the pattern of secondary flow strength, including its minimum and maximum magnitudes around and above the submerged vanes toward the water surface, was generally similar to that observed in the second section. However, at the intake inlet, although the overall pattern remained consistent with the second section, the maximum value of the secondary flow strength was decreased, and the core of negative flow strength values was positioned closer to the channel bed.

4. Conclusion:

This study investigated the flow structure of sediment-water in an experimental channel with a 180-degree bend and a lateral intake positioned at a 120-degree angle. To reduce sediment entry into the lateral intake, two rows of submerged vanes (each consisting of four vanes) were installed at a 45-degree angle relative to the main channel flow direction. The optimal computational mesh size was evaluated to be 2.7 × 1 units in the flow and channel width directions, respectively, yielding a sediment transport estimation error of only 0.55%. Results indicated that the optimal vane height and length were 6 cm and 15 cm, respectively—corresponding to 0.5 times the flow depth and 2.5 times the vane height. Furthermore, the optimal transverse and longitudinal spacings between the vanes were 2.17 and 5 times the vane height, while the distance from the closest vane row to the intake was twice the vane height.

A comparison of this study's results with previous research reveals that Ouyang [32] identified the optimal vane height as ranging from 0.58 to 0.7 times the flow depth. The present study's result (H/y = 0.5) are in complete agreement with the presented range, but remains closely aligned with values reported by Odgaard and Wang [27]. Conversely, Tan et al. [31] reported a smaller optimal height range of 0.125 to 0.33 times the flow depth, which differs significantly from the findings of this study. Additionally, Tan et al. [31] investigated vane length and found the optimal range to be 2.5 to 10 times the flow depth, whereas the current study determined a ratio of 1.25. A key factor contributing to the discrepancy may be that Tan et al. [31] accounted for bed form development in their analysis, which can significantly influence flow structure, depth, and sediment transport.

Although international studies have not extensively investigated the effects of varying the longitudinal and transverse spacing between submerged vanes, or their distance from the intake, local research provides some insights. Davoudi and Shafai [66] found that the optimal longitudinal spacing between vanes was eight times the vane height. Similarly, Montasseri et al. [67] reported that the optimal distance from the first row of vanes to the outer wall of the bend was two times the vane height, while the optimal transverse spacing between vanes was 1.5 times the vane height.

Kalathil et al. [51] reported that the use of collars and submerged vanes reduced sediment ingress into lateral channels by 46.82% and 85.36% at vane angles of 15° and 40°, respectively. Moradinejad et al. [7] demonstrated that combining skimming walls with spur dikes enhanced sediment reduction efficiency at intakes, achieving up to 81% effectiveness. Farshidnia et al. [3] found that optimizing the length and height of parallel skimming walls significantly improved sediment control at lateral intakes, with sediment reduction efficiencies reaching up to 74%. Fahmy et al. [68] employed baffle columns as an alternative to avoided walls, achieving a 71% reduction in accumulated sediment within the intake. Ezz-Aldeen et al. [69] investigated sedimentation at a pumping station in the Mosul Dam reservoir through simulations. Their results showed that using a combination of dykes and strategic

placement reduced sediment deposition within the intake and pumping station by 42%. Despite variations in the experimental conditions across different studies, the reported reductions in sediment inflow to intake using different countermeasure structures were generally consistent with the findings of the present study. Here, by optimizing key design parameters, sediment inflow to the intake was reduced by up to 63%.

Analysis of the flow structure across all scenarios with optimal parameters revealed that near the bed, the cores of maximum stream-wise velocity were directed toward the outer bend and the intake. As the flow approached the water surface, these high-velocity cores expanded and became evident from the onset of the bend. The minimum vertical velocities (negative values) were concentrated at the intake inlet and decreased with increasing distance from the bed. At all depth levels within the intake, negative velocity streamlines covered a significant portion of the intake cross-section and tended toward the right wall. The findings also indicated that the highest stream-wise velocities in the intake occurred near the right wall, whereas the maximum vertical velocities were concentrated near the left wall. Reducing the vane length from 18 cm to 15 cm led to a decrease in stream-wise velocity both in the main channel—particularly in regions influenced by the submerged vanes—and within the intake. A reduction in the transverse spacing between vanes also resulted in lower maximum streamwise velocities. Karami et al. [34] demonstrated that increasing the longitudinal spacing between consecutive submerged vanes leads to greater velocity gradients—a finding corroborated by the results of the present study. Additionally, while reducing the distance between the submerged vanes and the intake had minimal impact on the velocity distribution at higher elevations above the bed, it generally contributed to a reduction in streamwise velocity throughout the flow field.

This study also examined the presence and intensity of secondary currents. In the absence of submerged vanes, the maximum secondary current strength was concentrated near the bed and extended across the entire width of the main channel. However, the introduction of submerged vanes altered the distribution pattern of secondary current strength. With the vanes in place, the cores of maximum secondary current strength shifted to the left side of the vanes, and the region exhibiting negative current strength near the intake showed a noticeable reduction in surface area. This research's findings provide engineers and designers with valuable guidance for the effective implementation of submerged vanes, enabling a substantial reduction in sediment ingress. This improvement not only lowers operational and maintenance costs but also contributes meaningfully to the sustainable management of water resources. The findings of this research, when combined with economic considerations and analyses, can open new avenues for future studies in river engineering. By identifying the optimal dimensions and installation spacing of submerged vanes, these results can support more effective implementation in river management and planning projects.

Statements and Declarations

Data availability

All data are available on request.

Funding

This research received no external funding.

Conflict of interest

The authors declare that they have no conflict of interest.

Artificial intelligence (AI) usage

During the preparation of this work, the author(s) used [ChatGPT] in order to improve text writing. After using this tool/service, the authors reviewed and edited the content as needed and take full responsibility for the content of the publication.

Author contributions

All authors contributed to the study conception and design. Conceptualization: [Author 2, Author 3]; Methodology:

[Author 1]; Formal analysis and investigation: [Author 1, Author 2, Author 3]; Writing - original draft preparation: [Author 2]; Writing - review and editing: [Author 2, Author 1]; Resources: [Author 2, Author 1]; Supervision: [Author 2]

References

1. Fatehi-Nobarian B, Farshidnia S, Saneie M. Effect of hydraulic and geometrical parameters of skimming wall on controlling sediment entering lateral intakes using harmony search algorithm. Advance Researches in Civil Engineering. 2022 Dec 1;4(4):55-70.
2. Moradinejad A, Haghiabi A, Saneie M, Yonesi HA. Investigation of the effect of sediment control structures on the kinetic energy of turbulent in the intake entrance. Irrigation and Drainage Structures Engineering Research. 2021 Apr 21;22(82):121-46.
3. Farshidnia S, Saneie M, Hajikandi H, Rostami M. Experimental investigation of impact of length and height of parallel skimming walls on controlling inlet sediment to lateral intake. Water Supply. 2020 May 1;20(3):997-1005.
4. Farshidnia S, Saneie M, Hajikandi H, Rostami M. Experimental Study on the Placement of the Angle and the Distance of Parallel Skimming Walls to Reduce Inlet Sediment in a Lateral Intake. Slovak Journal of Civil Engineering. 2020;28(2):23-9.
5. Pandey M, Valyrakis M, Qi M, Sharma A, Lodhi AS. Experimental assessment and prediction of temporal scour depth around a spur dike. International Journal of Sediment Research. 2021 Feb 1;36(1):17-28.
6. Zamani M, Rabiefar H, Rostami M. Experimental evaluation of spur dikes placement position effect on the hydraulic and erosion conditions of intakes. Water supply. 2020 May 1;20(3):900-8.
7. Moradinejad A, Saneie M, Ghaderi A, Zamanieh Shahri SM. Experimental study of flow pattern and sediment behavior near the intake structures using the spur dike and skimming wall. Applied Water Science. 2019 Nov;9(8):1-1.
8. Pandey M, Ahmad Z, Sharma PK. Scour around impermeable spur dikes: a review. ISH journal of hydraulic engineering. 2018 Jan 2;24(1):25-44.
9. Firmansyah R, Jauzi MZ, Istiyanto DC, Subarkah A, Sujoko SU, Wibowo M, Yuniardi RC. Study on the design and implementation of BPPT-lock armored groin for sediment control structure in front of sea water intake. Zona Laut Jurnal Inovasi Sains Dan Teknologi Kelautan. 2023 Nov 9:240-7.
10. Fahmy WA, Halawa MA, Hekal NT. Reduction of sedimentation and water turbidity at intakes of drinking water treatment plants. Water Science. 2023 Dec 31;37(1):40-56.
11. Attia K, Elsaid G. The hydraulic performance of oriented spur dike implementation in open channel. InJournal of International Water Technology Conference, IWTC, Alexandria, Egypt 2006 (No. 10, pp. 281-298).
12. Yossef MF. The effect of groynes on rivers. Literature Review. 2002 Aug 23.
13. Haider R, Qiao D, Yan J, Ning D, Pasha GA, Iqbal S. Flow characteristics around permeable spur dike with different staggered pores at varying angles. Arabian Journal for Science and Engineering. 2022 Apr;47(4):5219-36.
14. Moradinejad A, Haghiabi AH, Saneie M, Younesi H. Experimental Study on Sediment Control in a Lateral Intake Channel by Using a Spur Dike Combined with a Skimming Wall. Advances in Civil Engineering and Environmental Science. 2025 May 27;2(2):85-96.
15. Jafari R, Sui J. Velocity field and turbulence structure around spur dikes with different angles of orientation under ice covered flow conditions. Water. 2021 Jul 1;13(13):1844.
16. Veisi F, Jafari A. Three-dimensional Study of Flow Turbulence Extension around Straight, T and L Shaped Groynes in Open Channles using Physical Model. Irrigation

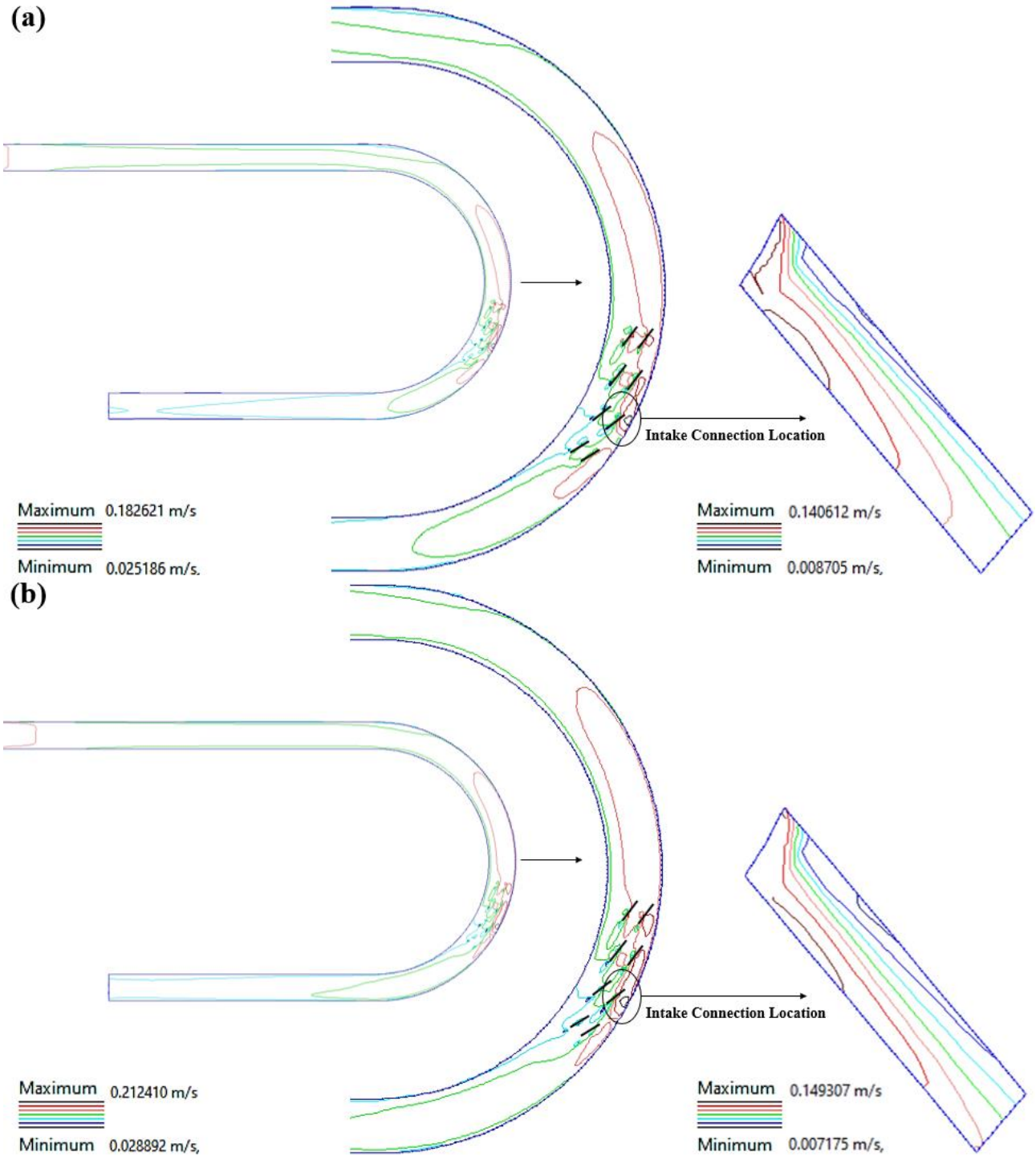
Sciences and Engineering. 2019 Jan 1;42(1):15-29.
17. Kumar L, Afzal MS. Numerical simulations of scour around vertical wall abutments with varying aspect ratios under combined waves and current flows. Journal of Marine Science and Engineering. 2023 Sep 28;11(10):1886.
18. Fathi A, Zarrati AR, Salamatian SA. Scour depth at bridge abutments protected with a guide wall. Canadian Journal of Civil Engineering. 2011 Dec;38(12):1347-54.
19. Vaghefi M, Solati S, Abdi Chooplou C. The effect of upstream T-shaped spur dike on reducing the amount of scouring around downstream bridge pier located at a 180 sharp bend. International journal of river basin management. 2021 Jul 3;19(3):307-18.
20. Hamidi M, Sadeqlu M, Khalili AM. Investigating the design and arrangement of dual submerged vanes as mitigation countermeasure of bridge pier scour depth using a numerical approach. Ocean Engineering. 2024 May 1;299:117270.
21. Dadamahalleh PA, Hamidi M, Khalili AM. Bed sill effect on bridge pier scour with debris obstruction: an experimental investigation. Innovative Infrastructure Solutions. 2024 May;9(5):142.
22. Safaripour N, Vaghefi M, Mahmoudi A. Experimental study of the effect of submergence ratio of double submerged vanes on topography alterations and temporal evaluation of the maximum scour in a 180-degree bend with a bridge pier group. International Journal of River Basin Management. 2022 Oct 2;20(4):427-41.
23. Safaripour N, Vaghefi M, Mahmoudi A. The influence of the submergence ratio of submerged vanes on the slope of the hole around the pier groups in a sharp bend. Journal of Hydraulic Structures. 2024 Apr 1;10(3):90-118.
24. Mahdian Khalili A, Akbari Dadamahalleh P, Hamidi M. Experimental evaluation of dune formation downstream of pier scour hole with upstream debris accumulation. Journal of Hydraulic Structures. 2024 Mar 1;10(1):13-28.
25. Odgaard AJ, Lee HY. Submerged vanes for flow control and bank protection in streams. Iowa City, IA, USA: Iowa Institute of Hydraulic Research, the University of Iowa; 1984 Jul.
26. Odgaard AJ, Mosconi CE. Streambank protection by submerged vanes. Journal of Hydraulic Engineering. 1987 Apr;113(4):520-36.
27. Odgaard AJ, Wang Y. Sediment management with submerged vanes. I: Theory. Journal of Hydraulic Engineering. 1991 Mar;117(3):267-.
28. Barkdoll BD, Hagen BL, Odgaard A. Sediment exclusion at hydropower intakes using submerged vanes. American Society of Civil Engineers, New York, NY (United States); 1995 Dec 31.
29. Marelius F, Sinha SK. Experimental investigation of flow past submerged vanes. Journal of Hydraulic Engineering. 1998 May;124(5):542-5.
30. Gupta UP, Sharma N, Ojha CS. Performance evaluation of tapered vane. Journal of Hydraulic Research. 2007 Jul 1;45(4):472-7.
31. Tan SK, Yu G, Lim SY, Ong MC. Flow structure and sediment motion around submerged vanes in open channel. Journal of waterway, port, coastal, and ocean engineering. 2005 May;131(3):132-6.
32. Ouyang HT. Investigation on the dimensions and shape of a submerged vane for sediment management in alluvial channels. Journal of Hydraulic Engineering. 2009 Mar;135(3):209-17.
33. Sharma H, Jain B, Ahmad Z. Optimization of submerged vane parameters. Sādhanā. 2016 Mar;41:327-36.
34. Karami H, Farzin S, Sadrabadi MT, Moazeni H. Simulation of flow pattern at rectangular lateral intake with different dike and submerged vane scenarios. Water Science and Engineering. 2017 Jul 1;10(3):246-55.
35. Biswas P, Barbhuiya AK. Countermeasure of river bend scour using a combination of submerged vanes and riprap. International Journal of Sediment Research. 2018 Dec 1;33(4):478-92.

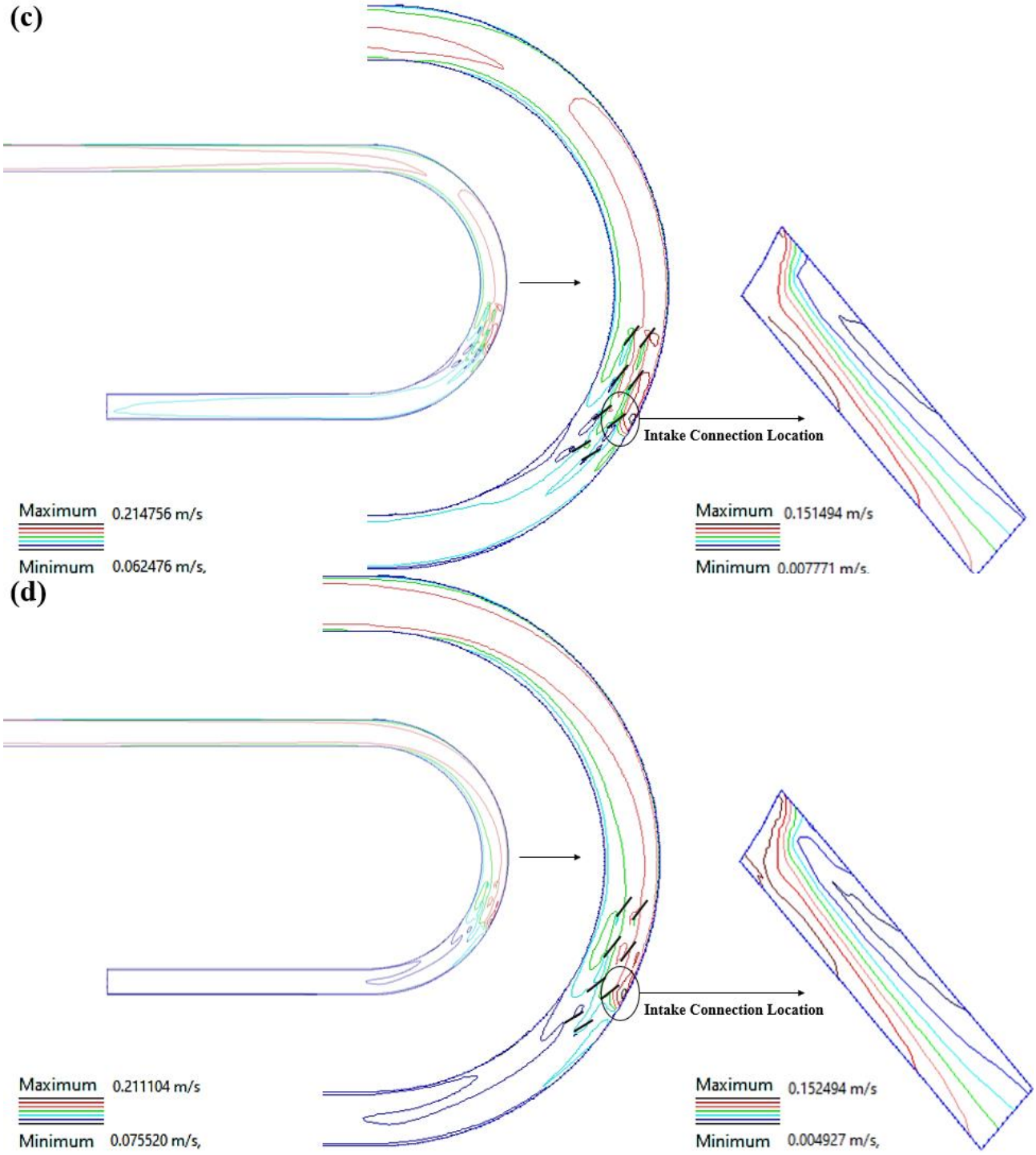
36. Nakato T, Kennedy JF, Bauerly D. Pump-station intake-shoaling control with submerged vanes. Journal of Hydraulic Engineering. 1990 Jan;116(1):119-28.
37. Raudkivi AJ. Sedimentation: exclusion and removal of sediment from diverted water. CRC Press. 1993.
38. Wang Y, Odgaard AJ, Melville BW, Jain SC. Sediment control at water intakes. Journal of Hydraulic Engineering. 1996 Jun;122(6):353-6.
39. Ouyang HT. Design optimization of submerged vane system for sediment control. The University of Iowa; 2001.
40. Ho J, Johnson A, White S. 3-D numerical simulation study of permanent sediment control submerged vanes.
41. Michell F, Ettema R, Muste M. Case study: Sediment control at water intake for large thermal-power station on a small river. Journal of Hydraulic Engineering. 2006 May;132(5):440-9.
42. Sarhadi A, Jabbari E. Investigating effect of different parameters of the submerged vanes on the lateral intake discharge located in the 180 degree bend using the numerical model. Civil Engineering Journal. 2017 Dec 10;3(11):1176-87.
43. Tseng CY, Lee J, Guala M, Musa M. Experimental Tests of Lateral Bedload Transport Induced by a Yawed Submerged Vane Array in Open-Channel Flows. Journal of Hydraulic Engineering. 2024 Nov 1;150(6):04024045.
44. Mhsen MA, Hilo AN. The effects of different lateral channel discharge on one row of submerged vanes. InAIP Conference Proceedings 2023 Dec 22 (Vol. 2977, No. 1). AIP Publishing.
45. Hilo AN. The Effects of submerged vanes inclination angle on sediment transport into sub-channel. Wasit Journal of Engineering Sciences. 2023 Apr 1;11(1):105-15.
46. Aminian P, Jorabloo M, Ahmadi A. Numerical Study of the Effects of Inlet Geometry on the Performance of the Sediment Bypass Tunnel using SSIIM Numerical Model. Journal of Hydraulic and Water Engineering. 2023 Jul 1;1(1):65-75.
47. Chauhan V, Singhal GD, Chavan R. A review of sediment deflection in rivers using submerged vanes. ISH Journal of Hydraulic Engineering. 2023 Aug 8;29(4):514-30.
48. Gumgum F, Cardoso AH. Optimizing the desilting efficiency of submerged vane fields at lateral diversions. Journal of Hydraulic Engineering. 2023 Jan 1;149(1):04022031.
49. Bor A. Experimental investigation of 90 intake flow patterns with and without submerged vanes under sediment feeding conditions. Canadian Journal of Civil Engineering. 2022;49(3):452-63.
50. Baltazar J, Alves E, Bombar G, Cardoso AH. Effect of a submerged vane-field on the flow pattern of a movable bed channel with a 90 lateral diversion. Water. 2021 Mar 18;13(6):828.
51. Kalathil ST, Murugesan MR, Chandra V. Control of sediment entry into intake canals using submerged vanes with collar. InWater Security and Sustainability: Proceedings of Down To Earth 2019 2021 (pp. 209-216). Springer Singapore.
52. Serajian MT, Kamanbedast AA, Masjedi A, Heidarnejad M, Hasonizadeh H. Laboratory evaluation of the combined effect of convergence and submerged vanes on lateral Intakes' sediment input at 90 river bends. Ain Shams Engineering Journal. 2020 Mar 1;11(1):245-52.
53. Karami Moghadam M, Keshavarz A, Sabzevari T. The Effect of Diversion Flow, Intake Inlet Shape, Topography and Bed Roughness on the Flow Separation Dimensions and Shear Stress at the Lateral Intake. Irrigation and Drainage Structures Engineering Research. 2019 Feb 20;19(73):113-26.
54. OLSEN NR. SIMULATION OF SEDIMENT MOVEMENTS IN WATER INTAKES WITH MULTIBLOCK OPTION. 5007.
55. Rijn LC. Mathematical modelling of morphological processes in the case of

suspended sediment transport. Waterloopkundig Laboratorium; 1987.
56. Harlow FH, Nakayama PI. Turbulence transport equations. The Physics of Fluids. 1967 Nov 1;10(11):2323-32.
57. Launder BE, Spalding DB. Mathematical models of turbulence, text book.
58. Shirali S, Masjedi A. Control of sediment at lateral intake with using submerged vanes in river bend. Water Resources Engineering. 2018 Aug 23;11(37):13-22.
59. Odgaard AJ. River training and sediment management with submerged vanes. American Society of Civil Engineers. 2009.
60. Baduna Koçyiğit M, Koçyiğit Ö. Experimental Investigation of Bridge Scour under Pressure Flow Conditions. Water. 2024 Sep 29;16(19):2773.
61. Neary VS, Odgaard AJ. Three-dimensional flow structure at open-channel diversions. Journal of Hydraulic Engineering. 1993 Nov;119(11):1223-30.
62. Shaheed R, Mohammadian A, Yan X. A review of numerical simulations of secondary flows in river bends. Water. 2021 Mar 24;13(7):884.
63. Brethouwer G. Turbulent flow in curved channels. Journal of Fluid Mechanics. 2022 Jan;931:A21.
64. Odgaard AJ, Kennedy JF. River-bend bank protection by submerged vanes. Journal of hydraulic engineering. 1983 Aug;109(8):1161-73.
65. Neary VS, Sotiropoulos F, Odgaard AJ. Three-dimensional numerical model of lateral-intake inflows. Journal of Hydraulic Engineering. 1999 Feb;125(2):126-40.
66. Davoodi L, Shafai Bejestan M. Application of submerged vanes for sediment control at Intakes from Irrigation trapezoidal channels. Water and Irrigation Management. 2012 Feb 20;1(2):59-71.
67. Montaseri H, Godsian M, Salehi Neyshabouri SAA. Experimental study on design parameters of submerged vanes for sediment control at lateral intake in a 180 degree bend. Modares Civil Engineering journal. 2020 20(1): 161-176 (In Persian).
68. Fahmy WA, Ali AM, El-Bahlol MN, Ibrahim MM, Samy A. Enhancing baffle columns' performance to mitigate sedimentation at intake structures. Applied Water Science. 2024 May;14(5):89.
69. Ezz-Aldeen M, Al-Ansari N, Abd-Albaki Y, Knutsson S, Laue J. Sediment control strategies for sustainable water intake. Dams and Reservoirs. 2021 Mar;31(1):21-30.

© 2025 by the authors. Licensee SCU, Ahvaz, Iran. This article is an open access article distributed under the terms and conditions of the Creative Commons Attribution 4.0 International (CC BY 4.0 license) (http://creativecommons.org/licenses/by/4.0/).

Appendix


(a)
Intake Connection Location
Maximum 0.182621 m/s
Minimum 0.025186 m/s.
Maximum 0.140612 m/s
Minimum 0.008705 m/s,
(b)
Intake Connection Location
Maximum 0.212410 m/s
Minimum 0.028892 m/s,
Maximum 0.149307 m/s
Minimum 0.007175 m/s,


(c)
Intake Connection Location
Maximum 0.214756 m/s
Minimum 0.062476 m/s,
Maximum 0.151494 m/s
Minimum 0.007771 m/s.
(d)
Intake Connection Location
Maximum 0.211104 m/s
Minimum 0.075520 m/s,
Maximum 0.152494 m/s
Minimum 0.004927 m/s,

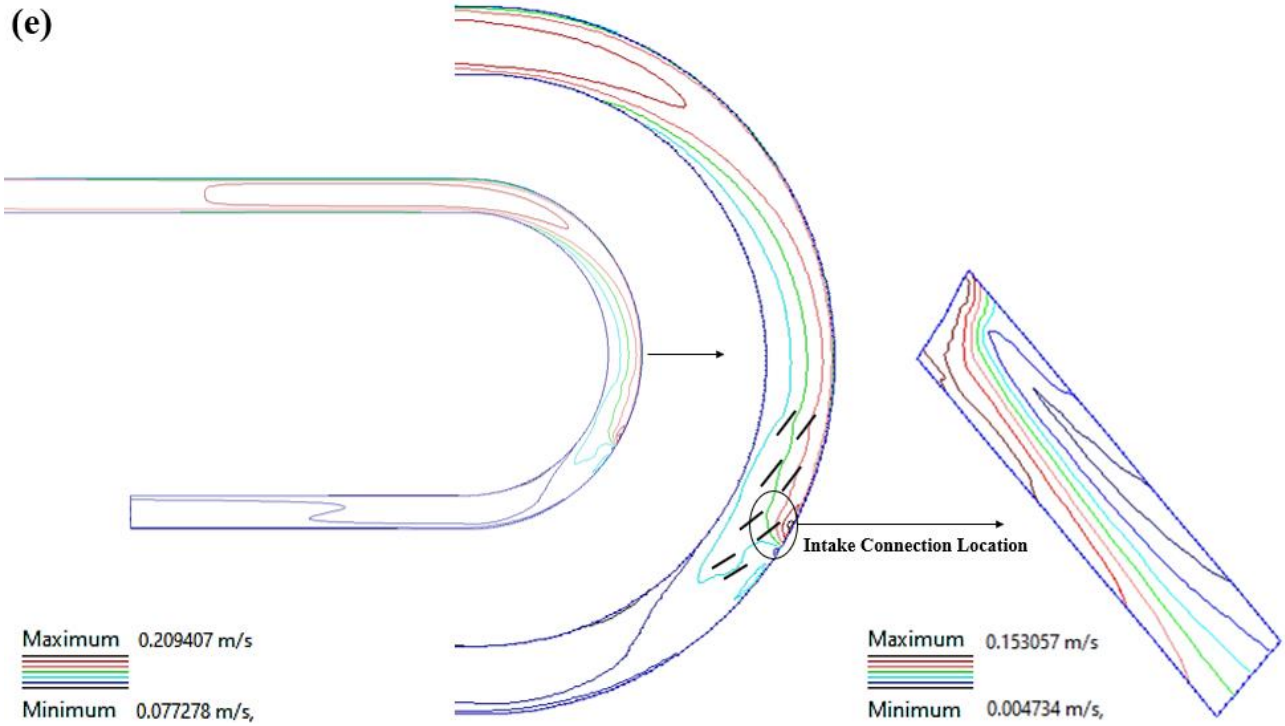
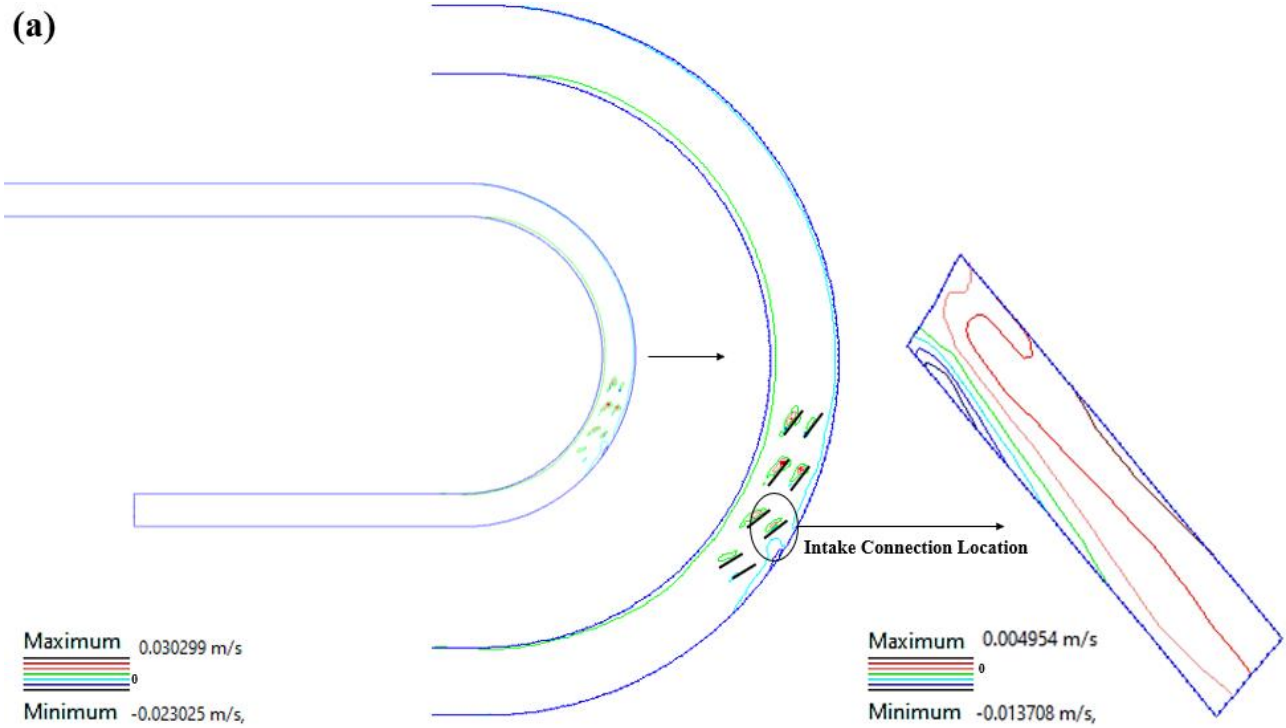
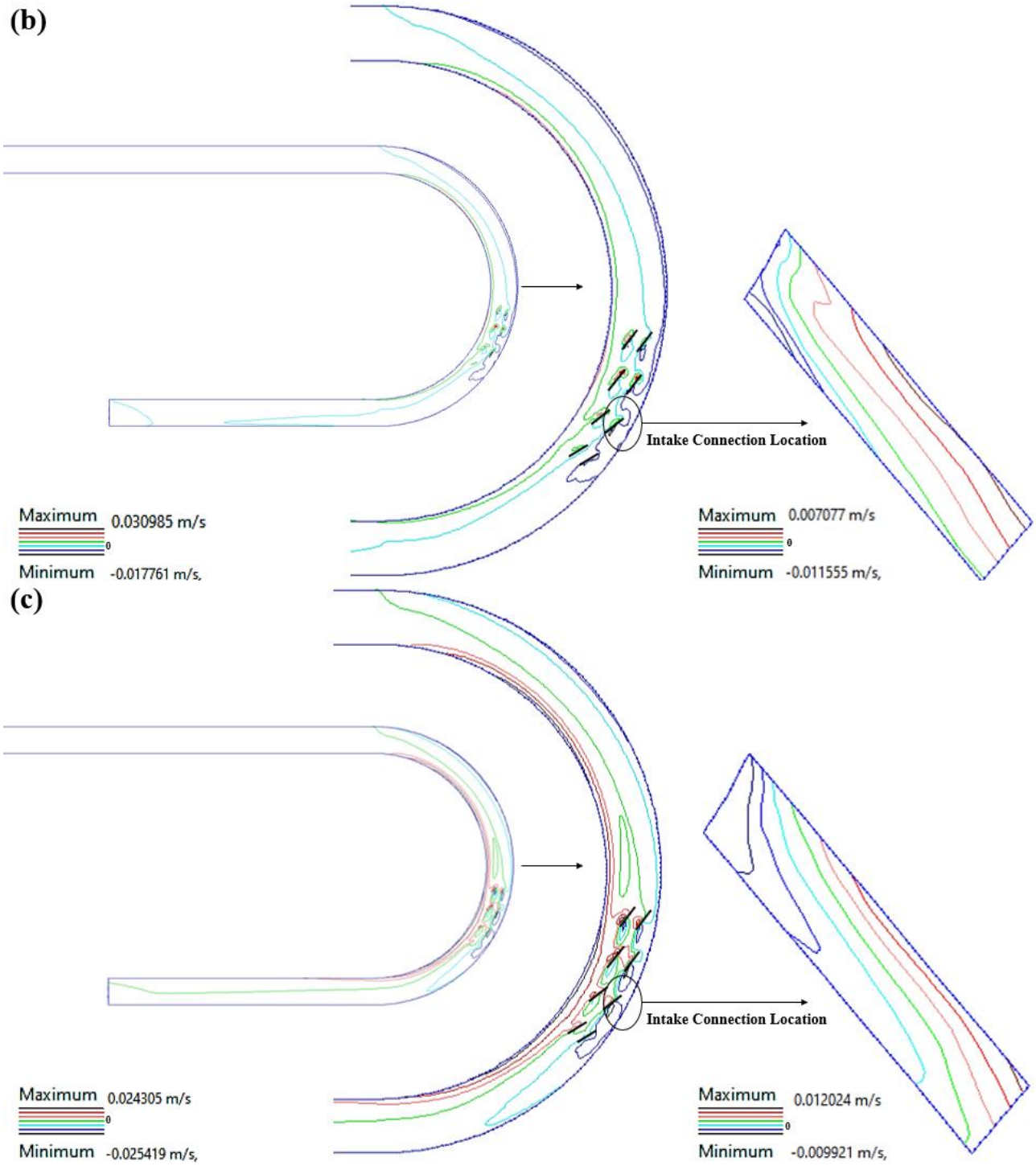


Fig. App.1 Stream-wise velocities in main channel and intake (Vane Length is 15cm) a) h/y=0, b) h/y=0.3, c) h/y=0.6, d) h/y=0.8, e) h/y=0.975




(b)
Intake Connection Location
Maximum 0.030985 m/s
0
Minimum -0.017761 m/s,
Maximum 0.007077 m/s
0
Minimum -0.011555 m/s,
(c)
Intake Connection Location
Maximum 0.024305 m/s
0
Minimum -0.025419 m/s,
Maximum 0.012024 m/s
0
Minimum -0.009921 m/s,

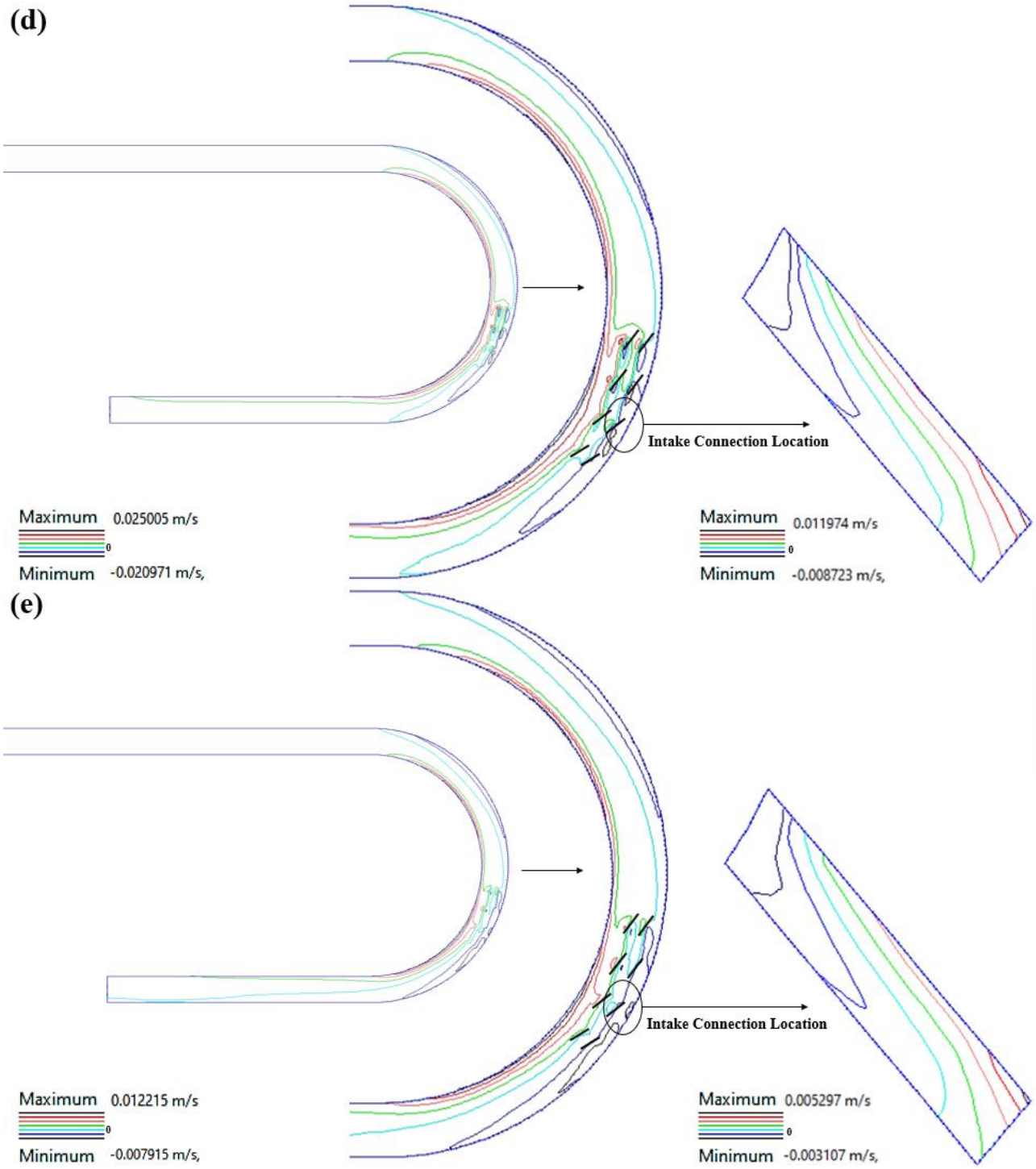
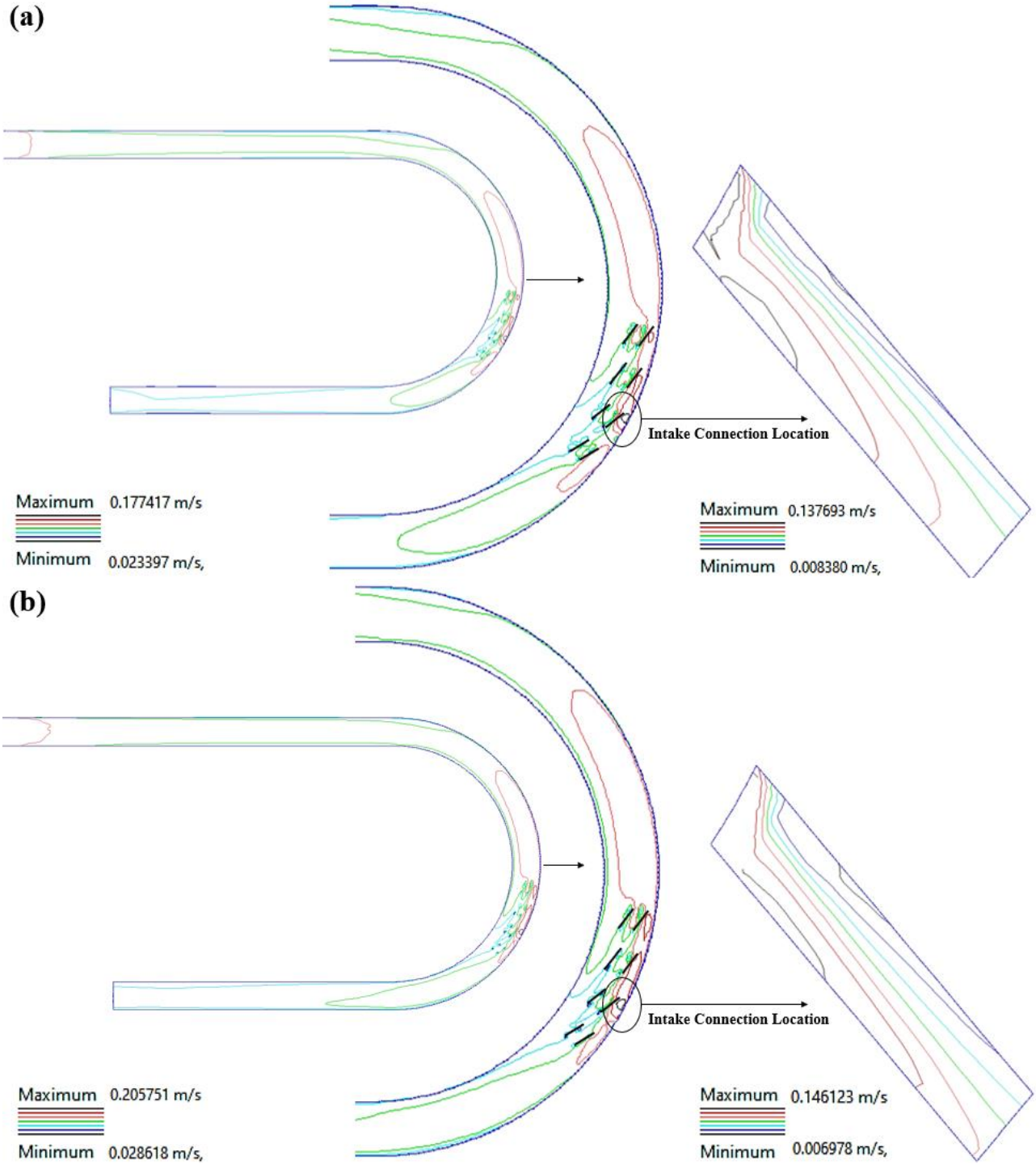
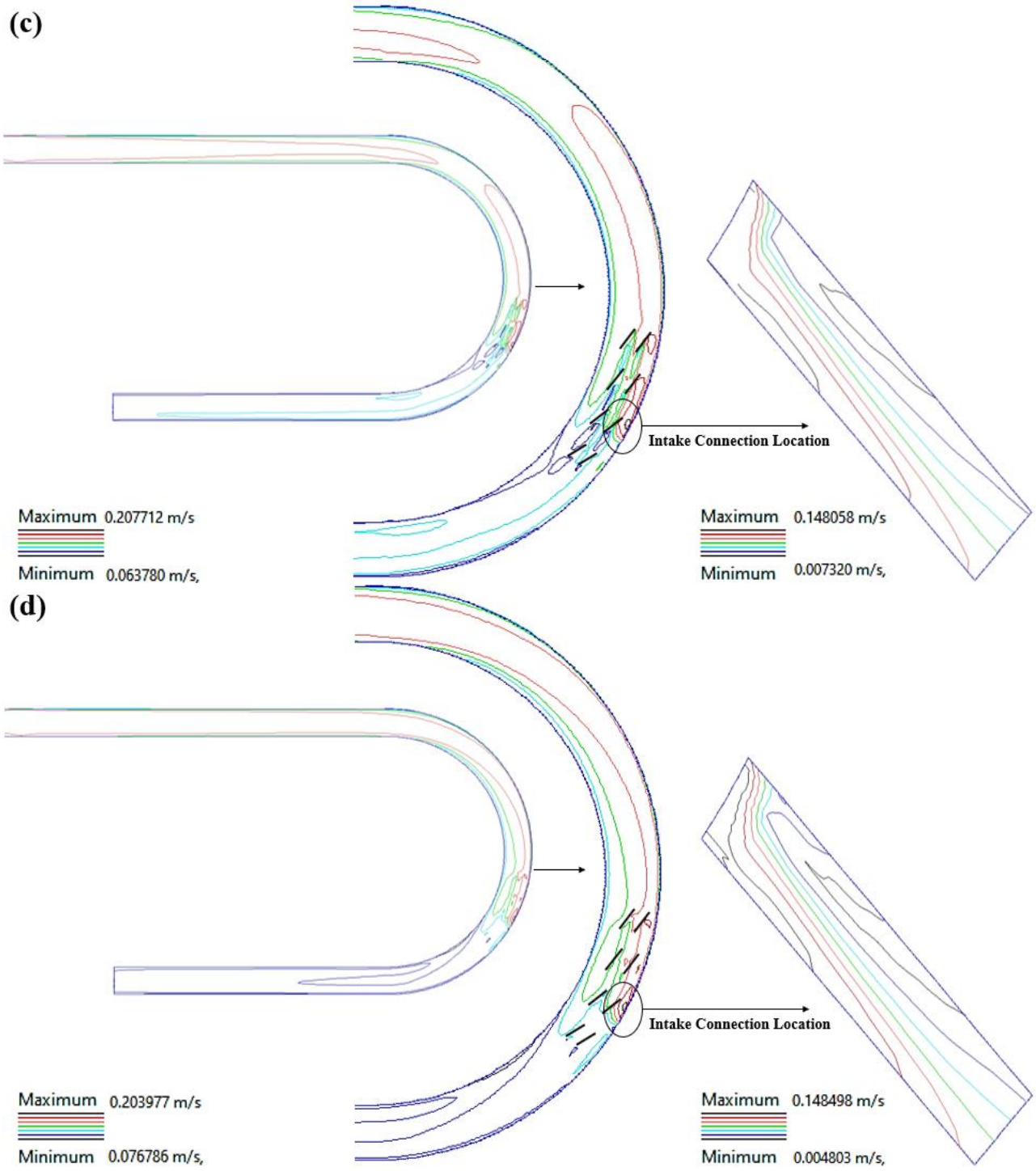


Fig. App.2 Vertical velocities in main channel and intake (Vane Length is 15cm) a) h/y=0, b) h/y=0.3, c) h/y=0.6, d) h/y=0.8, e) h/y=0.975

A.1. Influence of the transverse distance of Vanes




(c)
Intake Connection Location
Maximum 0.207712 m/s
Minimum 0.063780 m/s,
Maximum 0.148058 m/s
Minimum 0.007320 m/s,
(d)
Intake Connection Location
Maximum 0.203977 m/s
Minimum 0.076786 m/s,
Maximum 0.148498 m/s
Minimum 0.004803 m/s,

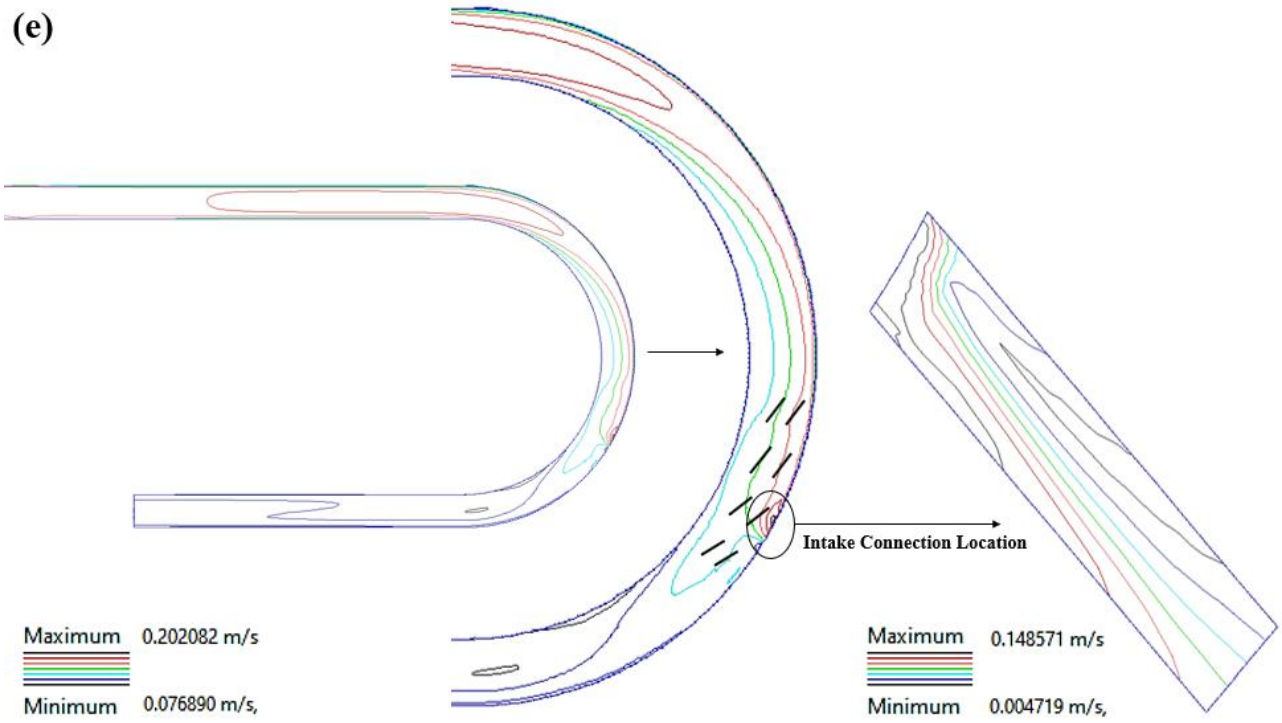
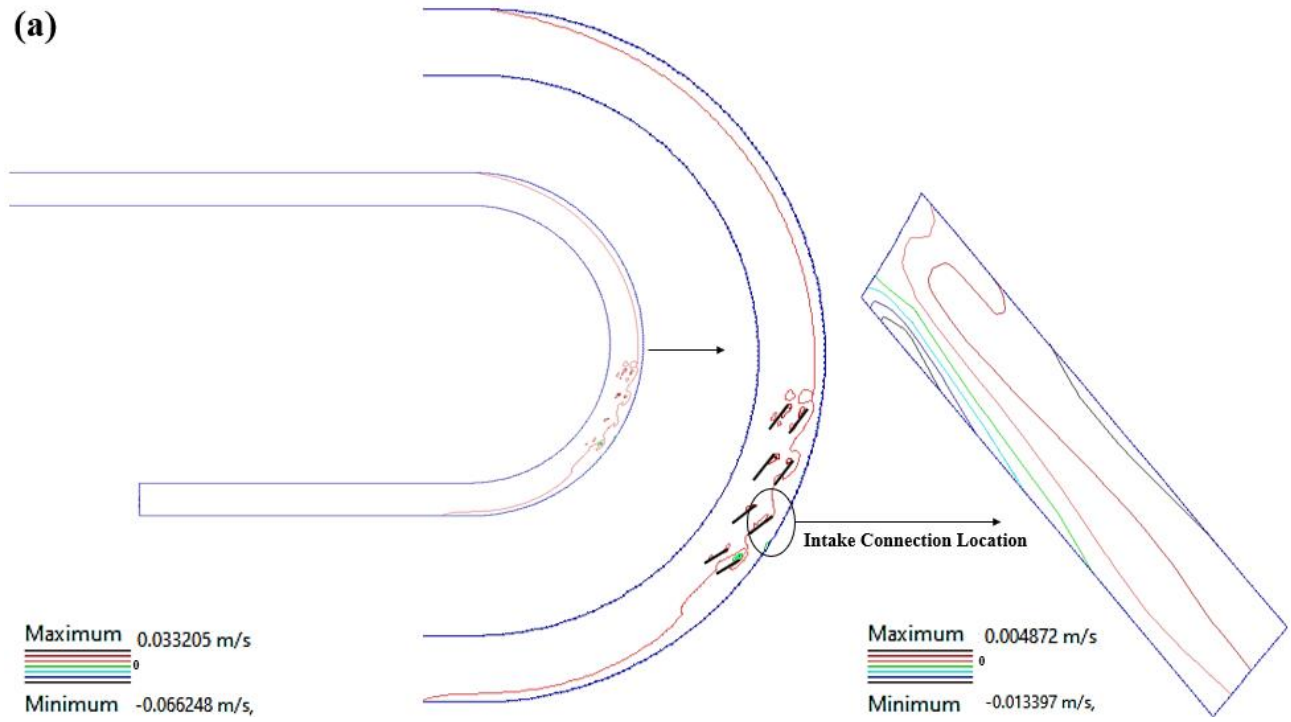
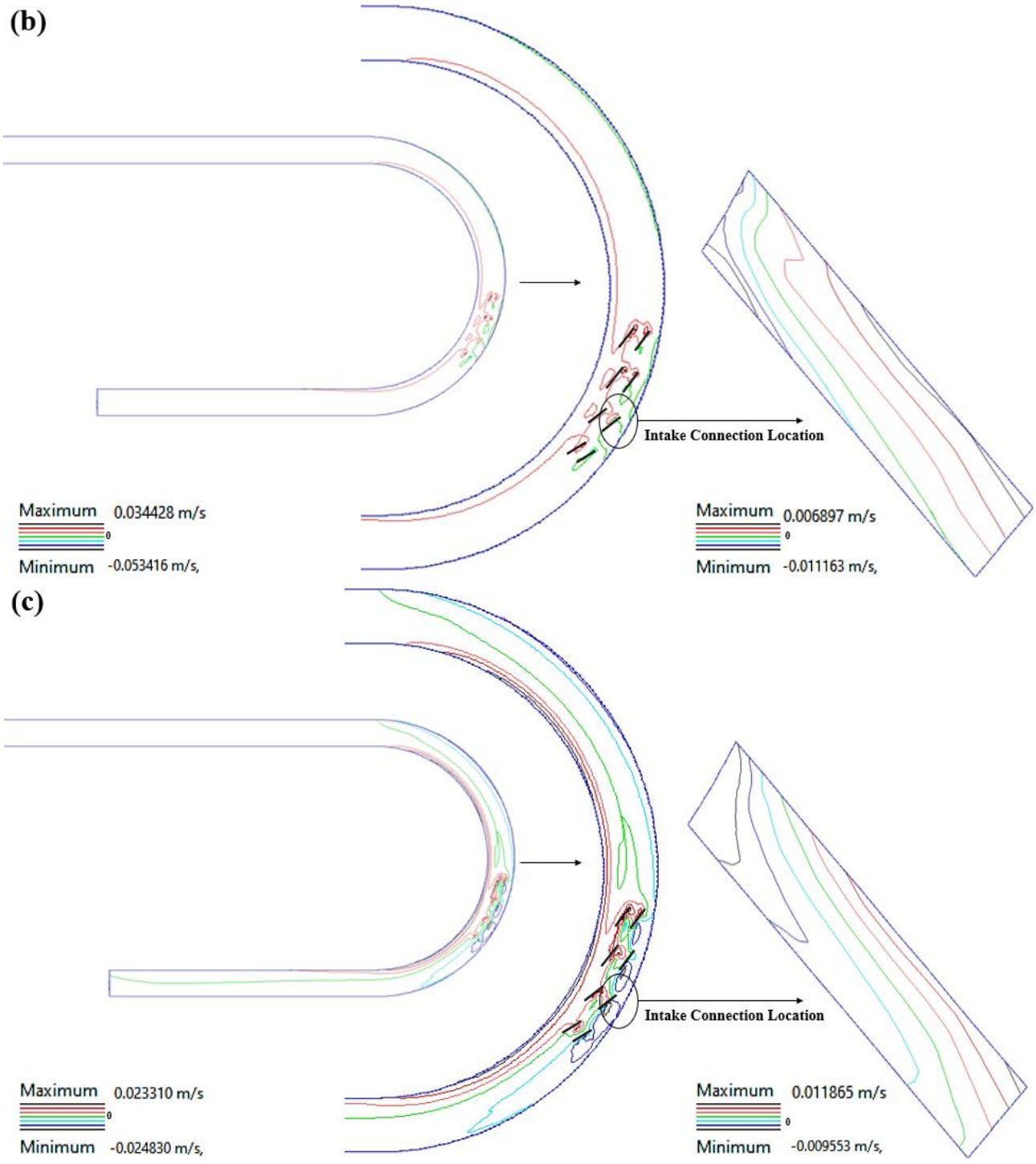


Fig. App.3 Stream-wise velocities in main channel and intake (transverse distance of Vanes is 13cm) a) h/y=0, b) h/y=0.3, c) h/y=0.6, d) h/y=0.8, e) h/y=0.975




(b)
Intake Connection Location
Maximum 0.034428 m/s
0
Minimum -0.053416 m/s,
Maximum 0.006897 m/s
0
Minimum -0.011163 m/s,
(c)
Intake Connection Location
Maximum 0.023310 m/s
0
Minimum -0.024830 m/s,
Maximum 0.011865 m/s
0
Minimum -0.009553 m/s,

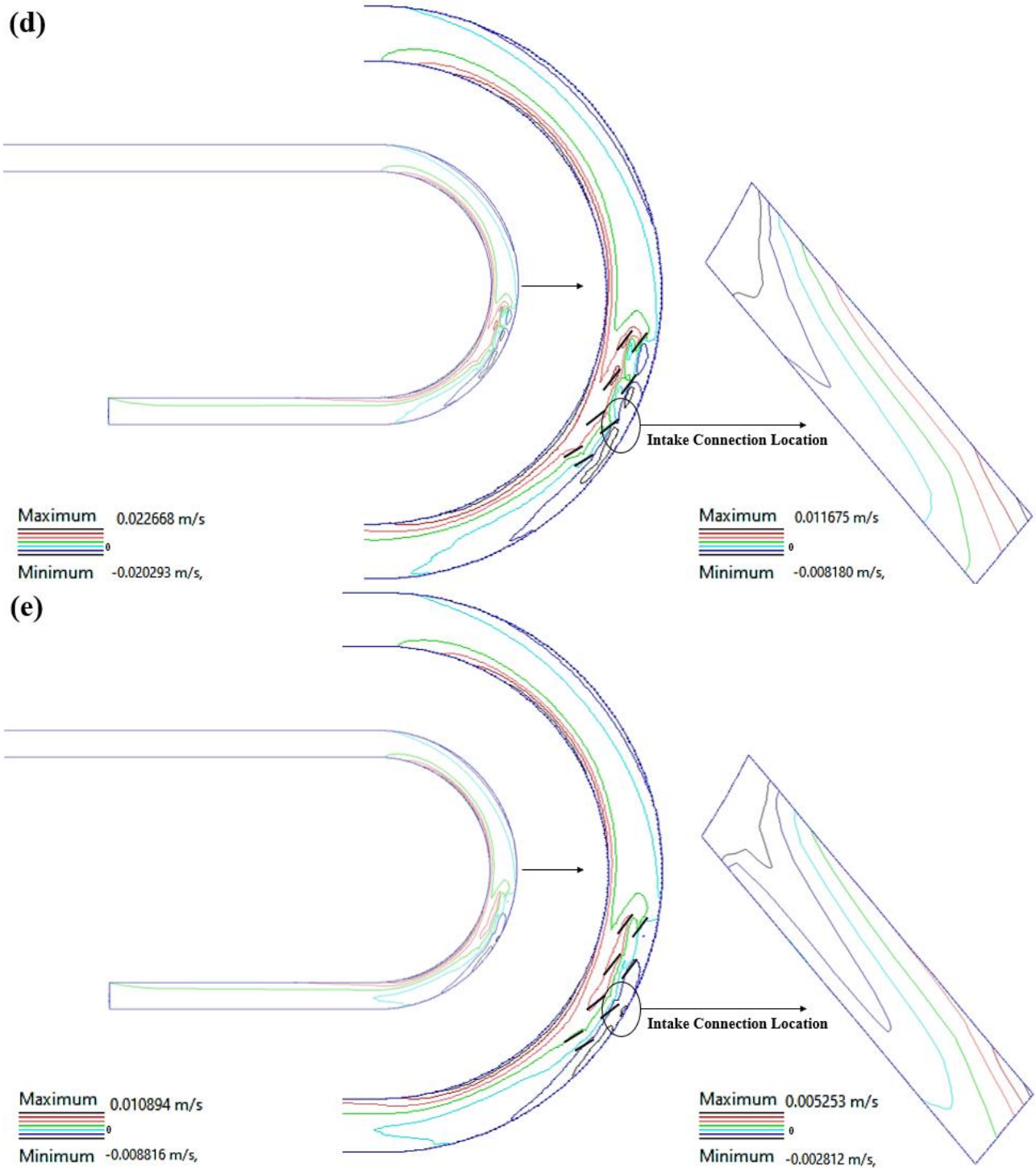
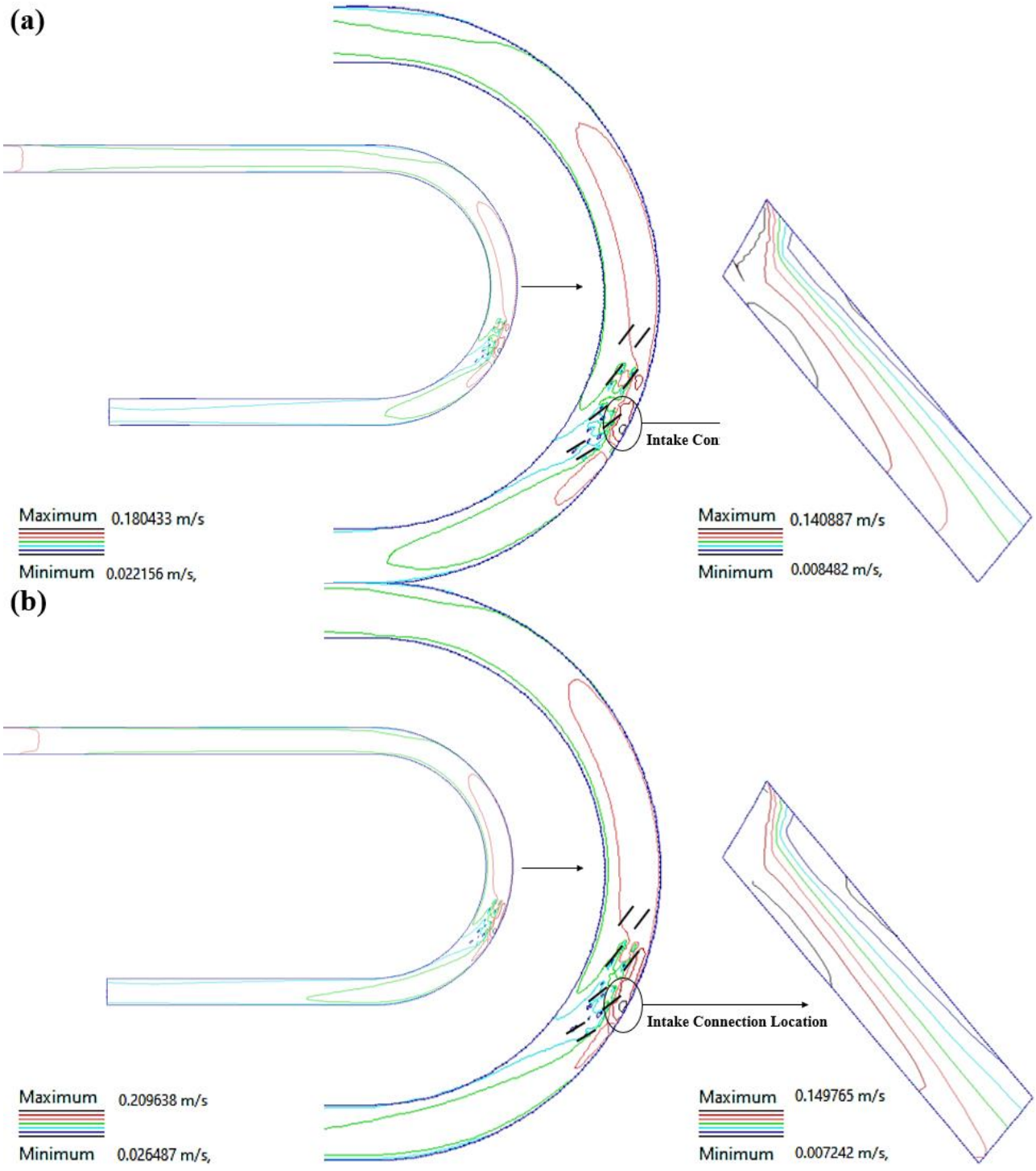
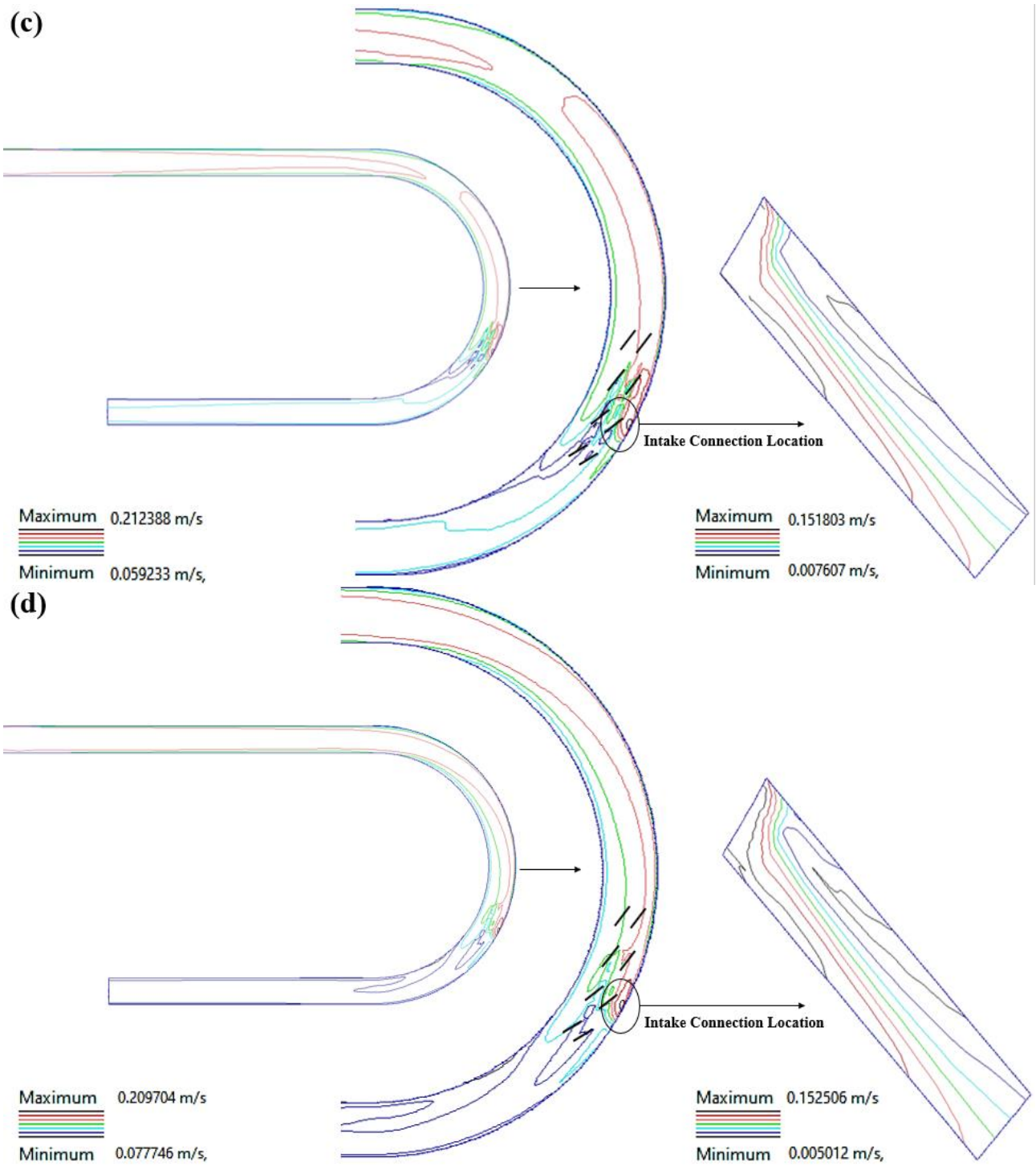


Fig. App.4 Vertical velocities in main channel and intake (transverse distance of Vanes is 13cm) a) h/y=0, b) h/y=0.3, c) h/y=0.6, d) h/y=0.8, e) h/y=0.975

A.2. Influence of the Longitudinal Distance of Vanes


(a)
Intake Con
Maximum 0.180433 m/s
Minimum 0.022156 m/s,
Maximum 0.140887 m/s
Minimum 0.008482 m/s,
(b)
Intake Connection Location
Maximum 0.209638 m/s
Minimum 0.026487 m/s,
Maximum 0.149765 m/s
Minimum 0.007242 m/s,


(c)
Intake Connection Location
Maximum 0.212388 m/s
Minimum 0.059233 m/s,
Maximum 0.151803 m/s
Minimum 0.007607 m/s,
(d)
Intake Connection Location
Maximum 0.209704 m/s
Minimum 0.077746 m/s,
Maximum 0.152506 m/s
Minimum 0.005012 m/s,

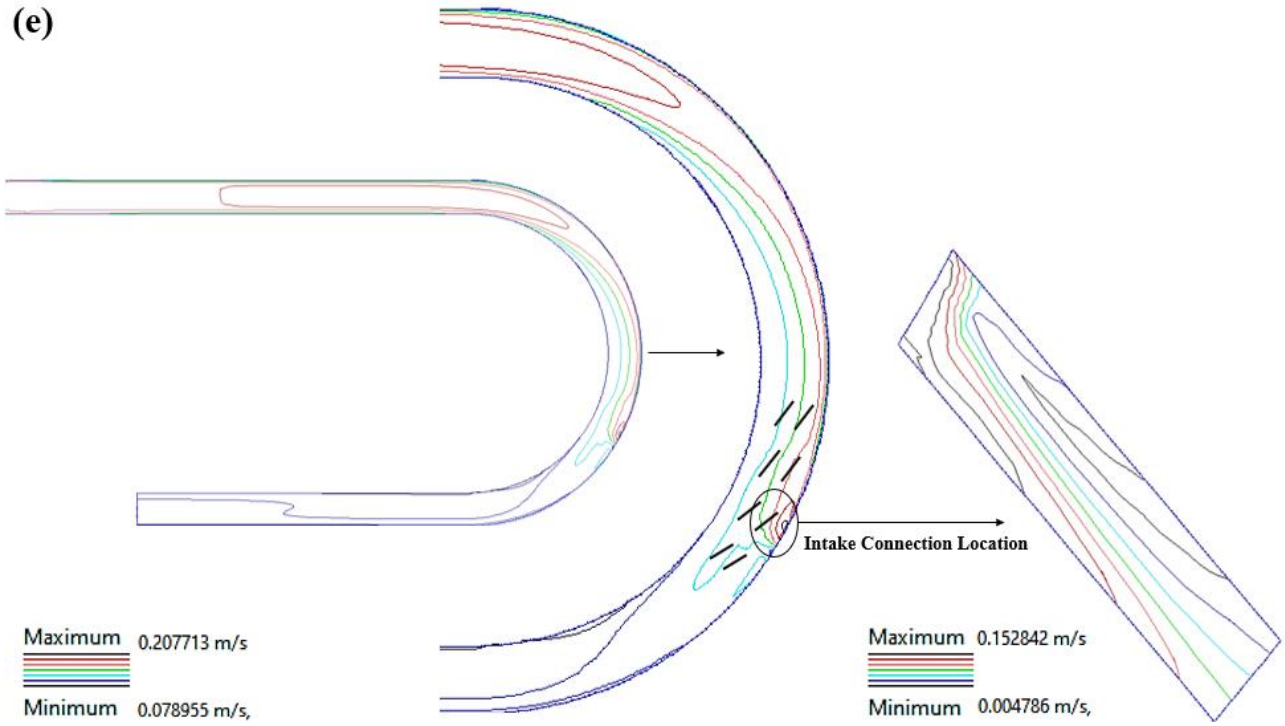
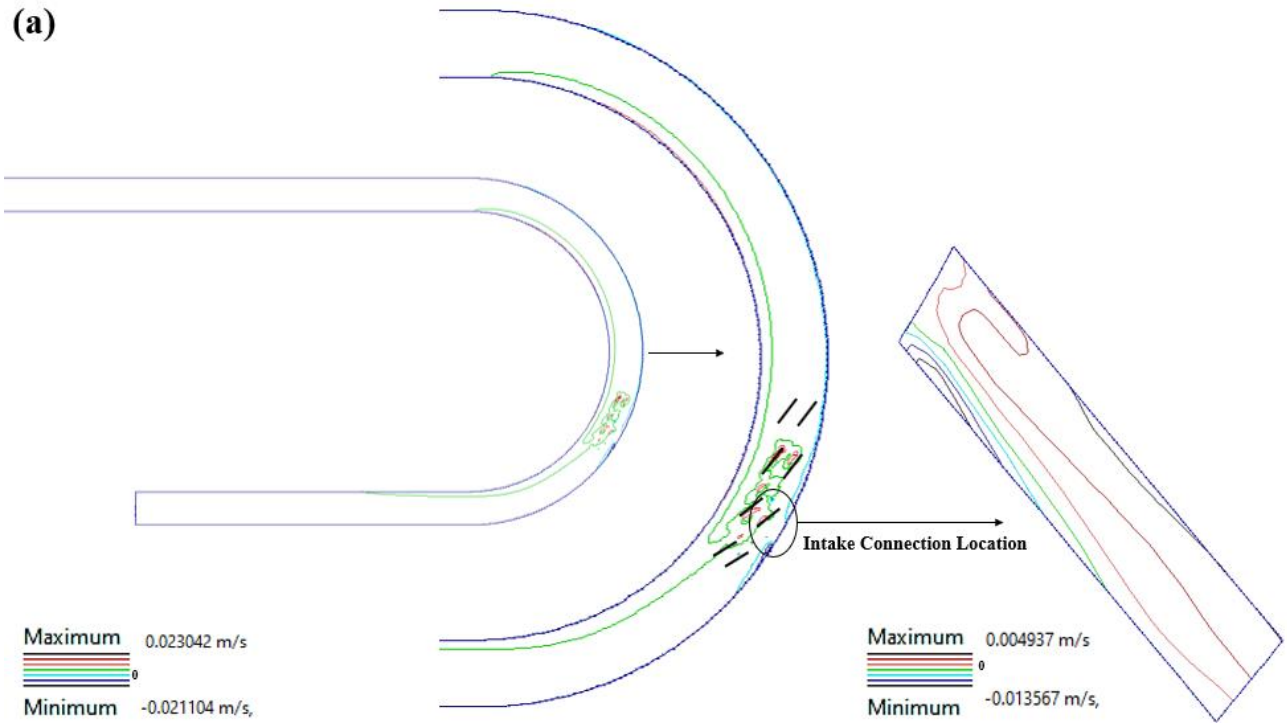
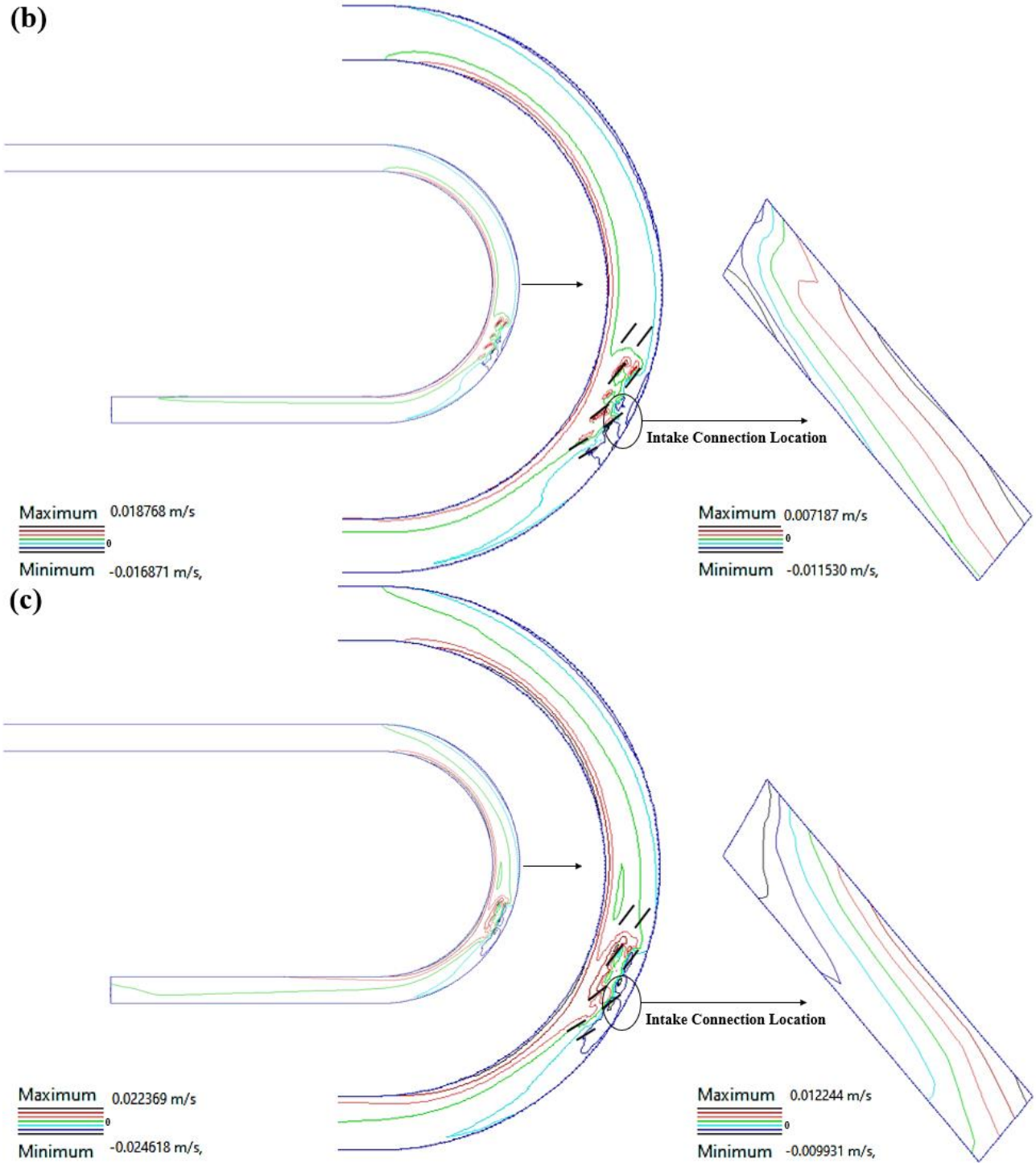


Fig. App.5 Stream-wise velocities in main channel and intake (longitudinal distance of Vanes is 30cm) a) h/y=0, b) h/y=0.3, c) h/y=0.6, d) h/y=0.8, e) h/y=0.975




(b)
Intake Connection Location
Maximum 0.018768 m/s
0
Minimum -0.016871 m/s,
Maximum 0.007187 m/s
0
Minimum -0.011530 m/s,
(c)
Intake Connection Location
Maximum 0.022369 m/s
0
Minimum -0.024618 m/s,
Maximum 0.012244 m/s
0
Minimum -0.009931 m/s,

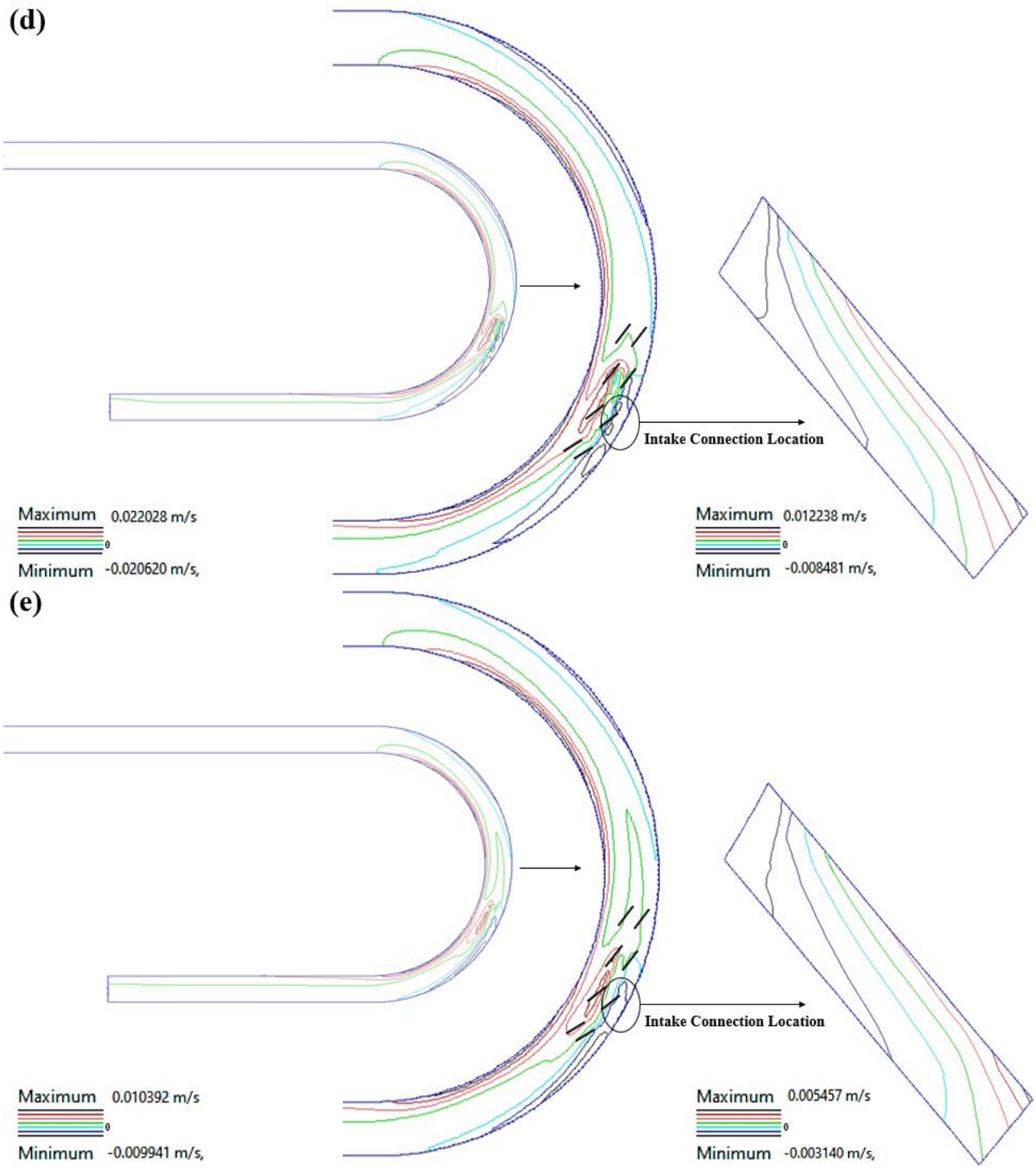
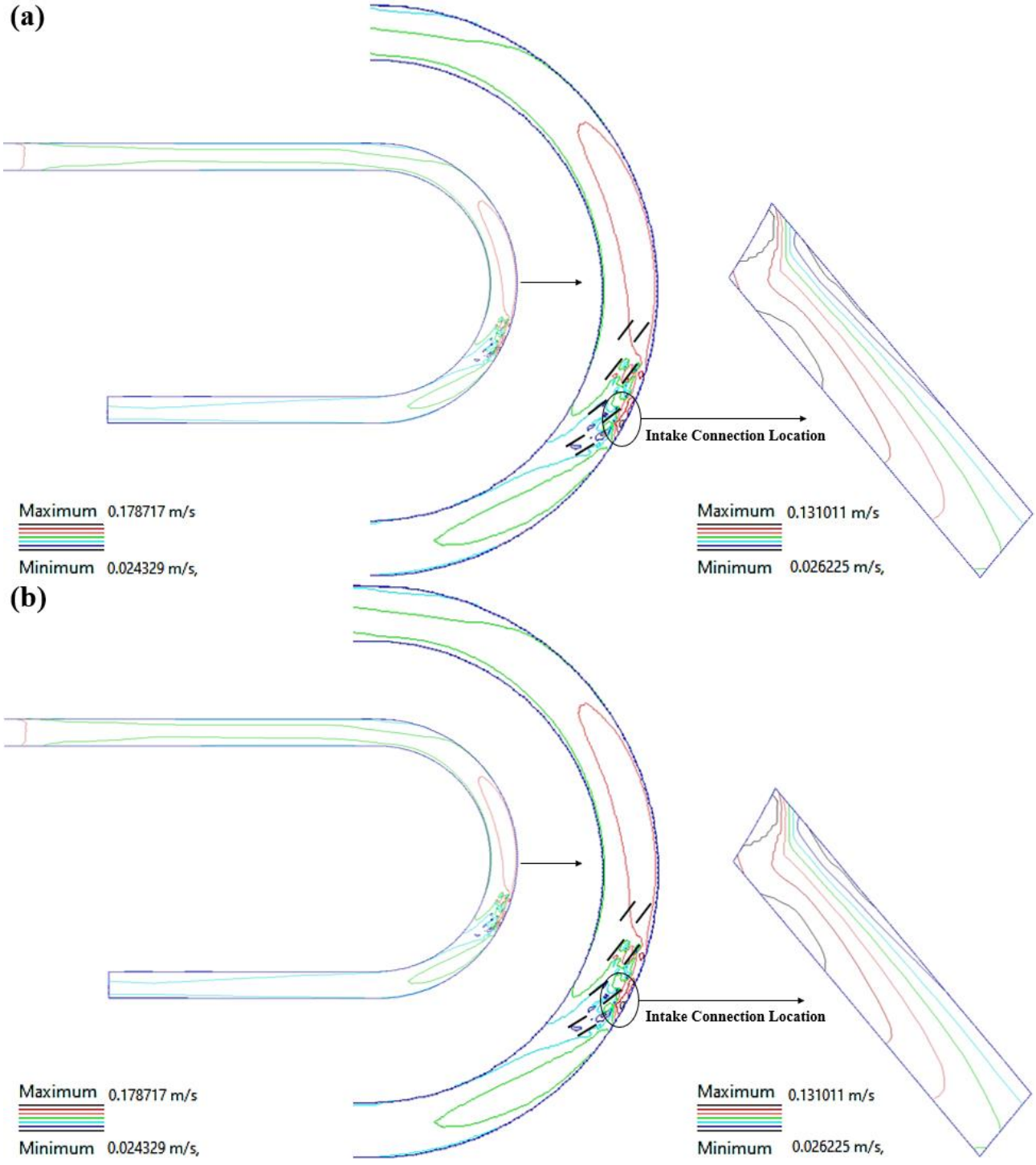
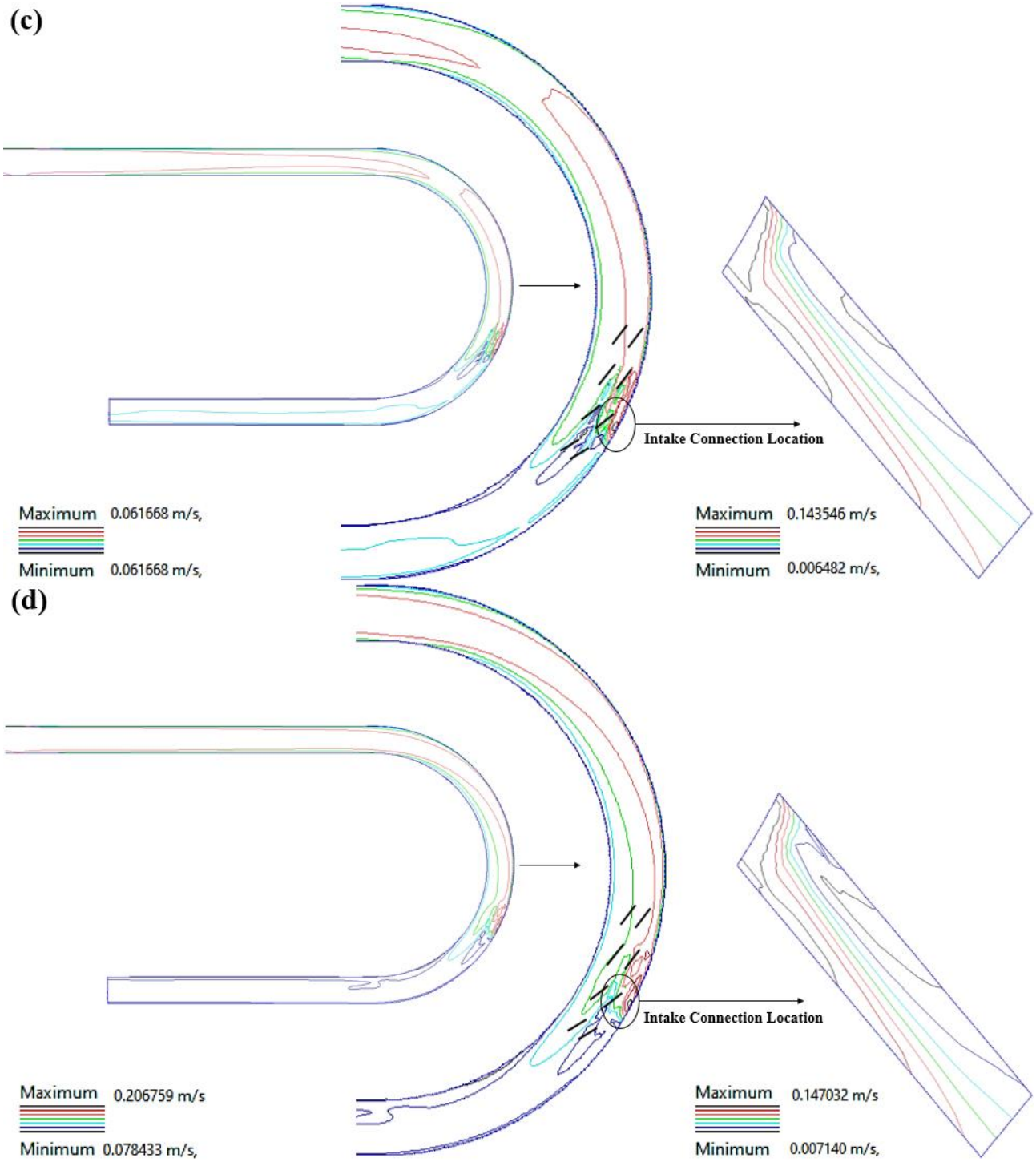


Fig. App.6 Vertical velocities in main channel and intake (longitudinal distance of Vanes is 30cm) a) h/y=0, b) h/y=0.3, c) h/y=0.6, d) h/y=0.8, e) h/y=0.975

A.3. Influence of the distance of the first row from the intake




(c)
Intake Connection Location
Maximum 0.061668 m/s,
Minimum 0.061668 m/s,
Maximum 0.143546 m/s
Minimum 0.006482 m/s,
(d)
Intake Connection Location
Maximum 0.206759 m/s
Minimum 0.078433 m/s,
Maximum 0.147032 m/s
Minimum 0.007140 m/s,

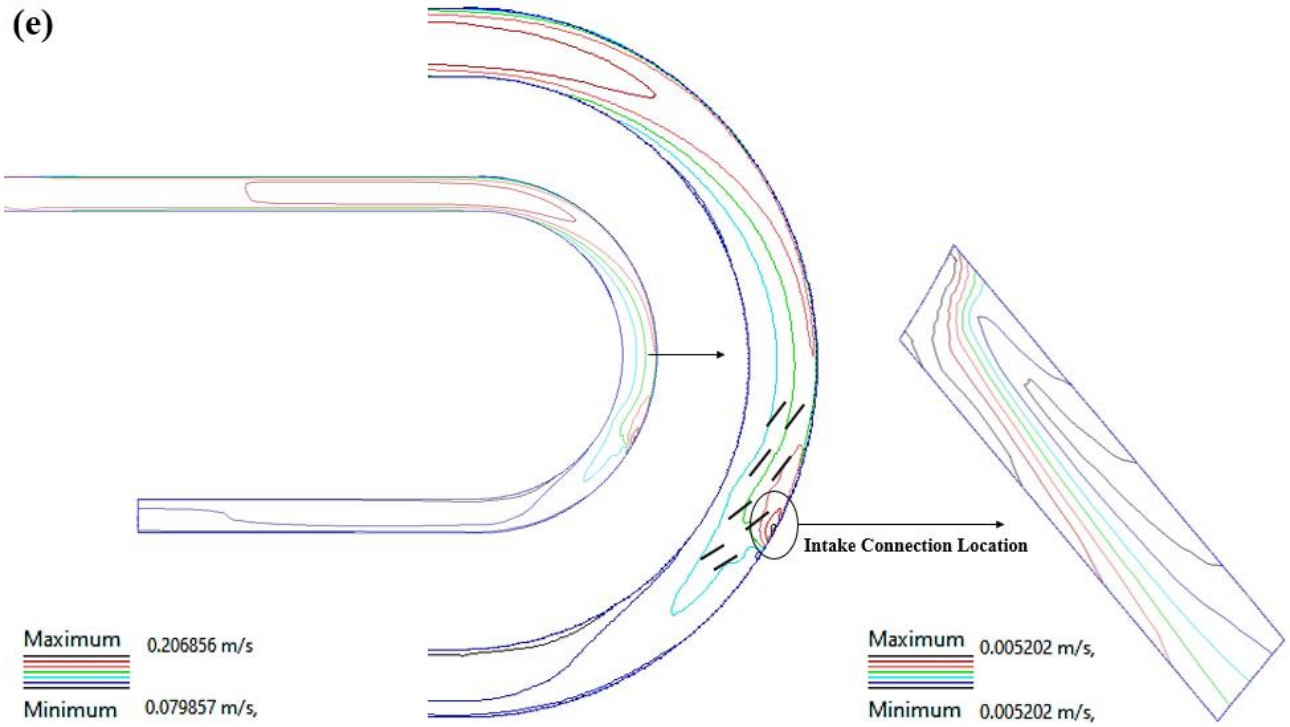
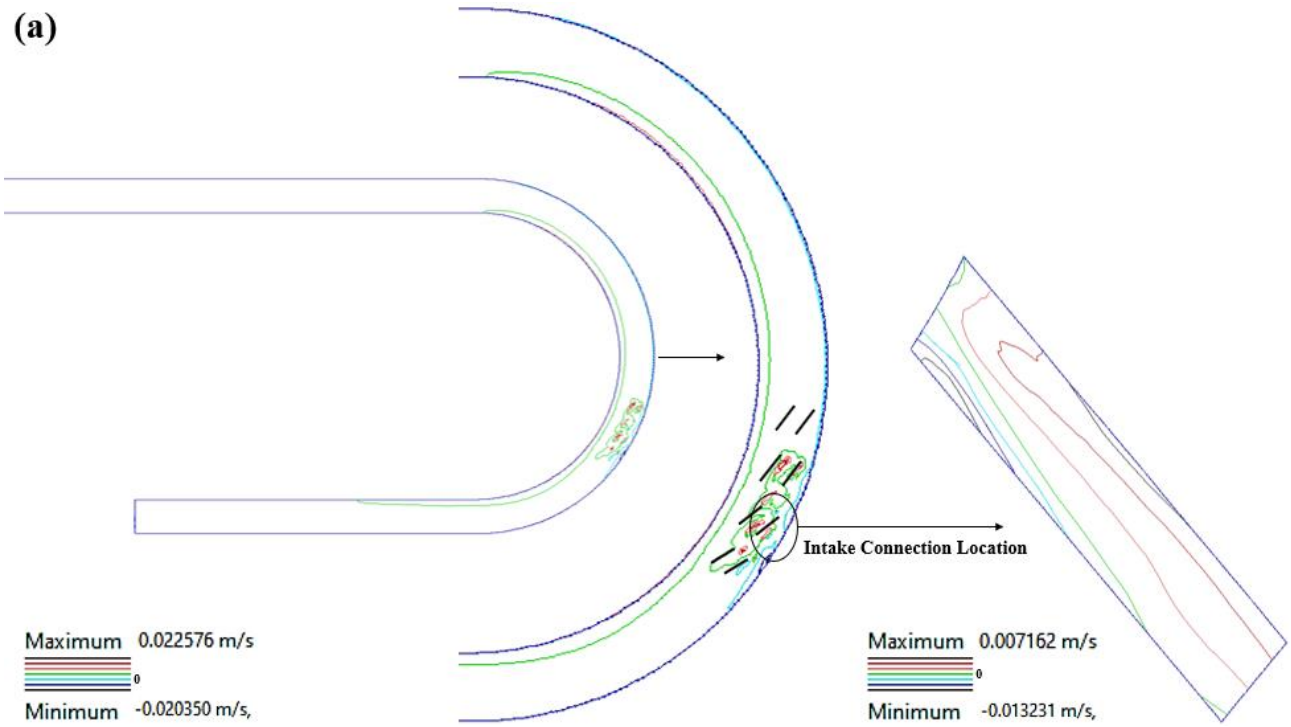
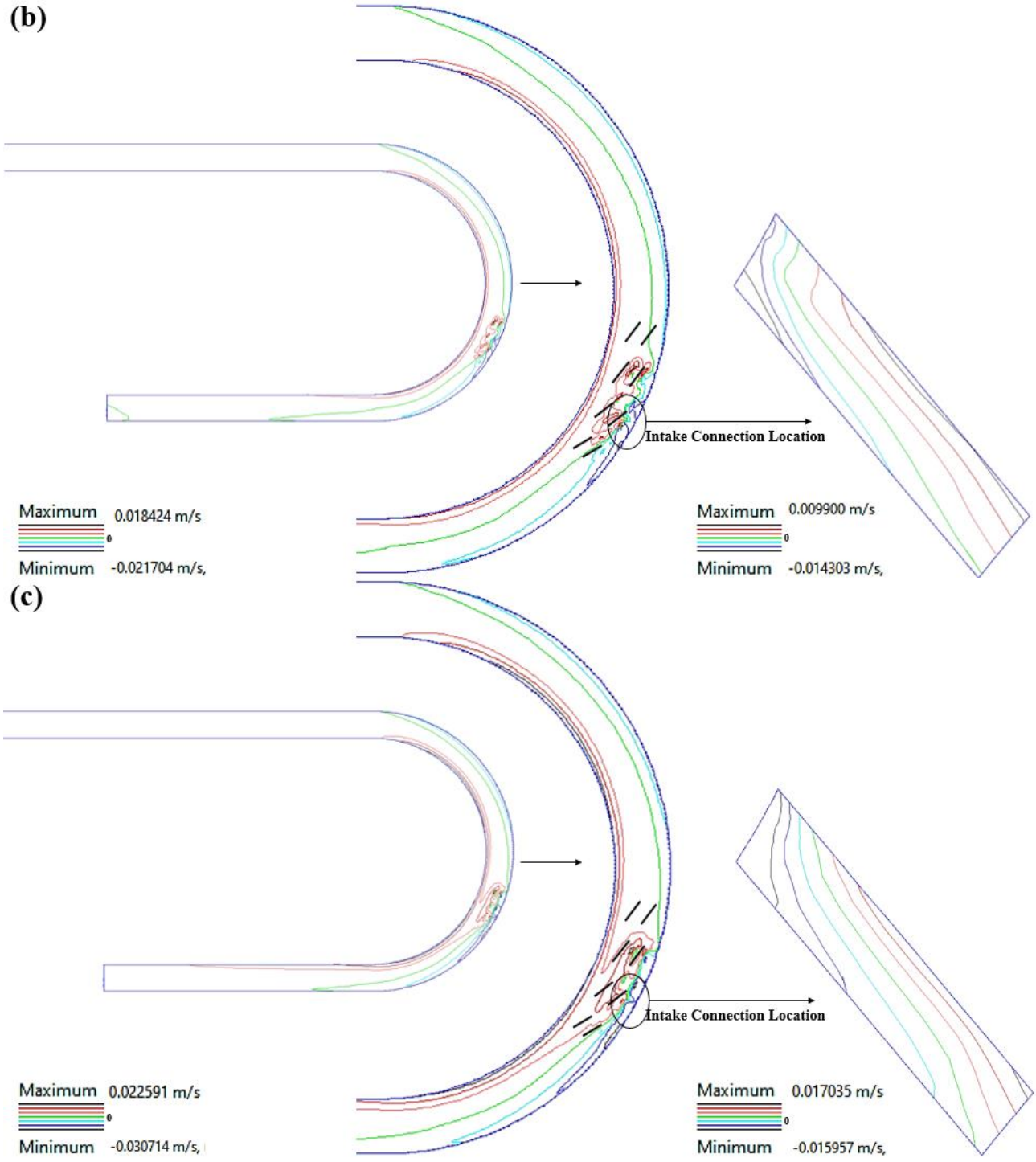


Fig. App.7 Stream-wise velocities in main channel and intake (distance of the first row from the intake is 12cm) a) h/y=0, b) h/y=0.3, c) h/y=0.6, d) h/y=0.8, e) h/y=0.975




(b)
Intake Connection Location
Maximum 0.018424 m/s
0
Minimum -0.021704 m/s,
Maximum 0.009900 m/s
0
Minimum -0.014303 m/s,
(c)
Intake Connection Location
Maximum 0.022591 m/s
0
Minimum -0.030714 m/s,
Maximum 0.017035 m/s
0
Minimum -0.015957 m/s,

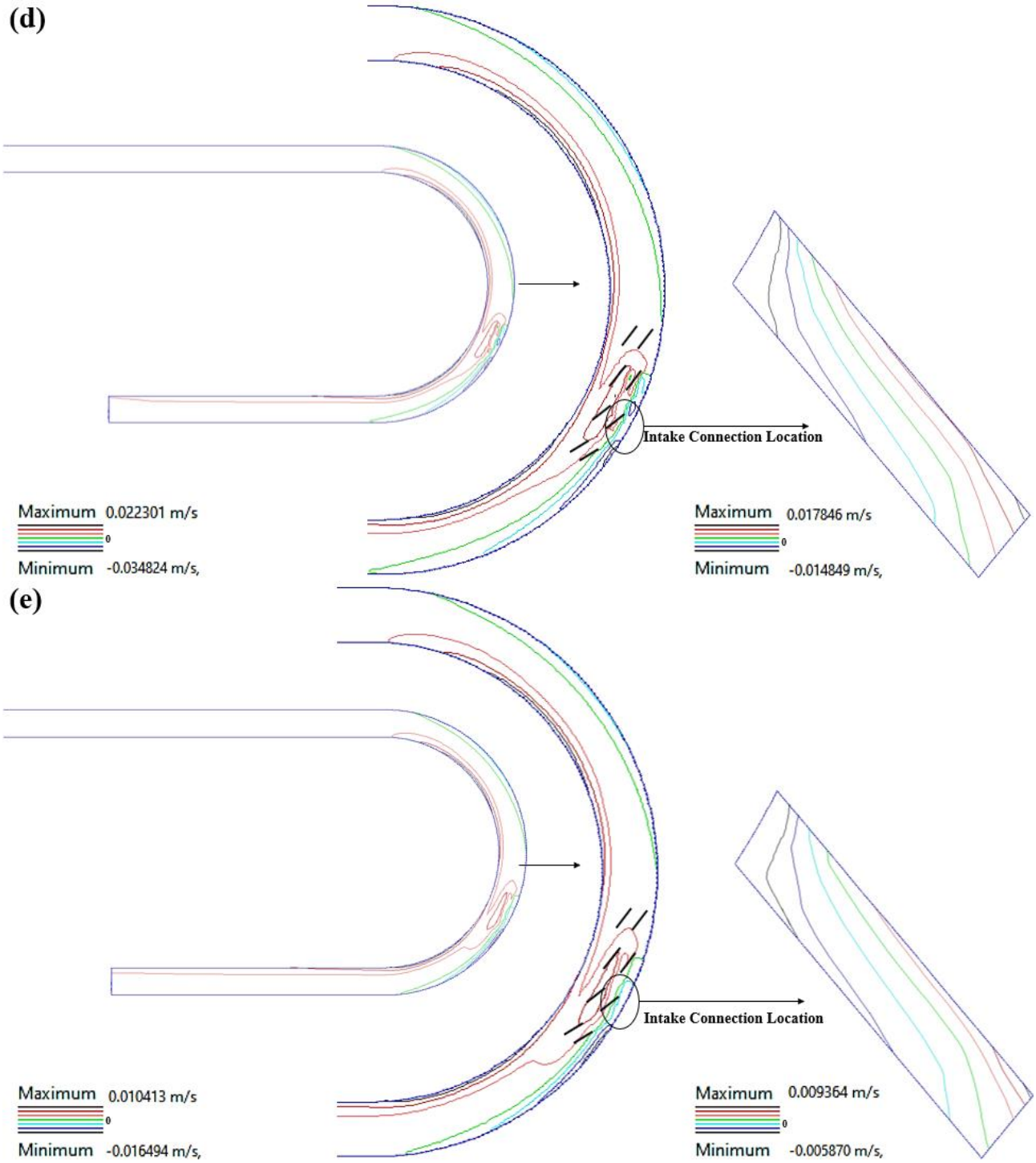


Fig. App.8 Vertical velocities in main channel and intake (distance of the first row from the intake is 12cm) a) h/y=0, b) h/y=0.3, c) h/y=0.6, d) h/y=0.8, e) h/y=0.975

Assessment of Site Suitability and Capacity for Sustainable Aquaculture Development Along the Northern Persian Gulf Coast

Morteza Jedari Attari [*,1], Aref Farhangmehr [1]

1. Institute of Geophysics University of Tehran, Iran, Institute of Geophysics University of Tehran, Iran

***Corresponding Author:**
Morteza Jedari Attari,

Email: mortezajedariattari@gmail.com
Received: 2025.07.06
Accepted: 2025.09.02
J. Hydraul. Struct., 12(2):103-119
DOI: 10.22055/jhs.2025.50100.1358

ABSTRACT

Marine fish cage culture (aquaculture/mariculture) is a rapidly growing food production method globally and in the Persian Gulf, yet it is highly sensitive to site selection. A sustainable approach to site selection can result in nutrient-rich, healthy, and continuous food production yields. Conversely, poor site selection can lead to excessive pollution, low yields, and operational failures, which can severely degrade the coastal/marine environment. Although the Persian Gulf has a history of aquaculture, suitable site identification and capacity assessment remain underexplored. Targeted research is crucial to optimize sustainable aquaculture, supporting both economic and ecological goals. This research presents a comprehensive sustainable method for probing and selecting appropriate sites for mariculture along the northern Persian Gulf coastlines. The selection process considers various factors, including hydrodynamic and meteorological parameters that impose restriction on mariculture practice as well as environmental parameters that affect fish production, potential environmental impacts, infrastructure availability, and the interests of other coastal users. Considerations also include the impact on coastal security, environmentally protected areas, recreational activities, tourism, navigation, and other fishery interests. By integrating all geographic data layers into GIS, suitable areas and potential capacity for the practical implementation of sustainable fish cage culture along the northern Persian Gulf coastlines were revealed. The analysis reveals the identification of six distinct regions along the northern shoreline of the Persian Gulf, encompassing a total area of one million square kilometers. These delineated areas currently are able to facilitate a cage culture production capacity estimated at approximately 200 kilotons per annum.

KEYWORDS
Site Selection, Mariculture, Fish Cage Culture, GIS.

1. Introduction

Marine aquaculture is recognized as one of the fastest-growing and most vital industries globally [1], [2], [3], [4], offering a means to alleviate pressures on marine and coastal ecosystems while meeting essential food demands [5]. Furthermore, marine aquaculture plays a significant role in enhancing food security [6], [7]. According to the United Nations Food and Agriculture Organization, "Food fish has a nutrient profile superior to all terrestrial meats, serving as an excellent source of high-quality animal protein and highly digestible energy". It also provides abundant omega-3 polyunsaturated fatty acids (PUFAs), fat-soluble vitamins (A, D, and E), water-soluble vitamins (B complex), and essential minerals (calcium, phosphorus, iron, iodine, and selenium).

Fish is considered a staple animal protein source with the potential to address various aspects of global malnutrition. When mariculture operations are both sustainable and profitable, they enhance food availability and access, essential for alleviating poverty and bolstering economic resilience. Additionally, mariculture can reduce the pressure on wild fish populations, allowing these stocks to stabilize if properly managed, thereby supporting the traditional fishing industry. Success in the practice of mariculture of various animal and plant species in terms of both quantity and value and maintaining a diverse production portfolio ensures a stable food supply amidst fluctuating prices and the availability of wild fish [8]. Moreover, a profitable commercial aquaculture industry generates employment, supports ancillary businesses, contributes to tax revenues, and fosters further investment in the science and technology of sustainable aquaculture.

Commercial mariculture can have devastating impacts on coastal environments, particularly coral reefs. Eutrophic pollution from mariculture operations has been documented to affect coral reefs up to 80 kilometers away [9]. Several commercial mariculture operations worldwide have caused significant environmental degradation and destruction to coral reefs [10], [11], [12], [13], [14]. In response, regional and national governments have had to permanently shut down these operations. These failures resulted from exceeding the environmental carrying capacity of their locations, leading to eutrophic “Dead Zones” characterized by decreased dissolved oxygen levels and the accumulation of inhospitable hydrogen sulfide in both the benthic environment and water column. However, some commercial mariculture operations near coral reefs have demonstrated minimal environmental impacts. These successful operations typically ensure that mariculture activities do not exceed the environmental carrying capacity of the location and actively reduce the enrichment load of the operation to maintain this balance. Determining the environmental carrying capacity of a proposed mariculture site is crucial for designing sustainable operations. Despite this, environmentally sustainable mariculture density levels are often not optimal for profitability or product yields. As a result, many operations increase fish density and growth rates to enhance profitability, which can gradually lead to environmental degradation. Gao and Dong [15] reviewed the technical, environmental, spatial, and governance challenges associated with expanding mariculture offshore. Their findings suggest that site selection must integrate ecological sustainability with socio-economic factors. Their study underscores the importance of robust regulatory frameworks and stakeholder engagement in ensuring the long-term viability of offshore fish cage culture.

wave and current dynamics play a crucial role in site selection. Properly understanding and modeling these forces can prevent structural failures and optimize fish cage placement for better stability and productivity. The environmental carrying capacity for sea cage culture in the Persian Gulf, emphasizes the importance of current velocity and other hydrodynamical characteristics and their effect on rate of deposition of organic matter onto sediment, in site selection. Therefore, careful consideration of such parameters can significantly enhance fish production while minimizing ecological impacts. This approach ensures sustainable development in aquaculture by balancing productivity with environmental protection. Lapenkov et al. [16] investigated the seasonal dynamics of geochemical characteristics in sediments around fish farms in Lake Ladoga, Russia. Their findings reveal that seasonal variations in organic pollution can influence site suitability. The study advocates for current speed being an important parameter in site selection, as it plays the most significant role in transporting out the pollutants. Jiang et al. [17] modeled the impact of aquaculture

facilities on hydrodynamics and solute transport in the North Yellow Sea. Their research highlights the importance of understanding the interactions between culture systems and the marine environment. Proper site selection considering hydrodynamic characteristics such as minimum and maximum current speed in the region should account for these interactions to prevent adverse effects on water quality and marine ecosystems. Liu et al. [18] utilized numerical simulation and similarity theory to model the settling flux of biodeposition in cage culture environments. Their research, conducted in a bay setting, provides insights into managing nutrient loads and maintaining water quality. This methodology is pivotal for sustainable cage culture practices, emphasizing the need for detailed hydrodynamic studies in site selection processes.

The importance of effects of extreme sea conditions on cage structure, mooring loads, carrying capacity and fish yields have been probed by many researchers [19], [20], [21], [22], [23]. Lee et al. [21] examined the dynamic responses of floating fish cages to waves and currents, crucial for structural integrity and fish health. Their simulation studies indicate that careful consideration of hydrodynamic forces is essential in site selection to prevent structural failures and ensure the safety and productivity of the aquaculture operations. Lader et al. [22] conducted an experimental investigation on the wave response of closed flexible fish cages. Their findings are crucial for selecting sites that minimize wave-induced stress on cage structures. By understanding the interactions between waves and cage systems, aquaculture operators can choose locations that enhance the structural stability and safety of their operations. Swift et al. [23] focused on the effects of biofouling on the carrying capacity of marine fish cages. Their experimental work suggests that biofouling can significantly increase drag forces, leading to structural stress and reduced water flow. This study emphasizes the need for considering both minimum and maximum current speeds in site selection in areas with substantial biofouling risks to ensure the longevity and efficiency of fish cages.

Inland facilities and supporting infrastructure are crucial for the successful operation of aquaculture facilities. Despite being theoretically perfect for aquaculture, the majority of coastal areas require extensive infrastructure development before they can realize their full production potential [24]. Key infrastructure components include access to all-weather roads to facilitate efficient transportation of operational supplies, personnel, and harvested fish. Additionally, proximity to an electrical supply is essential for powering water pumps, office air-conditioning, and ice-making facilities, especially at nurseries and fish landing sites. Furthermore, cage culture sites should be equipped with a jetty featuring sufficient water depth to safely accommodate boats carrying feed and harvested fish, even under adverse weather conditions. The effects on recreation and tourism, as well as the impact on navigation and other fishery interests, must be carefully considered to ensure that the selected site is suitable for cage aquaculture and does not adversely affect other important coastal activities and interests.

Geographic Information Systems (GIS) can significantly aid in solving site selection problems by analyzing spatial data to identify optimal locations based on various criteria such as proximity to resources, geophysical constraints, environmental conditions, and infrastructure availability. Micael et al. [25] utilized Geographic Information Systems (GIS) in a multi-criteria decision-making tool for mariculture site selection. Their approach integrates physical, chemical, and socio-economic factors, providing a holistic framework for identifying optimal sites. This study underscores the value of advanced spatial analysis techniques in making informed site selection decisions. A study by Salama et al. [26] identified suitable sites for finfish cage farming along the eastern Red Sea coast of Saudi Arabia. The research utilized GIS-based models to analyze water quality,

temperature, and current patterns. Their approach highlights the importance of site-specific environmental assessments to optimize fish growth and minimize ecological disturbances. Jayanthi et al. [27] employed a spatial analysis method to map coastal lagoon characteristics, crucial for determining suitable sites for aquaculture. Their study on the southeast coast of India highlights the importance of environmental parameters such as salinity, water depth, and substrate type. This comprehensive approach ensures optimal site selection that minimizes ecological impact while maximizing aquaculture productivity.

The study area of this study encompasses the northern shoreline of the Persian Gulf (Figure 1). The Persian Gulf is a shallow, semi-enclosed water body with a total surface area of 251,000 km². It is situated between the Arabian Peninsula and Iran, extending 1,259 km from the Arvand River delta to the Strait of Hormuz. The deepest point of the basin reaches 120 meters near Small Tunb Island, with potentially greater depths in the Strait of Hormuz. The shallowest points range from 0 to 30 meters. Despite the longstanding utilization of the Persian Gulf for aquaculture, a comprehensive understanding of the most suitable locations and the actual capacity for such practices remains inadequately explored. This oversight hinders the optimization of aquaculture potential in the region, underscoring the necessity for targeted research and assessment. Identifying ideal sites and quantifying their capacities are essential steps toward enhancing sustainable aquaculture practices in the Persian Gulf, thereby fostering both economic growth and ecological balance.

In the Persian Gulf, local resistant fish species include Gilthead Seabream (Sparus aurata), European Seabass (Dicentrarchus labrax), and Sobaity Seabream (Sparidentex hasta) [28]. Additionally, several candidate species have been identified for potential cage culture development, such as Silver Pomfret (Pampus argenteus), Milkfish (Chanos chanos), Cobia (Rachycentron canadum), Asian Seabass (Lates calcarifer), Rabbitfish (Siganus canaliculatus), and other Seabream species (Sparidentex hasta ‘sheim’ and Acanthopagrus latus ‘sobiaty’) [29]. At present, no comprehensive site selection study or authoritative reference exists specifically addressing the details of cage culture of any above-mentioned species within the Persian Gulf. The data and results presented in this study aim to provide a preliminary framework for investors, planners, and policymakers to support the strategic development of the marine aquaculture sector. The threshold values for environmental and technical parameters used in this assessment were derived from widely accepted scientific and official sources and relevant literature.

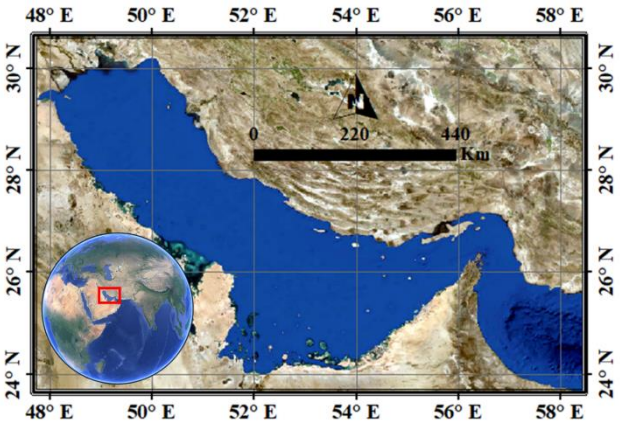


Figure 1: Study Area, the Persian Gulf

Jahani et al. [30] explored the impacts of cage aquaculture on the benthic environment in the Persian Gulf. Their research demonstrated that organic enrichment from fish farming significantly affects sediment quality. The study highlights the need for site selection criteria that consider sediment health to mitigate negative environmental impacts, advocating for more stringent regulatory measures in the site selection process. Risk et al. [28] developed a hydrodynamic circulation model for the Persian Gulf, allowing the tracking of dissolved material paths. In a model run simulating one year of full operation for the proposed number of fish farms, it is estimated that most reefs on the Iranian side will be exposed to nutrient levels too high for reef survival. Significant trans-border movement of nutrients is expected, affecting the waters of neighboring countries. In fact, within a few years, the entire Gulf will be impacted. These planned aquaculture projects have the potential to damage mangroves and destroy all reefs in the Persian Gulf in a very short period of time. Abbasian et al. [14] conducted a numerical experiment, along with data gathering from sediment samples, showing that the farms' "footprint" of anoxic bottom conditions extends much beyond the actual size of the farms (exceeding 2 km) in the Persian Gulf, due to dominant tidal currents. These studies indicate that it is essential to consider the hydrodynamic characteristics of the study area, including currents, waves, winds, and surges, as the primary limiting factors for selecting sites for fish cage culture.

Despite the valuable efforts made to identify various aspects of cage aquaculture in the Persian Gulf, a comprehensive site selection study that considers all effective parameters is still unavailable. This study developed a comprehensive and sustainable methodology for selecting appropriate sites along the northern Persian Gulf coastlines, aiming to identify optimal locations for mariculture activities. The process requires evaluating multiple parameters, including environmental factors influencing fish production, potential ecological impacts, infrastructure availability, and the interests of other coastal stakeholders. By integrating and visualizing data layers using GIS, it became possible to evaluate multiple factors simultaneously, streamline the selection process, and make informed, data-driven choices aligned with the scope of this study. Specific considerations, such as hydrodynamic and meteorological restrictions, proximity to conservation areas, operational techniques, local planning context, landscape impacts, and access to essential infrastructure, were implemented as the main criteria. This inclusive approach ensures that the proposed mariculture sites are environmentally sustainable while addressing the needs and concerns of all parties involved in the management of coastal resources.

2. Materials and methods

It is necessary to determine the most effective criteria in site selection for cage aquaculture. Based on reviews in the literature, the selection of suitable sites for mariculture is influenced by several factors. Environmental (chemo-physical) parameters are crucial in determining a site's suitability for fish production. Additionally, potential environmental impacts must be considered, along with the infrastructure needed to service aquaculture operations. Safeguarding the interests of other users of coastal waters is also essential. Proximity to existing fish farms, which may influence the viability and sustainability of the proposed site, must be thoroughly evaluated. Proximity to nature conservation interests, including coral reefs and environmentally protected areas, is another critical consideration. The planning context, including local plans or coastal zone designations and existing aquaculture zones or plans, plays a significant role in determining the feasibility of a new site. Potential impacts on the landscape and visual seascape must be evaluated, along with the availability of land access and necessary infrastructure. Additionally, the impact and proximity to areas of coastal security and other activities or restrictions, such as

environmental protected areas or military zones, are important factors.

The capacity for fish production by cage culture depends on several parameters, and fish farms cannot be placed very close together. The primary reason for this spacing is to allow sufficient water current to pass along the cages, flushing out bio-deposits. Another major concern is to maintain a contingency plan for epidemic diseases, preventing widespread infections among adjacent farms. Laws and regulations vary significantly worldwide. In this study, a minimum distance of 3 km between medium-sized farms with a capacity of 1500 tons per year is assumed to be sufficient, according to FAO/World Bank [31]. Such a farm would comprise 12 floating cages, each with a capacity of 125 tons per year, featuring a high-density polyethylene (HDPE) collar diameter of 28 meters and a net depth of 10 meters. This cage size is commonly used by local fish industries. This estimation approach yields a nominal production capacity based on the suitable sea surface area. However, many of these sea areas are adjacent to undeveloped lands that lack the infrastructure necessary to support a viable mariculture industry. Accordingly, a practical capacity should also be estimated, as it is substantially lower than the nominal figures. Finally—and importantly—this study does not address the total carrying capacity of the Persian Gulf. As a semi-enclosed water body, it has a finite ability to absorb biomass discharges without compromising its ecological integrity. Accurately estimating this overall carrying capacity would require extensive environmental monitoring and detailed biogeochemical analyses, which lie beyond the scope of this study.

A good data collection method for the Persian Gulf's metocean in relation to aquaculture should combine direct measurements, satellite observations, and numerical model outputs. Instruments like ADCPs, buoys, tide gauges, and CTDs help measure currents, waves, sea level, and water quality. Satellite data (e.g., from MODIS [32]) provide useful large-area information like sea surface temperature and chlorophyll. Additionally, local and global ocean models (such as HYCOM [33]) can supply continuous and historical datasets needed for planning and monitoring aquaculture operations. Satellites such as MODIS help monitor sea surface temperature and algae. Weather stations add wind and air data. Aquaculture sites should be checked often for temperature, oxygen, pH, and ammonia. GIS can help choose safe and useful locations. All data should be stored in one system, checked for accuracy, and used to make models and simple reports. This helps farmers and planners protect the sea and grow healthy fish.

Site selection in this study is based on a set of geophysical, environmental, and logistical criteria aimed at identifying areas suitable for fish cage culture. These include water depth and distance from the shoreline. Sea surface temperature, wind and wave conditions, and current speed limits are dynamic variables that can exhibit significant seasonal and interannual variability, potentially influencing operational feasibility and productivity. In this study, a general approach has been adopted to avoid the complexities associated with accounting for interannual variations. For example, a conservative temperature range was defined to ensure that environmental conditions remain broadly suitable for the cultivation of conventional aquaculture fish species throughout the year, thereby minimizing the risk of temperature-related production limitations. Additionally, the analysis excludes areas that would interfere with coastal and navigational activities or overlap with designated environmental protected areas, which are typically fixed but may be subject to future regulatory changes. Acknowledging the temporal nature of some criteria is essential for understanding the robustness and adaptability of proposed sites. It should be noted that this study aims to estimate the aggregative total capacity for mariculture along the northern shoreline of the Persian Gulf, rather than to prescribe specific site-level recommendations. While the applied

criteria help identify broadly suitable areas, a detailed investigation and feasibility study would be essential for each prospective sub-area to account for localized environmental, technical, and regulatory conditions.

The primary approach adopted in this study for identifying suitable zones for fish cage culture assumes that all areas along the coastline are initially considered appropriate. However, any area that fails to meet the acceptable range for any of the specified criteria is excluded from consideration. In other words, all criteria are treated equally, and failure to satisfy even one constraint results in the disqualification of that region as a potential site.

A comprehensive economic feasibility assessment of all potential cage culture projects was beyond the scope of this study. It is important to note that the economic viability of aquaculture initiatives is influenced not only by site-specific physical, socio-political and socio-economic conditions but also by investor-specific factors such as financial capacity, operational background, and strategic goals. Such variables that are not accessible to the authors at this stage. Therefore, the focus of the present study is limited to identifying coastal areas that are biophysically and hydrodynamically suitable for fish cage culture, providing a foundational framework for further, more detailed investigations.

The identification and selection of sites for coastal and marine aquaculture (mariculture) involved integrating satellite imagery with various mapped datasets, including environmentally protected areas, navigation routes, infrastructure (e.g., ports and offshore facilities), and coastal features such as bathymetry and topography, wind and wave and current characteristics. Geographic Information Systems (GIS) were employed to conduct spatial analysis on the collected datasets, enabling the identification of suitable aquaculture sites through a stepwise process. This process included data collection and compilation, database integration and preparation, initial mapping via database analysis, conversion and transfer of information layers to ILWIS software, elimination of unsuitable areas based on predefined criteria, and finally, the export of areas meeting the acceptable site characteristics. The essential criteria that were considered on a broad scale for the selection of potentially appropriate sites for cage aquaculture include the following items:

2.1. Water Depth and Distance from Shoreline

Water depth is likely the most critical criterion for the siting of cages, as it facilitates the dispersion of particulate matter and enhances water exchange. Additionally, deeper nets can maintain more stable water quality and temperature while reducing water movement during storms [7]. Bathymetric data were collected from various sources, including the National Cartographic Center (INCC), ETOPO, and the General Bathymetric Chart of the Oceans (GEBCO). Based on our field investigations and interviews with industry professionals actively engaged in fish cage culture, it is evident that the most prevalent type of cages used in the Persian Gulf region are HDPE floating cages with nets extending to a depth of 10 meters. Consequently, we recommend a depth range of 20 to 60 meters for identifying optimal aquaculture sites for these fish species.

The location of fish breeding sites should be in proximity to a port with a pier, allowing boats from the farm to berth in a sheltered area. This proximity ensures efficient access for distributing farm products, transporting food, juvenile fish, fuel, equipment, and other necessary materials [24]. It also facilitates increased site inspections by farm managers and experts. To ensure timely transportation, the travel duration from the port to the farm should not exceed 2 hours, corresponding to a maximum distance of 20 kilometers assuming a typical boat speed of 7 knots. Practically, suitable harbors for berthing farm boats should accommodate vessels of at least 15 meters in length. This approach accounts for the currently available production capacity. However, to estimate

the ultimate (nominal) aquaculture potential of the northern Persian Gulf coastline, proximity to existing ports and harbors must be excluded from consideration, and only the distance to the nearest shoreline should be applied. Consequently, fish production capacity is calculated for both scenarios: the ultimate capacity based on geographic potential alone, and the current capacity constrained by existing infrastructure.

2.2. Sea Surface Temperature

The temperature range of the water must be appropriate for the species being cultured. Consequently, seawater temperature data should be collected and analyzed to inform species selection. Temperature directly influences fish metabolism and, subsequently, their oxygen consumption, activity levels, and the production of ammonia and carbon dioxide. In general, sea surface temperatures in the Persian Gulf have shown significant variability, ranging from about 22°C to 35°C, influenced by seasonal and climate-related factors [34], [14]. Recent studies suggest that the optimal water temperature for marine fish cage culture in the Persian Gulf ranges from approximately 20°C to 32°C.A research conducted in northwestern parts of the Persian Gulf indicates that water temperatures varied from 11.8°C to 32.5°C, with significant environmental and ecological impacts observed within this range [30]. These temperature ranges are consistent with general recommendations for marine aquaculture, emphasizing the importance of monitoring and managing water temperatures to ensure the sustainability of fish stocks in the region. In this study, although resilient fish species are considered, regions with a temperature range of 13-30°C are presumed suitable for aquaculture. In this study, oceanographic data were obtained from HYCOM [35].

2.3. Wind and Wave Conditions

Strong winds, such as typhoons and cyclones can destroy all structures above the water and may damage in-water structures. The optimal wind speed range for cage aquaculture in the Persian Gulf has been identified to ensure effective water circulation, minimize structural stress on cages, and maintain water quality. Wind speeds between 3 to 6 m/s are ideal for these conditions. Recent studies suggest that for floating cages, the maximum permissible wind and wave limits are 40 km/hr (11.11 m/s) and 1 m respectively [36]. Another implication of high wind speeds is the consequent wave induced turbulence which drastically degrade the fish production quality and quantity. For instance, research by Barbier et al. [37] highlights that high wind speeds can lead to significant turbulence, which may cause increased stress on cage structures and potentially disrupt the growing environment for aquatic species. Similarly, a study by UNDP/FAO [38] emphasizes that maintaining wind speeds below 10 knots (5.14 m/s) for floating cages helps in balancing water circulation and minimizing the risk of damage to the cages. Accordingly, the wave heights should not exceed 1.0 m. The wind field dataset (ERA5) was collected from the European Centre for Medium-Range Weather Forecasts (ECMWF) and the National Centers for Environmental Prediction (NCEP) data center [39]. In the current study, weather condition surveys were conducted, and areas with wind speeds below 15 nautical miles per hour (7.7 m/s) were identified as suitable for the construction of cage aquaculture sites.

Besides the cage structure stability, there is a more restricting criterion imposed by waves. Based on interviews with farmers and experts, it was determined that delaying fish feeding for three to five days annually poses no issues in the breeding process. In rudimentary feeding methods, boat activity is restricted to maximum wave heights of less than one meter. Jedari Attari et al. [40] developed a comprehensive wave hindcasting/forecasting system for the Persian Gulf. Analysis on the 25-year long wave climate data reveals that some areas in the study area experience severe wave heights repeatedly, making them inappropriate for cage culture practice.

Therefore, locations in the Persian Gulf experiencing storm events with waves exceeding 1 meter and lasting longer than three days are deemed unsuitable. This determination ensures additional security by excluding areas where such events occur more than six times in 25 years (approximately every four years on average).

2.4. Current Speed limits

Adequate water exchange in cage culture systems is vital for oxygen supply and waste removal, but strong currents can deform cages and reduce their volume. Maintaining optimal current speeds ensures water quality, effective waste dispersion, and reduced stress on both cages and cultured species. The currents within the Persian Gulf are primarily tide-dominated, meaning tidal forces largely govern their movement and circulation patterns. [41], [42], [43]. López et al. [44] conducted a study to on structural stress imposed on the collar HDPE pipe of the fish nets and suggested that while existence of minimum currents maintain the quality of surrounding water, current speeds beyond 1 m/s exert excessive stresses on the structure of the nets. Huang et al., [45] also suggested that farming sites should be positioned in zones where the current velocities are below 1 m/s. Prema [36] suggests a range between 0.05 m/s to a maximum of 1 m/s would be satisfying current velocity for cage culture. Analysis on hydrodynamic current data [46] reveals that the Persian Gulf experiences tide-dominated currents, with typical velocities in coastal areas ranging from 0 to 0.8 m/s. In certain locations, such as areas characterized by funneling and shallowness, current velocities can reach up to 1.2 m/s. In this study, a flow current range of 0.3 (a minimum to ensure adequate carrying capacity of the site) to 0.8 m/s (a maximum to avoid imposing stress both on structures and fish) has been identified as suitable for the construction of cage aquaculture sites. Maintaining current speeds within this range ensures efficient waste removal and optimal oxygen levels, which are critical for the health of the cultured species.

2.5. Avoiding interference with Coastal and Navigational Activities

Mariculture site selection must consider several exclusion zones to ensure operational safety and environmental protection [47]. Sites should be located at least 1 km away from waste dumping points and coastal underwater pipe outlets to prevent contamination. Additionally, areas with underwater cables or conduits should maintain a minimum distance of 200 m to avoid interference with moorings or cages. Due to potential military activities, such as navigation routes or firing ranges, a buffer zone of 5 km is recommended around areas of military importance. Furthermore, aquaculture cages should be kept at least 500 m away from vessel anchorage areas, typically found near harbors or industrial zones, where marine traffic standby anchorage is managed. For optimal fish production and safety considerations, fish cage licenses should be situated at least 1 km away from designated navigation routes to mitigate disturbances caused by large vessels, including waves and underwater engine noise. Additionally, to minimize potential conflicts with tourism activities, mariculture sites should be located at least 3 km away from tourist hotels and beaches, particularly in areas where tourism is integrated with residential districts near major urban centers. Furthermore, due to security sensitivities, aquaculture facilities should avoid placement near national border areas.

2.6. Avoiding Environmental Protected Areas

The Persian Gulf coast supports coral reefs extending from Khark Island in the northwest to Qeshm and beyond in the southeast [48]. Recent field observations indicate that the northern coastline of the Persian Gulf harbors more coral than previously reported [28]. These reefs are critically important for fisheries, serving as nurseries for juvenile fish and refugia for adults. Fisheries yields from reef areas are significantly higher than those from adjacent sediment plains. The major threats to the

reefs of the Persian Gulf include sedimentation, pollution, nutrient enrichment, and overfishing [49]. These threats are well-documented globally [50]. Overfishing is considered a significant factor in the global decline of coral reefs [51], while others argue that nutrient increases are a major driver of this decline [52]. Harmful algal blooms, such as red and brown tides driven by nutrient influx, pose a threat to the Persian Gulf reefs and those in other regions. For example, Namin et al. [53] reported widespread coral mortality near the Strait of Hormuz following a red tide event in 2008-2009.

The development of aquaculture in environmentally sensitive areas necessitates a meticulous approach to minimize potential risks to these ecosystems [54] [55]. It is imperative to recognize that the restoration of natural habitats can be a protracted process, often demanding significant time and resources [56]. Stakeholders must prioritize sustainable practices that not only enhance aquaculture productivity but also preserve the ecological integrity of affected regions. Through careful planning and responsible management, we can ensure that the benefits of aquaculture do not come at the expense of our vital natural resources. To safeguard protected areas, a minimum distance of 5 km from these sites has been adhered to. The dataset identifying marine protected areas was compiled through collaboration between consulting teams and the Department of Environment, likely based on GPS positions and distributed in GIS format. It is crucial to prioritize the protection of sites of particular ecological significance, including marine protected areas, conservation areas, habitats crucial for bird populations, wetlands supporting waterfowl, coral reefs, tidal flats and mangrove forests.

3. Result and Discussion

In this study, we employed a Geographic Information System (GIS) platform to identify suitable areas for cage aquaculture in the Persian Gulf. Various constraining parameters were collectively considered, including navigational corridors, oil and gas pipelines, protected areas, unsuitable current speeds and wave heights, inconvenient water depths, and distance from the shoreline. Figure 2 maps the spatial distribution of these restricting criteria.

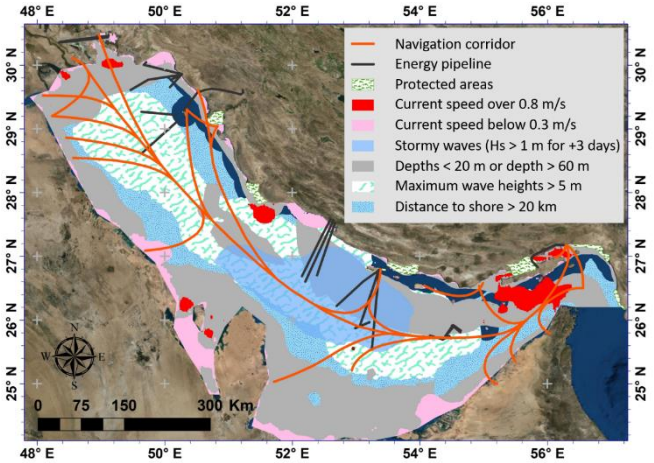


Figure 2: Mapping restricting criteria.

Unfortunately, there is a lack of scientific evidence or official documentation to ascertain the extent of capacity utilization within the fish cage culture sector in the Persian Gulf. According to a report from a reputable news agency, the current production from fish cage culture in this region amounts to approximately 40 kilotons [56]. Despite this production figure, an evaluation of the existing roadways and land

infrastructure indicates that there remains substantial potential for further investment in the industry, suggesting an opportunity for growth and enhancement of production capabilities. Figure 3 depicts the areas identified as suitable for cage culture based on GIS layer analysis. After excluding non-favorable regions, six distinct areas (A to F) have been identified as potentially suitable for profitable and sustainable fish cage culture practices, ensuring the protection of environmentally valuable areas. Table 1 lists the geographical characteristics and hydrodynamical properties of the proposed selected sites, along with current and future nominal potential fish cage culture capacity. Based on calculations, it is estimated that the northern shoreline of the Persian Gulf currently possesses the capacity to support up to 200 kilotons of fish production through cage culture. This estimation takes into account the accessibility of inland facilities and transportation routes essential for the efficient utilization of these areas.

However, should the entirety of the coastline be developed and suitable infrastructure (powerline, roads, harbors, …) be established along the shoreline, the nominal potential capacity for fish aquaculture yields could reach nearly one million tons annually. This ambitious projection underscores the significant opportunities available within the sector, contingent upon strategic planning and investment in sustainable practices. Such developments would not only enhance food security but also contribute to the economic vitality of coastal communities. It should be carefully noted that the estimated value presented herein serves as a highly hypothetical approximation, derived primarily from the geometric assessments and spatial evaluations of identified desirable regions. This estimate does not take into account the ecological constraints that inherently influence biological systems. A comprehensive investigation into nutrient cycling and the intricate biogeochemical processes at play would be essential to elucidate the practical maximum capacity for aquaculture within the specified area. Understanding these dynamics is critical for informed decision-making regarding sustainable practices in aquaculture development [57].

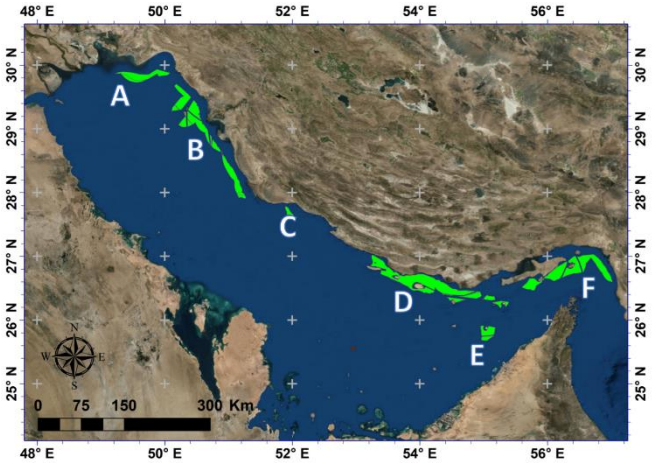


Figure 3: Suitable Areas (A~F) for fish cage culture along the northern coastlines of the Persian Gulf.

The main scope of this study was to spot suitable sites for conducting cage culture practice. We have not considered the biogeochemical processes involved in aquaculture. Consequently, rough estimation of aquaculture production capacity just based on geometry, physical and general environmental restrictions may result in extraordinary huge numbers which does not match with biogeochemical carrying

capacity of the study area. For future research, it is recommended to focus on enhancing the sustainability and resilience of mariculture operations through a robust monitoring framework. A comprehensive approach should involve assessing current fish farm monitoring initiatives, designing a tailored program suitable for the Persian Gulf environment, establishing standardized data collection protocols, leveraging collected data for impact evaluations, and crafting a specialized monitoring guide that addresses the region's distinct geographic characteristics. These efforts are pivotal for maintaining operational viability and environmental harmony amidst dynamic challenges and changing circumstances. Additionally, integrating principles from Integrated Multi-Trophic Mariculture (IMTM) could optimize environmental conservation efforts which involves cultivating multiple species across different trophic levels to utilize eutrophic waste, particularly from finfish. This approach mimics natural nutrient cycling, reducing eutrophic input and maintaining environmental capacity [58], [59]. By implementing IMTM strategies, future studies can effectively mitigate environmental impacts, sustain operational viability, and preserve biodiversity in coral reefs and seagrass beds amid evolving challenges [60], [61].

Table 1. Geographical, hydrodynamical, and fish production characteristics of selected proposed sites.

Areas	A	B	C	D	E	F	Total
Total Area (km2)	758.01	2591.4	183.55	3561.66	405.61	2440.49	9940.72
Average Depth (m)	14	28	32	38.1	45	34.2	-
Average Distance to Shoreline (km)	17.5	12.7	14.3	7.7	7.6	8.6	-
Average No. of Excess Wave Events in 25 years	1	1.3	1.4	1.5	3	1	-
25-Year Significant Wave Height	3.53	3.18	3.91	4.42	4.87	3.33	-
Averaged Maximum Current Speed (m/s)	0.53	0.5	0.41	0.6	0.62	0.53	-
Averaged Distance to Environmentally Protected Areas (km)	269.5	202.7	64.7	183.9	271	184	-
Averaged Distance to Wild-Life Habitat Areas (km)	67.8	52.2	178.7	112.3	197	175	-
Current Fish Yield (kt/year) [a]							40 [a]
Current Fish Production Capacity (kt/year) [b]	6.8	66	7.4	65	6.4	48.4	200 [b]
Nominal Ultimate Fish Production Capacity (kt/year) [c]	45	355	17	380	39	160 [d]	996 [c]

a) This value was obtained based on estimates reported by news agencies [56]. To date, no official reports from authorized institutions or peer-reviewed scientific references have been published to verify this figure.

b) It is important to note that the current potential capacity is contingent upon the availability of essential inland infrastructure, including transportation routes, power lines, harbors, utilities, and industrial support services.

c) This estimation is derived from geometric analysis and a limited set of criteria considered in this study. Three key assumptions underpin these projections: (1) that all prerequisite infrastructure along the coastline is fully developed, and (2) that the overall carrying capacity of the Persian Gulf (being a semi-enclosed water body) has not

been accounted for. A thorough ecological and biophysical assessment is needed to understand the cumulative impact of organic loading in an environment with limited self-purification capacity. Additional factors, such as the emergence of contagious diseases that can significantly reduce yields, must also be considered. Furthermore (3), socio-economic conditions will inevitably influence the extent to which this industry can sustainably expand.

d) Regarding Site F, despite its considerable spatial extent, it has been assigned a lower future nominal capacity. This assessment is primarily due to its dependence on a few remote and relatively small islands for land-based infrastructure support. Even under the assumption that these islands are fully developed and populated, they are unlikely to offer the level of logistical and industrial support required for the intensive demands of cage culture operations.

4. Conclusions

In this study, a set of scientifically grounded criteria was applied to identify suitable sites along the northern coastline of the Persian Gulf. These criteria included water depths ranging from 20 to 60 meters, proximity to ports within 20 kilometers, and sea surface temperatures between 13°C and 30°C. Sites were limited to areas with maximum wind speeds of 7.7 m/s and excluded zones frequently affected by waves during storm conditions (defined as wave heights exceeding 1 meter for more than three consecutive days occurring more than once every four years). Additionally, acceptable current speeds ranged from 0.3 to 0.8 m/s, and a 5-kilometer buffer zone was maintained to avoid interference with both navigation/coastal activity areas and environmentally protected zones. Using these criteria, GIS layers were generated wherein areas not meeting all criteria were excluded. The resulting GIS layers identified several suitable spots for establishing cage aquaculture farms, extending from the northwest coastal areas in front of Mahshahr (Khozestan Province) to the southeast, strait of Hormuz (Hormozgan Province). The developed approach not only enhances the potential for sustainable aquaculture development but also serves as a model for integrating spatial analysis with environmental management in coastal and marine ecosystems. Implementing the cage culture practice in the sites proposed by this study ensures a profitable and sustainable mariculture business and moreover mitigates the potential environmental hazards threatening the precious coral reefs and coastal habitats in the region. The findings of this study indicate that the northern coast of the Persian Gulf possesses the capacity to sustain approximately 200,000 tons of fish production annually through cage culture, given the constraints of existing infrastructure. Notably, the region's theoretical maximum potential could reach nearly one million tons per year, provided that spatial suitability is fully realized without logistical restrictions. However, it is imperative to acknowledge that this projection is based on a spatial analysis utilizing a limited array of physical and operational criteria and does not account for critical ecological factors, including the overall carrying capacity of the Persian Gulf as a semi-enclosed water body. Therefore, a comprehensive investigation into the biogeochemical processes and total carrying capacity of the region is essential prior to the implementation of aquaculture in all identified suitable areas proposed by this study. Nevertheless, integrating future ecological monitoring and feedback systems, such as Integrated Multi-Trophic Aquaculture (IMTA) and Life Cycle Assessment (LCA), is essential for promoting sustainable resource use and minimizing environmental impact [62], [63]. These systems enable real-time data collection, adaptive management, and informed decision-making to enhance ecosystem health, resilience, and long-term productivity.

Funding Statement

This research received no external funding.

Conflict of Interest

The authors declare that they have no conflict of interest.

Acknowledgement

The authors would like to acknowledge the support by Oceans Research Co. for providing access to data. The data over the study area can be accessible through info@oceansresearch-co.com.

References

1. Ma Z, Qin J. New techniques in marine aquaculture. J Mar Sci Eng. 2023;11(12):2239. https://doi.org/10.3390/jmse11122239
2. Li J, Shapira P, Gao L, Kwon S. Emerging development pathways of marine aquaculture: Key trends and dynamics. ICES J Mar Sci. 2021;78(1):315–326. https://doi.org/10.1093/icesjms/fsaa173
3. Føre H, Filgueira R, FAO. Towards environmental sustainability in marine finfish aquaculture. Frontiers in Marine Science. 2018.
4. Asche F. Farming the sea. Mar Resour Econ. 2008;23:527–547. https://www.journals.uchicago.edu/doi/abs/10.1086/mre.23.4.42629678
5. Lucas JS, Southgate PC. Reproduction, life cycles and growth. In: Lucas JS, Southgate PC, editors. Aquaculture: Farming Aquatic Animals and Plants. Chichester: John Wiley & Sons; 2012. p.113–126.
6. Godfray HCJ, Beddington JR, Crute IR, Haddad L, Lawrence D, Muir JF, Toulmin C. Food security: The challenge of feeding 9 billion people. Science. 2010;327:812–818. https://doi.org/10.1126/science.1185383
7. FAO. The State of World Fisheries and Aquaculture 2014: Opportunities and Challenges. Rome: Food and Agriculture Organization of the United Nations; 2014.
8. Flaaten O. Fisheries and Aquaculture Economics. Norway: Plant and Industry Management; 2018.
9. Loya Y, Lubinevsky H, Rosenfeld M, Kramarsky-Winter E. Nutrient enrichment caused by in situ fish farms at Eilat, Red Sea is detrimental to coral reproduction. Mar Pollut Bull. 2004;49:344–351. https://doi.org/10.1016/j.marpolbul.2004.06.011
10. Eng CT, Paw JN, Guarin FY. The environmental impact of aquaculture and the effects of pollution on coastal aquaculture development in Southeast Asia. Mar Pollut Bull. 1989;20:335–343. https://www.sciencedirect.com/science/article/abs/pii/0025326X89901574
11. Edinger EN, Jompa J, Limmon GV, Widjatmoko W, Risk MJ. Reef degradation and coral biodiversity in Indonesia: effects of land-based pollution, destructive fishing practices and changes over time. Mar Pollut Bull. 1998;36:617–630. https://www.sciencedirect.com/science/article/abs/pii/S0025326X98000472?via%3Dihub
12. Shaihidul I, Tanaka. Impacts of pollution on coastal and marine ecosystems including coastal and marine fisheries and approach for management. Mar Pollut Bull. 2004.
13. Naylor RL, Hardy RW, Buschmann AH, et al. A 20-year retrospective review of global aquaculture. Nature. 2021;591:551–563. https://doi.org/10.1038/s41586-021-03308-6
14. Abbasian M, Haghshenas SA, Shah-Hosseini M, Farhangmehr A, Rezai H, Razavi Arab A, Risk MJ. Biodeposit dispersion around a deep cage finfish farm in the Northern Persian Gulf. Regional Studies in Marine Science. 2023;63. https://doi.org/10.1016/j.rsma.2023.102950.
15. Gao QF, Dong SL. Cage Farming of Fish in Open Waters. In: Dong SL, Tian XL, Gao QF, Dong YW, editors. Aquaculture Ecology. Singapore: Springer; 2023.
16. Lapenkov A, Guzeva A, Zaripova K, Slukovskii Z. The seasonal dynamics of geochemical characteristics of sediments in the impact zone of the fish farm (Lake Ladoga, Russia). Aquaculture Fisheries. 2023.
17. Jiang H, Ji Y, Zhang M. Modeling impact of culture facilities on hydrodynamics and solute transport in marine aquaculture waters of North Yellow Sea. Water Sci Eng. 2023.
18. Liu Y, Chen Y, Ge C. Numerical simulation of the settling flux of biodeposition in a bay with cage culture through similarity theory and a simplified pollution source. J Ocean

Univ China. 2024;23:247–254. https://doi.org/10.1007/s11802-023-5696-0
19. Johannesen Á, Patursson Ø, Kristmundsson J, Dam SP, Mulelid M, Klebert P. Waves and currents decrease the available space in a salmon cage. PLoS ONE. 2022;17(2):e0263850. https://doi.org/10.1371/journal.pone.0263850
20. Faltinsen OM, Shen Y. Wave and current effects on floating fish farms. J Mar Sci Appl. 2018;17:284–296. https://doi.org/10.1007/s11804-018-0033-5
21. Lee CW, Kim YB, Lee GH, Choe MY, Lee MK, Koo KY. Dynamic simulation of a fish cage system subjected to currents and waves. Ocean Eng. 2023.
22. Lader P, Fredriksson D, Volent Z, Decew J, Rosten T, Strand IM. Wave response of closed flexible bags. J Offshore Mech Arctic Eng. 2017;139. https://doi.org/10.1115/1.4036676
23. Swift MR, Fredriksson DW, Unrein A, Fullerton B, Patursson O, Baldwin K. Drag force acting on biofouled net panels. Aquac Eng. 2006. https://doi.org/10.1016/j.aquaeng.2006.03.002
24. FAO. Cage aquaculture, Regional reviews and global overview. Fisheries Technical Paper 498. 2007.
25. Micael J, Costa AC, Aguiar P, Medeiros A, Calado H. Geographic information system in a multi-criteria tool for mariculture site selection. Coast Manage. 2015;43(1):52–66. https://doi.org/10.1080/08920753.2014.985178
26. Salama AJ, Satheesh S, Balqadi AA, et al. Identifying suitable fin fish cage farming sites in the Eastern Red Sea Coast, Saudi Arabia. Thalassas. 2016;32:1–9. https://doi.org/10.1007/s41208-015-0001-7
27. Jayanthi M, Samynathan M, Thirumurthy S, et al. Mapping coastal lagoon characteristics for the aquaculture suitability using multi-criteria decision support (MCDS) spatial analysis: A case study from south-east coast of India. J Earth Syst Sci. 2021; 130:56. https://doi.org/10.1007/s12040-021-01560-y
28. Risk MJ, Haghshenas SA, Razavi Arab A. Cage aquaculture in the Persian Gulf: a cautionary tale for Iran and the world. Mar Pollut Bull. 2021; 166. https://doi.org/10.1016/j.marpolbul.2021.112079
29. Regunathan C, Kitto MR. Persian Gulf fish culture in Iran–pointers for success. Aquaculture Asia. 2005.
30. Jahani N, Nabavi SNB, Dehghan Madiseh S, Mortezaie SRS, Fazeli N. The effect of marine fish cage culture on benthic communities using BOPA index in Ghazale Creek. Iranian J Fisheries Sci. 2012;11(1):78–88. doi:10.22092/ijfs.2018.114186
31. FAO/World Bank. Aquaculture zoning, site selection and area management under the ecosystem approach to aquaculture. A handbook. Rome: FAO & The World Bank; 2017.
32. Yazdanbakhsh S, Koochakzaei A, Achachluei MM. Sclerochronology of Callista umbonella to extract the transfer function for reconstructing climates in some parts of Persian Gulf. Geo-Mar Lett. 2025;45(2):15.
33. Yao F, Johns WE. A HYCOM modeling study of the Persian Gulf: 2. Formation and export of Persian Gulf Water. J Geophys Res. 2010;115:C11018. doi:10.1029/2009JC005788.
34. Noori R, Tian F, Berndtsson R, Abbasi MR, Naseh MV, Modabberi A, Soltani A, Kløve B. Recent and future trends in sea surface temperature across the Persian Gulf and Gulf of Oman. PLoS One. 2019;14(2):e0212790. doi:10.1371/journal.pone.0212790
35. Chassignet EP, Hurlburt HE, Metzger EJ, Smedstad OM, Cummings J, Halliwell GR, et al. U.S. GODAE: Global Ocean prediction with the Hybrid Coordinate Ocean Model (HYCOM). Oceanography. 2009; 22(2):64–75. https://link.springer.com/chapter/10.1007/1-4020-4028-8_16
36. Prema D. Importance of water quality in marine life: cage culture. Tech Cent Mar Fish Res Inst. 2009.
37. Barbier E, Oppedal F, Hvas M. Atlantic salmon in chronic turbulence: Effects on growth, behaviour, welfare, and stress. Aquaculture. 2024; 582:740550. https://doi.org/10.1016/j.aquaculture.2024.740550.
38. UNDP/FAO. Site selection criteria for marine finfish netcage culture in Asia. UNDP/FAO Reg Seafarming Dev

Demonstration Project. Network Of Aquaculture Centres in Asia; 1989.
39. Hersbach H, Bell B, Berrisford P, et al. Complete ERA5 from 1940: Fifth generation of ECMWF atmospheric reanalyses of the global climate. Copernicus Climate Change Service (C3S) Data Store; 2017. DOI:10.24381/cds.143582cf.
40. Jedari Attari M, Haghshenas SA, Soltanpour M, Allahyar MR, Ghader S, Yazji D, Razavi Arab A, Hajisalimi Z, Ahmadi SJ, Bakhtiari A. Developing the Persian Gulf wave forecasting system. J Coastal Mar Eng. 2018;1(1):13–18.
41. Ranji Z, Soltanpour M. Optimization of bottom friction coefficient using inverse modeling in the Persian Gulf. Ocean Sci J. 2021;56:331–343. doi:10.1007/s12601-021-00040-0
42. Razzaghi S, Haghshenas SA, Ghader S, Yagi D, Delkhosh E, Farhangmehr A. 3D numerical modelling of shallow and deep water currents in the Persian Gulf. Iran J Geophys. 2019;13(3):69–85.
43. Mashayekh Poul H, Backhaus J, Dehghani A, Huebner U. Effect of subseabed salt domes on tidal residual currents in the Persian Gulf. J Geophys Res Oceans. 2016;121:3372–3380. doi:10.1002/2015JC011421
44. López J, Hurtado CF, Toledo JP, Suazo G, Zamora V, Queirolo D, Gutiérrez A. Structural integrity of a submersible sea cage exposed to extreme oceanographic conditions. J World Aquac Soc. 2024;55(3):e13052. https://doi.org/10.1111/jwas.13052
45. Huang C, Tang H, Liu J. Effects of waves and currents on gravity-type cages in the open sea. Aquac Eng. 2008;38. https://www.sciencedirect.com/science/article/abs/pii/S0144860908000022
46. Jedari Attari M, Bakhtiari A, Haghshenas SA, Hamidian JE, Sasaki J. Long-term suspended sediment transport patterns over the North-Western part of the Persian Gulf, applying a three-dimensional hydrodynamic model. In: Book of abstracts, 13th Int Conference Cohesive Sediment Transport Processes; 2015 Sep.
47. Yoo SL, Jeong JC. Safe navigation distance between marine routes and aquaculture farms in South Korea using Gaussian mixture model. Sensors (Basel). 2020;20(5):1246. doi:10.3390/s20051246
48. Burt J, Hume B, D'Angelo C, Baker AC, Riegl B. Corals from the Persian/Arabian Gulf as models for thermotolerant reef-builders: prevalence of clade C3 Symbiodinium, host fluorescence and ex-situ temperature tolerance. Mar Pollut Bull. 2014. https://www.sciencedirect.com/science/article/abs/pii/S0025326X1200570X?via%3Dihub
49. Maghsoodi M, Soltanpour M, Haghshenas SA. Study of the effects of suspended sediment transport on coral reefs (case study–Chabahar Bay). In: Proceedings 11th Int Conference on Coasts, Ports & Marine Structures (ICOPMAS); Tehran; 2014.
50. Risk MJ, Edinger E. Impacts of sediment on coral reefs. In: Encyclopedia of Modern Coral Reefs. 2011.
51. Jackson J. Reefs since Columbus. Coral Reefs. 1997;(Suppl 1):S23–S32. https://doi.org/10.1007/s003380050238
52. Lapointe BE. Nutrient thresholds for bottom-up control of macroalgal blooms on coral reefs in Jamaica and southeast Florida. Limnol Oceanogr. 1997;42(5 Pt 2):1119–1131. https://doi.org/10.4319/lo.1997.42.5_part_2.1119
53. Namin KS, Risk MJ, Hoeksema BW, Zohari Z, Rezai H. Coral mortality and serpulid infestations associated with red tide, in the Persian Gulf. Coral Reefs. 2010;29:509. doi:10.1007/s00338-010-0601-x
54. Pérez OM, Telfer TC, Ross LG. Geographical information systems-based models for offshore floating marine fish cage aquaculture site selection in Tenerife, Canary Islands. Aquac Res. 2005. https://doi.org/10.1111/j.1365.
55. Piccolotti F, Lovatelli A. Construction and installation of hexagonal wooden cages for fish farming: A technical manual. FAO Fisheries and Aquaculture Technical Paper. 2013.
56. Khabar Farsi. https://khabarfarsi.com/u/20535945 [Accessed 2025 Jul 23].
57. Nasseri Doust Sh, Abbasian M, Haghshenas SA, Risk MJ, Downs CA. Integrating hydrodynamic modeling with ecological risk assessment for selecting sites for artificial reef deployment: avoiding coastal pollution risks in Kish Island, Persian Gulf.

Oceans. 2024;5(4):51. doi:10.3390/oceans5040051
58. Troell M, Joyce A, Chopin T, Neori A, Buschmann AH, Fang J-G. Ecological engineering in aquaculture—potential for integrated multi-trophic aquaculture (IMTA) in marine offshore systems. Aquaculture. 2009;297:1–9. https://doi.org/10.1016/j.aquaculture.2009.09.010
59. Chopin T, Robinson SMC, Troell M, Neori A. Multitrophic Integration for Sustainable Marine Aquaculture. In: Jorgensen SE, Fath BD, editors. The Encyclopedia of Ecology. Ecological Engineering. Elsevier; 2014.
60. Hallock P. Global change and modern coral reefs: New opportunities to understand shallow-water carbonate depositional processes. Sediment Geol. 2005;175:19–33. https://www.sciencedirect.com/science/article/abs/pii/S0037073805000515
61. Neori A, Chopin T, Troell M, Buschmann AH, Kraemer GP. Integrated aquaculture: rationale, evolution and state of the art emphasizing seaweed biofiltration in modern mariculture. Aquaculture. 2004;231:361–391. https://doi.org/10.1016/j.aquaculture.2003.11.015
62. Hughes C, King JW. Habitat suitability modelling for an integrated multi-trophic aquaculture (IMTA) system along Europe's Atlantic coast. Ecol Model. 2023;484:110459. doi:10.1016/j.ecolmodel.2023.110459.
63. Hala AF, Chougule K, Cunha ME, Mendes MC, Oliveira I, Bradley T, Forbes J, Speranza LG. Life cycle assessment of integrated multi-trophic aquaculture: A review on methodology and challenges for its sustainability evaluation. Aquaculture. 2024;590:741035. doi:10.1016/j.aquaculture.2024.741035.

© 2025 by the authors. Licensee SCU, Ahvaz, Iran. This article is an open access article distributed under the terms and conditions of the Creative Commons Attribution 4.0 International (CC BY 4.0 license) (http://creativecommons.org/licenses/by/4.0/).

Journal of Hydraulic Structures

Volume 12 – Issue 2 – April 2026

Contents:

01 Geostatistical Analysis of Groundwater Levels at Tangab Dam Using IDW, Kriging, and Sequential Gaussian Simulation

Reza Dehshibi; Hadi Farhadian

22 Analytical solutions for steady downward flow of a wetting fluid in unsaturated soil using the Adomian decomposition method

Hamed Reza Zarif Sanayei

34 Assessing the Impact of Multi-Reservoir Rationing on Downstream Drought Occurrence: A Case Study of Dez and Gotvand Reservoirs

Sama Banitamim; Seyed Mohammad Ashrafi; Arash Adib

51 Numerical Study of Impulsive Wave Overtopping at Rigid Hydraulic Structures Using Incompressible Smoothed Particle Hydrodynamics Model

Rasoul Memarzadeh

74 The Optimal Selection of Submerged Vanes Geometric Dimensions in Curved Channels with Sediment Flow

Parisa Rezaei; Elham Fazel Najafabadi; Mohammad Shayannejad

103 Assessment of Site Suitability and Capacity for Sustainable Aquaculture Development Along the Northern Persian Gulf Coast

Morteza Jedari Attari; Aref Farhangmehr

Shahid Chamran University of Ahvaz